Mastering the influence of thermal fluctuations on the magnetization switching dynamics of spintronic devices

Bertrand Lacoste

UNIVERSITÉ DE GRENOBLE

THÈSE

POUR OBTENIR LE GRADE DE

Docteur de l'Université de Grenoble

SPÉCIALITÉ : **Physique**

ARRÊTÉ MINISTÉRIEL : 7 août 2006

PRÉSENTÉE PAR

Bertrand Lacoste

THÈSE DIRIGÉE PAR **Bernard Dieny**

PRÉPARÉE AU SEIN DU **Laboratoire SPINTEC**
ET DE L' **Ecole Doctorale de Physique de Grenoble**

Mastering the influence of thermal fluctuations on the magnetization switching dynamics of spintronic devices

Maîtrise de l'influence des fluctuations thermiques sur la dynamique de commutation des dispositifs spintroniques

THÈSE SOUTENUE PUBLIQUEMENT LE **13 Novembre 2013**,
DEVANT LE JURY COMPOSÉ DE :

Mme Claudine Lacroix
D.R. CNRS, Institut Néel, CNRS/UJF, Grenoble, Président
Mr André Thiaville
D.R. CNRS, Laboratoire de Physique des Solides, Université Paris XI, Orsay, Rapporteur
Mr Vincent Cros
D.R. CNRS, Unité mixte de Physique CNRS/Thalès, Palaiseau, Rapporteur
Mr Stéphane Mangin
Prof., Institut Jean Lamour, Nancy, Examinateur
Mr Olivier Klein
Ing. CEA, IRAMIS, CEA, Saclay, Examinateur
Mr Bernard Dieny
D.R. CEA, SPINTEC, Grenoble, Directeur de thèse

Abstract : Spin-transfer torque magnetic random-access memory (STTRAM) are very promising non-volatile and enduring memories to replace charged-based RAM. However, in conventional in-plane or out-of-plane STTRAM technologies, the switching time is limited to about 10 ns because the reversal process is stochastic i.e. it is triggered by thermal fluctuations.
In order to render the reversal deterministic and faster, an approach consists in adding to the magnetic tunnel junction (MTJ) stack another spin-polarizing layer whose magnetization is orthogonal to that of the MTJ reference layer. We particularly investigated the case where a perpendicular polarizer is added to an in-plane magnetized tunnel junction. The STT from the perpendicular polarizer initiates the reversal, but it also creates oscillations of the resistance between its two extremal values. This behavior is usually interesting to realize STT nano-oscillators (STO).
In this thesis, the dynamics of the system comprising an in-plane free layer, an in-plane reference layer and a perpendicular polarizer is studied both experimentally and theoretically (analytically and by simulations) in the framework of the macrospin approximation.
For a single layer free layer oscillating due to the STT of the perpendicular polarizer, an accurate description of the oscillations is presented, in which the anisotropy field, the applied field and the in-plane STT are treated as perturbations.
In the particular case of a synthetic ferrimagnetic (SyF) free layer, analytical expressions of the critical currents and of the oscillations equation of motion are computed and compared to simulations.
These results are used to determine the phase diagram of the complete system. The in-plane anisotropy field is found to play a dramatic role, which is confirmed by experimental data from real-time measurements on MgO-based nano-pillars. It is shown that the cell aspect ratio can be used to tune the relative influence of the STT from the in-plane reference layer and from the out-of-plane polarizer. This allows achieving well controlled sub-nanosecond switching in STTRAM.

Keywords : Spintronics, Magnetic tunnel junction, Out-of-plane precession, Perpendicular polarizer

Résumé : Les mémoires magnétiques à couple de transfert de spin (STTRAM) sont des mémoires vives non-volatiles et endurantes très prometteuses pour remplacer les mémoires à base de condensateurs. Cependant, pour les technologies actuelles de STTRAM à aimantation planaire ou hors-du-plan, le temps de commutation est limité à 10 ns car le processus de renversement de l'aimantation est stochastique, déclenché par les fluctuations thermiques.
Dans l'optique de rendre la commutation déterministe et plus rapide, une approche consiste à ajouter à la jonction tunnel magnétique une autre couche polarisante en spin, avec une aimantation orthogonale à celle de la couche de référence. Nous nous sommes intéressé plus particulièrement aux jonctions tunnels magnétiques planaires avec un polariseur perpendiculaire (à aimantation hors du plan). Le STT du polariseur perpendiculaire amorce le retournement d'aimantation, mais il provoque aussi des oscillations de la résistance de la jonction entre ses valeurs extrêmes. Cette particularité est mise à profit pour la réalisation de nano-oscillateurs (STO).
Dans cette thèse, la dynamique d'aimantation du système comprenant une couche libre planaire, une couche de référence planaire et un polariseur perpendiculaire est étudiée, aussi bien expérimentalement que théoriquement (analytiquement et en simulations), dans l'approximation de macrospin.
Dans le cas d'une couche libre oscillante sous l'action du STT du polariseur perpendiculaire, une description précise de ces oscillations est présentée, dans laquelle le champ d'anisotropie, le champ appliqué et le STT de la couche de référence planaire sont traités en perturbations.
Dans le cas d'une couche libre ferrimagnétique synthétique (SyF), les expressions analytiques des courants critiques et des équations du mouvement sont calculées et comparées aux simulations.
Ces résultats sont ensuite utilisés pour réaliser le diagramme de phase du système complet. L'anisotropie uniaxiale joue un role important, ce qui est confirmé par des mesures de retournement en temps réel réalisées sur des échantillons de nano-piliers à base de MgO. L'influence relative des STT provenant de la couche de référence et du polariseur perpendiculaire peut être ajsutée en jouant sur le rapport d'aspect des cellules, ce qui permet d'obtenir un retournement controlé en moins d'une nanoseconde avec une STTRAM.

Mots-clés : Spintronique, Jonction tunnel magnétique, Précession hors du plan, Polariseur perpendiculaire.

A room almost dark.
At last I opened the door,
It was night outside.

"End or beginning?"
Pseudonymous haiku

Remerciements

Je remercie mes encadrants pour m'avoir accompagné et aidé pendant ces trois années de thèse. Merci à Ricardo Sousa pour m'avoir accueilli dans l'équipe MRAM et merci pour m'avoir aider dans les manips. Je remercie Ursula Ebels, pour les discussions, pour les répétitions avant présentation à ma première conférence, et surtout pour m'avoir inclus dans les projets. Merci à Liliana Buda pour toute l'aide que tu m'as apportée, pour ton suivi, tes conseils pratiques, ta gentillesse. J'aurais bien aimé faire un peu de micromagnétisme quand même... Et merci à Bernard Diény, de m'avoir fait confiance, de m'avoir permis d'aller en conférence et merci pour tous tes conseils, avisés.

Je voudrais remercier André Thiaville et Vincent Cros d'avoir corrigé mon manuscript, ainsi que Olivier Klein, Stéphane Mangin et Claudine Lacroix pour avoir accepté de participer à mon jury de thèse.

Je tiens aussi à remercier Thibault Devolder pour nous avoir permis de réaliser les mesures basse température à Orsay. Merci à Andrei Slavin pour les discussions et les pistes pour d'autres calculs.

Un grand merci aussi à tous les gens de SPINTEC et assimilés, pour ces agréables moments quotidiens, merci pour votre bonne humeur. Merci aux personnes du groupe MRAM, merci à celles du groupe Oscillateurs. Merci aux organisateurs de tous les pots et sorties qui rythment la vie au labo. Merci à la faction internationale pour leur amitié : Felipe de Zaragoza, Lara y Ales, Hongxin, Giovanni, Mario, Adrien, Murat, Karol (non, pas Karol), Marina, Miguel et Karla. Merci aussi à Sylvain et Emilie. Merci à Elmer, mon péruvien préféré. Merci à Pablo et Kamil pour m'avoir appris l'albanais, ça peut toujours servir.

Merci aussi à mes colocataires, Olivier, Flo, Dima, merci pour ces trois années passées ensembles, les balades en montagne, les confitures, les séances de cinéma. Merci à mes amis qui sont resté coincé à Paris, merci Charles d'avoir fait le déplacement pour ma soutenance. Je remercie également très fort ma famille pour leur soutien. Et merci à Irma, pour tout.

Outline

Introduction

The discovery of giant magnetoresistance (GMR) independently by A. Fert and P. Grünberg in 1988, marks the beginning of spintronics. Since this discovery, for which their authors were awarded the Nobel Prize in 2005, electronics devices that take advantage of the intrinsic magnetic moment of the electron, commonly known as its spin, have flourished. One of the most famous spintronics device is certainly the high capacity hard-disk drives (HDD) that equip most computers. Due to spin-dependent scattering and/or to the spin polarization of the conduction electrons, the resistance of a stack composed of two magnetic layers depends on the relative magnetic orientation of the layers. The two layers usually have parallel (P) or antiparallel (AP) magnetization directions, resulting in two different resistance states. In hard drive heads, the two magnetic layers are separated by a non-magnetic metallic spacer. However, the difference between the two resistance states is enhanced if the two magnetic layers are separated by an insulating layer. Hence, the magnetoresistive (MR) effect can be used to read the information stored in magnetic bits composed of nanopillars with two magnetic layers separated by an insulating layer, a so-called magnetic tunnel junction (MTJ). MTJ are used to realize magnetic random-access memory (MRAM), that present several advantages : non-volatility, almost-infinite endurance, speed, high density and low power consumption.
Predicted in 1996 by J.C. Slonczewski and L. Berger, spin transfer torques (STT) allow to change the magnetization direction of a layer in a nanopillar by a current flowing through the junction. By combining the two effects, MR for reading and STT for writing, a new generation of MRAM was designed, the so-called STT-MRAM, which are under active research and development. Several new research directions for STT-MRAM are investigated : stacks with perpendicular-to-plane magnetized layers, thermally-assisted switching, orthogonal polarizer, etc... This thesis is mostly focused on the last type of STT-MRAM, an in-plane MTJ with an additional perpendicular-to-plane magnetized layer.
In conventional STT-MRAMs, the storage layer is reversed by STT because of the spin polarized current due to the other in-plane magnetized layer, the reference layer. However, the STT vanishes if the storage layer magnetization is aligned with the reference layer magnetization. In contrast, it is maximum if the storage and reference layer magnetizations are orthogonal. So, with the magnetizations of the two layers aligned, the switching is stochastic, triggered by random thermal fluctuations. This leads to switching times of the order of 10 ns. For replacement of SRAM, such write-time is sufficient, but to use STT-MRAM as cache memory, write-time of less than 1 ns is expected. The addition of a perpendicular polarizer, with a magnetization direction orthogonal to the storage layer magnetization, was proposed in 2001 in a patent by O. Redon et al. from SPINTEC. In 2009, O.J. Lee et al. and C. Papusoi et al. showed experimentally a reduction of the switching time to less than 1 ns in such structures, all metallic. M. Marins showed in 2011, that the perpendicular polarizer induces an oscillation of the storage layer magnetization that is detrimental for memory applications. In fact, perpendicular polarizers are also used to realize radio frequency STT nano-oscillators, thus the oscillating and switching behaviors are both obtained from the same structure.
This thesis is focused on understanding the dynamics of in-plane MTJ with a perpendicular polarizer, by studying such structure theoretically, with macrospin simulations and experimentally. Hence, the structure can be optimized to reduce the switching time and make the reversal deterministic. The advantage of using a synthetic ferromagnetic storage layer is also discussed.

The conditions for an oscillating and a switching behaviors are determined theoretically and compared to macrospin simulations. Real-time measurements of the magnetization dynamics of the storage layer are then performed, that confirm the results of the theoretical analysis.

Part I introduces the spintronics phenomena and devices of importance for this thesis. Chapter 1 presents the principle of the magnetoresistance and the dynamics of a magnetic free layer. The free layer dynamics is described by the Landau-Lifshitz-Gilbert-Slonczewski (LLGS) equation in the macrospin approximation. It includes a conservative term related to the magnetic energy of the layer, plus a dissipative term with damping and STT. The stability of the equilibrium magnetic configuration is studied by linearizing the equation of motion. Critical fields and critical currents are extracted from the linearization of the LLGS equation. Chapter 2 gives a description of STT-MRAM of the first and second generation, then of STT nano-oscillators using a perpendicular polarizer. The structure of interest for this thesis, the in-plane MTJ with a perpendicular polarizer is introduced.

Part II presents some preliminary theoretical analysis of the complete structure. In Chapter 3, a free layer composed of a synthetic ferromagnet is studied. We describe the dynamics under an applied current with a perpendicular polarizer, and with an in-plane reference layer, independently. The critical currents and qualitative behavior are compared to a single layer free layer. Chapter 4 presents a theoretical study of the out-of-plane precession of the free layer magnetization (of a single layer) due to the STT from a perpendicular polarizer, in which the external field, the anisotropy field and the STT from the reference layer are included as perturbations. This approach allows to calculate the change in frequency due to these perturbations, and the modified critical currents.

Part III presents a macrospin theoretical analysis of the in-plane MTJ with a perpendicular polarizer. Specifically, the relative influence of the two polarizing layers is studied, as well as the influence of the anisotropy field on the dynamics of the free layer, oscillating or switching. These results are compared to micromagnetic simulations, that confirm that a large anisotropy field favors the bipolar switching behavior instead of the oscillating behavior. Finally, real-time measurements are performed on experimental elliptical nanopillars with different cross-section aspect ratios. The same trend is observed, with low aspect ratio samples showing an oscillating behavior, and high aspect ratio samples exhibiting a reversal in 1 ns. The effect of thermal fluctuations in both regimes is also studied experimentally.

Annexe A is dedicated to the analytical treatment of thermal fluctuations in the macrospin model. Some results on the probability of switching with an applied current are presented in the solvable case of a perpendicular-to-plane magnetized free layer. The application of these results to the structure of interest in this thesis is discussed.

Part I

Spintronics phenomena and devices

Chapter 1

Spintronics phenomena and magnetization dynamics

1.1 Origin of magnetism

In a classical approach, magnetism comes from the rotation of the electrons around the nuclei. Because electrons are charged particules, their motion creates an electrical current on a closed-loop, that results in a magnetic moment $\boldsymbol{\mu}$, like in a coil. The magnetic moment is expressed in $A \cdot m^2$ and it is proportional to the angular momentum of the electron. However, this picture did not entirely survive to quantum mechanics.

In quantum mechanics, the total magnetic moment of an atom comes from the nuclei, but it is negligible (except for *nuclear magnetic resonance* experiments, for instance), and from the electrons. As for the magnetic moment of one electron $\boldsymbol{\mu}$, it has two origins : the *orbital magnetic moment* $\boldsymbol{\mu}_L$, that is proportional to the *orbital angular momentum*, eigenvalue of the operator $\hat{\boldsymbol{L}}$ from the classical picture; the *spin magnetic moment* $\boldsymbol{\mu}_S$, due to the intrinsic *spin angular momentum* $\hat{\boldsymbol{S}}$ (also called simply *spin*) of the electron. The total angular momentum $\hat{\boldsymbol{J}}$ is the (operator) sum of the orbital and spin angular momentum :

$$\begin{aligned} \boldsymbol{\mu} &= \boldsymbol{\mu}_L + \boldsymbol{\mu}_S \\ \boldsymbol{J} &= \boldsymbol{L} + \boldsymbol{S} \end{aligned}$$

The orbital and spin magnetic moments relate to the angular momenta :

$$\begin{aligned} \boldsymbol{\mu}_L &= -\frac{g_L \mu_B}{\hbar} \boldsymbol{L} \qquad \text{with } g_L = 1 \\ \boldsymbol{\mu}_S &= -\frac{g_S \mu_B}{\hbar} \boldsymbol{S} \qquad \text{with } g_S \approx 2 \end{aligned}$$

Here μ_B is the Bohr magneton, $\hbar$ the reduced Planck constant. Because of the different g-factors, $\boldsymbol{\mu}$ and $\boldsymbol{J}$ are not colinear, but the observable magnetic moment $\boldsymbol{\mu}_J$ is the projection of $\boldsymbol{\mu}$ along $\boldsymbol{J}$, so that :

$$\boldsymbol{\mu}_J = -\frac{g_J \mu_B}{\hbar} \boldsymbol{J} \tag{1.1}$$

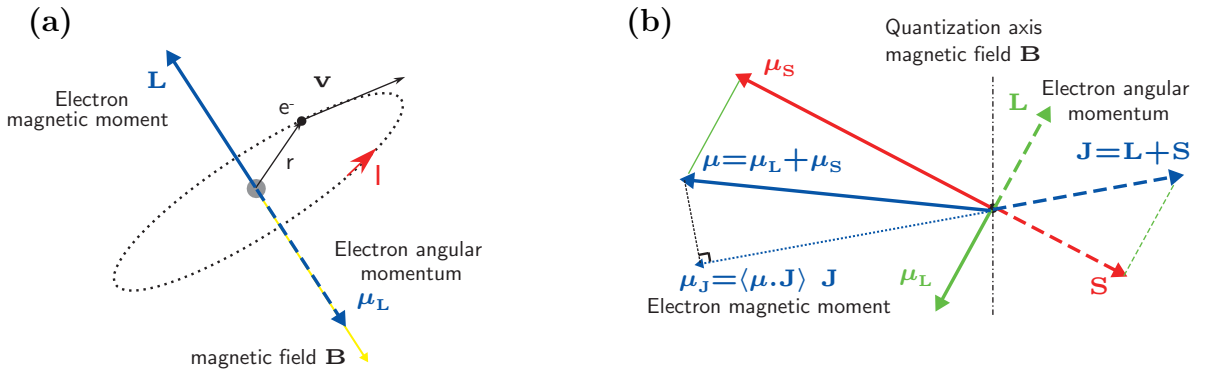

Figure 1.1 – (a) Classical picture of an electron rotating around the nucleus, at distance r and with speed v, with angular momentum $\boldsymbol{L}$. It creates a current I and a magnetic moment $\boldsymbol{\mu_L}$. (b) Quantum picture including the orbital ($\boldsymbol{L}$) and spin ($\boldsymbol{S}$) angular momentum, and the associated magnetic moments, $\boldsymbol{\mu_L}$ and $\boldsymbol{\mu_S}$. The total angular momentum $\boldsymbol{J}$ is not proportional to the total magnetic moment $\boldsymbol{\mu}$. The quantization axis is defined by the magnetic field direction. The size of the orbital angular momentum and orbital magnetic moment is exaggerated, in transition metals it is negligible.

Here g_J depends on the spin, orbital and total quantum numbers of the electron.
The classical and the quantum descriptions of the magnetic moments are illustrated in Fig. 1.1. In transition metals, the orbital magnetic moment is reduced due to electronic shielding, so if the spin-orbit coupling effects are excluded, the magnetic moment of an atom is given by the total spin angular momentum of its electrons :

$$\boldsymbol{\mu} = -\gamma \boldsymbol{S}$$

With $\gamma = \dfrac{g_S \mu_B}{\hbar}$ the gyromagnetic ratio, μ_B the Bohr magneton, $\hbar$ the reduced Planck constant, and g_S the spin g-factor of the electron, with a value of 2. The value of γ is $1.76{\times}10^{11}$ rad.s^{-1}.T^{-1}.

The angular momentum is modified by the action of torques, the most simple being the torque due to an external applied field $\boldsymbol{H}_a$ (in A/m). The expression of this torque $\boldsymbol{T}$ can be derived from classical dipole equation, or from the Heisenberg equation in quantum mechanics :

$$\boldsymbol{T} = \boldsymbol{\mu} \times \mu_0 \boldsymbol{H}_a \qquad\qquad \dot{\boldsymbol{S}} = \boldsymbol{\mu} \times \mu_0 \boldsymbol{H}_a \tag{1.2}$$

Where $\dot{\boldsymbol{S}}$ denotes the time derivative of the magnetic moment. This expression comes from the expression of the Zeeman energy, $E = -\mu_0 \boldsymbol{\mu} \cdot \boldsymbol{H}_a$, with μ_0 the vacuum permeability. It is important to realize that $\mu_0 \boldsymbol{H}_a = -\dfrac{\partial E}{\partial \boldsymbol{\mu}}$.

We shall come back to a more expansive description of the torques acting on the magnetic moments after describing more the ferromagnetic phase and the electronic transport in magnetic structures.

1.2 Spin dependent transport

1.2.1 Collective ferromagnetic ordering

The filling of electron bands abide by the Pauli's exclusion principle. Therefore the filled inner shells, s and p electrons usually, have compensated total spin and magnetism is due to the valence electrons, $3d$ electrons for transition metals (Fe, Co, Ni), $4f$ electrons for rare-earth magnetic elements. The orientation of the spins of the partially filled electron band is also governed by the Pauli's exclusion principle and by Coulomb electronic repulsion, so that two spins $\boldsymbol{S}_i$ and $\boldsymbol{S}_j$ in the lattice are subject to an interaction energy of the form $E = -J_{ex}(\boldsymbol{r})\boldsymbol{S}_i \cdot \boldsymbol{S}_j$. If $J_{ex} > 0$ the interaction is said ferromagnetic, it favors a parallel alignment of the spins; if $J_{ex} < 0$ the interaction is antiferromagnetic. If the electrons responsible for magnetism are localized, like for instance in rare-earth metals, this magnetic phase is described by the Heisenberg model for localized spins, with Hamiltonian :

$$\mathcal{H} = -J_{ex} \sum_{i,j} \boldsymbol{S}_i \cdot \boldsymbol{S}_j \tag{1.3}$$

The Heisenberg model describes well antiferromagnetic materials, in which the electrons responsible for magnetism are localized.
In transition metals, the electrons responsible for magnetism are itinerant (see Fig. 1.2.(a-b)), hence ferromagnetism is better described by the Stoner model, or more generally by the Hubbard model. The spin of an electron can take only two values, $\pm\frac{1}{2}\hbar$ along the quantization axis, so the electrons can be divided in two populations, with positive or negative spins. In fact the sign of the spin is arbitrary (depending on the vector direction chosen for the quantization axis), so one speaks about majoritary spins (spin up) and minority spins (spin down), and we note $N_\uparrow$ and $N_\downarrow$ the number of electrons per site with these spin orientations. The total number of electrons per site is $N = N_\uparrow + N_\downarrow$ and the spin polarization is defined as $m = (N_\uparrow - N_\downarrow)/N$. The Hamiltonian in k-space of the Hubbard model is given by[Timm 2011] :

$$\mathcal{H} = \frac{\mathcal{I}N^2}{4}m^2 + \sum_{\boldsymbol{k}\sigma} \Big(\epsilon_{\boldsymbol{k}} - \sigma\frac{\mathcal{I}N}{2}m\Big)a^\dagger_{\boldsymbol{k}\sigma}a_{\boldsymbol{k}\sigma} \tag{1.4}$$

Here $\mathcal{I}$ is the Coulomb interaction energy, $\sigma = \pm 1$ or $(\uparrow, \downarrow)$, $\epsilon_{\boldsymbol{k}}$ is the on-site energy and $a^\dagger_{\boldsymbol{k}\sigma}$ ($a_{\boldsymbol{k}\sigma}$) is the spin-σ electron creation (annihilation) operator. Computing the ground state of the Hubbard Hamiltonian by treating the electrons as free electrons leads to the so-called Stoner criteria for the existence of magnetic order ($m \neq 0$) :

$$\mathcal{I}D(\epsilon_F) > 1 \tag{1.5}$$

Where $D(\epsilon_F)$ is the electronic density of state (DOS) at the Fermi level of the material, calculated as if it was a paramagnet (same populations of spin up and down).
According to this model, itinerant ferromagnets are conductors with two conduction channels that have different energies : spin-up (majority) and spin-down (minority) conduction electrons, with energy $\epsilon_F \pm \frac{m\mathcal{I}}{2}$. Schematically, Fig. 1.2.c shows the density of state for spin-up and

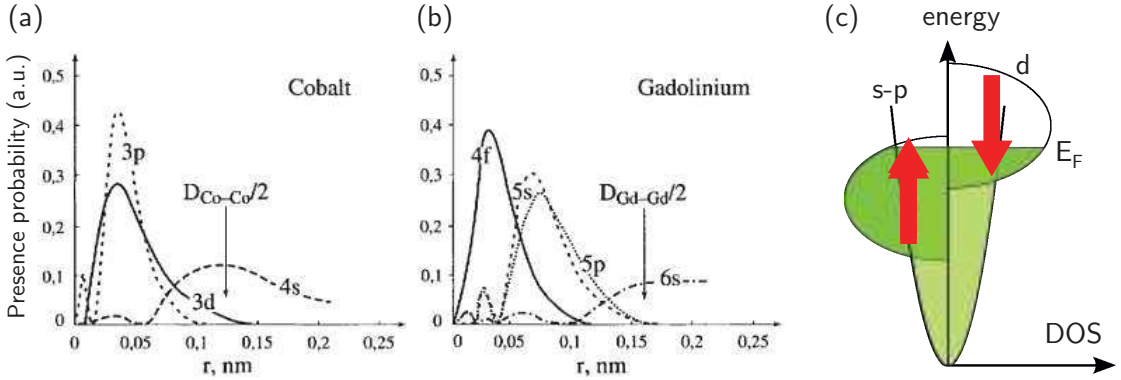

Figure 1.2 – (a-b) From [Coey 2010]. Probability of presence versus distance from the nucleus of electrons from different shells in (a) Cobalt, a transition metal, and (b) Gadolinium, a rare-earth. In Cobalt, $3d$ electrons, responsible for magnetism, are (partially) itinerant, whereas in Gadolinium, $4f$ electrons, responsible for magnetism, are localized. (c) Spin-up and spin-down electrons have different density of state (DOS), specially at the Fermi energy E_F, so the two population of electrons have different conductivity.

spin-down electrons. The picture of two channels is particularly adapted to describe the Giant Magneto-Resistance (GMR) effect, first discovered by A. Fert and P. Grünberg[Baibich 1988, Binasch 1989], for what they were awarded the Nobel Prize in 2007. This was also the beginning of spintronics.

1.2.2 Giant magnetoresistance

The GMR is found in spin-valve structures : let us consider two identical ferromagnetic layers, labeled right layer (F_R) and left layer (F_L), separated by a non-magnetic metallic spacer (NM) of thickness d. The thickness d is supposed to be small, so that the resistance of the metallic spacer can be neglected[1], and also neglect spin-flip (spontaneous flip of the electron spin) of the electrons flowing through the spacer. Electronic transport is considered in the direction orthogonal to the interfaces F_R/NM/F_L, that is labeled x-axis. The ferromagnetic layers are considered to be uniformly magnetized along the same direction, say along $\boldsymbol{u}_z$, and their relative orientation can be either parallel (P) or antiparallel (AP). The electron current I_e along the x-axis is separated in spin up and spin down electrons, relatively to the quantization z-axis :

$$I_e = I_+ + I_- \tag{1.6}$$

Because the two spin channels are populated differently, with different DOS, the resistivity is different for the two channels, giving different resistances $R_\uparrow$ and $R_\downarrow$ within the magnetic layers for the majority and minority spins, respectively. We consider then the two relative magnetization orientations of the layers :

[1]The spacer is omitted for this very simple picture, however it plays a capital role and we ought to take it into account to calculate the resistance for arbitrary angle between the magnetizations of the two layers.

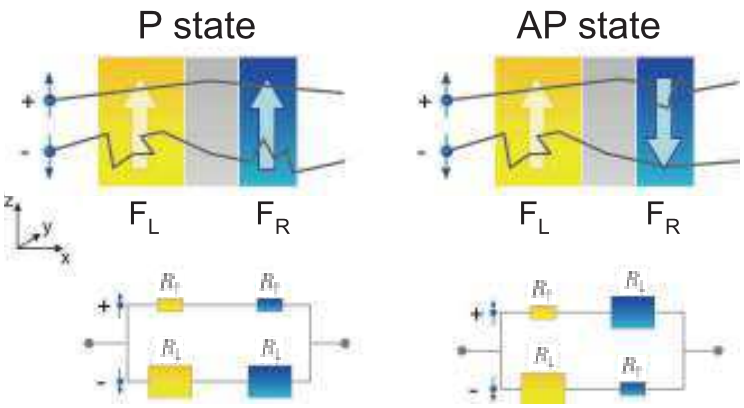

Figure 1.3 – Schematic representation of the origin of GMR. Parallel (P) and antiparallel (AP) configurations of the two ferromagnets F_L and F_R. The minority spin resistance $R_\downarrow$ and the majority spin resistance $R_\uparrow$ have different value. From [Houssameddine 2009]

(i) in P configuration, say both magnetizations are oriented along $+\boldsymbol{u}_z$, the spin-+ electrons are majority spins in both layers so the spin-+ current I_+ feels the resistance $2R_\uparrow$, and I_- feels $2R_\downarrow$, so the total resistance is :

$$R_P = \frac{2R_\uparrow R_\downarrow}{R_\uparrow + R_\downarrow}$$

(ii) in AP configuration, say F_L oriented along $+\boldsymbol{u}_z$ and F_R along $-\boldsymbol{u}_z$, the spin-+ electrons are majority spins in F_L and minority spins in F_R, and vice versa for spin-− electrons. Hence the resistances of I_+ and I_- channels are both $R_\uparrow + R_\downarrow$, and the total resistance is :

$$R_{AP} = \frac{R_\uparrow + R_\downarrow}{2}$$

The resistance R_{AP} is higher than R_P, if the resistivities for the two channels differ. This is usually the case in all magnetoresistive effects, the antiparallel configuration shows a higher resistance than the parallel configuration. The equivalent electrical circuit in the P and AP configurations are compared in Fig. 1.3.
Let χ be the GMR ratio, usually given in percentages :

$$\chi = \frac{R_{AP} - R_P}{R_P} \tag{1.7}$$

Only two relative magnetic configurations of the layers are considered, P and AP. In fact, when the current flows perpendicular to the plane of the layers (CPP geometry), the magnetoresistance can be computed for any arbitrary angle θ_R between the two layer magnetizations $\boldsymbol{m}_L$ and $\boldsymbol{m}_R$. Here $\cos\theta_R = \boldsymbol{m}_L \cdot \boldsymbol{m}_R$. The equivalent electrical circuit for the system with similar magnetic layers was introduced by Slonczewski[Slonczewski 2002]. He found that the

resistance is given by :

$$R(\theta_R) = R_P(1 + \chi r(\theta_R)) \qquad \text{with} \qquad r(\theta_R) = \frac{1 - \cos^2(\theta_R/2)}{1 + (\Lambda^2 - 1)\cos^2(\theta_R/2)} \tag{1.8}$$

The parameter Λ was calculated by Slonczewski, it depends on the conductance G_N of the non-magnetic spacer and on the AP magnetoresistance : $\Lambda = G_N R_{AP}$. It can be treated as a phenomenological parameter.

1.2.3 Tunneling magnetoresistance

The advantage of spin-valves lies in the relatively simple fabrication process, because all the layers are metallic. However the overall GMR is not particularly high for applications, usually around a few percents in CPP geometry and the CPP resistance is very small (mΩ to Ω) making it very difficult to use in combination with CMOS transistor. A similar effect, the tunneling magnetoresistance (TMR), that arises when two magnetic leads are separated by an insulating non-magnetic barrier, enhances the ratio between the two resistance states. The whole structure is called magnetic tunnel junction (MTJ). Contrary to GMR, the barrier plays a tremendous role as a spin filter, hence the quality of the barrier, as well as the interfaces with the ferromagnets, are very important to obtain a high value of the TMR ratio (noted χ also, and with the same definition as for GMR).
In a MTJ, the tunneling current depends on the applied voltage between the magnetic leads, and on the relative orientation of the magnetizations of the two layers, i.e. the angle θ_R :

$$J(V, \theta_R) = J_0(V)\Big(1 + \imath(V)\cos\theta_R\Big) \qquad \text{with} \qquad \imath(V) = P_L(V)P_R(V) \tag{1.9}$$

$J_0(V)$ is the "normal" tunnel current, if the leads were not magnetic. P_L and P_R are the spin polarization of the left and right leads, respectively. With the free electron model[Slonczewski 2005], the spin polarizations include barrier dependent terms, for i=(L, R) :

$$P_i = \frac{k_{i\uparrow} - k_{i\downarrow}}{k_{i\uparrow} + k_{i\downarrow}} \frac{\kappa_i^2 - k_{i\uparrow}k_{i\downarrow}}{\kappa_i^2 + k_{i\uparrow}k_{i\downarrow}} \tag{1.10}$$

Let the voltage V be applied to the left lead, then the previous wave vectors write for $\sigma = (\uparrow, \downarrow)$:

$$k_{L\sigma}^2 = 2m_e(E_{L\sigma} + eV)/\hbar^2 \qquad \kappa_L^2 = 2m_e(B - eV)/\hbar^2$$
$$k_{R\sigma}^2 = 2m_e(E_{R\sigma})/\hbar^2 \qquad \kappa_R^2 = 2m_e(B)/\hbar^2$$

Here m_e is the mass of the electron, B is the barrier height and $E_{i\sigma}$ are the kinetic energy at Fermi level for spin-σ electrons in the lead i.

The dependence of the TMR ratio χ with the voltage is shown in Fig. 1.4. Its expression is given by :

$$\chi = \frac{2\imath(V)}{1 - \imath(V)}$$

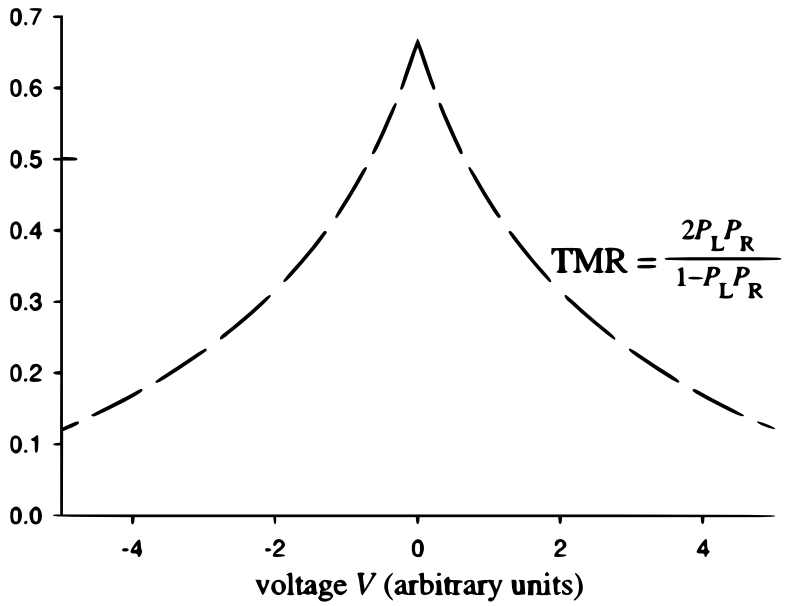

Figure 1.4 – Variation of the tunneling magnetoresistance (TMR) ratio χ versus applied voltage. From [Slonczewski 2005]

1.2.4 Tunnel filtering effects

In fact, the tunnel barrier also has a filtering effect, i.e. electrons belonging to different energy bands are scattered differently by the barrier. There are four electrons bands in the MgO crystal : Δ_1, Δ_5, Δ_2 and Δ_2'. They correspond to different symmetries of the Bloch states. The different bands have a different decay rate within the barrier, with the Δ_1 band being less attenuated, as seen in Fig.1.5.c and d. Therefore, mainly electrons with the Δ_1 symmetry tunnel trough the barrier. The MgO has a symmetry filter effect. In ferromagnetic materials, the two spin channels have different band structures, and interestingly in (100)-Fe, but it is also the case in Co and CoFe crystals, the Δ_1 band is occupied at the Fermi level only for majority-spin electrons. For the minority-spin electrons, Δ_5 and Δ_2 bands are occupied at the Fermi level. The band structures of majority and minority electrons in (100)-Fe are shown in Fig.1.5.a and b. Thus, depending on the relative alignment of the two ferromagnetic electrodes, two scenarios occur, described on Fig.1.5.c and d, for FeCo electrodes.
The minority electrons are not transmitted much because of the large decay rate of their corresponding symmetry bands in MgO, and the conductivity is due to the majority Δ_1 band electrons. When the two electrodes magnetizations are parallel (Fig.1.5.c), the majority electrons in the Δ_1 band from the left electrode, are transmitted through the MgO barrier and occupy the majority Δ_1 band in the right electrode. The conductivity of the stack is large. In the AP configuration (Fig.1.5.d), the majority Δ_1 electrons from the left electrode are transmitted to the right electrode, where they are minority electrons. However, the Δ_1 band does not exist for minority electrons, so the density of Δ_1 electrons continues decaying inside the right electrode. The conductivity is then much reduced in the AP alignment.

This symmetry filtering effect results in enhanced TMR ratios, as reported theoretically[Butler 2001, Zhang 2004], of more than 1000% with (100)-Fe electrodes, and even more for CoFe electrodes. Experimentally, a TMR of 600% at room temperature was ultimately reported in CoFeB / MgO / CoFeB stacks[Tsunekawa 2005, Ikeda 2008].
To observe such high TMR ratios, the Δ_1 symmetry of the MgO crystal must be conserved in the magnetic electrodes. For this, the interface between the ferromagnets and the insulator should have no defect and the two materials should have the same crystallographic order. That is why the stacks with the highest TMR ratios are realized by epitaxy. CoFeB electrodes present the advantage of being amorphous. After annealing, the MgO imposes its crystallographic structure to the CoFeB electrodes, so the interfaces conserve the band symmetry.

The electronic transport is modified by the magnetized layers, similarly electronic currents can modify the magnetization orientation in the layers as we will see in the next section.

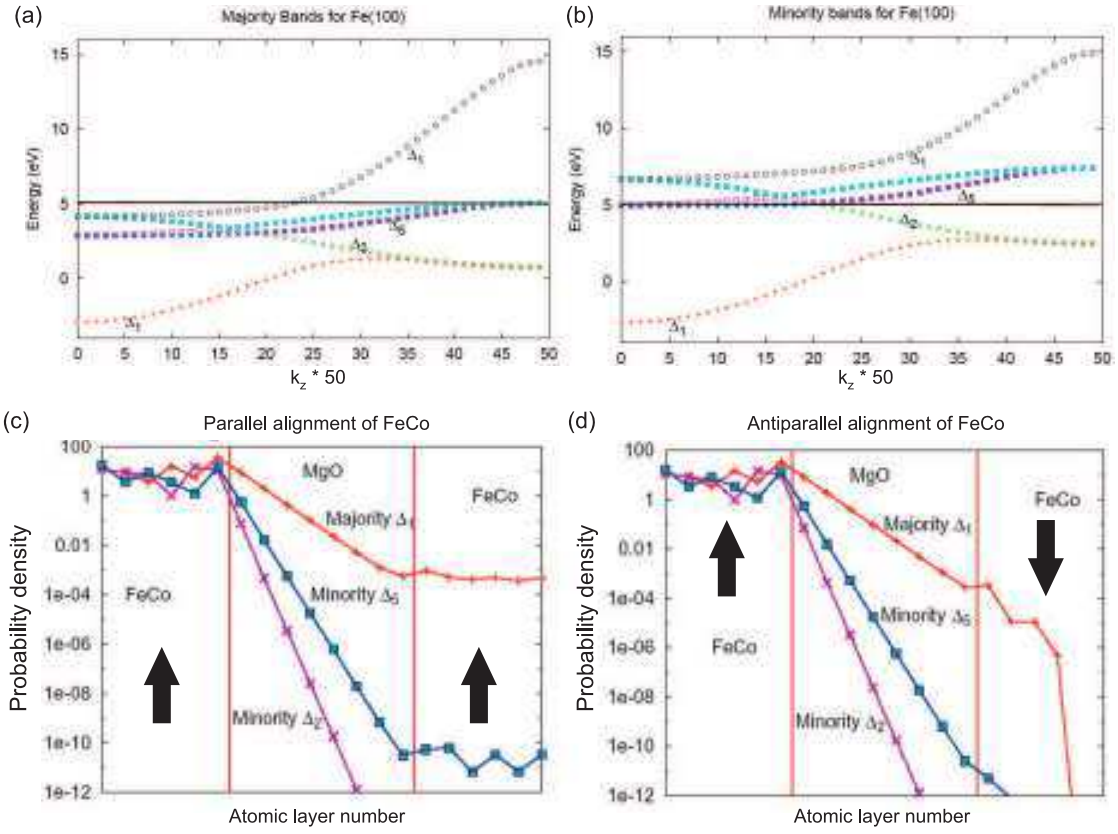

Figure 1.5 – (a-b) Band structure of (100)-Fe for the majority-spin (left panel) and the minority-spin (right panel) electrons. The hybridized Δ_1 band is present at the Fermi energy only for majority electrons. (c-d) Probability density of the different symmetry bands in a FeCo/MgO/FeCo stack at $k_{\parallel} = 0$, in the P (left panel) and AP (right panel) configuration of the electrodes. The Δ_1 band has the slowed decay rate inside the MgO barrier. The Δ_1 band does not exist for minority-spin, therefore it continues decaying in the right electrode for the AP configuration. From [Butler 2008].

1.3 Magnetization equation of motion

1.3.1 Conservative Landau-Lifshitz equation

Magnetic moments change their orientation due to an external magnetic field according to eq. 1.2. For continuous media, it is more convenient to approximate individual magnetic moments by an average over a small region. Henceforth, let a magnetic layer of volume V be composed of a lattice of identical magnetic moments $\boldsymbol{\mu}$ with a density n per unit volume. Instead of discrete quantities, continuous variables describe the media. Let $\boldsymbol{M} = n\boldsymbol{\mu}$ be the magnetic moment by unit volume (also known simply as magnetization), M_S be the saturation magnetization and $\boldsymbol{m}$ the magnetization direction, which is a unit vector so that $\boldsymbol{M} = M_S\boldsymbol{m}$. M_S is expressed in A/m. In general, the magnetization direction $\boldsymbol{m}$ depends on the coordinates : $\boldsymbol{m}(\boldsymbol{r})$. The local external magnetic field $\boldsymbol{H}_{eff}(\boldsymbol{r})$ exerts a torque on the local magnetization direction, given by :

$$\boxed{\dot{\boldsymbol{m}}(\boldsymbol{r}) = -\mu_0\gamma\boldsymbol{m}(\boldsymbol{r}) \times \boldsymbol{H}_{eff}(\boldsymbol{r})} \tag{1.11}$$

For any quantity X, $\dot{X}$ denotes the time derivative of this quantity, so $\dot{\boldsymbol{m}} = \dfrac{\partial \boldsymbol{m}}{\partial t}$.

The local magnetic field comprises the external field H_a, but also the magnetic field created by the neighboring magnetic matter. Therefore it is not spatially uniform. However, in thermodynamics equilibrium, the local magnetic field derives (in the functional sense) from the Gibbs free energy E (the relation remains valid for non-equilibrium thermodynamics) :

$$\boldsymbol{H}_{eff}(\boldsymbol{r}) = \frac{-1}{\mu_0 M_S V}\frac{\partial E}{\partial \boldsymbol{m}(\boldsymbol{r})}$$

Where $\dfrac{\partial E}{\partial \boldsymbol{m}(\boldsymbol{r})}$ is the functional derivative of the free energy with respect to the magnetization direction.
It leads to the Larmor equation :

$$\dot{\boldsymbol{m}}(\boldsymbol{r}) = \frac{\gamma}{M_S V}\boldsymbol{m}(\boldsymbol{r}) \times \frac{\partial E}{\partial \boldsymbol{m}(\boldsymbol{r})} \tag{1.12}$$

The free energy E is an extensive thermodynamics potential, accounting for the interaction of the magnetic moments with an external magnetic field, but also for the interaction of each magnetic moment with local fields created by the neighbouring magnetic matter.

In general, the Larmor equation can be solved in the context of micromagnetics, which means that the magnetization depends on the space coordinates. In this case the computation of the free energy E is rather complicated.
In this work, we take the assumption that the magnetization is uniform in the layers. Hence each layer magnetization can be represented by its average magnetization direction $\boldsymbol{m}$. This is the so-called macrospin approximation. The validity of this model is discussed with the description of the exchange interaction.

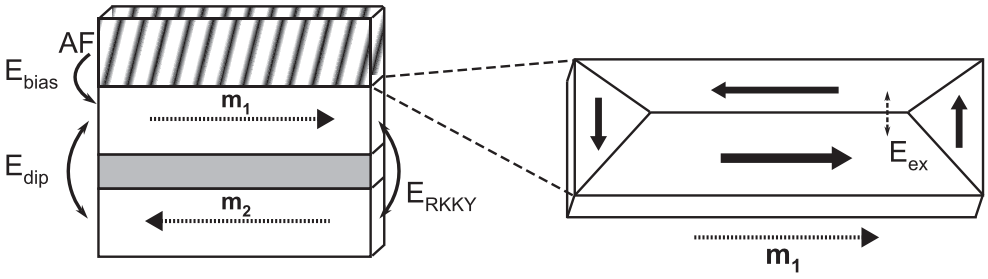

Figure 1.6 – Example of magnetic stack (left) with the magnetic energies involving the free layer magnetization $\boldsymbol{m}_1$: Exchange bias energy E_{bias}, dipolar energy E_{dip} and RKKY energy E_{RKKY}. Detail of the magnetic domains of the free layer magnetization (right). The competition between the exchange energy E_{ex} and the magnetostatic energy (not shown) creates domains. In the macrospin approximation, the magnetization $\boldsymbol{m}_1$ of the free layer is considered uniform (dotted-arrow). The Zeeman and magnetocrystalline energies are not shown.

In magnetic tunnel junctions, the free layer magnetization is subjected to several energy contributions. Some are internal, other are external, for instance because of adjacent layers of an external field. The interactions treated in this thesis are gathered on Fig. 1.6. In this framework, the free energy E is divided in the following terms :

$$E = E_Z + E_{crys} + E_{dem} + E_{bias} + E_{dip} + E_{RKKY} + E_{ex} \tag{1.13}$$

Each term will be described further : E_Z the Zeeman energy of interaction with an external field, E_{crys} the magnetocrystalline anisotropy energy, E_{dem} the demagnetizing field energy, E_{bias} the bias field energy, E_{dip} the dipolar field energy and E_{RKKY} the Ruderman-Kittel-Kasuya-Yosida (RKKY) interaction energy and E_{ex} the exchange energy.
Except for the exchange energy E_{ex} that is purely micromagnetics (and actually defines the validity of the macrospin approximation), all these terms will be expressed in the macrospin approximation.
If the system comprises several layers, the energy terms of each layer add up, plus two interaction energy : the dipolar field energy and the RKKY interaction energy. They account for the interaction energy between two magnetic layers, labelled 1 and 2.

1.3.1.1 Zeeman energy : E_Z

The Zeeman energy is the interaction between an external magnetic field and the magnetic moments. Its expression was given above for an isolated magnetic moment. In macrospin, it writes :

$$E_Z = -\mu_0 M_S V \boldsymbol{H}_a \cdot \boldsymbol{m} \tag{1.14}$$

Where $\boldsymbol{H_a}$ is the external applied field, given in A/m. The Zeeman energy is minimal when the magnetization is aligned with the external magnetic field H_a.

1.3.1.2 Magnetocrystalline anisotropy energy : E_{crys}

The magnetocrystalline anisotropy energy is due to the geometry of the lattice and the interactions between neighbouring atoms. Because of the lattice, one (or several) direction is usually favored for the direction of the resulting magnetic moment of an atom. When one direction is favored, the anisotropy is uniaxial. To first order, it is then given by :

$$E_{crys} = K_{anis} V \Big(1 - (\boldsymbol{u}_K \cdot \boldsymbol{m})^2\Big) \tag{1.15}$$

Where K_{anis} is the anisotropy energy per unit volume, and $\boldsymbol{u}_K$ is the favored direction of the uniaxial anisotropy. This energy is minimal when the magnetization is along the anisotropy axis. The energy minimum is degenerate, corresponding to $\pm\boldsymbol{u}_K$. Let H_K be the anisotropy field :

$$H_K = \frac{2K_{anis}}{\mu_0 M_S} \tag{1.16}$$

In particular, the so-called perpendicular magnetic anisotropy (PMA) should be mentioned. The perpendicular anisotropy can have a bulk and an interfacial contributions. Its expression is :

$$E_\perp = (K_V^\perp V + K_S^\perp S)\Big(1 - (\boldsymbol{u}_\perp \cdot \boldsymbol{m})^2\Big) \tag{1.17}$$

Where S is the surface that is responsible for the anisotropy and $\boldsymbol{u}_\perp$ is normal to this surface. In the context of MTJ, this anisotropy usually appears at the interface between a magnetic metal and an oxide. For instance, at the interface between a magnetic lead and the tunnel barrier oxide. In this case, the amplitude of $K_S^\perp$ was found to be related to the TMR of the junction[Monso 2002, Rodmacq 2003, Manchon 2008, Rodmacq 2009, Yang 2011, Nistor 2010]. PMA also appears at the interface between Co or Fe and Platinum or Palladium. Thus, perpendicular-to-plane magnetized stacks are realized with multilayers of ferromagnetic material (FM) and, for instance, Platinum layer : $[\mathrm{FM/Pt}]_n$, with n repetitions.

Contrary to most of the other energy contributions, the interfacial PMA does *not* scale with the volume, but with the surface. This is potentially interesting to improve the thermal stability while decreasing the magnetic volume.

1.3.1.3 Demagnetizing field energy : E_{dem}

The demagnetizing field energy corresponds to the interaction of the magnetization with the demagnetizing field $\boldsymbol{H}_{dem}$ of magnetostatic origin :

$$E_{dem} = -\frac{1}{2}\mu_0 M_S V \ \boldsymbol{H}_{dem} \cdot \boldsymbol{m} \tag{1.18}$$

The magnetostatic laws of Maxwell state that the divergence of the magnetic induction must vanish, where the magnetic induction is the sum of the magnetization and the demagnetizing field. This is equivalent to say that inside the sample, a field in created to oppose the magnetization, and outside, the magnetic flux lines must be closed. The computation of the

demagnetizing field is rather complicated, because it depends on the magnetic configuration in the whole sample, but also on its shape and geometry. In macrospin, things are only slightly easier, and under the assumption that the sample is an ellipsoid, the demagnetizing field $\boldsymbol{H}_{dem}$ is uniform. In fact, it is the tensorial product of the magnetization $\boldsymbol{m}$ by a constant symmetric tensor $\boldsymbol{N}$:

$$\boldsymbol{H}_{dem} = -M_S \boldsymbol{N} \cdot \boldsymbol{m} \tag{1.19}$$

The tensor is diagonal in the basis composed by the three axes of the ellipsoid, and its trace is unity. If the three main axes are noted $\boldsymbol{u}_x$, $\boldsymbol{u}_y$ and $\boldsymbol{u}_z$, then :

$$\boldsymbol{H}_{dem} = -M_S N_{xx} m_x \boldsymbol{u}_x - M_S N_{yy} m_y \boldsymbol{u}_y - M_S N_{zz} m_z \boldsymbol{u}_z \tag{1.20}$$

With $N_{xx} + N_{yy} + N_{zz} = 1$. Roughly, The thinner the ellipsoid in one main direction $\boldsymbol{u}_i$, the largest the associated coefficient N_{ii}. Namely, for flat samples with thickness along the z-axis much smaller than the other directions $\boldsymbol{u}_x$ and $\boldsymbol{u}_y$, $N_{zz} \approx 1$.
In the approximation of ellipsoid samples, with the three privileged directions $\boldsymbol{u}_x$, $\boldsymbol{u}_y$ and $\boldsymbol{u}_z$, the demagnetizing field energy is given by :

$$E_{dem} = \frac{1}{2}\mu_0 M_S^2 V \left(N_{xx} m_x^2 + N_{yy} m_y^2 + N_{zz} m_z^2 \right) \tag{1.21}$$

The demagnetizing field energy minimum depends on the value of the diagonal terms of the tensor $\boldsymbol{N}$[Osborn 1945] :

(i) For a spherical material, for instance a nano-particle, $N_{xx} = N_{yy} = N_{zz} = 1/3$, the demagnetizing field energy is constant, independent of $\boldsymbol{m}$.

(ii) For an elongated cylinder with a diameter much smaller than the height along $\boldsymbol{u}_z$, $N_{zz} \approx 0$ and $N_{xx} = N_{yy} \approx 1/2$, a magnetization along $\boldsymbol{u}_z$ minimizes the demagnetizing field energy.

(iii) For a cylindric thin film with an elliptical cross-section, $N_{zz} \approx 1$. Say the larger axis of the ellipse is along $\boldsymbol{u}_x$, then $N_{xx} < N_{yy} \ll N_{zz}$. Hence the energy minimum is reached when the magnetization is along $\pm\boldsymbol{u}_x$.

1.3.1.4 Bias field energy : E_{bias}

Exchange bias is a phenomenon that occurs when a ferromagnetic layer is in contact with an antiferromagnetic (AF) layer. The first atomic layers of the AF pin the ferromagnet in the direction of the (staggered) magnetization of the AF. Because of this pinning, it requires a higher field to rotate the magnetization of the ferromagnet. Ferromagnetic layer coupled by exchange bias to an antiferromagnet usually show shifted hysteresis loops. In macrospin, the exchange bias is modeled by an additional constant field $\boldsymbol{H}_b$ acting on the ferromagnetic layer, with energy:

$$E_{bias} = -\mu_0 M_S V \boldsymbol{H}_b \cdot \boldsymbol{m} \tag{1.22}$$

The strength of the field $\boldsymbol{H}_b$ depends on the nature of the antiferromagnet and on the defects at the interface. Its direction is set when the sample is annealed and cooled down under external field from a temperature close to the Néel temperature. When the AF layer is heated above its Néel temperature, it loses its magnetic alignment, whereas the magnetization of the ferromagnetic layer, which Curie temperature is usually higher, aligns with the external field. When cooling down, the first atomic layer of the AF aligns with the ferromagnet, and to the external field applied during annealing.

1.3.1.5 Dipolar field energy : E_{dip}

The dipolar field energy is formally part of the demagnetizing field energy, but because it describes the interaction of the magnetization of one layer with the field created by another layer, they are treated separately. The name dipolar field reminds that the two layers are considered as magnetic dipoles, and that this energy is in fact a dipole-dipole interaction energy. As for the demagnetizing field, in macrospin, the dipolar field is calculated for two ellipsoids, labelled 1 and 2, with the same privileged directions. In this case the uniform magnetization $\boldsymbol{m}_2$ of the ellipsoid 2 with saturation magnetization M_{S2} interacts with the uniform magnetization $\boldsymbol{m}_1$ of the ellipsoid 1 with saturation magnetization M_{S1}, giving the interaction energy :

$$E_{dip} = \mu_0 M_{S1} M_{S2}\, \boldsymbol{m}_1\, \underline{\underline{\boldsymbol{D}}}\, \boldsymbol{m}_2 \tag{1.23}$$

Where $\underline{\underline{\boldsymbol{D}}}$ is a diagonal constant tensor that depends on the volume of the two layers, but also on the distance between layer 1 and layer 2. The field $\boldsymbol{H}_{\text{stray}}$ exerted by the layer 2 on layer 1, of volume V_1, is called the stray field :

$$\boldsymbol{H}_{\text{stray}} = -\frac{M_{S2}}{V_1} \underline{\underline{\boldsymbol{D}}}\, \boldsymbol{m}_2$$

1.3.1.6 RKKY interaction energy : E_{RKKY}

The Ruderman-Kittel-Kasuya-Yosida (RKKY) interaction is a coupling mechanism between two localized spins through conduction electrons. It accounts for the coupling of two magnetic layers separated by a thin metallic spacer. In macrospin, the RKKY interaction energy between two layers writes :

$$E_{RKKY} = -S\, J_{RKKY}\, \boldsymbol{m}_1 \cdot \boldsymbol{m}_2 \tag{1.24}$$

Here J_{RKKY} is the interaction energy per unit area and S is the interface area. J_{RKKY} depends on the non-magnetic material and it shows a damped oscillating dependence to the non-magnetic material thickness, alternating between positive and negative value. If $J_{RKKY} < 0$, the coupling is said to be antiferromagnetic (AF) as, in the minimum energy configuration, the two magnetic layers are antiparallel.

1.3.1.7 Exchange energy : E_{ex}

Contrary to the previous energy contributions, the exchange energy vanishes in the macrospin model.The exchange energy accounts for spin-spin interactions from the discrete Heisenberg model of localized interacting spins in a lattice. It is a short distance interaction, without classical analog and it is responsible for the order in ferromagnetic materials. In other words, without the exchange interaction, collective ferromagnetic ordering would be impossible. Its expression depends on the space gradient of the magnetization direction $\nabla_{\boldsymbol{r}}\boldsymbol{m}(\boldsymbol{r})$ (which vanishes in the macrospin model) :

$$E_{ex} = A_{ex} \int_V \mathrm{d}\boldsymbol{r} \left(\nabla_{\boldsymbol{r}}\boldsymbol{m}\right)^2 \tag{1.25}$$

A_{ex} is the exchange constant, which takes a value between $A_{ex} = 1 \times 10^{-11}$J/m and $A_{ex} = 3 \times 10^{-11}$ J/m for transition metals (Fe, Co, Ni). The exchange energy is minimal when the magnetization in the whole sample is uniform, i.e. in the macrospin approximation.
The macrospin approximation is valid when the cost in energy to create a domain wall in the system exceeds the gain in magneto-static energy due to the breaking of the magnetization into domains. For values of the anisotropy energy per unit volume of $K_{anis} = 10$ e3 J/m^3, and of saturation magnetization $M_S = 1.2$ e6 A/m, encountered in thin films, the typical size where the macrospin approximation is valid is 60 nm. Experimentally, it was shown[Sato 2011] that the magnetization nucleates into domains at such sizes. This is the order of magnitude of the lateral sizes of spintronics device nowadays. Hence micromagnetics effects (as domain propagation, domain walls, vortices ...) are not negligible, even if they are not preponderant.
In this work, we discuss magnetization dynamics in the framework of the macrospin approximation because it allows to capture important features of the dynamics. However one should remember that some interesting effects are passed over.

1.3.2 Gilbert damping torque

Written as eq. 1.11, with the effective field deriving from the free energy E, the magnetization dynamics are conservative, because the energy E is conserved. The time derivative of the energy is given by :

$$\dot{E} = \dot{\boldsymbol{m}} \cdot \frac{\partial E}{\partial \boldsymbol{m}} = \frac{\gamma}{M_S V} \frac{\partial E}{\partial \boldsymbol{m}} \cdot \left(\boldsymbol{m} \times \frac{\partial E}{\partial \boldsymbol{m}}\right) = 0 \tag{1.26}$$

The conservative part is a precessional term, it makes the magnetization oscillate on a constant energy trajectory. However, because of dissipative processes, the magnetic energy is not conserved, so an additional phenomenological torque must be added to the equation of motion.

The origin of the Gilbert damping is a relaxation in the lattice[Widom 2010]. A generic dissipative process is introduced, so the equation of motion writes :

$$\dot{\boldsymbol{m}} = \frac{\gamma}{M_S V} \boldsymbol{m} \times \frac{\partial E}{\partial \boldsymbol{m}} + \alpha \boldsymbol{m} \times \dot{\boldsymbol{m}} \tag{1.27}$$

Here α is the phenomenological adimensional Gilbert damping constant. This dissipation usually takes place due to spin-orbit interactions which gradually convert magnetic excitations into lattice excitations (phonons) and ultimately heat[2].
By taking the vectorial product of this equation with $\boldsymbol{m}$, the term $\boldsymbol{m} \times \dot{\boldsymbol{m}}$ rewrites :

$$\boldsymbol{m} \times \dot{\boldsymbol{m}} = \boldsymbol{m} \times \left(\frac{\gamma}{M_S V} \boldsymbol{m} \times \frac{\partial E}{\partial \boldsymbol{m}} \right) + \alpha (\boldsymbol{m} \cdot \dot{\boldsymbol{m}}) \boldsymbol{m} - \alpha |\boldsymbol{m}|^2 \dot{\boldsymbol{m}}$$

Taking into account that $\boldsymbol{m}$ is a unitary vector, with a constant norm, the second term in the previous equation vanishes, and the equation of motion rewrites as the Landau-Lifshitz-Gilbert equation :

$$\dot{\boldsymbol{m}} = \frac{\gamma}{1+\alpha^2} \frac{1}{M_S V} \boldsymbol{m} \times \frac{\partial E}{\partial \boldsymbol{m}} + \frac{\gamma}{1+\alpha^2} \frac{\alpha}{M_S V} \boldsymbol{m} \times \left(\boldsymbol{m} \times \frac{\partial E}{\partial \boldsymbol{m}} \right)$$

This equation can be written using a modified gyromagnetic ratio $\gamma^* = \gamma/(1+\alpha^2)$. However the damping constant α is small, approximately 0.02 in transition metals, and maximum 0.1 if the material contains a lot of defects, so the change in the gyromagnetic ratio is negligible. Therefore, in the following, the notation γ (except explicitly mentioned) is used to refer to the modified ratio :

$$\boxed{\dot{\boldsymbol{m}} = \frac{\gamma}{M_S V} \boldsymbol{m} \times \frac{\partial E}{\partial \boldsymbol{m}} + \alpha \frac{\gamma}{M_S V} \boldsymbol{m} \times \left(\boldsymbol{m} \times \frac{\partial E}{\partial \boldsymbol{m}} \right)} \tag{1.28}$$

With this additional term, the energy variation writes :

$$\dot{E} = -\alpha \frac{\gamma}{M_S V} \left| \boldsymbol{m} \times \frac{\partial E}{\partial \boldsymbol{m}} \right|^2 = -\alpha \frac{\gamma}{M_S V} \left| \frac{\partial E}{\partial \boldsymbol{m}} \right|^2 \tag{1.29}$$

Due to damping, the energy decreases until the system reaches its energy minimum, either global or local.

The relaxation time τ_D is given by :

$$\tau_D = \frac{1}{\alpha \mu_0 \gamma H_{eff}} \tag{1.30}$$

If the effective field only contains an external field with an amplitude of 10 kA/m, and we suppose that the damping constant is 0.02, the typical relaxation time is of 20 ns.

The relaxation time has to be compared to the typical precession period due to the conservative torques. The precession typical time is noted τ_C and it can be evaluated from eq. 1.11. Hence precessional dynamics occur in shorter times than the relaxation process, of the order $\tau_C = \alpha \tau_D$, supposedly down to 400 ps. The precession time corresponds to an oscillation frequency in the GHz range.

[2]The damping constant α also depends on the adjacent layers and their ability to absorb spin currents but here we do not take into account these effects. It is also possible to increase the damping constant by adding impurities with a high spin-orbit coupling.

As a result, it seams important to involve conservative dynamics to realize faster spintronics devices.

The damping torque drives the magnetization to a local energy minimum, therefore, if the magnetization is already in equilibrium, the only way of changing the magnetization orientation is by changing the energy map and transform the local energy minimum in a saddle-point. This is done by applying an external magnetic field. However, it is also possible to change the magnetization direction without magnetic field, but by applying a current that is spin polarized (with uneven spin populations). This torque, called spin transfer torque (STT), was predicted by Slonczewski[Slonczewski 1996] and Berger[Berger 1996] as a counter-part of the GMR and TMR.

1.3.3 Spin transfer torque

Two ferromagnets, labeled F_L and F_R, are separated by a metallic spacer or a tunnel barrier, labeled NM. The notations introduced in the magnetoresistance section are used, except for the left lead magnetization, which is considered fixed (for instance by exchange bias) with direction $\boldsymbol{m}_L$, and for the right lead magnetization, which is "free", with magnetization direction $\boldsymbol{m}$ for commodity. The free layer F_R is submitted to torques. The electrons in the left (right) lead are spin polarized in the direction $\boldsymbol{m}_L$ ($\boldsymbol{m}$, resp.). When a current is applied, say electrons are flowing from the left fixed layer to the right free layer, spin polarized electrons along $\boldsymbol{m}_L$ are injected in the free layer. There, the injected electrons realign towards the $\boldsymbol{m}$ direction. However, the change of spin angular momentum of the itinerant electrons must be compensated : spin angular momentum from the itinerant electrons is transfered to the localized electrons of F_R, responsible for the global magnetization $\boldsymbol{m}$. Hence the free layer magnetization $\boldsymbol{m}$ feels a torque due to the electrons polarized by the layer F_L, with magnetization direction $\boldsymbol{m}_L$.

The spin transfer torque depends on the relative orientation of the two layers θ_R, on the applied current density J and on other parameters relative to the materials that were introduced for the GMR and TMR expressions. In general, the free layer magnetization experiences two additional torques :

$$\boldsymbol{T}_{STT} = a_J(J,\theta_R)\ \boldsymbol{m} \times (\boldsymbol{m} \times \boldsymbol{m}_L) \qquad \boldsymbol{T}_{IEC} = b_J(J,\theta_R)\ \boldsymbol{m} \times \boldsymbol{m}_L \tag{1.31}$$

$\boldsymbol{T}_{STT}$ is the torque that is commonly called "spin transfer torque", with amplitude a_J. In the following, it is the torque that STT will refer to. $\boldsymbol{T}_{IEC}$ is called interlayer exchange coupling (IEC), or field-like torque because it has the same form as the torque due to an external field, with amplitude b_J. Fig. 1.7.a describes a magnetic junction with the two torques, STT and IEC, acting on the two magnetizations. Depending on the form chosen for the LLG equation, eq. 1.27 or eq. 1.28, the expressions of a_J and b_J may change. However, b_J maximum value is 30% that of a_J, so the a_J term only differ by αb_J between the wo forms, which is negligible. Thus, a_J is supposed to be the same in both forms.

The STT amplitude has different expressions for a metallic spacer or for a tunnel barrier. The notation adopted here fits both cases :

$$a_J = -\frac{\hbar}{2e}\frac{J}{\mu_0 M_S t}\frac{\eta}{1+\lambda\cos\theta_R} \tag{1.32}$$

Where the current density J is defined as positive when electrons are flowing from the fixed layer to the free layer. $\hbar$ is the (modified) Planck constant, and e is the elementary electronic charge (e>0). t is the thickness of the free layer (the cross-section area is S, so that $V = S \cdot t$). η is called the spin polarization of the fixed layer, it is equal to $\eta_{MTJ} = P_R$ defined earlier for a symmetric tunnel barrier[Slonczewski 2005], or to $\eta_{\text{metal}} = \frac{2\Lambda^2}{\Lambda^2+1}\frac{R_\downarrow - R_\uparrow}{R_\downarrow + R_\uparrow}$ for a metallic spacer[Slonczewski 2002]. Because all these parameters are phenomenological, η is preferentially used.
The spin polarization asymmetry λ vanishes for a symmetric tunnel barrier and takes the value $\lambda = \frac{\Lambda^2-1}{\Lambda^2+1}$ for a metallic spacer. Again, λ is used instead of the other parameters, as it fits both cases. It is also a good approximation of the case of asymmetric MTJ[Manchon 2006], where λ is small. $\lambda = 0.5$ is an acceptable value for a metallic spacer.

Another justification for the spin polarization asymmetry λ, is that experimentally, it is common to use a constant voltage instead of a constant current source. However, the STT is proportional to the density of current J. Taking the expression of the tunneling current, and assuming that the polarization term $\imath$ is independent of the voltage, and $J_0(V) = V/(RS)$, then the STT amplitude is :

$$a_J = -\frac{\hbar}{2e}\frac{V\eta}{\mu_0 M_S RSt}(1+\imath\cos\theta_R) \underset{\imath\ll 1}{\approx} -\frac{\hbar}{2e}\frac{V\eta}{\mu_0 M_S RSt}\frac{1}{1-\imath\cos\theta_R} \tag{1.33}$$

So the spin polarization asymmetry λ can account for asymmetric STT amplitude in terms of voltage.

There is still controversy about the expression of b_J, it is supposed proportional to a_J in this thesis. For most of the theoretical and numerical analysis presented in this thesis, the *intrinsec* IEC term is neglected, but an effective IEC term is present that results from the transformation of LLGS from the form 1.27 to the form 1.28. This effective term is the "damping" of the STT term and it has the value $-\alpha a_J$. In order to take into account the intrinsic IEC, the overall b_J coefficient is written, in the frame of this work, as :

$$b_J = -\alpha\beta_{IEC}\, a_J \tag{1.34}$$

With this definition, β_{IEC} is unity when not considering the intrinsic IEC, but only the "damping" of the STT term. The order of magnitude of β_{IEC} is between 1 and 10 in other cases[Oh 2009].
Notice also that b_J and a_J may have a different current dependence, in this case the current dependence is carried by the coefficient $\beta_{IEC}(J)$. In symmetric junctions, b_J is found to be

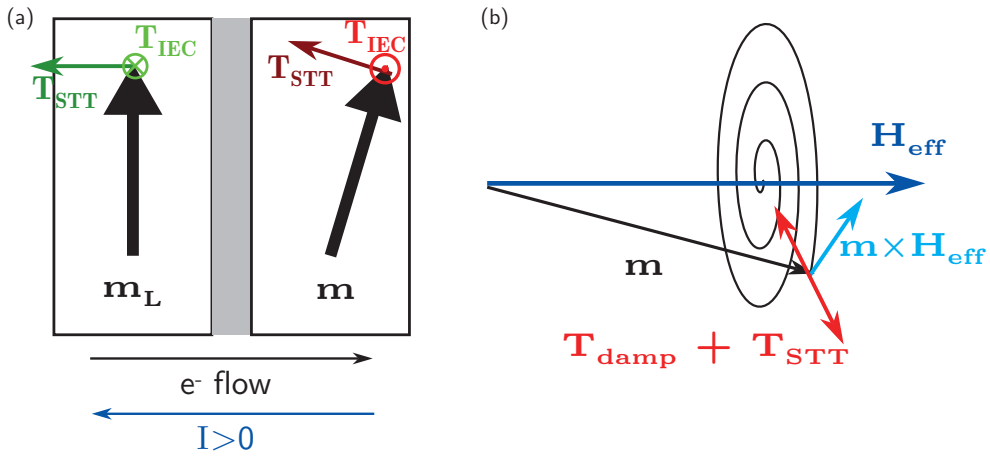

Figure 1.7 – (a) Schematic of the torques acting on the free layer magnetization $\boldsymbol{m}$ and on the fixed layer $\boldsymbol{m}_L$. The STT torques are in the $(\boldsymbol{m}, \boldsymbol{m}_L)$ plane, whereas the IEC torques are normal to this plane. The current I is positive for electron flowing towards the free layer. (b) Conservative ($\boldsymbol{m} \times \boldsymbol{H}_{eff}$) and dissipative (damping and STT) torques acting on the free layer magnetization $\boldsymbol{m}$. Alone, the conservative torque forces the magnetization to precess around the effective field $\boldsymbol{H}_{eff}$.

quadratic in the current, whereas a_J is linear[Theodonis 2006].

With the addition of these two torques, the equation of motion of the free layer is called Landau-Lifshitz-Gilbert-Slonczewski (LLGS) equation :

$$\dot{\boldsymbol{m}} = \frac{\gamma}{M_S V}\boldsymbol{m} \times \frac{\partial E}{\partial \boldsymbol{m}} + \alpha \frac{\gamma}{M_S V}\boldsymbol{m} \times \left(\boldsymbol{m} \times \frac{\partial E}{\partial \boldsymbol{m}}\right) + \gamma\mu_0 a_J\, \boldsymbol{m} \times (\boldsymbol{m} \times \boldsymbol{m}_L) - \gamma\mu_0\alpha\beta_{IEC}\, a_J \boldsymbol{m} \times \boldsymbol{m}_L \tag{1.35}$$

It appears that the STT expression is very similar to the damping torque, and the IEC is very similar to the conservative torque. In fact, the STT is also called anti-damping. It would be natural to gather the terms with the same "effect", i.e. the conservative torque with the IEC, and the damping torque with the STT. In this context, a new potential P is introduced, that we call spin torque potential. It plays a role similar to the magnetic free energy E.

The effective field was defined as the functional derivative of the energy with respect to the magnetization $\boldsymbol{m}$. Similarly, let "$a_J(\theta_R)\boldsymbol{m}_L$" write as the functional derivative of the spin torque potential P. Given the expression of a_J and using the fact that $\cos\theta_R = \boldsymbol{m} \cdot \boldsymbol{m}_L$, we define :

$$P = I\frac{\hbar}{2e}\frac{\eta}{\lambda}\ln(1 + \lambda \boldsymbol{m} \cdot \boldsymbol{m}_L) \tag{1.36}$$

$$a_J \boldsymbol{m}_L = \frac{-1}{\mu_0 M_S V}\frac{\partial P}{\partial \boldsymbol{m}}$$

Here I is the applied current, with positive values for electrons flowing towards the free layer. $\ln(x)$ is the natural logarithm of x. Notice that for MTJ, with $\lambda = 0$, the spin torque potential is found by taking the limit of $\lambda \to 0$, namely $P = I(\hbar/2e)\eta\, \boldsymbol{m} \cdot \boldsymbol{m}_L$.
The LLGS rewrites in the condensed way :

$$\boxed{\dot{\boldsymbol{m}} = \frac{\gamma}{M_S V}\boldsymbol{m} \times \left[\frac{\partial}{\partial \boldsymbol{m}}(E + \alpha\beta_{IEC}P)\right] + \frac{\gamma}{M_S V}\boldsymbol{m} \times \left(\boldsymbol{m} \times \left[\frac{\partial}{\partial \boldsymbol{m}}(\alpha E - P)\right]\right)} \tag{1.37}$$

In this equation, two potentials appear :

- **Conservative potential** : $\boldsymbol{\mathcal{H} = E + \alpha\beta_{IEC}P}$
- **Dissipative potential** : $\boldsymbol{\Gamma = \alpha E - P}$.

Because $\alpha \approx 0.02$ and the switching appears for applied currents such that $P \sim \alpha$, the conservative potential is larger than the dissipative potential, for reasonable values of current. This allows a very important simplification : the magnetization trajectory is governed by the conservative part, and the dissipative part controls the stability of the dynamics, as shown in Fig. 1.7.b.
We saw that $\beta_{IEC} \lesssim 10$, so $\alpha\beta_{IEC}P \ll E$. In most of the calculations shown here, the IEC is then neglected.

If the IEC term is neglected, the conservative potential corresponds to the free energy E. Its evolution is given by :

$$\dot{E} = -\frac{\gamma}{M_S V}\frac{\partial E}{\partial \boldsymbol{m}} \cdot \frac{\partial \Gamma}{\partial \boldsymbol{m}} \tag{1.38}$$

Because the sign of Γ depends on the current I, it is possible to increase the free energy of the system by applying a current. Therefore, it is possible to switch the magnetization direction from one minimum of energy to another without modifying the energy levels. That is the principle behind STT magnetic random-access memories (STT-MRAM). The STT also generates self-sustained oscillations of the magnetization around a minimum or maximum of energy. The frequency range is the gigahertz, that correspond to a typical precession period of 500 fs mentioned earlier. These oscillations are suitable for frequency detection or micro-wave generators.

For studying switching mechanism and self-sustained oscillation in the macrospin model, one has to linearize of the LLGS equation around an equilibrium state . For convenience, this linearization is done in spherical coordinates.

1.4 Linearization of the equation of motion

The LLGS is written in the condensed form of eq. 1.37 with the two potentials $\mathcal{H}$ and Γ. Under this form, change of basis are easily achieved because the two potential are basis-independent.

In fact, the LLGS equation is usually expressed in cartesian coordinates, in the basis $(\boldsymbol{u}_x, \boldsymbol{u}_y, \boldsymbol{u}_z)$: $\boldsymbol{m} = (m_x, m_y, m_z)$. This coordinate system is a global map, however it does not reflect the fact that the magnetization evolves on the sphere $|\boldsymbol{m}| = 1$. As illustrated in Fig. 1.8, the magnetization can be expressed in spherical coordinates in the basis $(\boldsymbol{u}_r, \boldsymbol{u}_\theta, \boldsymbol{u}_\phi)$, with $r = 1$:

$$\begin{aligned} m_x &= \sin\theta\cos\phi \\ m_y &= \sin\theta\sin\phi \\ m_z &= \cos\theta \end{aligned}$$

The change of basis matrix is $\underline{\underline{P}}$:

$$\underline{\underline{P}} = \begin{pmatrix} \sin\theta\cos\phi & \cos\theta\cos\phi & -\sin\phi \\ \sin\theta\sin\phi & \cos\theta\sin\phi & \cos\phi \\ \cos\theta & -\sin\theta & 0 \end{pmatrix} \qquad \text{with :} \quad \underline{\underline{P}}^{-1} = \underline{\underline{P}}^{\intercal}$$

Where $\underline{\underline{P}}^{\intercal}$ is the matrix transpose of $\underline{\underline{P}}$.

The Jacobian $\underline{\underline{J}} = \dfrac{\partial(m_x, m_y, m_z)}{\partial(r, \theta, \phi)}$, is defined for $r = 1$ by :

$$\underline{\underline{J}} = \begin{pmatrix} \sin\theta\cos\phi & \cos\theta\cos\phi & -\sin\theta\sin\phi \\ \sin\theta\sin\phi & \cos\theta\sin\phi & \sin\theta\cos\phi \\ \cos\theta & -\sin\theta & 0 \end{pmatrix} = \underline{\underline{P}} \cdot \underline{\underline{g}} \qquad \text{with :} \quad \underline{\underline{g}} = \begin{pmatrix} 1 & 0 & 0 \\ 0 & 1 & 0 \\ 0 & 0 & \sin\theta \end{pmatrix}$$

Notice that the Jacobian determinant is equal to $\sin\theta$, so the transform is not defined for $\sin\theta = 0$, i.e. $m_z = \pm 1$. The matrix $\underline{\underline{g}}$ is not to be mistaken with the metric tensor g_{ij} in spherical coordinates, in fact it is the square root of the covariant metric tensor.
In spherical coordinates, with the notation $\boldsymbol{R} = (r, \theta, \phi)$, let the LLGS write :

$$\begin{aligned} \underline{\underline{P}}^{-1}\dot{\boldsymbol{m}} &= \underline{\underline{P}}^{-1}\underline{\underline{J}}\dot{\boldsymbol{R}} \\ &= \frac{\gamma}{M_S V}\left(\underline{\underline{P}}^{-1}\boldsymbol{m}\right) \times \left(\underline{\underline{P}}^{-1}\frac{\partial \mathcal{H}}{\partial \boldsymbol{m}}\right) + \frac{\gamma}{M_S V}\left(\underline{\underline{P}}^{-1}\boldsymbol{m}\right) \times \left(\left(\underline{\underline{P}}^{-1}\boldsymbol{m}\right) \times \left(\underline{\underline{P}}^{-1}\frac{\partial \Gamma}{\partial \boldsymbol{m}}\right)\right) \\ &= \frac{\gamma}{M_S V}\begin{pmatrix}1\\0\\0\end{pmatrix} \times \left(\underline{\underline{P}}^{-1}\left(\underline{\underline{J}}^{-1}\right)^{\intercal}\frac{\partial \mathcal{H}}{\partial \boldsymbol{R}}\right) + \frac{\gamma}{M_S V}\begin{pmatrix}1\\0\\0\end{pmatrix} \times \left(\begin{pmatrix}1\\0\\0\end{pmatrix} \times \left(\underline{\underline{P}}^{-1}\left(\underline{\underline{J}}^{-1}\right)^{\intercal}\frac{\partial \Gamma}{\partial \boldsymbol{R}}\right)\right) \\ &= \frac{\gamma}{M_S V}\begin{pmatrix}0 & 0 & 0\\ 0 & 0 & -1\\ 0 & 1 & 0\end{pmatrix}\underline{\underline{g}}^{-1}\frac{\partial \mathcal{H}}{\partial \boldsymbol{R}} - \frac{\gamma}{M_S V}\begin{pmatrix}0 & 0 & 0\\ 0 & 1 & 0\\ 0 & 0 & 1\end{pmatrix}\underline{\underline{g}}^{-1}\frac{\partial \Gamma}{\partial \boldsymbol{R}} \end{aligned}$$

Because the projection along $\boldsymbol{u}_r$ vanishes, the system of three equations reduces to only two equations, with $\boldsymbol{R} = (\theta, \phi)$ and $\underline{\underline{g}} = \begin{pmatrix} 1 & 0 \\ 0 & \sin\theta \end{pmatrix}$, now. Let $\Omega_1 = \begin{pmatrix} 0 & -1 \\ 1 & 0 \end{pmatrix}$ and $\partial_{\boldsymbol{R}} = \dfrac{\partial}{\partial \boldsymbol{R}}$:

$$\underline{\underline{g}}\dot{\boldsymbol{R}} = \frac{\gamma}{M_S V}\left(\Omega_1 \underline{\underline{g}}^{-1}\partial_{\boldsymbol{R}}\mathcal{H} - \underline{\underline{g}}^{-1}\partial_{\boldsymbol{R}}\Gamma\right) \tag{1.39}$$

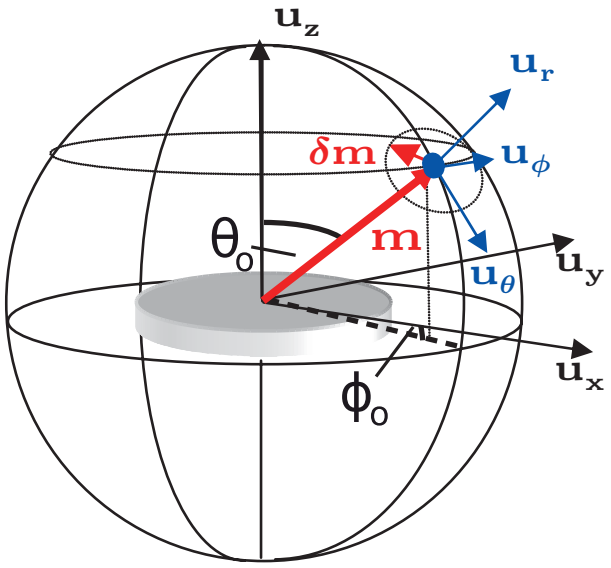

Figure 1.8 – Magnetization of the free layer $\boldsymbol{m}$ in spherical coordinates (θ, ϕ). $\boldsymbol{m}$ has a constant norm of unity. Small deviation $\boldsymbol{\delta m}$ around an hypothetical equilibrium state (θ_0, ϕ_0). Adapted from [Ebels 2008].

$$\begin{pmatrix} \dot{\theta} \\ \dot{\phi}\sin\theta \end{pmatrix} = \frac{\gamma}{M_S V} \begin{pmatrix} -\dfrac{\partial_\phi \mathcal{H}}{\sin\theta} - \partial_\theta \Gamma \\ \partial_\theta \mathcal{H} - \dfrac{\partial_\phi \Gamma}{\sin\theta} \end{pmatrix} \tag{1.40}$$

In spherical coordinates, the two terms of the LLGS equation are clearer : the conservative part behaves like a hamiltonian system, with the antisymmetric matrix ω_0 (in fact a symplectic matrix), and the dissipative part is simply a gradient flow. We shall come back to that later.

To study the stability of an equilibrium, one needs to differentiate the right-hand side of the LLGS equation, to obtain the 2x2 dynamical matrix, labeled L[Guckenheimer 1983]. The dynamical matrix L is formally obtained by studying the evolution of a small deviation $\delta\boldsymbol{m}$ around the equilibrium $\boldsymbol{m}_0$. For a general dynamical system $\dot{\boldsymbol{m}} = \boldsymbol{F}(\boldsymbol{m})$, where $\boldsymbol{F}$ is called the vector field :

$$\delta\dot{\boldsymbol{m}} = \boldsymbol{F}(\boldsymbol{m}_0 + \delta\boldsymbol{m}) - \boldsymbol{F}(\boldsymbol{m}_0) = \boldsymbol{\nabla F}(\boldsymbol{m}_0) \cdot \delta\boldsymbol{m}$$

$L = \boldsymbol{\nabla F}(\boldsymbol{m}_0)$ is the gradient of a vector field, its expression in spherical coordinates is a bit more complicated than in cartesian coordinates. Formally :

$$L = \frac{\gamma}{M_S V} \left(\Omega_1 \, \mathbf{Hess}[\mathcal{H}] - \mathbf{Hess}[\Gamma]\right)$$

For any arbitrary scalar function A, the 2x2 matrix $\mathbf{Hess}[A] = \boldsymbol{\nabla}\boldsymbol{\nabla}A$ is the Hessian of A (gradient of gradient of A) expressed in spherical coordinates. The coefficients of the Hessian are given by $\mathbf{Hess}[A]_{ij} = \dfrac{1}{h_i h_j}(A_{ij} - A_k \Gamma^k_{ij})$, where Γ^k_{ij} are the Christoffel symbol (of second kind) in spherical coordinates and $h_\theta = 1$, $h_\phi = \sin\theta$ are the scale factors. Using the standard notation for the second derivative, $A_{\theta\phi} = \dfrac{\partial^2 A}{\partial\theta\partial\phi}$, it is defined in spherical coordinates and in orthonormal basis by :

$$\mathbf{Hess}[A] = \begin{pmatrix} A_{\theta\theta} & \dfrac{A_{\theta\phi}}{\sin\theta} - \dfrac{\cos\theta}{\sin^2\theta}A_\phi \\ \dfrac{A_{\theta\phi}}{\sin\theta} - \dfrac{\cos\theta}{\sin^2\theta}A_\phi & \dfrac{A_{\phi\phi}}{\sin^2\theta} + \dfrac{\cos\theta}{\sin\theta}A_\theta \end{pmatrix}$$

The second derivatives are evaluated at the equilibrium state $\boldsymbol{m}_0$. Hence the dynamical matrix L writes :

$$L = \frac{\gamma}{M_S V}\begin{pmatrix} -\dfrac{\mathcal{H}_{\theta\phi}}{\sin\theta} + \cot\theta\ \dfrac{\mathcal{H}_\phi}{\sin\theta} - \Gamma_{\theta\theta} & -\dfrac{\mathcal{H}_{\phi\phi}}{\sin^2\theta} - \cot\theta\ \mathcal{H}_\theta - \dfrac{\Gamma_{\theta\phi}}{\sin\theta} + \cot\theta\ \dfrac{\Gamma_\phi}{\sin\theta} \\ \mathcal{H}_{\theta\theta} - \dfrac{\Gamma_{\theta\phi}}{\sin\theta} + \cot\theta\ \dfrac{\Gamma_\phi}{\sin\theta} & \dfrac{\mathcal{H}_{\theta\phi}}{\sin\theta} - \cot\theta\ \dfrac{\mathcal{H}_\phi}{\sin\theta} - \dfrac{\Gamma_{\phi\phi}}{\sin^2\theta} - \cot\theta\ \Gamma_\theta \end{pmatrix} \tag{1.41}$$

This matrix can be further reduced by using the fact that the right-hand side of eq. 1.40 vanishes, but we choose to keep it this way.

To evaluate the dynamical matrix, the free energy E and the spin polarization potential P are expressed in spherical coordinates.

The linearized LLGS writes $\delta\dot{\boldsymbol{m}} = L \cdot \delta\boldsymbol{m}$. Its formal solution for an initial deviation $\delta\boldsymbol{m}_0$ is :

$$\delta\boldsymbol{m}(t) = (\delta\boldsymbol{m}_0 \cdot \boldsymbol{v}_+)e^{\lambda_+ t}\boldsymbol{v}_+ + (\delta\boldsymbol{m}_0 \cdot \boldsymbol{v}_-)e^{\lambda_- t}\boldsymbol{v}_-$$

Where $\boldsymbol{v}_\pm$ are the eigenvectors of L and $\lambda_\pm$ their associated eigenvalues. The eigenvalues of the dynamical matrix L involve its trace $\mathrm{Tr}(L)$, and determinant $\det(L)$, as solutions of the quadratic equation :

$$\lambda_\pm^2 - \lambda_\pm \mathrm{Tr}(L) + \det(L) = 0 \tag{1.42}$$

Let ω_0 be the natural frequency[Smit 1955] :

$$\omega_0^2 = \left(\frac{\gamma}{M_S V}\right)^2 \left[E_{\theta\theta}\left(\frac{E_{\phi\phi}}{\sin^2\theta} + \cot\theta\ E_\theta\right) - \left(\frac{E_{\theta\phi}}{\sin\theta} - \cot\theta\ \frac{E_\phi}{\sin\theta}\right)^2\right]$$

The natural frequency is the positive imaginary solution of eq. 1.42, i.e. the square root of the opposite of the determinant of the dynamical matrix L, if we only take into account the conservative part. As it was already mentioned, the conservative part is larger by a factor α

than the dissipative part, hence, in most situations, the natural frequency is much larger than other terms in the determinant of L. Therefore the dynamical matrix L has two eigenvalues that are complex-conjugate (i is the imaginary unit, $i^2 = -1$) :

$$\lambda_{\pm} = \frac{\Delta\omega}{2} \pm i\omega_0 \sqrt{1 + \left(\frac{\gamma}{M_S V}\right)^2 \frac{\epsilon}{\omega_0^2}} \tag{1.43}$$

With Δ_R being the Laplace operator in spherical coordinates, the expression of the linewidth $\Delta\omega$ is given by :

$$\Delta\omega = -\frac{\gamma}{M_S V}\Delta_R\Gamma = -\frac{\gamma}{M_S V}\left(\Gamma_{\theta\theta} + \cot\theta\ \Gamma_\theta + \frac{\Gamma_{\phi\phi}}{\sin^2\theta}\right)$$

Most of the times, the ϵ term is negligible. Its expression is :

$$\begin{aligned}\epsilon = &\left[\Gamma_{\theta\theta}\left(\frac{\Gamma_{\phi\phi}}{\sin^2\theta} + \cot\theta\ \Gamma_\theta\right) - \left(\frac{\Gamma_{\theta\phi}}{\sin\theta} - \cot\theta\ \frac{\Gamma_\phi}{\sin\theta}\right)^2\right] - \frac{1}{4}\left(\Gamma_{\theta\theta} + \cot\theta\ \Gamma_\theta + \frac{\Gamma_{\phi\phi}}{\sin^2\theta}\right)^2 \\ &+ E_{\theta\theta}\left(\frac{\Gamma_{\theta\phi}}{\sin\theta} - \cot\theta\ \frac{\Gamma_\phi}{\sin\theta}\right) + \left(\frac{E_{\phi\phi}}{\sin^2\theta} + \cot\theta\ E_\theta\right)\left(-\frac{\Gamma_{\theta\phi}}{\sin\theta} + \cot\theta\ \frac{\Gamma_\phi}{\sin\theta}\right) \\ &- \Gamma_{\theta\theta}\left(\frac{E_{\theta\phi}}{\sin\theta} - \cot\theta\ \frac{E_\phi}{\sin\theta}\right) - \left(\frac{\Gamma_{\phi\phi}}{\sin^2\theta} + \cot\theta\ \Gamma_\theta\right)\left(-\frac{E_{\theta\phi}}{\sin\theta} + \cot\theta\ \frac{E_\phi}{\sin\theta}\right)\end{aligned}$$

It appears that $\Delta\omega = \mathrm{Tr}(L)$ and $\omega_0 \approx |\Im(\lambda_\pm)|$, the absolute value of the imaginary part of $\lambda_\pm$. In fact, by definition, the linewidth is twice the real part of the eigenvalues $\Delta\omega = 2\Re(\lambda_\pm)$, and the so-called relaxation frequency is its imaginary part. However, this definition stands only if both eigenvalues are complex conjugates. Moreover, the relaxation frequency is very close to what was defined as the natural frequency, so the two terminologies are used as equivalent here. The natural frequency is also called ferromagnetic resonance (FMR) frequency, because the free layer absorbs micro-wave magnetic fields emitted at this frequency.

With the approximation that $\lambda_\pm = \Delta\omega/2 \pm i\omega_0$, the solution of the linearized LLGS equation becomes :

$$\delta\boldsymbol{m}(t) = e^{\frac{\Delta\omega}{2}t}\left((\delta\boldsymbol{m}_0 \cdot \boldsymbol{v}_1)\boldsymbol{v}_1 \cos(\omega_0 t) + (\delta\boldsymbol{m}_0 \cdot \boldsymbol{v}_2)\boldsymbol{v}_2 \sin(\omega_0 t)\right)$$

Where $\boldsymbol{v}_1$ and $\boldsymbol{v}_2$ are orthonormal vectors. The norm of the deviation follows :

$$|\delta\boldsymbol{m}(t)|^2 = |\delta\boldsymbol{m}_0|^2\ e^{\Delta\omega\, t}$$

where $\Delta\omega$ can be either positive or negative.
Fig. 1.9 describes the evolution of a small deviation $\delta\boldsymbol{m}_0$ close to the equilibrium, it follows a spiral in the plane tangent to the sphere.

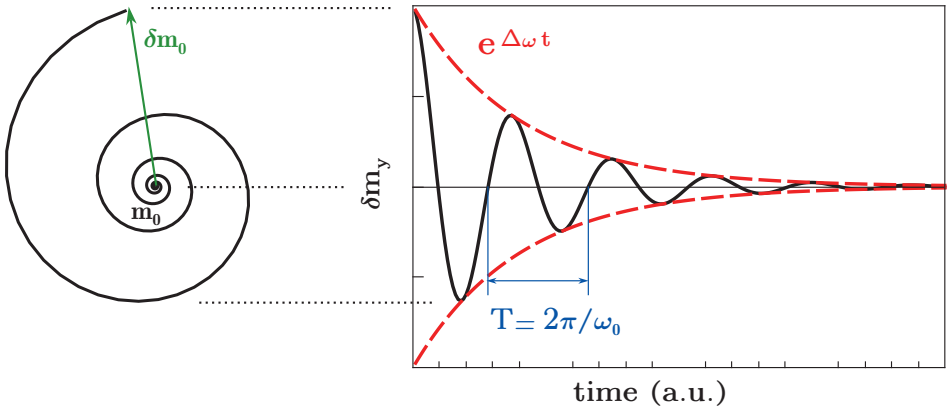

Figure 1.9 – Dynamics of a small deviation $\delta \boldsymbol{m}_0$ around the equilibrium $\boldsymbol{m}_0$ in a case where $\Delta\omega < 0$. (Left) In the plane tangent to the sphere. (Right) Along one direction, versus time. The relaxation to the equilibrium shows oscillations of frequency $2\pi\omega_0$ and of envelope $e^{\Delta\omega\, t}$.

The linewidth $\Delta\omega$ and the natural frequency ω_0 are important parameters for the dynamics of the free layer. If the linewidth $\Delta\omega$ is negative the system relaxes to the equilibrium with damped oscillations of frequency ω_0 and amplitude decay rate $\Delta\omega$. If the linewidth is positive, the magnetization exponentially diverges from the equilibrium. Therefore, the stability of equilibrium configurations is governed by these two parameters. Note that in the absence of STT, the linewidth as defined here is always negative, but may become positive under STT influence.

Notice that the equilibrium nature (stable or not) also depends on the FMR frequency. When the FMR frequency becomes zero due to the applied field, the two eigenvalues become real and the FMR frequency now adds (or subtracts, for the second eigenvalue) to the linewidth. Because the FMR frequency is two order of magnitude larger than the linewidth, the eigenvalues become approximately $\lambda_\pm = \pm\omega_0$, one positive, the other negative. Therefore, the vanishing of the FMR frequency is also changing the stability of the equilibrium.

As an example, let's consider a cylindrical thin film (thickness is along $\boldsymbol{u}_z$) with an elliptical cross-section. The greater axis of the ellipse is along $\boldsymbol{u}_x$. So the magnetostatic energy of this free layer is given by $E_{dem} = \frac{1}{2}\mu_0 M_S^2 V\left(N_{xx}m_x^2 + N_{yy}m_y^2 + N_{zz}m_z^2\right)$, with $N_{zz} \approx 1$, $N_{xx} < N_{yy} \ll N_{zz}$. Because $\boldsymbol{m}$ is normalized to 1, $m_x^2 + m_y^2 + m_z^2 = 1$, and because constant energy terms are not important, the demagnetizing energy rewrites :

$$E_{dem} = \frac{1}{2}\mu_0 M_S^2 V\left(N_z m_z^2 - Q m_x^2\right) \tag{1.44}$$

Where $N_z = N_{zz} - N_{yy}$ and $Q = N_{yy} - N_{xx}$.

The parameter Q is called anisotropy factor. In the macrospin approximation, it gives the same contribution as a magneto-crystalline anisotropy H_K^{crys} along the x axis. The magnetostatic

contribution is called shape anisotropy. In fact the two uniaxial anisotropy contributions are usually included in the factor Q, $Q = N_{yy} - N_{xx} + H_K^{\text{crys}}/M_S$, and the anisotropy field is $H_K = QM_S$. The materials used in MTJ are usually polycrystalline, therefore the magneto-crystalline anisotropy has no preferential direction and the uniaxial anisotropy is mainly given by the shape anisotropy.

Perpendicular magnetic anisotropy (PMA) field $H_\perp$ along the z-axis may also contribute to the easy-plane anisotropy. It is included in the parameter N_z, in fact substracted from $(N_{zz} - N_{yy})$, and we speak of reduced demagnetizing factor or field. If the PMA is strong enough, the demagnetizing field H_d can change sign, so the layer will become perpendicularly magnetized. Magnetic layers with "negative" reduced demagnetizing field are used to realize perpendicular polarizers. Free layers with "positive" reduced demagnetizing field are considered in this thesis, so the magnetization is in-plane at equilibrium.

The x-axis is called easy axis of magnetization, because the energy is minimal when the magnetization lays in this direction. The y-axis is called hard axis of magnetization.

The Zeeman energy due to the external field applied along the x-axis $H_x\boldsymbol{u}_x$ is added to the demagnetizing field energy and the uniaxial anisotropy field. The stray field created by the reference layer on the free layer is neglected and the conservative potential $\mathcal{H}$ is supposed to be only composed of the free energy E, the IEC is neglected.
The total energy E writes :

$$E = \mu_0 M_S V \Big(\frac{1}{2} H_d m_z^2 - \frac{1}{2} H_K m_x^2 - H_x m_x\Big) \tag{1.45}$$

In spherical coordinates, it rewrites :

$$E = \mu_0 M_S V \Big(\frac{1}{2} H_d \cos^2\theta - \frac{1}{2} H_K \sin^2\theta \cos^2\phi - H_x \sin\theta\cos\phi\Big) \tag{1.46}$$

For the spin polarization potential P, the most usual case is considered : a polarizing layer along $+\boldsymbol{u}_x$. Thus :

$$P = I\frac{\hbar}{2e}\frac{\eta}{\lambda}\ln(1 + \lambda\sin\theta\cos\phi) \tag{1.47}$$

Suppose the magnetization is at rest in the $\boldsymbol{m} = +\boldsymbol{u}_x$ configuration. The stability of this equilibrium depends on the linewidth $\Delta\omega$, and on the FMR frequency ω_0 calculated for this configuration :

$$\omega_0 = \mu_0\gamma\sqrt{(H_d + H_K + H_x)(H_K + H_x)} \tag{1.48}$$

$$\Delta\omega = -2\alpha\mu_0\gamma\left(\frac{H_d}{2} + H_K + H_x + I\frac{\hbar}{2e}\frac{\eta}{\alpha\mu_0 M_S V}\frac{1}{1+\lambda}\right) \tag{1.49}$$

Without applied field or current, the linewidth is negative, so the equilibrium is stable. The FMR frequency is equal to the Kittel's frequency, $\omega_0 \approx \mu_0\gamma\sqrt{H_d H_K}$[Kittel 1963].

The linewidth becomes nonnegative when applying a negative field or a negative current. With

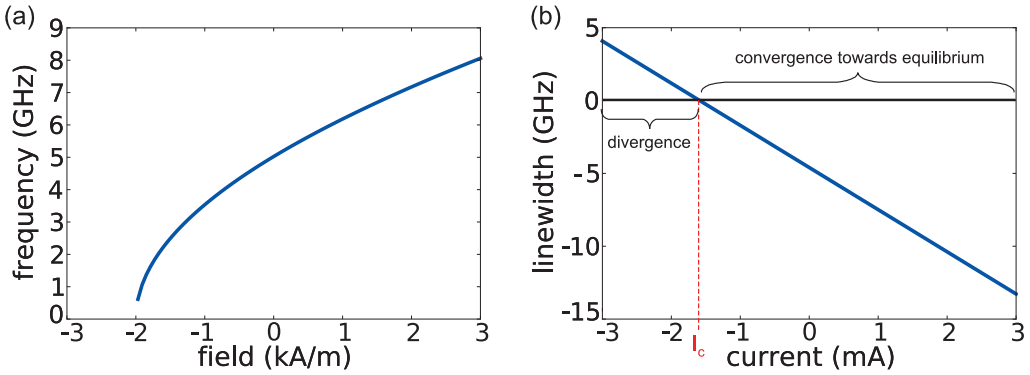

Figure 1.10 – (a) FMR frequency versus applied field following the Kittel's law. (b) FMR linewidth versus applied current.

a field, the FMR frequency vanishes before the linewidth becomes nonnegative, for $H_x = -H_K$, which defines the critical field. With a current, the vanishing of $\Delta\omega$ defines the value of the critical current. The variation of the FMR frequency with the field and of the linewidth with the current are reported on Fig. 1.10.

The linearization analysis confirms the statement that the dissipative part of LLGS controls the stability and relaxation rate, whereas the conservative part defines the oscillating trajectory of the magnetization. The applied current induces dissymmetry, because it contributes mainly to the dissipative part, whereas the applied field contributes equally to both.

The dynamics induced by an applied current through STT are presented in the next section, with two very important technological applications : magnetic memory and nano-oscillators.

Chapter 2

Spintronics devices

In this chapter, we present two already existing applications of the spin-transfer torque (STT) : (i) for random-access memory (STT-MRAM) and (ii) for micro-wave nano-oscillators (STO). The main idea of this work is to take advantage of the rapid precession encountered in STO to realize ultra-fast memories.

2.1 Magnetic random-access memory

The interest for MRAM got strongly renewed after the discovery of the TMR at room temperature. Magnetic tunnel junctions indeed offer larger resistance values and larger magnetoresistance amplitude than GMR stacks. As a result, MTJ are much easier to implement with CMOS components in electronic circuits and in particular memory chips.

Formally, a magnetic tunnel junction (MTJ) is composed of three layers :

(i) A layer with the magnetization fixed in one specific direction. It is also called the reference layer (RL).

(ii) A non-magnetic insulating tunnel barrier, most often made of MgO.

(iii) A layer with "free" magnetization direction, called free layer (FL) or storage layer.

The reference layer is usually composed of two layers : a ferromagnetic layer, in contact with an antiferromagnetic layer. Both layers are coupled by exchange interactions. The antiferromagnet is stiff, its magnetic ordering does not change under field or current application. Therefore the ferromagnetic layer feels a bias field that keeps its magnetization direction unchanged. Its magnetization is supposed to be fixed in the direction $+\boldsymbol{u}_x$.

The magnetization of the free layer has two stable configurations : parallel (P) or antiparallel (AP) to the RL magnetization. Because the magnetoresistance (MR) depends on the relative orientation of the FL and RL magnetizations, the resistance of the stack is maximum (usually) in the AP configuration and minimum in the P configuration.
The magnetic stacks are processed in nanopillars, with electrical connection at the top and the

bottom, so the current is flowing perpendicular to the layer cross-section. This configuration shows more than 100% of resistance change. It is used to fabricate non-volatile replacement for random-access memory, because the magnetic configuration remains stable without power, and so the information.
The different MRAM types share the same current-based reading principle, by reading the resistance of the stack. However they differ by the type of writing.

2.1.1 Field-induced reversal

A first generation of MRAM consisted of magnetic field-based writing. The magnetic field is the Oersted field created by flowing a current in adjacent field-lines, according to Biot-Savart law. In the writing case, no current is applied through the MTJ. The equation of motion of the free layer magnetization $\boldsymbol{m}$ is given by the LLG equation 1.28. The only important quantity is the magnetic free energy E, because, as it was mentined, the damping torque only relaxes the magnetization towards the configuration with minimal energy.

Without applied field, there are two energy minima that correspond to P ($m_x = +1$) and AP ($m_x = -1$) configuration with respect to the reference layer magnetization.
Say the initial configuration is P, then a negative field H_x is applied along the easy x-axis, the P state remains a local minimum until $H_x = -H_K$. Then, only the AP state is a minimum, so the magnetization reverses. If the initial configuration is AP, a field higher than H_K is needed to reverse back the magnetization. The magnetization reversal experiences hysteresis due to the uniaxial anisotropy. In experiments, the macrospin model is not exactly valid, there is also the effect of temperature (the macrospin model is an approximation at 0 K). Thus, the field that needs to be applied to reverse the magnetization, named coercive field H_c, may be different from the uniaxial anisotropy field H_K, but approximately :

$$H_c = H_K \tag{2.1}$$

In order to realize a memory cell, several MTJ are grown in a two-dimensional array, as pictured in Fig. 2.1.a. The field lines are common to several junctions, therefore the switching of one particular junction cannot be achieved with only one field line, otherwise all the junctions along this line would reverse also. Instead, the selective switching of one junction is achieve using the two field lines, the bit line and the word line. The selected junction is reversed by the common action of one field along the easy axis H_x and one field along the hard axis H_y. The junction cannot be reversed with only one of these fields, therefore the other junctions on the same bit or word line are not reversed, because only one direction of the field is applied. On the selected junction, the switching field is characterized by the equation of the Stoner-Wohlfarth astroid, as represented on Fig. 2.1.b. The equation of the astroid is given by :

$$H_x^{2/3} + H_y^{2/3} = H_K^{2/3} \tag{2.2}$$

When the two field lines are activated, $H_x = H_y = H_a$, so that the reversal occurs at $H_a \approx 0.35 H_K$. The selectivity is ensured if the field lines create a field between $0.35 H_K$ and H_K.

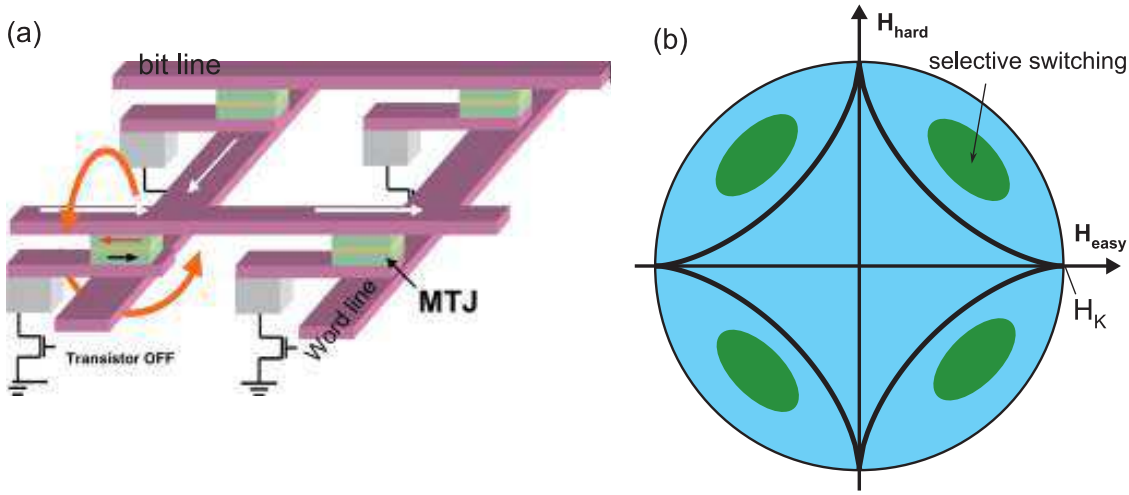

Figure 2.1 – (a) Picture of a 4 bits MRAM cell, with the two field lines to select one particular junction. (b) Stoner-Wohlfarth astroid with the field range for selective switching.

The principal disadvantage of field-induced reversal is the scalability of the field lines. As the size of the memory cells decreases, the field line cross-section decreases and its resistance increases. Hence to generate the same external field, more tension is needed at the field-line terminals. Another problem when decreasing the size, is that the field created for one specific junction may affect neighbouring junctions. On the contrary, current-induced writing is cell-selective and more efficient when the size is decreased.

2.1.2 Current-induced reversal

Instead of generating an external field, a pulse of current is sent through the magnetic junction to reverse the magnetization by spin transfer torque (STT). Tunnel junctions do not tolerate constant current, so instead current pulses of few nanoseconds are sent through the junction. The equation of motion is governed by the conservative potential, that is supposed to be equal to the free energy E and the dissipative potential $\Gamma = \alpha E - P$, with the spin torque potential P defined in eq. 1.36 with $\boldsymbol{m}_L = \boldsymbol{u}_x$. The current is supposed to affect essentially the dissipative potential : it does not change the energy, but the relaxation rate, or damping. To reverse the magnetization, the current needs to have the correct polarity depending on the initial equilibrium state, and a large enough amplitude so that the linewidth becomes positive, $\Delta\omega > 0$ (see eq. 1.49). There is an hysteresis with two critical currents depending on the initial state :

$$I_c^P = \frac{\alpha}{\eta}(1+\lambda)\frac{2e}{\hbar}\mu_0 M_S V(\frac{H_d}{2} + H_K) \tag{2.3}$$

$$I_c^{AP} = \frac{\alpha}{\eta}(1-\lambda)\frac{2e}{\hbar}\mu_0 M_S V(\frac{H_d}{2} + H_K) \tag{2.4}$$

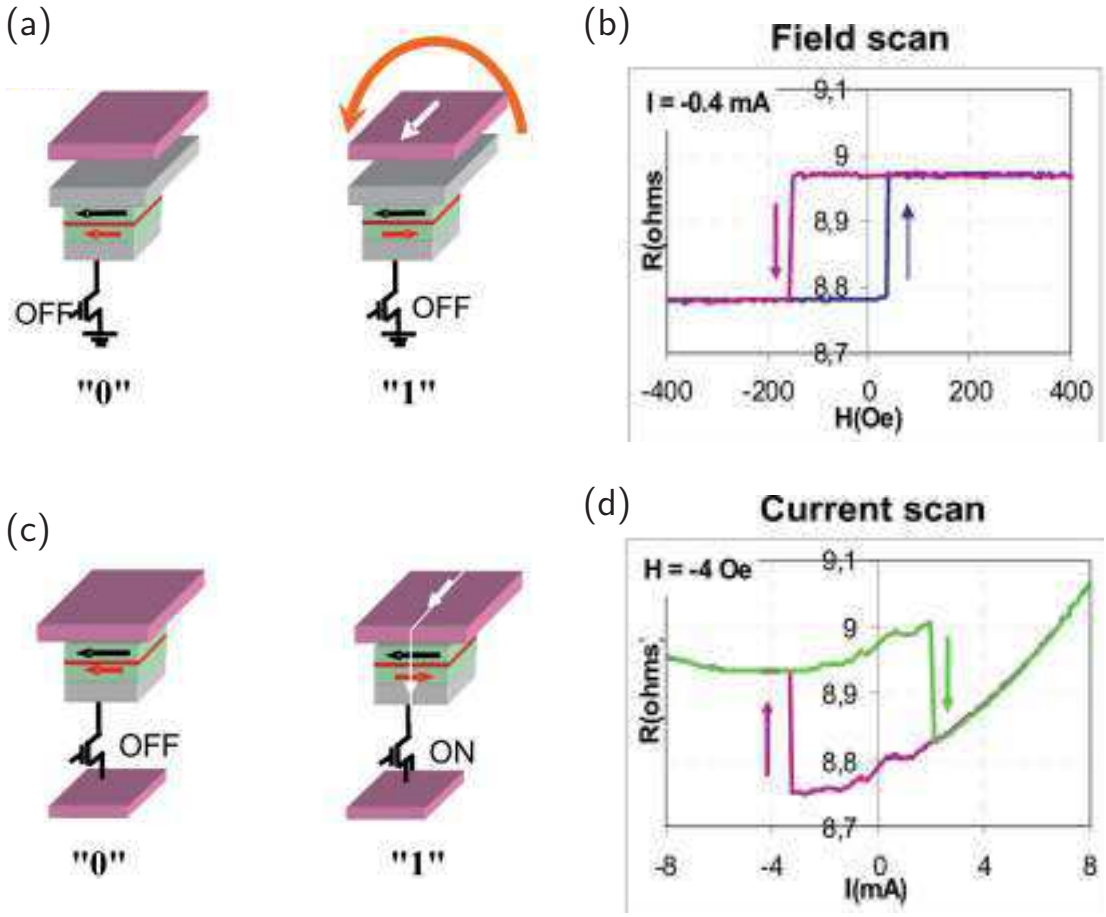

Figure 2.2 – (a) Field-induced and (c) current-induced switching of an MRAM cell from P to AP configuration. Hysteresis loop when sweeping (b) the field and (d) the current. Adapted from [Dieny 2010].

Current-induced switching is illustrated in Fig. 2.2.(c-d), as a comparison with field-induced switching in Fig. 2.2.(a-b).

Notice that, in the absence of applied field, the spin polarization asymmetry λ can be estimated by $\lambda = \dfrac{I_c^P - I_c^{AP}}{I_c^P + I_c^{AP}}$.
The critical current is proportional to the volume V, so it is decreased by decreasing the cell size. It is also proportional to H_d ($H_K \ll H_d$ in thin films), so it is interesting to reduce the demagnetizing field with a perpendicular anisotropy, which was indeed observed experimentally[Khalili Amiri 2011].

The mapping of the junction resistance with a combination of applied field and applied current provides the phase diagram of the magnetization, with regions where only the P configuration is available, where only AP is stable, and finally the bistable region, inside the hysteresis, with both configurations P or AP possible. The regions borders are given by the coercive field,

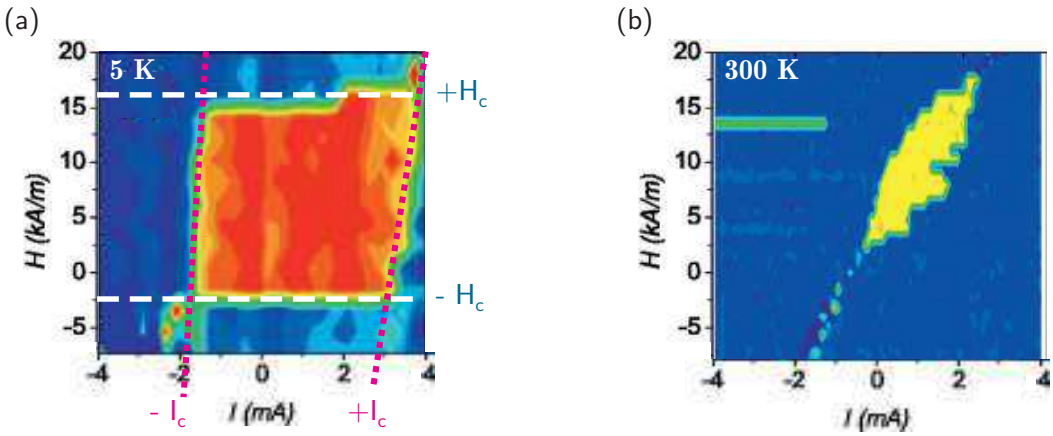

Figure 2.3 – Experimental phase diagram versus field and current, at (a) 5 K and (b) 300 K. The field is shifted due to a residual stray field. From [Schneider 2007].

that remains unchanged when a current is applied because it comes from the energy term, and by the critical current under field that is given for the two initial configurations P and AP by :

$$I_c^P = \frac{\alpha}{\eta}(1+\lambda)\frac{2e}{\hbar}\mu_0 M_S V(\frac{H_d}{2} + H_K + H_x) \tag{2.5}$$

$$I_c^{AP} = \frac{\alpha}{\eta}(1-\lambda)\frac{2e}{\hbar}\mu_0 M_S V(\frac{H_d}{2} + H_K - H_x) \tag{2.6}$$

The temperature modifies the region borders. Indeed, thermal fluctuations allow the switching to occur for lower currents or fields, as shown on Fig. 2.3. More details about the effect of temperature on the switching will be given in Appendix A.

2.1.3 Influence of the stray field

In most spintronic devices, in particular MTJ, the reference layer is creating a stray field on the storage layer.
The stray field is constant, as long as the RL magnetization remains fixed, and along $-\boldsymbol{u}_x$ (opposite to the RL magnetization direction). It shifts the storage layer hysteresis loop. The AP configuration is generally more stable than the P configuration. If the stray field is even larger than the coercive field, only the AP configuration is stable at remanence (zero external field).

In order to reduce or even cancel the stray field of the reference layer, a synthetic antiferromagnetic reference layer is used. In general, two magnetic layers separated by a metallic spacer, usually ruthenium Ru, that are coupled through RKKY exchange, is called a synthetic ferrimagnet (SyF). If the RKKY coupling is negative and the two layers have the same magnetic volume ($\mu_0 M_{S1} V_1 = \mu_0 M_{S2} V_2$), the structure is called a synthetic antiferromagnet (SAF). For

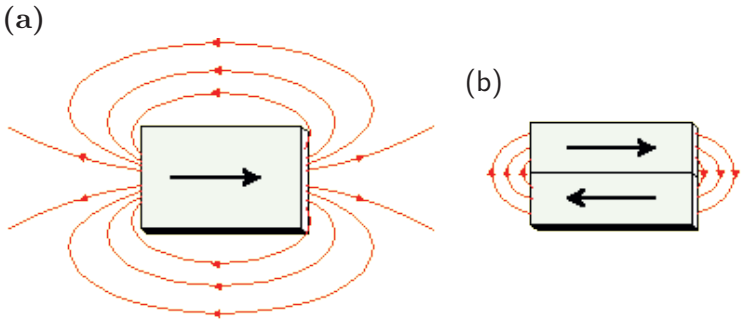

Figure 2.4 – Stray field generated by (a) a single layer uniformly magnetized and (b) a synthetic antiferromagnet (SAF).

a SAF reference layer, the overall stray field is much reduced, and by experimentally adapting slightly the thicknesses of each of its layers, the stray field on the free layer can be successfully canceled, as shown in Fig. 2.4.

A SyF layer offers other advantages than a reduced stray field, one of them is that the coercive field of a SyF free layer is increased compared to a single layer with the same magnetic volume. In Part II, we will come back to the advantages and downsides of a SyF free layer.

2.1.4 Thermally activated switching

The problem of thermal stability of the junction is not addressed here, but the fact that the switching is triggered by thermal fluctuations.

Like field-induced reversal, current-induced reversal is thermally activated. Indeed, the linearized equation of motion writes $|\delta \boldsymbol{m}(t)|^2 = |\delta \boldsymbol{m}_0|^2 \, e^{\Delta\omega \, t}$, so $\Delta\omega > 0$ is a necessary condition for switching, but an initial deviation $\delta \boldsymbol{m}_0$ is also needed. According to STT expression, proportional to $\boldsymbol{m} \times (\boldsymbol{m} \times \boldsymbol{u}_x)$, STT vanishes if the magnetization is exactly at equilibrium along the x-axis (notice that the same problem arises for field-induced switching). Thermal fluctuations generate such deviations from equilibrium, but as it is a random process, the switching is stochastic. In experiments, the switching of an in-plane MTJ occurs after some random incubation time as demonstrated by Devolder et al[Devolder 2008]. It must be emphasized that the incubation time is not reduced by applying the current, it is only due to thermal fluctuations. That makes it difficult to fabricate ultrafast switching MTJ with conventional MTJ embodiment. Below 10 ns the error rate increases dramatically.
One idea to accelerate the writing process is to exert a torque on the free layer magnetization that does not vanish at equilibrium. For field-induced switching, this is realized by applying a small transverse field (in-plane but along the y-axis). For current-induced switching, another layer can be added, in contact with the free layer, to polarize the spin of the conduction electrons in a transverse direction. Namely, for an in-plane magnetized MTJ, the additional layer is

magnetized out-of plane[1]. The combination of an in-plane free layer and a perpendicularly polarized layer, called perpendicular polarizer, was already used for application as nano-oscillator. We will present some of these results.

2.2 Spin transfer torque nano-oscillators

Before showing the combination of an in-plane free layer with a perpendicular polarizer, an explanation of in-plane spin transfer torque nano-oscillators (STO) is required. A general framework to deal with STO will also be introduced.

2.2.1 Limit cycle of a dynamical system

The macrospin model for an in-plane free layer under current comprises the two parts, conservative and dissipative. Once again, the conservative part $\mathcal{H}$ is supposed equal to the free energy E, the IEC is negligible. The dissipative potential is supposed to be smaller by a factor α than the free energy. From a dynamical system point of view, the LLGS equation is composed of a Hamiltonian flow (conservative part) with a gradient flow perturbation (dissipative part) as it clearly appeared in spherical coordinates. Among all the possible trajectories or orbits of the dynamical system, two kinds have a special interest :

- Equilibrium point : the state remains the same, $\boldsymbol{m}(t) = \boldsymbol{m}_0$. They are defined by a vanishing vector field, $\boldsymbol{F}(\boldsymbol{m}) = 0$. They are, for example, the P and AP states. But also the $m_z = \pm 1$ configurations (without applied field). Another couple of equilibrium state exists in the plane of the layers, they are defined by $m_y = \pm 1$ without applied field.
- Limit cycle : it is a periodic trajectory. It exists a period T, such that $\boldsymbol{m}(t+T) = \boldsymbol{m}(t)$ for all t. When the dissipative part is omitted, all trajectories are limit cycles, characterized by a constant energy.

Another distinction exists, between asymptotically stable and unstable equilibriums and limit cycles (there are also *hybrid* semi-stable orbits). A limit cycle (or an equilibrium) is asymptotically stable if the infinitesimally close orbits are attracted to the limit-cycle (or the equilibrium) in the long-time limit. For equilibriums, the asymptotic stability or instability is determined by the eigenvalues of the Jacobian of the vector field, as seen in the previous section. It is summarized on Fig. 2.5. For limit-cycles, one needs to calculate the stability in the associated Poincaré map. Usually it is a complicated problem. However for 2-dimensional systems, some simplifications exist.

From the expression of the linewidth $\Delta\omega$ of the different equilibriums without current or external field, the P and AP configurations are asymptotically stable equilibriums, whereas the out-of-plane configuration is unstable. The $m_y = \pm 1$ configurations present two real eigenvalues, one positive and one negative. It is semi-stable equilibrium, called a saddle-point.

[1]Because the in-plane anisotropy comes mainly from shape anisotropy, and it is similar for all the stack, it is complicated to realized another layer magnetized along the y-axis.

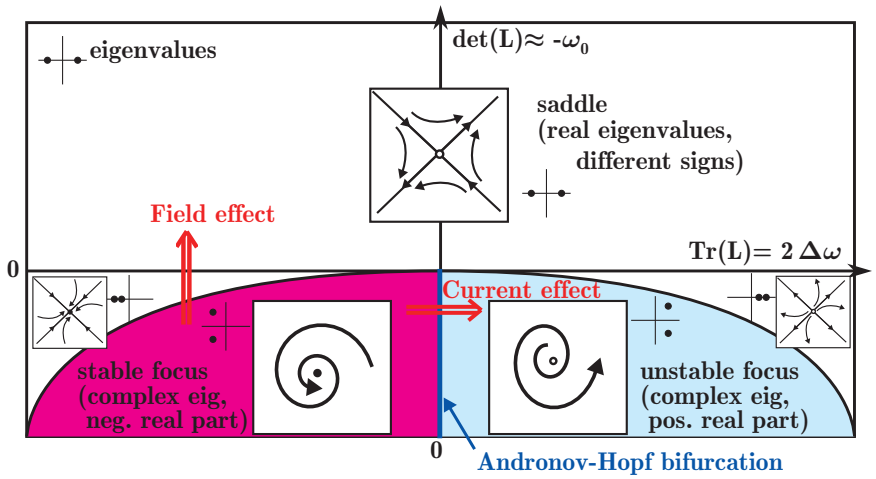

Figure 2.5 – Diagram of equilibrium, versus the trace and determinant of the dynamical matrix L. Without field or current, the equilibrium is a stable focus. Under field, the stable focus becomes a stable node (not labelled), then a saddle-point. Under current, the focus becomes unstable through an Andronov-Hopf bifurcation. Adapted from [Izhikevich 2010].

The constant energy limit cycles are unstable in the LLG equation without damping term, and they do not exist if the damping term is added, but they can become stable with the LLGS equation (damping and STT terms). It is closely related to the fact that the damping torque always decreases the energy, but the STT is giving energy to the system. With appropriate parameters, the energy is compensated on the periodic orbit in average, and the system oscillates. On a periodic orbit $\mathcal{C}$ with period T, the energy is globally conserved, so :

$$0 = E(T) - E(0) = \oint_{\mathcal{C}} \dot{E} \mathrm{d}t = -\frac{\gamma}{M_S V} \oint_{\mathcal{C}} \frac{\partial E}{\partial \boldsymbol{m}} \cdot \frac{\partial \Gamma}{\partial \boldsymbol{m}} \mathrm{d}t \tag{2.7}$$

The energy may not be constant along the limit cycle trajectory. In fact it is usually oscillating around an average energy.
The existence of limit-cycles, or self-sustained oscillations, depends on the material parameters, and also on the control parameters, external field and applied current. However, a limit cycle can only exist if its trajectory encompasses a stable or an unstable equilibrium point. So for in-plane MTJ, one distinguishes only four limit-cycles, of two types :

(i) Two limit-cycles around the minimum energy equilibriums P and AP ($\boldsymbol{m}_0 = \pm \boldsymbol{u}_x$), called in-plane precessional states (IPP).

(ii) Two limit cycles around the energy maximums $\boldsymbol{m}_0 = \pm \boldsymbol{u}_z$, called out-of-plane precessional states (OPP).

For vanishing current and applied field, no limit-cycle exists. When they are turned on, limit-cycles can appear. In the LLGS equation, limit cycles appear when an equilibrium changes types, from stable to unstable, in a so-called *Andronov-Hopf bifurcation*.

2.2.2 All-in-plane STO

Of great interest is the appearance of self-sustained oscillations when the current is increased above the critical current $I_c^{P/AP}$ defined earlier. It was mentioned that the equilibrium state P/AP becomes unstable for such current, but self-sustained oscillations, namely IPP, become in fact available. They exist until the current reaches another critical current $I_{c2}^{P/AP}$. The range of existence of IPP is determined by the average energy of the oscillations, that needs to be smaller than the saddle-point energy. The state diagram of Fig. 2.6 summarizes the region of existence of IPP and OPP, the energy profiles and the trajectories of the oscillations.
When the current is slightly above the critical current, the self-sustained oscillations can be described by the linearized LLGS equation. In fact, at the critical current, say $I = I_c^P$ from the P equilibrium state, the linewidth $\Delta\omega$ vanishes. Then a magnetization state close to the equilibrium will precess around the equilibrium with a frequency equal to the FMR frequency ω_0. By continuity, for a current slightly larger than I_c^P, the frequency of the oscillations will be very close to the FMR frequency ω_0. However, due to the complexity of LLGS equation, the periodic orbit of the self-sustained oscillation of the magnetization is not known exactly. The current dependence of the frequency is also unknown. The precessional state has to be computed numerically to extract the useful parameters. Also, the energy is not constant along the trajectory, but instead it oscillates around an average value. The frequency is found to decrease with increasing current, it is called frequency red-shift.

The magnetization oscillation is transformed into readable content via GMR (or TMR) effect. As the magnetization precesses, the resistance of the junction changes, because it depends on $\cos\theta_R = \boldsymbol{m} \cdot \boldsymbol{u}_x$. Hence, if a constant current flows through the junction, an alternating voltage is generated between the two ends. It is a radio-frequency (RF) source. However, the magnetization $\boldsymbol{m}$ oscillates very closely around $\boldsymbol{u}_x$, so $\cos\theta_R$ is quite small, and the amplitude of the output AC signal is rather small.

In-plane MTJ is the preferred geometry to realize STO, because sample fabrication process is mature and IPP give good performances in terms of noise. However, there is another geometry that exhibits self-sustained oscillation, but OPP instead of IPP. Its advantage is that the output signal is larger.Furthermore, the equation of motion in macrospin is solvable analytically in this case. This is the configuration with in-plane free layer and perpendicular polarizer described in the next section.

2.2.3 STO with a perpendicular polarizer

In IPP-STO, the precessional state is due to the STT coming from an in-plane reference layer. Instead, let the in-plane free-layer be separated by a spacer from a layer with fixed out-of-plane magnetization, that is called a perpendicular polarizer[Lee 2005, Houssameddine 2007, Ebels 2008].
The free energy is the same as previously, and so is the conservative potential (IEC is still negligible). There is no applied field. The dissipative potential Γ is changed compared to the

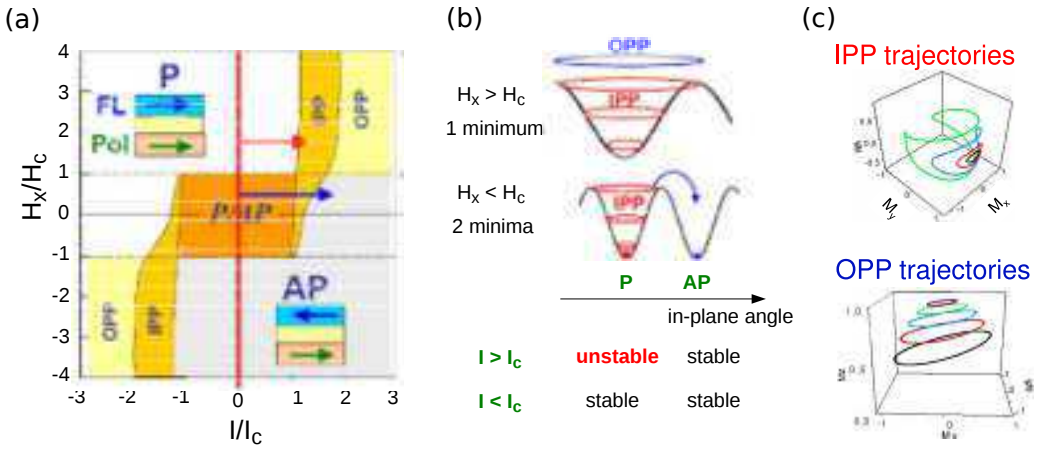

Figure 2.6 – (a) Phase diagram of the free layer magnetization versus field and current. (b) Energy profile versus in-plane angle, with an external field larger than H_c (top), showing one global minimum, and smaller than H_c (bottom), with two minima, P and AP. In the latter case, the equilibriums' stability depend on the current amplitude. (c) Constant energy trajectories, IPP and OPP. The self-sustained oscillations trajectories are very close to those ones. From [Quinsat 2012]

previous all-in-plane configuration, though. The spin torque potential P now writes :

$$P = I\frac{\hbar}{2e}\frac{\eta_z}{\lambda_z}\ln(1+\lambda_z \boldsymbol{m}\cdot\boldsymbol{u}_z) \tag{2.8}$$

The spin polarization and spin polarization asymmetry of the perpendicular polarizer are labeled η_z, and λ_z.
In this framework, the LLGS equation in spherical coordinates (θ,ϕ) writes :

$$\dot{\theta} = \mu_0\gamma\Big(- H_K \sin\theta\sin\phi\cos\phi + \alpha\sin\theta\cos\theta(H_d + H_K\cos^2\phi) - \frac{\hbar}{2e}\frac{I\eta_z}{\mu_0 M_S V}\frac{\sin\theta}{1+\lambda_z\cos\theta}\Big) \tag{2.9}$$

$$\dot{\phi}\sin\theta = \mu_0\gamma\sin\theta\Big(- \cos\theta(H_d + H_K\cos^2\phi) - \alpha H_K\sin\phi\cos\phi\Big) \tag{2.10}$$

Contrary to a longitudinal STT (along the x-axis), the perpendicular STT changes the equilibrium state under applied current. The equilibrium is computed by taking $\dot{\theta} = \dot{\phi} = 0$. The equilibrium angles (θ_0,ϕ_0) are defined by :

$$\cos\theta_0 = 0 \qquad\qquad 0 = -\frac{H_K}{2}\sin(2\phi_0) - \bar{\eta}I \tag{2.11}$$

Here $\bar{\eta} = \dfrac{\hbar}{2e}\dfrac{\eta_z}{\mu_0 M_S V}$. So an in-plane steady state (IPS) exists under applied current, defined by the in-plane angle ϕ_0 : $\sin(2\phi_0) = -2\bar{\eta}I/H_K$. It corresponds to the P or AP state at vanishing current. The equilibrium in-plane angle ϕ_0 cannot be larger than $\pm\dfrac{\pi}{4}$, that is reached for the critical current I_c^{PERP} :

$$I_c^{\mathrm{PERP}} = \frac{2e}{\hbar}\frac{\mu_0 M_S V}{\eta_z}\frac{H_K}{2} \tag{2.12}$$

Above this critical current, no equilibrium exists and the system has to be in a steady precessional state. However, this critical current does *not* correspond to an Andronov-Hopf bifurcation, and in fact steady precessional state can exist below this critical current.
Another equilibrium exists, which is defined by $\sin\theta_0 = 0$. It corresponds to $m_z = \pm 1$, an out-of-plane steady state (OPS). Contrary to the IPS equilibrium that is always stable[2], the OPS is unstable except for large enough currents.

The self-sustained oscillations are not easily identifiable in general, however they appear clearly in the LLGS equation, under the assumption that $H_K \ll \alpha M_S$. A way to properly deal with these terms will be exposed later, as for now the anisotropy terms is removed and the LLGS reduces to :

$$\dot{\theta} = \alpha\mu_0\gamma H_d\left(\cos\theta - \frac{\frac{\bar{\eta}I}{\alpha H_d}}{1+\lambda_z\cos\theta}\right) \tag{2.13}$$

$$\dot{\phi} = -\mu_0\gamma H_d\cos\theta \tag{2.14}$$

From these equations, it appears that a steady precessional state exists. It is defined by a constant out-of-plane angle θ_0, characterized by $\dot{\theta} = 0$, and a constant frequency f_0 :

$$\cos\theta_0 \approx \frac{\bar{\eta}I}{\alpha H_d} \qquad\qquad f_0 = \frac{\mu_0\gamma H_d}{2\pi}\cos\theta_0 = I\frac{\mu_0\gamma\bar{\eta}}{2\pi\alpha} \tag{2.15}$$

The self-sustained oscillations in a structure with a perpendicular polarizer are OPP oscillations : the magnetization rotates around the out-of-plane axis, in fact around the energy maximum defined by $\boldsymbol{m} = \pm\boldsymbol{u}_z$. The out-of-plane component of the magnetization $m_z = \cos\theta_0$, increases with increasing current. Hence, the oscillations frequency increases also with applied current, a so-called frequency blue-shift.
Notice that nothing forbids the precessional state to exist for currents below the critical current I_c^{PERP}. The transition equilibrium/OPP is "hysteretic".

The OPP steady state exists as long as the equilibrium out-of-plane angle θ_0 is defined, which is the case below the critical current called I_c^{OPP} :

$$I_c^{OPP} = \frac{2e}{\hbar}\frac{\mu_0 M_s V}{\eta_z}\alpha H_d \tag{2.16}$$

Above this critical current, the OPP cannot exist, and the OPS equilibrium is stable. In fact, it describes an Andronov-Hopf bifurcation of the OPS equilibrium. Unlike the scenario for IPP, the equilibrium *becomes* stable above the critical current. The critical currents, steady states and frequency versus current for the in-plane free layer with a perpendicular polarizer are represented on Fig. 2.7.

In this particular case where the anisotropy is omitted, the trajectories are *exactly* the constant-energy trajectories : the current, through STT, cancels the damping and allows the

[2]It is deduced from the computation of the dynamical matrix at the IPS equilibrium, as detailed in ref. [Ebels 2008]

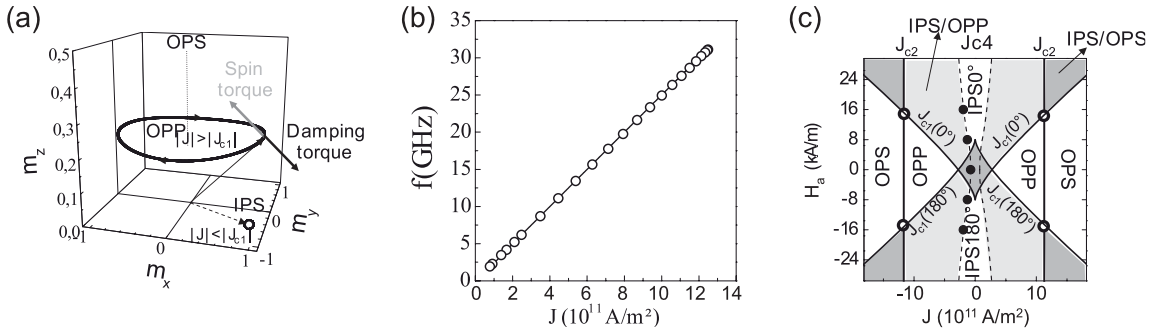

Figure 2.7 – In-plane free layer with a perpendicular polarizer from [Ebels 2008]. (a) Free layer magnetization in the three steady states : in-plane stable state (IPS), out-of-plane precession (OPP) and out-of-plane stable state (OPS). (b) Linear dependence of the frequency of the OPP with respect to the applied current density. (c) State diagram versus applied current density J and in-plane easy-axis applied field H_a representing the different critical currents.

system to reach and to stabilize in another energy level.
The effect of the STT due to the perpendicular polarizer on the magnetization dynamics can be summarized as : the STT drags the magnetization out-of-plane, in competition with the demagnetizing field, through the damping, which tends to bring the magnetization back in plane. Hence the two torques reach an equilibrium point, characterized by a constant out-of-plane angle θ_0. Moreover, the conservative part in LLGS equation induces a precession of the magnetization around the effective field, which, in this case, is the demagnetizing field. Because the conservative motion does not change the out-of-plane angle, it does not change the equilibrium between the damping and the STT. Unfortunately, this is not the case of other structures, like all-in-plane STO. It makes their trajectories more complex.

Contrary to all-in-plane STO, the magnetoresistive signal is large here. Indeed, the GMR or TMR signal is due to an in-plane reference layer (that was not included in the STT contributions, yet), so the magnetoresistive signal is sensitive to $m_x = \sin\theta\cos\phi$. During the precession, the magnetization is almost in-plane for low current, so the resistance oscillates between almost the P and AP resistance levels, giving a large output AC signal.

With typical values of saturation field of $M_S = 1.2\,\text{e}6$ A/m, $\alpha = 0.01$, $\eta_z = 0.3$, a volume of V=100x100x1 nm^3 and currents of $I = 0.1$ mA (corresponding to density of current of 1e10 A/m^2), the frequency f_0 is around 2 GHz. This corresponds to a half-precession in 250 ps. Therefore, a system with an in-plane MTJ with an additional perpendicular polarizer was envisaged for application in ultrafast MRAM, as described below.

2.3 Ultrafast MRAM : Precessional switching

As was already mentioned, the reversal in a classical STT-MRAM is stochastic. Therefore, even if the switching itself takes less than 1 ns, the incubation time makes that, in average, the current pulse needs to last at least 10 ns to have writing error rates compatible with ap-

plications. In order to make the switching deterministic, the idea is to provide an initial angle deviation from the equilibrium. For example by adding a perpendicular polarizer. This was first described in a patent by SPINTEC[Redon 2001].
Such a structure comprises an in-plane magnetic junction with a perpendicular polarizer, composed of five formal layers :

(i-iii) The "classical" in plane stack, with a reference layer (RL), the non-magnetic layer (NM) and the free layer (FL).

(iv) Another non-magnetic layer, which can be metallic or insulating.

(v) A perpendicular-to-plane magnetized layer, which acts as a current polarizer (PL).

In a first approximation, let's consider that the effect of the reference layer on the writing is negligible, so it gives no STT contribution. The reference layer is used only for reading.

In fact, the MRAM stack is very similar to an oscillator stack with perpendicular polarizer, except that oscillators work with a DC current, whereas for memory applications, current pulse of well-defined width are sent through the junctions.

Due to the STT contribution of the perpendicular polarizer, the magnetization will oscillate around the out-of-plane axis as long as the current is applied. The idea of precessional switching is to stop the current when the magnetization has operated half of a precession, so the magnetization relaxes in the opposite equilibrium configuration. As was already mentioned, it would be possible to reverse the magnetization, in a deterministic way, in around 500 ps. In fact, faster commutation can be achieved by increasing the current amplitude. As the frequency of the OPP is proportional to the current, the switching time is inversely proportional to the current. In consequence, the current pulse duration has to be decreased, though.

A similar deterministic switching technique is used to write an MRAM cell with a transverse external field. In this case, there is no perpendicular polarizer, and a pulse of transverse in-plane field (along $\boldsymbol{u}_y$) of controlled duration is sent to reverse the magnetization[Serpico 2003, Devolder 2011].

The drawback of these deterministic switching techniques is that the current pulse duration has to be very accurate (even for field-induced reversal, the field is generated by a current). In the case of in-plane MTJ with perpendicular polarizer that is the main subject of this work, it appears to be a very problematic aspect, as it will be shown in Part III. In a nutshell, for such reversal time, less than 1 ns, it is complicated to obtain sharp current pulses, hence the switching properties are altered.

2.4 Summary and problematic

The goal of the present work is to optimize the structure comprising an in-plane MTJ with a reference layer and a perpendicular polarizer, so that the reversal of the free layer occurs like

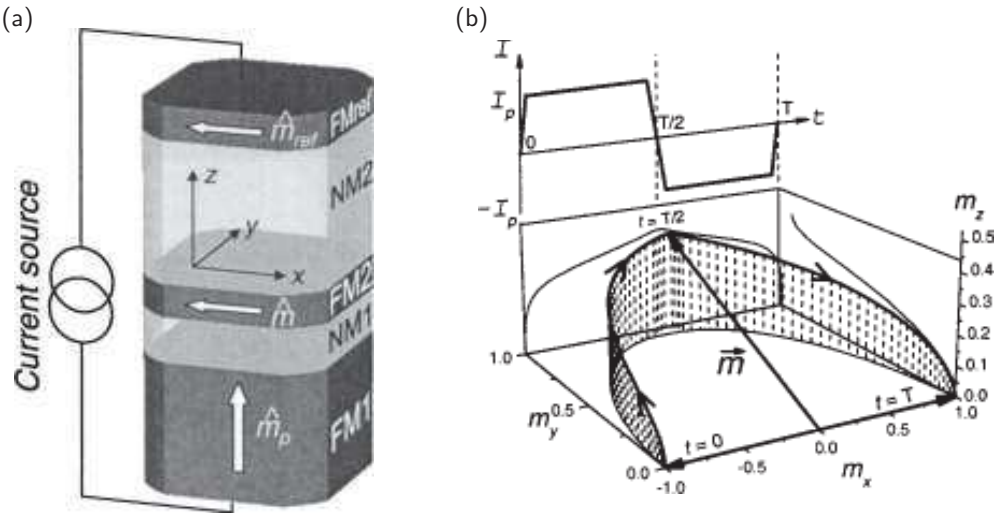

Figure 2.8 – (a) MRAM stack comprising, from top to bottom, a fixed in-plane reference layer (FMref), a non-magnetic spacer (NM2), an in-plane free layer (FM2), another spacer (NM1), a fixed perpendicular polarizer (FM1). (b) Free layer magnetization reversal with current pulses of alternating polarity. The first pulse ($+I_p$) pulls the magnetization out-of-plane, so it starts a quarter of a precession around the out-of-plane axis. The second pulse makes the magnetization rotate until the opposite equilibrium position. From [Kent 2004].

in a classical MTJ, from P to AP for positive current and AP to P for a negative current. This is called bipolar switching, to distinguish it from the oscillating state. First, it is important to understand more precisely how the different adjustable parameters in the structure modify its global behavior.

These preliminary results are presented in **Part II**.

Chapter 3 is focused on the properties of a synthetic free layer under STT, with the two contributions treated separately (see Fig. 2.9.a and b) : first with a perpendicular polarizer, second with an in-plane reference layer. In both cases the critical currents are computed and compared to a single layer free layer. With the STT from the perpendicular polarizer, the equation of the OPP is computed and the influence of the RKKY coupling is discussed. For the STT from the reference layer, different solutions to reduce the critical currents are proposed. Finally, the situation without any polarizing layer but with mutual STT between the layers is considered.

Chapter 4 presents the results of a perturbation analysis of the OPP steady state of a single layer free layer with a perpendicular polarizer. The applied field, anisotropy field and reference layer STT were not taken into account in earlier studies. They are introduced as small perturbations (see Fig. 2.9.c). The frequency change and second harmonics due to these perturbations are computed. The critical current for the existence of the OPP under such perturbations is also determined.

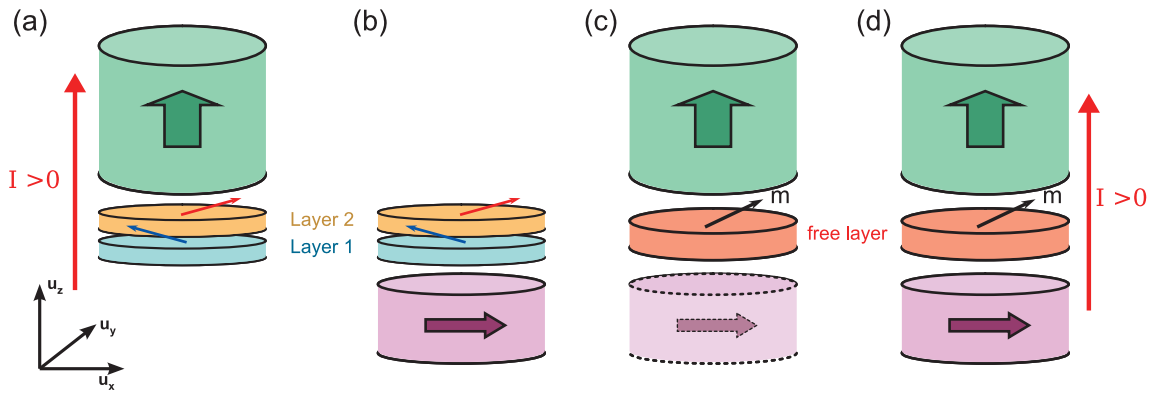

Figure 2.9 – Different configurations studied : (a) Synthetic ferrimagnet (SyF) free layer coupled by RKKY energy, with perpendicular polarizer. (b) SyF free layer with an in-plane reference layer. (c) Single layer free layer with a perpendicular polarizer. The spin torque from the reference layer is treated as a perturbation. (d) Free layer with an in-plane reference layer and a perpendicular polarizer for application as ultra-fast MRAM.

In **Part III**, the phase diagram of an in-plane MTJ with reference layer and a perpendicular polarizer (Fig. 2.9.d) is computed. The switching behavior of the free layer, oscillating or bipolar switching, is analyzed regarding relative influence of the two polarizing layers and the anisotropy field, that is related to the cell aspect ratio. The theoretical results are then confirmed by experiments, by measuring the transmitted pulse through the junction in real-time.

Part II

Macrospin simulations and analytical studies of self-sustained oscillations and critical currents

Chapter 3

STT induced OPP and critical currents in synthetic ferrimagnets

To realize in-plane STT-MRAMs, a synthetic ferromagnetic (SyF) free layer can be interesting because the magnetostatic stray field felt by the free layer from other layers is much reduced. Similarly, the reference layer is less affected by the free layer and is more stable. The perpendicular polarizer is also less affected by the stray field from the free layer, that tends to pull its magnetization in-plane. The stability of the whole structure is enhanced if the layers are SyF instead of single layers.
For STT-MRAMs, the magnetization is reversed by the applied current. Although the dynamics of a SyF free layer with external field are well known, the STT-induced dynamics of a SyF is still under active research. In order to realize STT-MRAM with two orthogonal polarizing layers, the option of using a SyF free layer has to be considered. Therefore, the STT excitation of a SyF free layer is studied for two different directions of the polarizing layer : perpendicular to the plane and along the magnetization easy axis. The two orientations of the polarizing layer are studied independently because of the complexity of the system comprising a SyF free layer and two polarizers with orthogonal magnetization directions. For each magnetization direction of the polarizing layer, a stability analysis of the equilibrium is performed, in order to determine the critical currents of a SyF free layer. In the case of a perpendicular polarizer, the self-sustained oscillations of the SyF free layer are described.

These two configurations of the polarizing layers show interesting behaviors, especially in the dependence to the RKKY coupling. Moreover, the choice of the relative thickness of the two layers adds a degree of liberty in the system, which is particularly interesting because the layer thickness is a parameter easier to adjust than other parameters, for instance the anisotropy of the layers.

3.1 Dynamics of the SyF

This section aims to present the general dynamics of a synthetic ferrimagnet (SyF) free layer. Like for a single layer (SL) free layer, the dynamics is described by two potentials, conservative and dissipative. They involve the total free energy of the two layers, and spin torque potentials for each layer.

3.1.1 Description of the system

The free layer is composed of two coupled magnetic layers, labeled 1 and 2. The total free energy E holds the demagnetizing energy of both layer, the uniaxial anisotropy and the in-plane field along the easy axis, plus an RKKY interaction term. The magnetization of layer 1 (2) is labeled $\boldsymbol{m}_1$ ($\boldsymbol{m}_2$), its saturation magnetization M_1 (M_2), its volume $V_1 = t_1 S$ (V_2) with thickness t_1 (t_2) and cross-section area S, its demagnetizing field H_{d1} (H_{d2}), its anisotropy field H_{k1} (H_{k2}) and the external field $H_{x1} = H_a + H_{ex1}$ ($H_{x2} = H_a + H_{ex2}$) is composed of the sum of the in-plane applied field H_a that is common to the two layers, and an exchange bias field H_{ex1} (H_{ex2}) that is different for the two layers.

$$\begin{aligned} E = &\frac{1}{2}\mu_0 V_1 M_1 H_{d1}(\boldsymbol{m}_1 \cdot \boldsymbol{u}_z)^2 + \frac{1}{2}\mu_0 V_2 M_2 H_{d2}(\boldsymbol{m}_2 \cdot \boldsymbol{u}_z)^2 - \frac{1}{2}\mu_0 V_1 M_1 H_{k1}(\boldsymbol{m}_1 \cdot \boldsymbol{u}_x)^2 \\ &- \frac{1}{2}\mu_0 V_2 M_2 H_{k2}(\boldsymbol{m}_2 \cdot \boldsymbol{u}_x)^2 - \mu_0 V_1 M_1 H_{x1} \boldsymbol{m}_1 \cdot \boldsymbol{u}_x - \mu_0 V_2 M_2 H_{x2} \boldsymbol{m}_2 \cdot \boldsymbol{u}_x \\ &- S J_{\mathrm{RKKY}} \boldsymbol{m}_1 \cdot \boldsymbol{m}_2 \end{aligned} \tag{3.1}$$

J_{RKKY} is the Ruderman-Kittel-Kasuya-Yosida (RKKY) coupling energy per unit area. A negative J_{RKKY} corresponds to an antiferromagnetic coupling between the layers. With an antiferromagnetic coupling, $J_{\mathrm{ex}} < 0$, the two stable equilibrium configurations are defined by ($\boldsymbol{m}_1 = \boldsymbol{u}_x$, $\boldsymbol{m}_2 = -\boldsymbol{u}_x$), called P, and ($\boldsymbol{m}_1 = -\boldsymbol{u}_x$, $\boldsymbol{m}_2 = \boldsymbol{u}_x$), called AP. With a ferromagnetic coupling, $J_{\mathrm{ex}} > 0$, they are ($\boldsymbol{m}_1 = \boldsymbol{u}_x$, $\boldsymbol{m}_2 = \boldsymbol{u}_x$) for P, and ($\boldsymbol{m}_1 = -\boldsymbol{u}_x$, $\boldsymbol{m}_2 = -\boldsymbol{u}_x$) for AP. The label P/AP refers to the orientation of the layer 1, independently of the sign of the RKKY coupling. Unlike the SL free layer case, there is no global spin polarization potential for the whole magnetic system. The reason for that is the existence of a mutual spin-torque between the layers. Instead a spin polarization potential P_1 and P_2 is defined for each layer, including the spin torque due to the perpendicular polarizer and to the reference layer, and the spin torque due to the other layer :

$$P_1 = -\frac{\hbar}{2e} I \frac{\eta_1}{\lambda_1} \ln(1 + \lambda_1 \boldsymbol{m}_1 \cdot \boldsymbol{u}_x) + \frac{\hbar}{2e} I \eta_{z1} \boldsymbol{m}_1 \cdot \boldsymbol{u}_z + \frac{\hbar}{2e} I \eta_{21} \boldsymbol{m}_1 \cdot \boldsymbol{m}_2 \tag{3.2}$$

$$P_2 = -\frac{\hbar}{2e} I \frac{\eta_2}{\lambda_2} \ln(1 + \lambda_2 \boldsymbol{m}_2 \cdot \boldsymbol{u}_x) + \frac{\hbar}{2e} I \eta_{z2} \boldsymbol{m}_2 \cdot \boldsymbol{u}_z - \frac{\hbar}{2e} I \eta_{12} \boldsymbol{m}_1 \cdot \boldsymbol{m}_2 \tag{3.3}$$

Here, a positive current corresponds to electrons flowing from the perpendicular polarizer towards the layer 2, then to layer 1, and finally to the reference layer. The spin polarization of the current due to the perpendicular polarizer on layer 1 (layer 2) is labeled η_{z1} (η_{z2}, resp.). The spin polarization asymmetry for the perpendicular polarizer is assumed to be zero for simplicity.

The spin polarization and spin polarization asymmetry due to the reference layer on the layer 1 (layer 2) are labeled η_1 (η_2) and λ_1 (λ_2, resp.). According to the convention for the current direction, the spin potential due to the reference layer receives a minus sign, whereas the one from the perpendicular polarizer receives a plus sign. The spin polarization of the current due to layer 1 (layer 2) that induces a torque on layer 2 (layer 1) is labeled η_{12} (η_{21}. resp.). The spin polarization asymmetry is assumed to vanish for the mutual spin torque. Notice the minus sign in front of the mutual spin-torque term (last term) in P_2, and the plus sign in P_1, because the layer 2 receives reflected electrons from layer 1, whereas layer 1 receives direct electrons from layer 2 at positive current.
Because the spin potential is not global, conservative and dissipative potentials $\mathcal{H}_1$,$\mathcal{H}_2$, Γ_1 and Γ_2 are defined for each layers :

$$\begin{cases} \mathcal{H}_1 = E + \alpha_1 \beta_{IEC} P_1 \\ \mathcal{H}_2 = E + \alpha_2 \beta_{IEC} P_2 \end{cases} \qquad \begin{cases} \Gamma_1 = \alpha_1 E - P_1 \\ \Gamma_2 = \alpha_2 E - P_2 \end{cases} \tag{3.4}$$

α_1 and α_2 are the Gilbert damping constants in layer 1 and 2, respectively. β_{IEC} is a factor that describes the IEC or field-like torques due to the current. It is supposed to be equal for the two layers.

The two layer magnetizations $\boldsymbol{m}_1$ and $\boldsymbol{m}_2$ are better described in spherical coordinates :

$$\begin{cases} m_x^1 = \sin\theta_1 \cos\phi_1 \\ m_y^1 = \sin\theta_1 \sin\phi_1 \\ m_z^1 = \cos\theta_1 \end{cases} \qquad \begin{cases} m_x^2 = \sin\theta_2 \cos\phi_2 \\ m_y^2 = \sin\theta_2 \sin\phi_2 \\ m_z^2 = \cos\theta_2 \end{cases}$$

Let $\boldsymbol{\Omega_1}$ be the symplectic matrix : $\boldsymbol{\Omega_1} = \begin{pmatrix} 0 & -1 \\ 1 & 0 \end{pmatrix}$

In spherical coordinates, the Landau-Lifshitz-Gilbert-Slonczewski (LLGS) equation writes :

$$\dot{\tilde{\boldsymbol{R}}}_1 = \frac{\gamma}{M_1 V_1} \left(\boldsymbol{\Omega_1} \partial_{\tilde{\boldsymbol{R}}_1} \mathcal{H}_1 - \partial_{\tilde{\boldsymbol{R}}_1} \Gamma_1 \right) \tag{3.5}$$

$$\dot{\tilde{\boldsymbol{R}}}_2 = \frac{\gamma}{M_2 V_2} \left(\boldsymbol{\Omega_1} \partial_{\tilde{\boldsymbol{R}}_2} \mathcal{H}_2 - \partial_{\tilde{\boldsymbol{R}}_2} \Gamma_2 \right) \tag{3.6}$$

At the risk of being a bit confusing (and less rigorous), $\dot{\tilde{\boldsymbol{R}}}_1$ is defined as $\dot{\tilde{\boldsymbol{R}}}_1 = (\frac{\mathrm{d}\theta_1}{\mathrm{dt}}, \sin\theta_1 \frac{\mathrm{d}\phi_1}{\mathrm{dt}})^\intercal$.
The indices are swapped to 2 for the spherical coordinates $\dot{\tilde{\boldsymbol{R}}}_2$ of layer 2.
Similarly for the differential operators : $\partial_{\tilde{\boldsymbol{R}}_1} = (\partial_{\theta_1}, \frac{\partial_{\phi_1}}{\sin\theta_1})^\intercal$ and with index 2 for layer 2.
The gyromagnetic ratio γ is supposed to be similar for the two layers, but keep in mind there is a minor factor difference of $(1 + \alpha_{1/2}^2)$ between them from the transform of the LLG equation.

To study the stability of equilibriums, the right-hand side of the LLGS equation has to be differentiated, to obtain the 4x4 dynamical matrix that is named L. The expression of L in

spherical coordinates is given by :

$$L = \begin{pmatrix} \mathbf{\Omega_1} & \mathbf{0} \\ \mathbf{0} & \mathbf{\Omega_1} \end{pmatrix} \mathbf{Hess}[\mathcal{H}_1,\, \mathcal{H}_2] - \mathbf{Hess}[\Gamma_1,\, \Gamma_2]$$

Inside the block matrix, $\mathbf{0}$ is the 2x2 null matrix. For two arbitrary scalar function A and B, the 4x4 matrix called $\mathbf{Hess}[A, B]$ is defined further, when the equilibrium configuration is assumed to be in-plane ($\cos\theta_1 = \cos\theta_2 = 0$). The standard notation for the second derivative, $A_{\theta_1\phi_2} = \dfrac{\partial^2 A}{\partial\theta_1\partial\phi_2}$ is used :

$$\mathbf{Hess}[A, B] = \begin{pmatrix} A_{\theta_1\theta_1} & A_{\theta_1\phi_1} & A_{\theta_1\theta_2} & A_{\theta_1\phi_2} \\ A_{\theta_1\phi_1} & A_{\phi_1\phi_1} & A_{\phi_1\theta_2} & A_{\phi_1\phi_2} \\ B_{\theta_1\theta_2} & B_{\phi_1\theta_2} & B_{\theta_2\theta_2} & B_{\theta_2\phi_2} \\ B_{\theta_1\phi_2} & B_{\phi_1\phi_2} & B_{\theta_2\phi_2} & B_{\phi_2\phi_2} \end{pmatrix}$$

3.1.2 Dynamics of in-plane SyF without applied current

For a SL free layer, the FMR frequency originated from the conservative part, or energy part, of the dynamical matrix. In fact, it was the square root of the opposite of the determinant of L, when only the conservative part was considered. As for the FMR frequency of a SyF, it is exactly the same. Because the conservative part is larger than the dissipative part, it is the dominant contribution to the FMR frequency. It will be shown below that this approximation is justified.

Nonetheless, the dynamical matrix is a 4x4 matrix for a SyF, therefore its eigenvalues are solutions of a quartic equation. If only the energy is taken into account in L, the quartic solution reduces to a bi-quadratic equation. The eigenvalues are then two pairs of purely imaginary complex-conjugate numbers. The two pairs of solutions identify to two different oscillation frequencies and modes of the excitation of the SyF. By definition, the mode with the highest frequency at zero applied field is called optical mode, while the mode with the lowest frequency is called acoustic mode.

The two modes are also associated with different eigenvalues as shown in Fig. 3.1. Let's consider the case of an antiferromagnetic coupling between the two layers of a SyF. In equilibrium, the two layers are antiparallel. After a small deviation from equilibrium, if this one is stable, the magnetization will relax to the equilibrium configuration by spiraling towards it. However, the magnetization rotates in the trigonometric direction around the effective field pointing upward, i.e. $\dot{\boldsymbol{m}} = \boldsymbol{H}_{eff} \times \boldsymbol{m}$. But the effective field points along $+\boldsymbol{u}_x$ for $\boldsymbol{m}_1$ and along $-\boldsymbol{u}_x$ for $\boldsymbol{m}_2$. Therefore, the two layers magnetizations rotate in opposite direction for an antiferromagnetic coupling. As a result, the RKKY energy cannot vanish at all time during the relaxation (or during self-sustained oscillations). The two modes of the SyF correspond of two different way of minimizing the RKKY energy in the dynamical state :

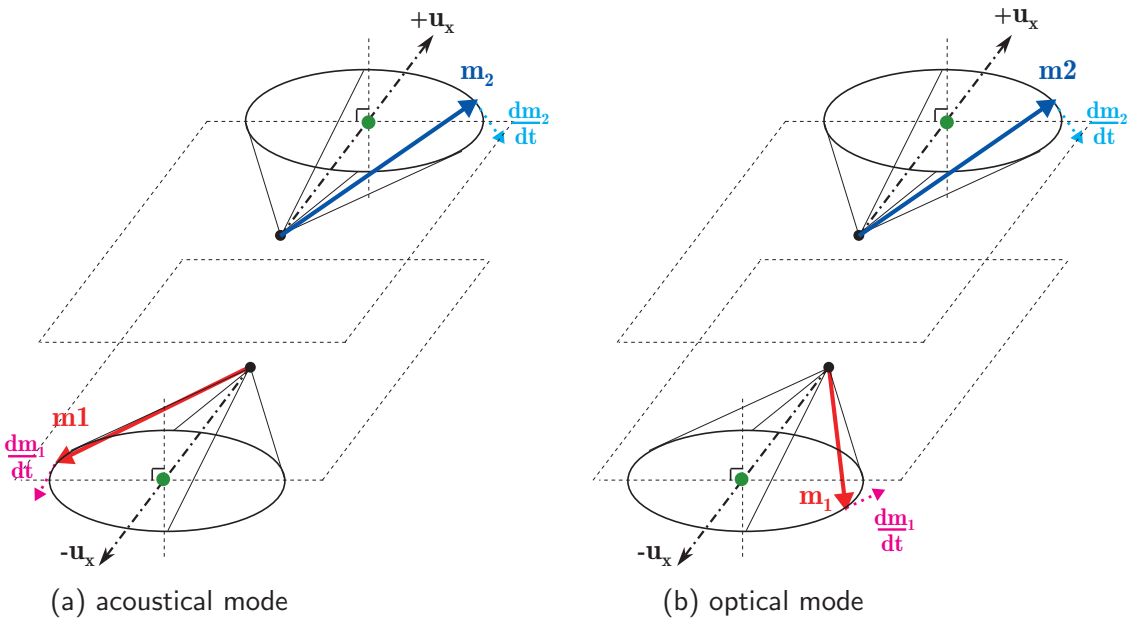

Figure 3.1 – The two modes of a SAF : (a) acoustic mode. The in-plane components of $\boldsymbol{m}_1$ and $\boldsymbol{m}_2$ lie along the same axis. The out-of-plane components have the same sign. (b) optical mode. The out-of-plane components have an opposite sign.

Acoustic mode The "in-plane" RKKY energy is minimized. Therefore, if, at any time, $\boldsymbol{m}_1$ and $\boldsymbol{m}_2$ are projected onto the plane of the layers, they fall approximately along the same axis. As a result of the antiferromagnetic coupling, in the dynamical regime, the out-of-plane components of each layer have the same sign at any time.

Optical mode The "out-of-plane" RKKY energy is minimized. At any time, the out-of-plane components of each layer cancel each other. However, the in-plane components result in a non-vanishing RKKY energy.

In the case of thin films, the demagnetizing field is the largest field of the problem, therefore it requires more energy for the magnetization to go out-of-plane than to be tilted in-plane. It results in a larger excursion for the in-plane angles than for the out-of-plane angles. Because the RKKY energy is proportional to the scalar product of $\boldsymbol{m}_1$ and $\boldsymbol{m}_2$, the overall RKKY energy is larger in optical mode than in acoustic mode. Similarly in crystals, acoustic phonons have a smaller interaction energy than optical phonons.

The response of a SyF free layer to an external applied field is slightly more complicated than for a SL free layer. Contrary to the SL, for which positive applied fields along the easy-axis stabilize the P configuration (and destabilize the AP configuration) and negative fields destabilize the P state, which is eventually reversed; for a SyF with antiferromagnetic coupling, or SAF, both polarities of the applied field ultimately destabilize the SyF, because the applied field affects oppositely the two layers 1 and 2. Another magnetic configuration exists in SAF,

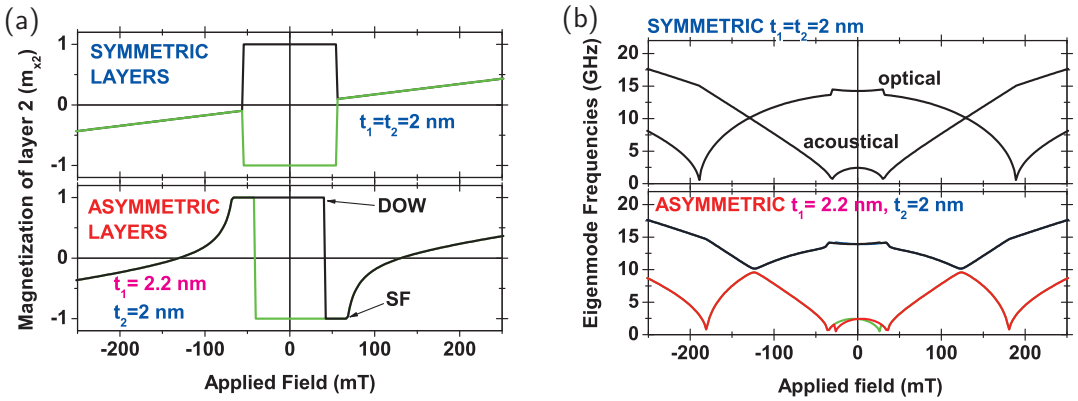

Figure 3.2 – (a) Equilibrium magnetization and (b) FMR frequency of the layer 2 under applied field, for a symmetric SyF with antiferromagnetic coupling (top in both panels) and an asymmetric SyF (bottom). The bistable region corresponds to fields between -50 mT and +50 mT. From [Devolder 2012].

the so-called spin-flop configuration, that is a stable equilibrium configuration under applied field, with the two magnetizations $\boldsymbol{m}_1$ and $\boldsymbol{m}_2$ lying in-plane but being non-collinear. This configuration is stable for fields between a so-called spin-flop field H_{SF} and a saturation field H_{sat}, above which both magnetizations are oriented parallel to the applied field. If the layers are asymmetric, there is a additional important field, smaller than H_{SF} that corresponds to the field at which both layers reverse in a rigid way, sometimes called direct-overwrite field H_{DOW}. In the bistable region, between $-H_{DOW}$ and $+H_{DOW}$, the FMR frequency of the optical mode is minimal for zero field. whereas it is maximal at zero field for the acoustic mode. The fields for which the FMR frequency for the acoustic mode vanishes correspond to $\pm H_{DOW}$. The hysteresis curves for the magnetization of layer 2 and the FMR frequencies for the two modes are drawn in Fig. 3.2, from [Devolder 2012].

This preliminary study of the SyF free layers do not include the STT effects due to a polarized current. Such analysis will be presented below with the STT originating, first from a perpendicular polarizer, second from an in-plane reference layer.

3.2 Perpendicular polarizer and SyF free layer

This section is focused on the dynamics of the system composed of a perpendicular polarizer, with fixed out-of-plane magnetization, and an in-plane SyF free layer. The spin torque from the reference layer is not taken into account. The techniques employed are derived from the ones used to treat the similar system where the free layer is a single layer (SL) :

- Taking into account the in-plane anisotropy of the layers, the critical current is computed. Its expression does not need the dynamical matrix, in the same manner as for a SL free layer. Instead, it is related to the existence of an in-plane equilibrium configuration.

- Above the critical current (and possibly below also), the SyF free layer follows a coupled out-of-plane precessional (OPP) motion. Like for the SL, the coupled OPP exists until another critical current. Other dynamical states of the SyF exist that are not described here, like decoupled OPP, one layer in equilibrium and the other one in OPP, etc...

In the following, $\eta_1 = \eta_2 = 0$ is assumed, and there is neither applied field ($H_a = 0$), nor exchange bias field ($H_{ex\,1} = H_{ex\,2} = 0$). The IEC is also neglected, so the conservative potentials are equal to the total free energy : $\mathcal{H}_1 = \mathcal{H}_2 = E$.

$$E = \frac{1}{2}\mu_0 V_1 M_1 H_{d1}(\boldsymbol{m}_1 \cdot \boldsymbol{u}_z)^2 + \frac{1}{2}\mu_0 V_2 M_2 H_{d2}(\boldsymbol{m}_2 \cdot \boldsymbol{u}_z)^2 - \frac{1}{2}\mu_0 V_1 M_1 H_{k1}(\boldsymbol{m}_1 \cdot \boldsymbol{u}_x)^2 - \frac{1}{2}\mu_0 V_2 M_2 H_{k2}(\boldsymbol{m}_2 \cdot \boldsymbol{u}_x)^2 - S J_{\mathrm{RKKY}} \boldsymbol{m}_1 \cdot \boldsymbol{m}_2$$

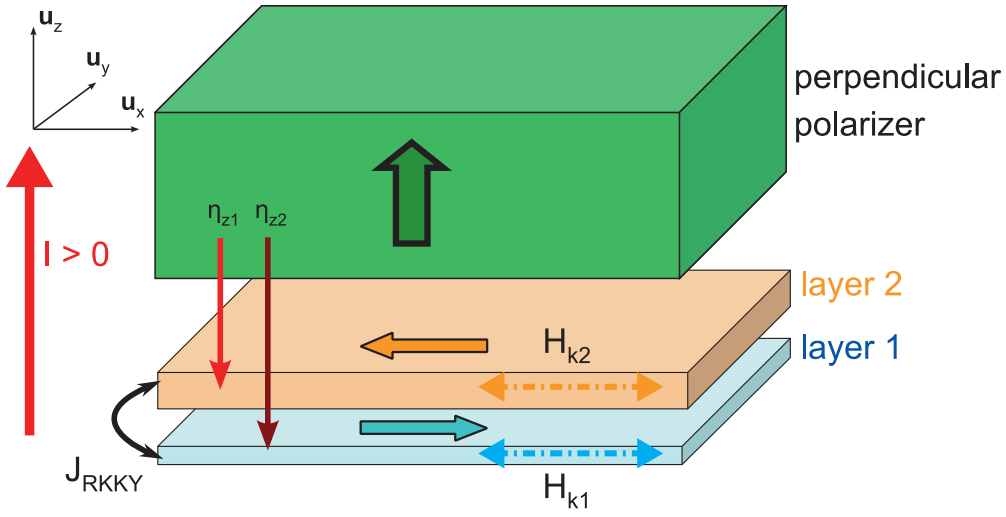

Figure 3.3 – Schematics of the SyF free layer with a perpendicular polarizer.

$$P_1 = +\frac{\hbar}{2e} I \eta_{z1} \boldsymbol{m}_1 \cdot \boldsymbol{u}_z + \frac{\hbar}{2e} I \eta_{21} \boldsymbol{m}_1 \cdot \boldsymbol{m}_2 \tag{3.7}$$

$$P_2 = +\frac{\hbar}{2e} I \eta_{z2} \boldsymbol{m}_2 \cdot \boldsymbol{u}_z - \frac{\hbar}{2e} I \eta_{12} \boldsymbol{m}_1 \cdot \boldsymbol{m}_2 \tag{3.8}$$

The geometry is described in Fig. 3.3. For a numerical study of this same configuration, refer to [Firastrau 2013]

3.2.1 Critical current

The critical current is computed by setting the time derivatives to zero and $\alpha = 0$ in the LLGS equation.
The resulting equations for the equilibrium angles $(\theta_1^0, \phi_1^0, \theta_2^0, \phi_2^0)$ (the superscript is omitted later) are not fully reported here because of their size. However, the "$\dot{\phi}_1$" and "$\dot{\phi}_2$" equations give that the equilibrium magnetizations are in-plane : $\cos\theta_1 = \cos\theta_2 = 0$. The two other equations are reported below :

$$0 = -\partial_{\phi_1} E + \partial_{\theta_1} P_1 = -\frac{1}{2}\mu_0 V_1 M_1 H_{k1} \sin(2\phi_1) + S J_{\mathrm{RKKY}} \sin(\phi_2 - \phi_1) - \frac{\hbar}{2e}\eta_{z1} I$$

$$0 = -\partial_{\phi_2} E + \partial_{\theta_2} P_2 = -\frac{1}{2}\mu_0 V_2 M_2 H_{k2} \sin(2\phi_2) - S J_{\mathrm{RKKY}} \sin(\phi_2 - \phi_1) - \frac{\hbar}{2e}\eta_{z2} I$$

Those two equations are rewritten as :

$$0 = \frac{1}{2}\mu_0 V_1 M_1 H_{k1} \eta_{z2} \sin(2\phi_1) - \frac{1}{2}\mu_0 V_2 M_2 H_{k2} \eta_{z1} \sin(2\phi_2) - (\eta_{z1} + \eta_{z2}) S J_{\mathrm{RKKY}} \sin(\phi_2 - \phi_1) \tag{3.9}$$

$$0 = \frac{1}{2}\mu_0 V_1 M_1 H_{k1} \sin(2\phi_1) + \frac{1}{2}\mu_0 V_2 M_2 H_{k2} \sin(2\phi_2) + \frac{\hbar}{2e}(\eta_{z1} + \eta_{z2}) I \tag{3.10}$$

The second equation looks very similar to the equation of the equilibrium in-plane angle for a SL free layer. Except that the two angles ϕ_1 and ϕ_2 appear. The static relation between the two angles is given by the first equation. In order to solve this problem, the angle variables are changed to the sum ϕ_s and difference ϕ_d of the two angles, taking into account the sign of the RKKY coupling, $n = \mathrm{sign}(J_{\mathrm{RKKY}})$:

$$\begin{cases} \phi_s = (\phi_2 - \dfrac{1-n}{2}\pi) + \phi_1 \\ \phi_d = (\phi_2 - \dfrac{1-n}{2}\pi) - \phi_1 \end{cases} \qquad \begin{cases} \phi_1 = \dfrac{\phi_s - \phi_d}{2} \\ \phi_2 = \dfrac{\phi_s + \phi_d}{2} + \dfrac{1-n}{2}\pi \end{cases} \tag{3.11}$$

Therefore the equilibrium equation rewrites :

$$0 = \frac{1}{2}\mu_0 V_1 M_1 H_{k1} \eta_{z2} \sin(\phi_s - \phi_d) - \frac{1}{2}\mu_0 V_2 M_2 H_{k2} \eta_{z1} \sin(\phi_s + \phi_d) - (\eta_{z1} + \eta_{z2}) S |J_{\mathrm{RKKY}}| \sin(\phi_d) \tag{3.12}$$

$$0 = \frac{1}{2}\mu_0 V_1 M_1 H_{k1} \sin(\phi_s - \phi_d) + \frac{1}{2}\mu_0 V_2 M_2 H_{k2} \sin(\phi_s + \phi_d) + \frac{\hbar}{2e}(\eta_{z1} + \eta_{z2}) I \tag{3.13}$$

After some trigonometric operations, the relation between ϕ_s and ϕ_d is obtained :

$$\tan\phi_d = \frac{\delta_K K \sin\phi_s}{1 + K\cos\phi_s} \qquad \text{with :} \quad K = \frac{\mu_0 V_1 M_1 H_{k1}\eta_{z2} + \mu_0 V_2 M_2 H_{k2}\eta_{z1}}{2(\eta_{z1}+\eta_{z2})S|J_{\mathrm{RKKY}}|}$$
$$\delta_K = \frac{V_1 M_1 H_{k1}\eta_{z2} - V_2 M_2 H_{k2}\eta_{z1}}{V_1 M_1 H_{k1}\eta_{z2} + V_2 M_2 H_{k2}\eta_{z1}}$$

Then the value of the angles with respect to the current is given by the second equation :

$$0 = \sin\phi_s\cos\phi_d - \kappa^*\cos\phi_s\sin\phi_d + \frac{I}{I^*}$$

$$\text{with :} \quad \kappa^* = \frac{V_1 M_1 H_{k1} - V_2 M_2 H_{k2}}{V_1 M_1 H_{k1} + V_2 M_2 H_{k2}} \qquad I^* = \frac{\mu_0 V_1 M_1 H_{k1} + \mu_0 V_2 M_2 H_{k2}}{2\frac{\hbar}{2e}(\eta_{z1}+\eta_{z2})}$$

Using the expression of the tangent of ϕ_d, one gets :

$$-I/I^* = \sin\phi_s \frac{1 - \kappa^*\cot\phi_s\tan\phi_d}{\sqrt{1+\tan^2\phi_d}} \tag{3.14}$$

3.2.1.1 High-coupling regime

This equation is not solvable analytically. However, under the assumption of high-coupling, so that the RKKY coupling is larger than the anisotropy field, namely $K \ll 1$, the expression of the difference of the in-plane angles ϕ_d vanishes and the sum of the in-plane angles ϕ_s is : $I/I^* = -\sin\phi_s$.

The equilibrium configuration exists as long as ϕ_s is defined, which means that the critical current with a SyF free layer in the assumption $K \ll 1$ is $I_{c1} = I^*$. It appears that it is independent of the RKKY coupling in first order in K. It corresponds to the critical current in a SL layer with anisotropy energy $E_{eff} = E_1 + E_2$, where E_1 and E_2 are the anisotropy energy of the two layers in the SyF, and with an effective spin polarization $\eta_{z\,eff} = (\eta_{z1} + \eta_{z2})$ of the perpendicular polarizer. For instance, when considering a SyF with identical layers of volume V, its critical current is the same as for a single layer of volume $2V$, with $\eta_{z1} = 0$. $\eta_{z1} = 0$ supposes that the spin torque is transmitted only to the layer in contact with the perpendicular polarizer.

3.2.1.2 Low-coupling regime

Alternatively, if the anisotropy is larger than the RKKY coupling, $K \gg 1$, the critical current can be derived, even if the equation of $\phi_s(I)$ is not known. The right-hand-side of eq. 3.14 is a function of ϕ_s, $f(\phi_s)$, which is continuous and differentiable for all ϕ_s. Therefore, the equation $f(\phi_s) = I/I^*$ is solved by finding the ϕ_s for which $f(\phi_s)$ crosses the horizontal line I/I^*. It is possible to find such a ϕ_s, as long as $I/I^* < \max_{\phi_s} f(\phi_s)$. Therefore the critical current is defined by : $I_{c1} = I^* \max_{\phi_s} f(\phi_s)$. The maximum of $f(\phi_s)$ is found by derivation. The equation $\frac{\mathrm{df}}{\mathrm{d}\phi_s} = 0$

is a quartic equation in $c = \cos\phi_s$. However, for symmetric layers ($\kappa^* = 0$) and using the fact that $K \gg 1$, it reduces to a bi-quadratic equation of solution :

$$\cos\phi_s = \sqrt{\frac{|\delta_K|}{1+|\delta_K|}} \tag{3.15}$$

The expression of $\cos\phi_s$ is then injected into eq. 3.14, so the critical current is given by :

$$I_{c1} = \frac{I^*}{1+|\delta_K|} \tag{3.16}$$

The critical current is found to be independent of the RKKY coupling in first order in $1/K$. Interestingly, the critical current in the low RKKY limit is always smaller than the one for large RKKY, because the denominator is always larger than unity. Nonetheless, because the RKKY coupling is small, the dynamics above the critical current should correspond to the one of two layers weakly coupled, with perhaps one layer which remains in an in-plane equilibrium state, while the other one oscillates in OPP. This will be confirmed in the next section.

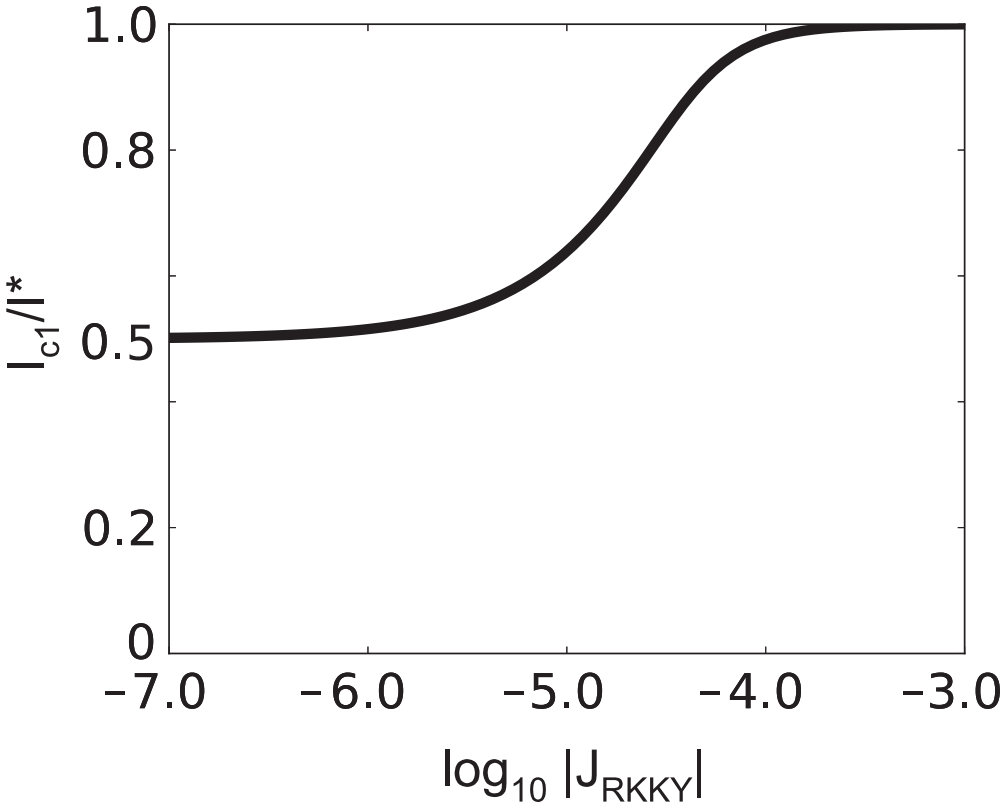

Figure 3.4 – Critical current I_{c1} versus logarithm (in basis 10) of the RKKY coupling constant expressed in J/m2. The anisotropy field H_k for the two layers is $H_k = 20e3$ A/m, $M_S = 1.2e6$ A/m and the layers have a thickness of $t_1 = t_2 = 1.5$ nm.

In the cross-over between the low-coupling and high-coupling regimes, the critical current is difficult to obtain analytically, instead the maximum of the function $f(\phi_s)$ is computed numerically. Fig. 3.4 shows the critical current I_{c1} normalized to I^* for symmetric layers versus the logarithm of K, which corresponds in Fig. 3.4, to a varying RKKY coupling constant, when the anisotropy H_K is fixed. The current I^* is the critical current of a single layer of volume $2V$, whereas $I^*/2$ is the critical current of a single layer of volume V, with V the volume of layer 1 (and layer 2 because the SyF is symmetric).

In the previous analysis, the in-plane applied field was not taken into account. However, it can be included, at the cost that the expression of the sum of the equilibrium in-plane angles ϕ_s are not known for any arbitrary applied current. The critical current can be obtained, though, using the same approach as for the low-coupling regime, by maximizing the adequate function f.

The dynamics of the SyF free layer with a perpendicular polarizer are treated in the next section.

3.2.2 Coupled dynamics

Like for the SL free layer, the dynamics in OPP can be exactly described if the in-plane field and the uniaxial anisotropy are not taken into account in the energy E. In this framework, the frequency of the OPP state appears directly, as it will be shown. The energy and spin torques potentials of the previous section are used, setting $H_{x1} = H_{x2} = H_{k1} = H_{k2} = 0$, and inserted in the LLGS equation 3.6. In the LLGS equation, the phase shift $\phi_2 - \phi_1$ appears. As for the static equations, the change of variables described in 3.11 is realized : $(\phi_1, \phi_2) \Rightarrow (\phi_s, \phi_d)$:

$$
\begin{aligned}
\dot{\phi_s} = &- \left(\mu_0\gamma H_{d1} - n\frac{\gamma S|J_{\mathrm{RKKY}}|}{M_2V_2}\right)\cos\theta_1 - \left(\mu_0\gamma H_{d2} - n\frac{\gamma S|J_{\mathrm{RKKY}}|}{M_1V_1}\right)\cos\theta_2 \\
&+ \cos\phi_d\gamma S|J_{\mathrm{RKKY}}|\left(\frac{\cos\theta_1\sin\theta_2}{M_1V_1\sin\theta_1} + \frac{\cos\theta_2\sin\theta_1}{M_2V_2\sin\theta_2}\right) \\
&+ \sin\phi_d\left(\left(\frac{\alpha_1\gamma S|J_{\mathrm{RKKY}}|}{M_1V_1} + n\frac{\hbar\gamma\eta_{21}I}{2eM_1V_1}\right)\frac{\sin\theta_2}{\sin\theta_1} - \left(\frac{\alpha_2\gamma S|J_{\mathrm{RKKY}}|}{M_2V_2} - n\frac{\hbar\gamma\eta_{12}I}{2eM_2V_2}\right)\frac{\sin\theta_1}{\sin\theta_2}\right) \\
\dot{\phi_d} = &+ \left(\mu_0\gamma H_{d1} + n\frac{\gamma S|J_{\mathrm{RKKY}}|}{M_2V_2}\right)\cos\theta_1 - \left(\mu_0\gamma H_{d2} + n\frac{\gamma S|J_{\mathrm{RKKY}}|}{M_1V_1}\right)\cos\theta_2 \\
&+ \cos\phi_d\gamma S|J_{\mathrm{RKKY}}|\left(\frac{\cos\theta_1\sin\theta_2}{M_1V_1\sin\theta_1} - \frac{\cos\theta_2\sin\theta_1}{M_2V_2\sin\theta_2}\right) \\
&- \sin\phi_d\left(\left(\frac{\alpha_1\gamma S|J_{\mathrm{RKKY}}|}{M_1V_1} + n\frac{\hbar\gamma\eta_{21}I}{2eM_1V_1}\right)\frac{\sin\theta_2}{\sin\theta_1} + \left(\frac{\alpha_2\gamma S|J_{\mathrm{RKKY}}|}{M_2V_2} - n\frac{\hbar\gamma\eta_{12}I}{2eM_2V_2}\right)\frac{\sin\theta_1}{\sin\theta_2}\right)
\end{aligned}
$$

$$\begin{aligned}
\dot{\theta}_1 = &-\frac{\hbar\gamma\eta_{z1}I}{2eM_1V_1}\sin\theta_1 + \alpha_1\mu_0\gamma H_{d1}\cos\theta_1\sin\theta_1 + \sin\phi_d\sin\theta_2\frac{\gamma S|J_{\rm ex}|}{M_1V_1} \\
&+ (\cos\phi_d\cos\theta_1\sin\theta_2 - n\sin\theta_1\cos\theta_2)\left(\frac{\alpha_1\gamma S|J_{\rm ex}|}{M_1V_1} + n\frac{\hbar\gamma\eta_{21}I}{2eM_1V_1}\right) \\
\dot{\theta}_2 = &-\frac{\hbar\gamma\eta_{z2}I}{2eM_2V_2}\sin\theta_2 + \alpha_2\mu_0\gamma H_{d2}\cos\theta_2\sin\theta_2 - \sin\phi_d\sin\theta_1\frac{\gamma S|J_{\rm ex}|}{M_2V_2} \\
&+ (\cos\phi_d\sin\theta_1\cos\theta_2 - n\cos\theta_1\sin\theta_2)\left(\frac{\alpha_2\gamma S|J_{\rm ex}|}{M_2V_2} - n\frac{\hbar\gamma\eta_{12}I}{2eM_2V_2}\right)
\end{aligned}$$

This transformation allows to identify three constants of motion : θ_1, θ_2 and ϕ_d. Indeed, the four equations do not depend on ϕ_s, so a solution that corresponds to a coupled out-of-plane precession of the two layers, if it exists, is given by the three former angles remaining constant, and the angle ϕ_s moving at a constant speed that is the frequency of the precession. The existence of a solution to the equations $\{\dot{\theta}_s = \dot{\theta}_d = \dot{\phi}_d = 0\}$ depends on the material and external parameters, like the current, the value of the RKKY coupling, etc...

In the general case, solving these equations is not straightforward, however for two identical layers without mutual spin-torque between the layers, the equations are solvable analytically. Namely : $\alpha = \alpha_1 = \alpha_2$, $H_d = H_d^1 = H_d^2$, $M_s = M_1 = M_2$, $V = V_1 = V_2 = tS$. For clarity, the adimensional quantities $i = \dfrac{\eta_{z1}+\eta_{z2}}{\alpha H_d}\dfrac{\hbar I}{2e\mu_0 M_S(2V)}$ and $j = \dfrac{S|J_{\rm ex}|}{\mu_0 M_s V H_d}$ are introduced. The (half) sum and difference of the out-of-plane angles are introduced : $\theta_s = (\theta_1+\theta_2)/2$ and $\theta_d = (\theta_1-\theta_2)/2$. Let $\omega_d = \mu_0\gamma H_d$ be the characteristic frequency. In this framework the equations $\{\dot{\theta}_s = \dot{\theta}_d = \dot{\phi}_d = 0\ ;\ \dot{\phi}_s = \text{constant}\}$ solve exactly[1] :

$$\begin{aligned}
\theta_d = 0 \qquad &\Rightarrow \quad \theta_1 = \theta_2 \\
\sin(\phi_d) &= \alpha\left(\frac{\eta_{z1}-\eta_{z2}}{\eta_{z1}+\eta_{z2}}\right)\frac{i}{j} \\
\cos\theta_s &= \frac{i}{1 - nj\,[1 - n\cos(\phi_d)]} \\
\dot{\phi}_s &= -2\omega_d\, i
\end{aligned}$$

Interestingly, the oscillation frequency is independent of the RKKY coupling, it is the frequency of an equivalent SL free layer of volume $2V$ with in-plane angle $\tilde{\phi} = \phi_s/2$, and with $\eta_{z1} = 0$. The relations for ϕ_d and, more dramatically, for θ_s, define the set of parameters

[1] In fact, it is *not exactly* the solution of the system presented here. To obtain this solution, the term in $\alpha J_{\rm RKKY}$ must be neglected in the equation of $\dot{\phi}_d$. However, if the IEC term is included in the conservative potential, with $\beta_{IEC} = 1$, i.e. when considering only the terms in αI from the transformation of $\alpha\boldsymbol{m}\times\frac{\rm dm}{\rm dt}$ in LLGS, in this case curiously, this solution set solves *exactly* the coupled OPP equations of a symmetric SyF.

for which coupled OPP exists. The range of available steady states angles (ϕ_d, θ_s) defines the critical currents for which the OPP bifurcates to the OPS equilibrium, or any other steady state. The critical current, higher boundary for existence of coupled OPP, is called I_{c2}, when extracted from $\cos\theta_s = 1$, and I_{c3} from $\sin\phi_d = 1$:

$$I_{c2} = \frac{2e}{\hbar}\frac{\mu_0 M_S(2V)\alpha H_d}{\eta_{z1}+\eta_{z2}}\left(1 + j(\cos\phi_d - n)\right) \tag{3.17}$$

$$I_{c3} = \frac{2e}{\hbar}\frac{2S|J_{\mathrm{RKKY}}|}{|\eta_{z1}-\eta_{z2}|} \tag{3.18}$$

The two following cases are considered : $I_{c2} < I_{c3}$ and $I_{c3} < I_{c2}$.

The case $I_{c2} < I_{c3}$ corresponds more or less to $\alpha < j$, i.e. relatively large RKKY coupling. In this regime, the phase shift ϕ_d is very small, and $\cos\phi_d \approx 1$. If the coupling is ferromagnetic $(n = 1)$, the critical current I_{c2} corresponds to the critical current for OPP I_c^{OPP} of a single layer of volume $2V$. However, for an antiferromagnetic coupling $(n = -1)$, $I_{c2} = (1 + 2j)I_c^{OPP}$. In this regime the RKKY coupling is supposed to be large, so $j \lesssim 1$, therefore the critical current for the existence of OPP may be consequently enhanced.

In the second case, $I_{c3} < I_{c2}$, the RKKY coupling is relatively small. Therefore, the two limits of the previous section are considered : the low-coupling and (relatively) high-coupling regime.
The high-coupling regime is defined by $K \ll 1$, which for the critical currents translates to $\frac{\eta_{z1}-\eta_{z2}}{\eta_{z1}+\eta_{z2}}\frac{I_{c1}}{I_{c3}} \ll 1$. Therefore the coupled OPP exists for an extended current range in this regime. At the contrary, in the low-coupling regime, the relation $\frac{\eta_{z1}-\eta_{z2}}{\eta_{z1}+\eta_{z2}}\frac{I_{c1}}{I_{c3}} \gg 1$ holds. If $\eta_{z1} = 0$, the coupled OPP is not available. Without applied current, the SyF is in one of the two equilibrium configuration, P or AP. When the current is increased, the equilibrium state rotates in the plane to the equilibrium sum-of-angle ϕ_s. When the critical in-plane angle is reached, for $I = I_{c1}$, the magnetizations of the two layers reach another steady state, which may be an OPS equilibrium for the two layers, or a mixed equilibrium : one layer in-plane, the other one out-of-plane; or one layer in in-plane equilibrium, the other one in (not coupled) OPP.
The different regimes are described in Fig. 3.5, representing the frequency versus applied current of the (coupled or not) OPP :

- In the high-coupling regime, $I_{c2} < I_{c3}$, the critical current for the coupled-OPP/OPS bifurcation is enhanced compared to the critical current of a single-layer of volume $2V$. Because $K \lll 1$, the critical current I_{c1} for the bifurcation IPS/coupled-OPP is very close to the critical current of a single layer of volume $2V$. It corresponds to $J_{RKKY} = -1 \cdot 10^{-3}$, $-3 \cdot 10^{-4}$, $-1 \cdot 10^{-4}$ J/m^2 on Fig. 3.5 (red, cyan and magenta dotted-line, resp.). The single layer of volume $2V$ is the black dashed-line, and in green dashed-line for the single layer of volume V.

- In the medium-coupling regime, $I_{c1} < I_{c3} < I_{c2}$, the critical current for the disappearance of coupled-OPP is I_{c3}, lower than the one for a single layer of volume $2V$. Above this

critical current, there is a range of current showing OPP of the layer 2 alone, at the frequency of a single layer of volume V. The layer 1 magnetization is in an in-plane equilibrium. Because $K < 1$, the critical current for the bifurcation IPS/coupled-OPP is almost the critical current of a single layer of volume $2V$, at least at order 1 in K. It corresponds to $J_{RKKY} = -3 \cdot 10^{-5}$ J/m^2 (yellow dotted-line).

- In the low-coupling regime, $I_{c3} < I_{c1} < I_{c2}$, the coupled-OPP are not available. Above the critical current I_{c1}, the layer 2 oscillates at the frequency of a single layer of volume V and the layer 1 remains in in-plane equilibrium. The critical current I_{c1} is almost the critical current of a single layer of volume V, according to eq. 3.16, with $\delta_K = -1$ and $\kappa^* = 0$.

Notice that the bifurcation IPS/OPP around I_{c1} is a hysteretic bifurcation : the OPP exist below this critical current. Therefore, in simulations, the system is sometimes found to be in OPP for currents smaller than I_{c1}. In fact, in simulations, the critical current I_{c1} depends on other parameters, namely the current pulse shape and the slope of the increasing ramp until the current reaches its nominal value. Consequently, the mismatch between analytical expressions and simulations for the critical current I_{c1} may be large.

Let $\eta_{z1} = 0$, so all the spin-torque is transfered to the first layer in contact to the perpendicular polarizer, namely the layer 2. For two identical layers, the coupled OPP are characterized by $\theta_d = 0$, or $\theta_1 = \theta_2$, and a non-vanishing in-plane phase shift between the two layers ϕ_d. If the coupling between the layers is ferromagnetic, $J_{\mathrm{RKKY}} > 0$, a parallel alignment of the two layers is energetically favorable. Therefore, it is intuitive that in coupled dynamics, the out-of-plane angles of both layers are the same. However, for an antiferromagnetic coupling, $J_{\mathrm{RKKY}} < 0$ or $n = -1$, the favorable static alignment is $\theta_1 = -\theta_2$. Nevertheless, if the two layers had opposite out-of-plane angles, they would feel opposite demagnetizing fields and so they would rotate in opposite direction. The fact that $\theta_d = 0$ is entirely due to dynamical effects. Notice that the difference between the ferromagnetic and antiferromagnetic coupling appears in the average out-of-plane angle θ_s. It is smaller in the antiferromagnetic case, to reduce as much as possible the RKKY interaction.

The phase shift ϕ_d between the in-plane angles is non-zero. This was already observed by Huygens in its pendula synchronization experiment. It is in qualitative agreement with the evolution of the phase shift in weakly coupled linear oscillators, or Adler equation :

$$\dot{\phi_d} = \Delta\omega + H(\phi_d) \tag{3.19}$$

Where $\Delta\omega$ is the frequency mismatch between the two layers and H is the antisymmetric part of the coupling between the two layers. With the assumption that $\eta_{z1} = 0$, the natural frequency of layer 1 is 0 and the natural frequency of layer 2 is given by $\omega_2 = \dot{\phi_2} = -\omega_d \frac{\eta_{z2}}{\alpha H_d} \frac{\hbar I}{2e\mu_0 M_S V} = -2\omega_d i$. The antisymmetric part of the coupling function is defined by $H(x) = H_{12}(-x) - H_{21}(x)$, where H_{12} (H_{21}) is the coupling term from the layer 1 (layer 2) in the equation of layer 2 (layer 1, resp.). The coupling is due to the RKKY energy here, so $H_{21}(\phi_2 - \phi_1) = +\mu_0\gamma S J_{\mathrm{RKKY}} \sin(\phi_2 - \phi_1)$ and $H_{12}(\phi_2 - \phi_1) = -\mu_0\gamma S J_{\mathrm{RKKY}} \sin(\phi_2 - \phi_1)$. Thus, $H(\phi_d) = 2\omega_d j \sin\phi_d$. For a constant phase shift ϕ_d, $\dot{\phi_d} = 0$ and the weekly coupled linear oscillators exhibit a phase shift defined by

$\sin\phi_d = i/j$. It differs with the coupled OPP by a factor α, as the spin-torque system is strongly non-linear, and because of the phase-amplitude coupling : the coupling between the two layer occurs not only through the in-plane angles ϕ_1 and ϕ_2, but also through the out-of-plane angles θ_1 and θ_2.
The phase-amplitude coupling and non-linearity of self-sustained oscillation in spin-torque oscillators (STO) is under active research : see [Slavin 2009, Quinsat 2012].

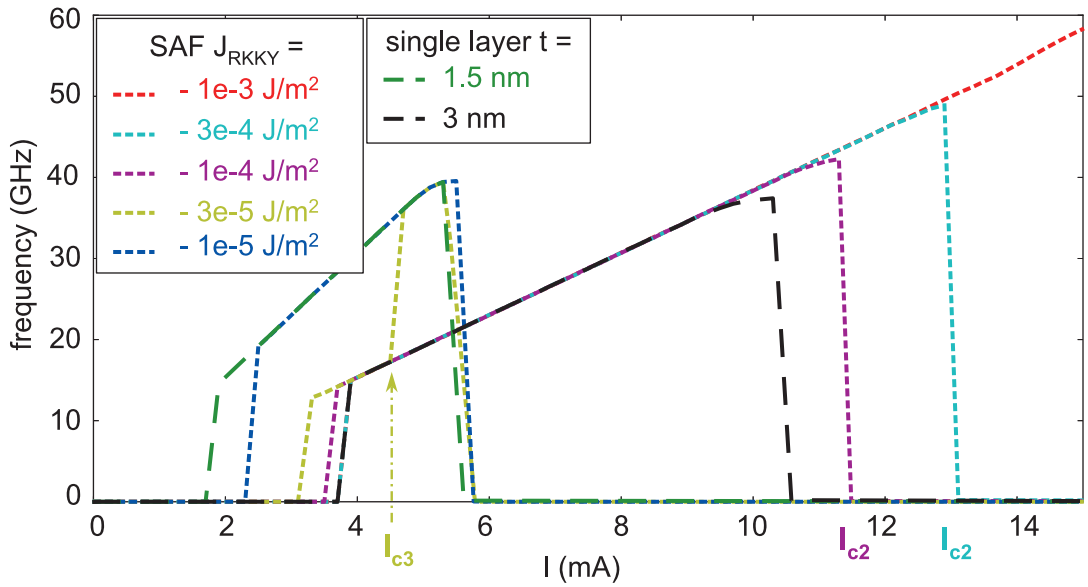

Figure 3.5 – Frequency versus applied current. OPP frequency of a single layer 1.5 nm (green dashed-line) and 3 nm (black dashed-line) thick. OPP frequency of the magnetization of layer 2 in a symmetric SAF with different RKKY coupling. For $J_{RKKY} = -1e-3$ J/m^2 (red dotted-line), $J_{RKKY} = -3e-4$ J/m^2 (cyan dotted-line) and $J_{RKKY} = -1e-4$ J/m^2 (magenta dotted-line), coupled-OPP, $I_{c2} < I_{c3}$. For $J_{RKKY} = -3e-5$ J/m^2, $I_{c1} < I_{c3} < I_{c2}$, coupled OPP until I_{c3}, then only layer 2 oscillates at the 1.5 nm thick single layer frequency. For $J_{RKKY} = -1e-5$ J/m^2, $I_{c3} < I_{c1}$, no coupled-OPP, only layer 2 oscillates. The simulation parameters are : $\alpha = 0.02$, $H_d = M_S = 1.2e6$ A/m and $H_K = 20e3$ A/m. $\eta_{z2} = 0.3$ and $\eta_{z1} = 0$.

3.3 Reference layer and SyF free layer

In this section, the spin torque due to the presence of a perpendicular polarizer is neglected ($\eta_{z1} = \eta_{z2} = 0$). Instead, the spin torque due to the reference layer is introduced and its effect on the magnetization dynamics is studied. Contrary to the previous section, the applied field and the IEC are fully integrated in the equation of motion. However, the self-sustained oscillations arising above the critical current are not studied here, because of the complexity of this problem (even for a SL free layer). The analysis is done on the linearized LLGS equation and the dynamical matrix L. The critical current is calculated. It is found to depend on the mode, acoustic or optical, that is destabilized.

From this general analysis, two applications of the results to practical systems are described : an MTJ composed of an in-plane SyF free layer and a fixed in-plane reference layer for memory application; and a SyF with mutual spin-torque between the two layers, without reference layer, for oscillator application.

3.3.1 Stability analysis

The total free energy of the system is the one expressed by eq. 3.2, including the applied field H_a and exchange bias field on the two layers, $H_{ex\,1}$ and $H_{ex\,2}$.
The IEC is also taken into account, as well as the mutual spin-torque between the layers.

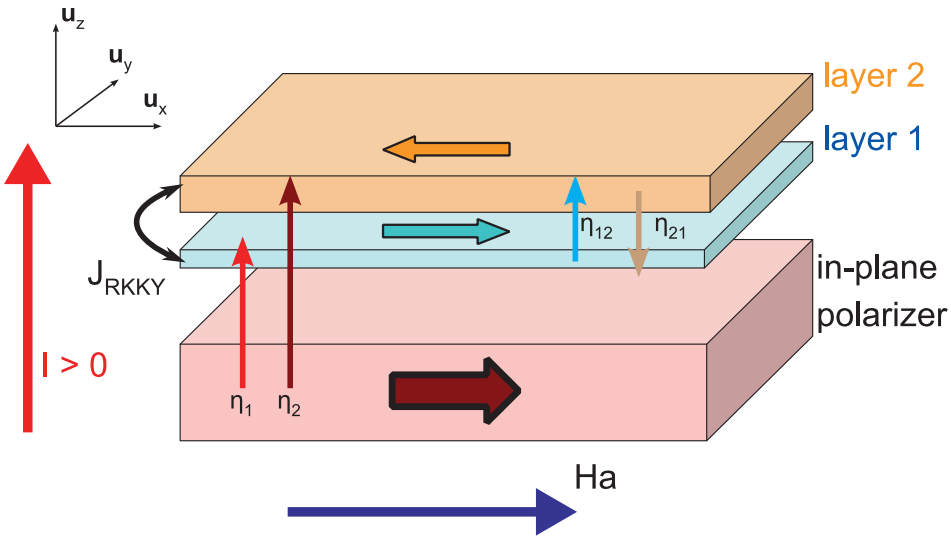

Figure 3.6 – Schematics of the synthetic ferrimagnet (SyF) as a free layer with a fixed in-plane polarizer.

$$E = \frac{1}{2}\mu_0 V_1 M_1 H_{d1}(\boldsymbol{m}_1 \cdot \boldsymbol{u}_z)^2 + \frac{1}{2}\mu_0 V_2 M_2 H_{d2}(\boldsymbol{m}_2 \cdot \boldsymbol{u}_z)^2 - \frac{1}{2}\mu_0 V_1 M_1 H_{k1}(\boldsymbol{m}_1 \cdot \boldsymbol{u}_x)^2 - \frac{1}{2}\mu_0 V_2 M_2 H_{k2}(\boldsymbol{m}_2 \cdot \boldsymbol{u}_x)^2 - \mu_0 V_1 M_1 H_{x1} \boldsymbol{m}_1 \cdot \boldsymbol{u}_x - \mu_0 V_2 M_2 H_{x2} \boldsymbol{m}_2 \cdot \boldsymbol{u}_x - S J_{\mathrm{RKKY}} \boldsymbol{m}_1 \cdot \boldsymbol{m}_2$$

$$P_1 = -\frac{\hbar}{2e} I \frac{\eta_1}{\lambda_1} \ln(1 + \lambda_1 \boldsymbol{m}_1 \cdot \boldsymbol{u}_x) + \frac{\hbar}{2e} I \eta_{21} \boldsymbol{m}_1 \cdot \boldsymbol{m}_2$$
$$P_2 = -\frac{\hbar}{2e} I \frac{\eta_2}{\lambda_2} \ln(1 + \lambda_2 \boldsymbol{m}_2 \cdot \boldsymbol{u}_x) - \frac{\hbar}{2e} I \eta_{12} \boldsymbol{m}_1 \cdot \boldsymbol{m}_2$$

The spin torque from the reference layer does not change the equilibrium configurations, which are labeled P ($\phi_1 = 0$) and AP ($\phi_1 = \pi$). It changes the stability of these equilibriums, though, much in the same way as for a single layer free layer. The stability of the equilibrium is studied by linearizing the LLGS equation around the equilibrium position. The eigenvalues of the 4x4 dynamical matrix L correspond to the FMR eigenmodes under current. The FMR eigenfrequency and linewidth correspond to the imaginary part and the double of the real part of the eigenvalues of L, respectively.

In the following, simplified notations are used to represent the average quantities over the two layers and the asymmetric quantities; some of them, n and j, have been introduced earlier :

$$n = \mathrm{sign}(J_{\mathrm{RKKY}}) \qquad \omega = \gamma_0(H_{d2} + H_{d1})/2 \qquad \alpha = (\alpha_2 + \alpha_1)/2$$
$$m = \cos\phi_1 \qquad \epsilon = \frac{H_{d2} - H_{d1}}{H_{d2} + H_{d1}} \qquad \zeta = \frac{\alpha_2 - \alpha_1}{\alpha_2 + \alpha_1}$$

$$b_1 = \frac{\gamma_0}{\omega}\left(H_{k1} + m(H_a + H_{ex1}) + \frac{|J_{\mathrm{RKKY}}|}{\mu_0 M_1 t_1}\right) \qquad Q = \frac{b_2 + b_1}{2}$$
$$b_2 = \frac{\gamma_0}{\omega}\left(H_{k2} + nm(H_a + H_{ex2}) + \frac{|J_{\mathrm{RKKY}}|}{\mu_0 M_2 t_2}\right) \qquad \kappa = \frac{b_2 - b_1}{b_2 + b_1}$$

$$j_1 = \frac{\gamma |J_{\mathrm{RKKY}}|}{\omega M_1 t_1} \qquad j = (j_2 + j_1)/2 \qquad J = \sqrt{j_1 j_2}$$
$$j_2 = \frac{\gamma |J_{\mathrm{RKKY}}|}{\omega M_2 t_2} \qquad \nu = \frac{j_2 - j_1}{j_2 + j_1}$$

$$i_1 = \frac{-mI}{1 + m\lambda_1} \frac{\gamma\hbar}{2e\omega S} \frac{\eta_1}{\alpha_1 M_1 t_1} \qquad i = (i_2 + i_1)/2$$
$$i_2 = \frac{-nmI}{1 + nm\lambda_2} \frac{\gamma\hbar}{2e\omega S} \frac{\eta_2}{\alpha_2 M_2 t_2} \qquad \mu = \frac{i_2 - i_1}{i_2 + i_1}$$

$$k_{21} = \frac{-nI}{1+n\lambda_{21}} \frac{\gamma\hbar}{2e\omega S} \frac{\eta_{21}}{\alpha_1 M_1 t_1} \qquad k = \frac{k_{12}+k_{21}}{2}$$
$$k_{12} = \frac{-nI}{1+n\lambda_{12}} \frac{\gamma\hbar}{2e\omega S} \frac{\eta_{12}}{\alpha_2 M_2 t_2} \qquad \rho = \frac{k_{12}-k_{21}}{k_{12}+k_{21}}$$

The dynamical matrix is evaluated at the two equilibrium positions, ($\theta_1 = \theta_2 = \pi/2$, $\cos\phi_1 = \pm 1$, $\cos\phi_2 = \pm 1$), labeled by the parameter $m = \cos\phi_1$: $m = 1$ is the parallel (P) equilibrium state, $m = -1$ is the antiparallel (AP) equilibrium state. If $n = 1$ the two layers of the SyF are parallel at equilibrium, if $n = -1$ they are antiparallel.

$$L = \omega \begin{pmatrix} -\alpha_1(1-\epsilon+b_1+i_1-k_{21}) & -b_1+\beta_{IEC}\alpha_1^2(i_1-k_{21}) & \alpha_1 n(j_1-k_{21}) & j_1+\beta_{IEC}\alpha_1^2 k_{21} \\ 1-\epsilon+b_1-\beta_{IEC}\alpha_1^2(i_1-k_{21}) & -\alpha_1(b_1+i_1-k_{21}) & -n(j_1+\beta_{IEC}\alpha_1^2 k_{21}) & \alpha_1(j_1-k_{21}) \\ \alpha_2 n(j_2+k_{12}) & j_2-\beta_{IEC}\alpha_2^2 k_{12} & -\alpha_2(1+\epsilon+b_2+i_2+k_{12}) & -b_2+\beta_{IEC}\alpha_2^2(i_2+k_{12}) \\ -n(j_2-\beta_{IEC}\alpha_2^2 k_{12}) & \alpha_2(j_2+k_{12}) & 1+\epsilon+b_2-\beta_{IEC}\alpha_2^2(i_2+k_{12}) & -\alpha_2(b_2+i_2+k_{12}) \end{pmatrix} \tag{3.20}$$

It is important to notice that the dynamical matrix L can be separated in four 2x2 blocks. The top-left (respectively bottom-right) correspond to the dynamical matrix of the layer 1 (resp. layer 2) alone, the other layer being fixed. Due to the RKKY interaction, the block corresponds to an isolated layer with exchange field coming from the coupling with the fixed layer. The two other 2x2 blocks contain only interaction terms proportional to the RKKY coupling and the mutual spin torque.

To compute the eigenvalues, one needs to solve a quartic equation. The fact that the eigenvalues are expected to be two pairs of complex-conjugate values implies that the quartic equation can be factorized into two quadratic equations. Hence the four eigenvalues are given by the following general expressions :

$$\lambda_i = \frac{\mathfrak{t}_1}{4} \pm_1 \frac{\sqrt{W}}{2} \pm_2 \frac{i}{2}\sqrt{2\mathfrak{a} + W \pm_1 \frac{2\mathfrak{b}}{\sqrt{W}}} \tag{3.21}$$

The four possibilities of the couples $\pm_1$ and $\pm_2$ yield four independent solutions, where $\pm_2$ distinguishes two complex-conjugate values. Here the quantity W is real positive, hence the real part of the eigenvalues (corresponding to half of the linewidth) is given by the sum of the first and second terms. The imaginary part is given by the square root term. This assumption is valid if the expression inside the radical is positive, which is supposed to be always the case here, otherwise it means that the FMR frequency vanishes. Whereas the parameter $\pm_2$ differentiates two complex conjugates eigenvalues, the parameter $\pm_1$ differentiates two eigenmodes of the SyF, the so-called optical and acoustic modes, which are associated to different eigenvectors. The optical mode is defined to be the mode with the highest frequency. By looking numerically at the eigenvectors of the optical mode, it appears that the in-plane angles of the two layers

magnetization with respect to the x-axis are in phase, whereas the out-of-plane angles are in antiphase. And vice-versa for the acoustic mode.

The parameters of eq. 3.21 depend on the coefficients of the characteristic polynomial of degree four. These coefficients are polynomial functions of the matrix traces of powers of the dynamical matrix L. Considering $\alpha \ll 1$ (except for $\mathfrak{b}$, that we calculate up to the third order in α), they are given by :

$$\begin{aligned}
&\mathfrak{t}_1 = \mathrm{trace}(L) \quad \mathfrak{t}_2 = \mathrm{trace}(L^2) \quad \mathfrak{t}_3 = \mathrm{trace}(L^3) \\
&\mathfrak{a} = -\frac{1}{2}\mathfrak{t}_2 + \frac{1}{8}\mathfrak{t}_1^2 \approx -\frac{1}{2}\mathfrak{t}_2 \\
&\mathfrak{b} = -\frac{1}{3}\mathfrak{t}_3 + \frac{1}{4}\mathfrak{t}_1\mathfrak{t}_2 - \frac{1}{24}\mathfrak{t}_1^3 \\
&\mathfrak{d} = \frac{5}{48}\mathfrak{t}_1^4 - \frac{1}{2}\mathfrak{t}_1^2\mathfrak{t}_2 + \frac{1}{4}\mathfrak{t}_2^2 + \frac{1}{3}\mathfrak{t}_1\mathfrak{t}_3 - 4\det(L) \approx \frac{1}{4}\mathfrak{t}_2^2 - 4\det(L)
\end{aligned}$$

And W is solution of the cubic equation :

$$W^3 + 2\mathfrak{a}W^2 + \mathfrak{d}W - \mathfrak{b}^2 = 0 \tag{3.22}$$

In most cases, the polynomial of eq. 3.22 can be reduced to a linear equation, because the parameter $\mathfrak{b}$ is small (it is of order α in ω unit) compared to $\mathfrak{a}$ and $\mathfrak{d}$ (of order 1 in ω unit). For small RKKY coupling energy per unit area compared to the anisotropy fields, namely $J_{\mathrm{RKKY}} < 5 \times 10^{-5}$ for $H_k = 20$ kA/m, the cubic equation may be approximated by a quadratic equation by droping the W^3 term to get a good approximation of the solution. For relatively high RKKY coupling, $J_{\mathrm{RKKY}} \approx 1 \times 10^{-4}$ or larger, the solution W of eq. 3.22 has the following expression :

$$W = \frac{\mathfrak{b}^2}{\mathfrak{d}}$$

The two modes, optical and acoustic, have different frequencies, but also different linewidths, which are twice the real part of λ_i. Let ω_{op}, ω_{ac}, $\Delta\omega_{op}$ and $\Delta\omega_{ac}$ be the eigenfrequency and linewidth of the optical and acoustic modes. They are given by :

$$\begin{aligned}
\omega_{op} &= \sqrt{\frac{\mathfrak{a}}{2} + \frac{\sqrt{\mathfrak{d}}}{2}} \qquad & \Delta\omega_{op} &= \frac{\mathfrak{t}_1}{2} + \frac{\mathfrak{b}}{\sqrt{\mathfrak{d}}} \\
\omega_{ac} &= \sqrt{\frac{\mathfrak{a}}{2} - \frac{\sqrt{\mathfrak{d}}}{2}} & \Delta\omega_{ac} &= \frac{\mathfrak{t}_1}{2} - \frac{\mathfrak{b}}{\sqrt{\mathfrak{d}}}
\end{aligned}$$

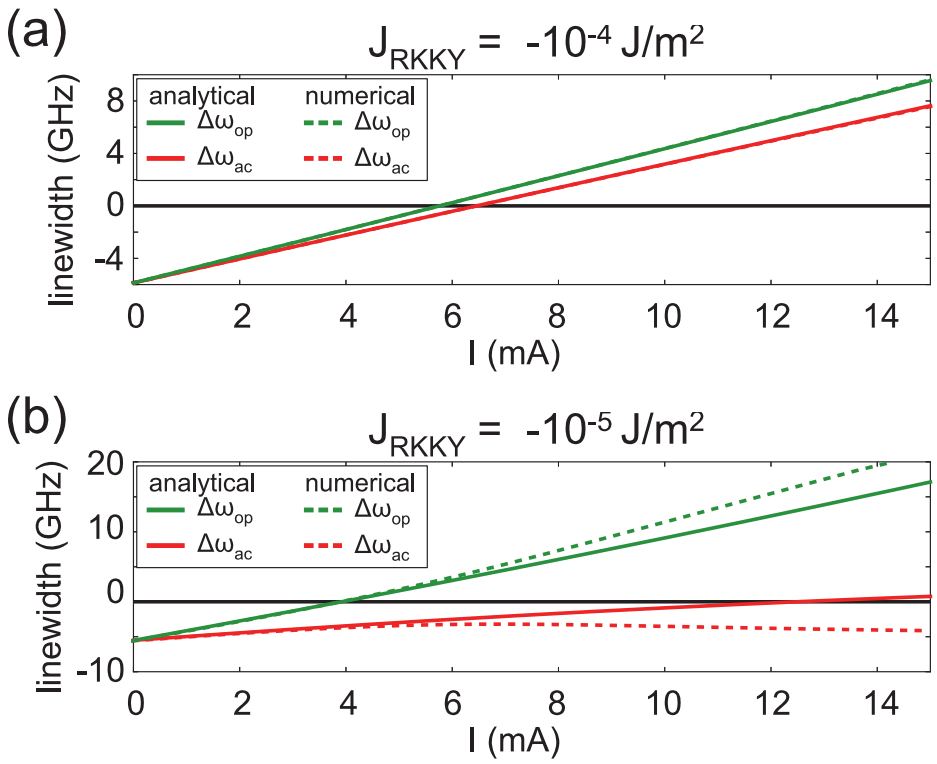

Figure 3.7 – Comparison of the analytical (full-lines) and numerical (dotted-lines) real parts of the eigenvalues of the two modes, optical (upper green lines) and acoustic (lower red lines) of a symmetric SyF with different RKKY coupling, (a) $J_{\mathrm{RKKY}} = -1 \times 10^{-4}$ J/m^2, (b) $J_{\mathrm{RKKY}} = -1 \times 10^{-5}$ J/m^2. The other parameters are $H_a = 2$ kA/m, $\alpha = 0.02$, $M_S = 1.2e6$ A/m, $H_{d1} = H_{d2} = 1.2e6$ A/m, $H_{k1} = H_{k2} = 20e3$ A/m, $\eta_1 = 0.3$ and $S = 10^{-14}$ m^2.

Neglecting the terms of order superior to 1 in α, the quantities $\mathfrak{t}_1$, $\mathfrak{a}$, $\mathfrak{d}$ and $\mathfrak{b}$ are given by :

$$\mathfrak{t}_1 = -2\alpha\omega\Big[1 + 2Q + 2i + 2\rho k + \zeta(\epsilon + 2\mu i + 2\kappa Q + 2k)\Big]$$

$$\mathfrak{a} = 2\omega^2\Big[Q(1+Q) + (\kappa Q)^2 + \epsilon\kappa Q + nJ^2\Big]$$

$$\mathfrak{d} = 4\omega^4 J^2\Big[\ \Big(\frac{Q}{J}\Big)^2\Big(\epsilon + \kappa(1+2Q)\Big)^2 + \frac{1+n}{2}\Big((1+2Q)^2 - \epsilon^2\Big) + \frac{1-n}{2}\Big(1 - (\epsilon + 2\kappa Q)^2\Big)\ \Big]$$

$$\begin{aligned}\mathfrak{b} = -2\alpha\omega^3\Big[\ & Q\Big(\epsilon + \kappa(1+2Q)\Big)\Big(\epsilon + 2\mu i + 2\kappa Q + 2k + \zeta(1 + 2i + 2Q + 2\rho k)\Big) \\ & + 2\Big(\frac{1+n}{2}\Big)(1+2Q)\Big(J^2 + kj(\rho - \nu) + \zeta kj(1 - \rho\nu)\Big) \\ & - \Big(\frac{1-n}{2}\Big)(\epsilon + 2\kappa Q)\Big[kj(1-\rho\nu) + 2\zeta\Big(J^2 + kj(\rho - \nu)\Big)\Big]\ \Big]\end{aligned}$$

For symmetric systems without fixed reference layer and with mutual spin-torque, $\mathfrak{b}$ vanishes. Hence we need the term of order 3 in α of $\mathfrak{b}$. Assuming the two layers have the same damping parameter ($\zeta = 0$), the third order of parameter $\mathfrak{b}$ is given by :

$$\begin{aligned}\mathfrak{b}_{\alpha^3} = \quad 2\alpha^3\omega^3\Big[\quad & \Big(\epsilon + 2\kappa Q + 2k + 2\mu i\Big)\Big(\frac{\epsilon}{2} + \beta_{IEC}\Big((k+\mu i)(1+2Q) + (i+\rho k)(\epsilon + 2\kappa Q)\Big)\Big) \\ & + \Big(\frac{1+n}{2}\Big)\, 2\beta_{IEC}\Big((1+2Q+2i+2\rho k)kj(\rho-\nu) - (1+2Q)k^2(1-\rho^2) \\ & \qquad\qquad + j^2(1-\nu^2)(2i+2\rho k)\Big) \\ & + \Big(\frac{1-n}{2}\Big)\, 2\beta_{IEC}kj(1-\rho\nu)(\epsilon + 2\kappa Q - 2k - 2\mu i) \quad \Big]\end{aligned}$$

To illustrate the validity of these expressions in the approximation of relatively strong RKKY coupling, Fig. 3.7 shows the error between the analytical expression of the linewidth and the values extracted from the numerical eigenvalues computation of the 4x4 matrix L. The linewidth versus applied current is computed for a symmetric SyF, with an anisotropy field of $H_k = 20$ kA/m and a small applied field $H_a = 2$ kA/m to differentiate the two modes. Fig. 3.7.a, with $J_{\mathrm{RKKY}} = -1 \times 10^{-4}$ J/m^2, shows a good agreement between the analytical and numerical expression, whereas in Fig. 3.7.b, with $J_{\mathrm{RKKY}} = -1 \times 10^{-5}$ J/m^2, the two expressions differ, especially for large currents.

The expressions of the eigenfrequencies for the two modes, optical and acoustic, are independent of α at the first order. Therefore, they could be extracted from the dynamical matrix of the conservative part alone. With only the conservative part, the 4x4 dynamical matrix has several vanishing coefficients, so it is easier to compute its determinant. The eigenfrequencies are consistent with previous publications[Devolder 2012] that do not take the dissipative part into account. At the first order in α, they are given by :

$$\frac{\omega^2_{op/ac}}{\omega^2} = Q(1+Q) + \kappa^2Q^2 + \epsilon\kappa Q + nJ^2 \pm \sqrt{\begin{aligned} & Q^2\Big(\epsilon + \kappa(1+2Q)\Big)^2 + \frac{1+n}{2}J^2\Big((1+2Q)^2 - \epsilon^2\Big) \\ & \qquad + \frac{1-n}{2}J^2\Big(1 - (\epsilon + 2\kappa Q)^2\Big)\end{aligned}} \tag{3.23}$$

3.3.2 Critical currents of the two modes

According to the previous expressions, ω_{op} and ω_{ac} are independent of the applied current up to order 1 in α, the current dependence of the eigenfrequencies is of order $\alpha^2 I$. Moreover, the difference of the squared frequencies of the two modes is proportional to the RKKY coupling :

$$\delta\omega^2 = \omega_{op}^2 - \omega_{ac}^2 = 2\omega^2 J\sqrt{\gamma_n} \qquad \text{with} \quad \gamma_n = \mathfrak{d}/(4\omega^4 J^2) \approx 1$$

The critical currents for the optical and acoustic modes are computed by solving $\Delta\omega_{op} = 0$ and $\Delta\omega_{ac} = 0$. However the linewidths of the two modes are different, so the critical current is given by the smallest of the two currents. Depending of which mode is destabilized first, the magnetization dynamics to escape the equilibrium are optical or acoustic-like.

In the case of two layers with the same damping constant, $\zeta = 0$, and without mutual spin-torque, the adimensional critical current (either optical or acoustic) is given by :

$$|i_{op/ac}^c| = \frac{1/2 + Q \pm (\kappa Q + \epsilon/2)\delta}{1 \pm \mu\delta} \tag{3.24}$$

Where $\delta = \dfrac{Q}{J\sqrt{\gamma_n}}\Big(\epsilon + \kappa(1+2Q)\Big)$.

Notice that the critical currents of the two modes are equal for $\delta = 0$.
In order to decrease the critical current in a SyF, the denominator of the previous expression needs to be increased, by increasing δ, defined above. Hence there are two different options to reduce the critical current in a SyF : (i) increasing the demagnetizing field mismatch ϵ; (ii) increasing the mismatch κ, by increasing the uniaxial anisotropy mismatch, or using an exchange field, or increasing the layers thickness mismatch. The three cases (the uniaxial anisotropy mismatch is not treated) are represented on Fig. 3.8.

On these figures, the phase diagram of single layer and SAF free layers versus applied current and field, obtained from macrospin simulations, are compared to the analytical expressions. The diagrams represent the average in-plane component along the easy axis of the magnetization of the first layer $\langle m_x^1 \rangle$, the one that is in contact (in fact it is separated by the MgO barrier) with the reference layer. This component is related to the TMR, so it is a physical parameter. The average of m_x^1 is taken between 8 and 10 ns of the 10 ns long current pulse. Hence the results are supposed to reflect less of the transient regime, and more of the steady state reached after the pulse is applied. The magnetization is initially in the P configuration : $m_x^1 = 1$, represented in red on the graphs. The AP configuration ($m_x^1 = -1$) is represented in blue.
Fig. 3.8.a represents the phase diagram of a single layer free layer, initially in the P configuration. The simulation parameters are : $\alpha = 0.02$, $M_S = 1.2e6$ A/m, $H_k = 20e3$ A/m, $\eta_1 = 0.3$ and $t = 3$ nm. The magnetization is reversed for around 5 mA at zero field. Only one direction of the field, negative fields, switches the free layer, the other direction actually stabilizes the free layer in the P configuration. The calculated critical line, corresponding to $\Delta\omega = 0$ from Chapter 1, is in good agreement with the simulations. Notice that the calculated critical line is composed of two parts :

- a "horizontal" line, that corresponds to the vanishing of the FMR eigenfrequency ω_0. Its equation is given by $H_x = H_k$.

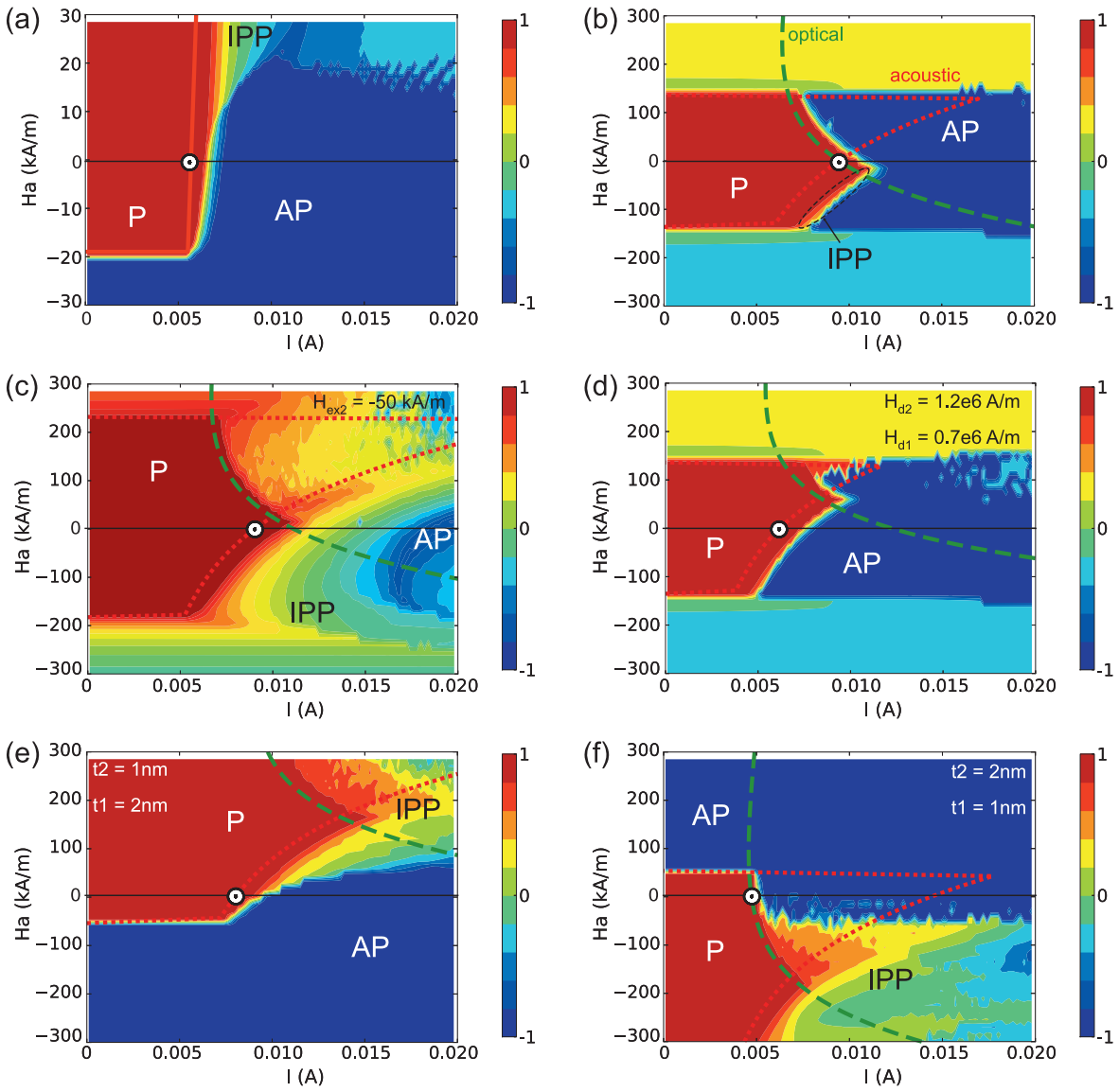

Figure 3.8 – Comparison of analytical calculations and macrospin simulations. Diagram of the average $\langle m_x^1 \rangle$ between 8 and 10 ns of a 10 ns long simulation with $m_x^1 = 1$ initially. Red line, calculated acoustic critical line. Green line, calculated optical critical line. Different configurations are represented : (a) single layer with an equivalent magnetic volume, $\alpha = 0.02$, $M_S = 1.2e6$ A/m, $H_k = 20e3$ A/m, $\eta_1 = 0.3$, $t = 3$ nm; (b) identical layers, $\alpha = 0.02$, $M_S = 1.2e6$ A/m, $H_{d1} = H_{d2} = 1.2e6$ A/m, $H_{k1} = 20e3$ A/m, $\eta_1 = 0.3$, $t_1 = t_2 = 1.5$ nm, $J_{\mathrm{RKKY}} = -1 \times 10^{-3}\mathrm{J/m^2}$. Same layers with mismatch : (c) $H_{ex2} = -50$ kA/m. (d) $H_{d1} = 0.7e6$ A/m, $H_{d2} = 1.2e6$ A/m. (e) $t_1 = 2$ nm, $t_2 = 1$ nm. (f) $t_1 = 1$ nm, $t_2 = 2$ nm.

- the critical current linear with respect to the field, that comes from the vanishing of the linewidth $\Delta\omega$. Its expression is given by eq. 2.6.

For large positive fields, the magnetization is destabilized in the IPP state instead of switching just above the critical current.

Fig. 3.8.b is the phase diagram of a symmetric SAF, initially in the P state ($m_x^1 = 1$, $m_x^2 = -1$). The simulation parameters are : $\alpha = 0.02$ ($\alpha_1 = \alpha_2$), $M_S = 1.2e6$ A/m ($M_{S1} = M_{S2}$), $H_{d1} = H_{d2} = 1.2e6$ A/m, $H_{k1} = H_{k2} = 20e3$ A/m, $\eta_1 = 0.3$, $\eta_2 = 0$, $t_1 = t_2 = 1.5$ nm, $J_{\mathrm{RKKY}} = -1 \times 10^{-3}\mathrm{J/m^2}$. These parameters are the same for Fig. 3.8.c-f, except otherwise mentioned. The calculated critical line for the acoustic mode (red dotted-line) and the optical mode (green dashed-line) are in agreement with the simulations. The optical critical line is defined by the vanishing of the optical linewidth, $\Delta\omega_{op} = 0$. The acoustic critical line is composed of two parts, like in the single layer case :

- two horizontal lines, corresponding to the vanishing of the acoustic eigenfrequency ω_{ac}. As shown on Fig. 3.2, ω_{ac} vanishes for both directions of the applied field. The two critical field values, for positive and negative field can be different, as seen in the other graphs of Fig. 3.8. In the symmetric case they have the same absolute value, defined by eq. 3.23.

- the part corresponding to the vanishing of the acoustic linewidth, $\Delta\omega_{ac} = 0$. It is defined by eq. 3.24.

Notice that the calculated critical lines correspond to the critical lines computed numerically from the eigenvalues of the dynamical matrix. The analytical expressions are in agreement with the numerical computation of the eigenvalues with the condition of a large RKKY coupling, as it was stated previously.

For negative fields, the acoustical critical current is smaller than the optical critical current. Just above the acoustical critical current, the magnetization is destabilized following the acoustic mode, and it reaches an IPP steady state, with an oscillation frequency close to the acoustic FMR frequency. For currents slightly larger than the acoustic critical current, the IPP state does not survive and the magnetization switches. The range of IPP state is not clearly visible on the graph because of its small current range. It spans close to the border between P and AP region in negative fields.

For positive fields, the optical critical current is smaller than the acoustic critical current. Hence, above the optical critical current, the magnetization is destabilized and grows away from the equilibrium (with optical-like oscillations) to eventually switch.

For a symmetric SyF as described in Fig. 3.8.b, the evolutions of the transverse in-plane components of the magnetization, m_{1y} and m_{2y}, above the optical and acoustic critical lines are shown in Fig. 3.9. The destabilization mode is different in the two cases, positive and negative fields of $H_a = \pm 50$ kA/m, and with the same applied current of $I = 9.2$ mA (above the critical current in both cases). For positive fields, the mode is optical, characterized by a high oscillation frequency and in-phase transverse in-plane components. On the contrary, for negative fields, the mode is acoustic, with a lower frequency and out-of-phase in-plane transverse components.

Fig. 3.8.c-f show the phase diagram of asymmetric SAF. In Fig. 3.8.c, the layer 2 is subjected to an exchange bias field of $H_{ex2} = -50$ kA/m, all the other simulation parameters are the same as for the symmetric case. This exchange bias field can originate from an antiferromagnetic layer in contact with layer 2. The critical lines define the same "arrow" shape than in the symmetric case, but slightly shifted towards the positive fields. The critical fields are also larger than in the symmetric case. For negative fields, the IPP range is expanded compared to the symmetric case.
The critical current at zero field is slightly reduced compared to the symmetric case.

In Fig. 3.8.d, the demagnetizing field of the layer 1 is reduced to the value $H_{d1} = 0.7e6$ A/m. The demagnetizing field of layer 1 is unchanged. The reduced demagnetizing field can be achieved, for instance, by improving the interface between layer 1 and the MgO barrier to increase the interface perpendicular anisotropy. In this case, the arrow shape of the critical lines of the two modes is shifted towards positive fields. The critical field at zero field is much reduced compared to the symmetric case. Notice that the IPP region has disappeared in this case.

In Fig. 3.8.e and f, the two layers of the SAF have different thicknesses : $t_1 = 2$ nm, $t_2 = 1$ nm, and $t_1 = 1$ nm, $t_2 = 2$ nm, respectively. The total thickness remains 3 nm, like for the symmetric SAF and the single layer. Thus the comparison is made with systems with the same magnetic volume. The thickness asymmetry provokes a shift of the arrow shape of the critical lines, towards either positive or negative field (respectively). In both cases, the critical current at zero field is reduced compared to the symmetric case. Interestingly, because the IPP seem to exist only in the acoustic mode, at zero field, the magnetization switches above the critical current for $t_1 < t_2$ (lower right graph). There is a small current range of IPP before the switching region if $t_1 > t_2$. This difference is of great interest for application as oscillator or as memory.
The present analysis does not permit to conclude on the existence or not of an IPP region. For this, a different approach should be used, based on the work of Slavin et al.[Slavin 2008]. In this theory, not only the linear part of the LLGS equation is computed, but also the non-linear part that describes the self-sustained oscillations.

Even if the range of existence of in-plane precession (IPP) cannot be known from this equilibrium analysis, macrospin simulations show that self-sustained IPP are acoustic-like. Therefore, the IPP were never encountered above the optical critical current. This is specially interesting to use SyF free layer for memory application. If we assume that the spin torque originating from the reference layer is totally transmitted to the first layer of the SyF, then in the case of an asymmetric SyF with $t_1 < t_2$ (see Fig. 3.8.f), the critical current at zero field is always optical. With the other current polarity, the destabilization of the AP equilibrium is also optical. Therefore, no self-sustained oscillations (with reasonable applied currents) can be obtained at zero field. For memory application, it ensures that the magnetization of layer 1 (and layer 2 simultaneously) is reversed with an applied current larger than the critical current.

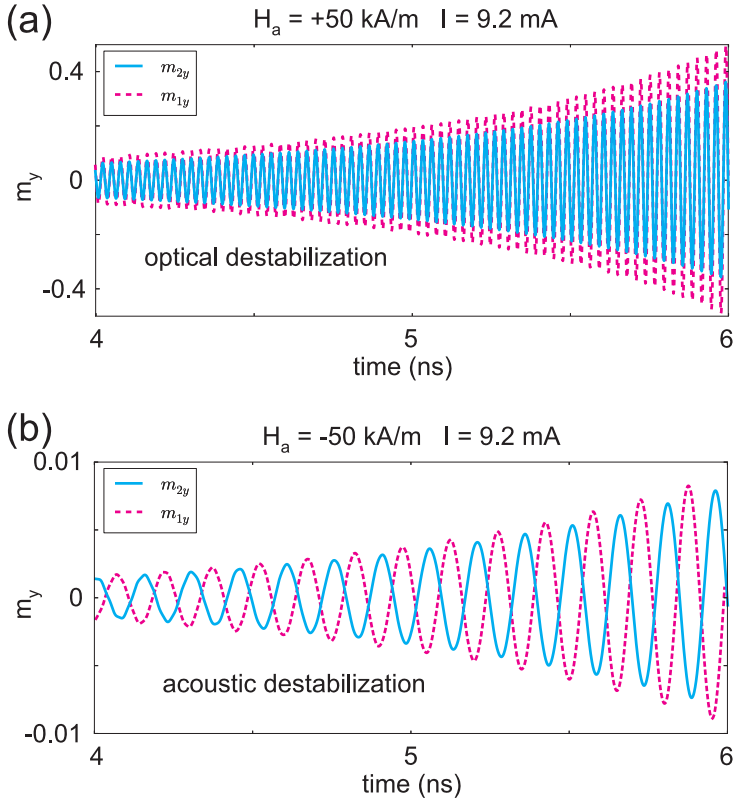

Figure 3.9 – Evolution between 4 and 6 ns of the transverse in-plane components of the magnetization of the two layers, m_{1y} and m_{2y}, with an applied current density of 9.2×10^{11} A/m^2 (9.2 mA with $S = 10^{-14}$ m^2). The SyF is symmetric, corresponding to the case of Fig. 3.8.b. (a) Positive applied field of $H_a = 50$ kA/m : high frequency optical destabilization. (b) Negative field of $H_a = -50$ kA/m : low frequency acoustic destabilization.

3.3.2.1 Decrease of the critical current of a SyF free layer

It was shown that the critical current of a SyF free layer could be reduced by introducing asymmetry in the structure. However no quantitative comparison was given with the critical current of a single layer (SL) free layer. To investigate this, the expression of the critical currents of SyF and SL free layer will be compared in the given framework (as in Fig. 3.8) : (i) the layers of the SyF and of the SL of comparison have the same saturation magnetization M_S (meaning that all the layers are made of the same material) and the total thickness of the SyF, $t_1 + t_2$, is equal to the thickness t of the single layer; (ii) all the layers have the same damping α and there is no spin-efficiency asymmetry ($\lambda_1 = \lambda_2 = 0$).; (iii) the spin-torque originating from the reference layer is neglected on the second layer in the SyF ($i_2 = 0$). There are some evidence that the spin-torque may be transferred to the second layer[Ichimura 2009, Ichimura 2011], however the STT on the second layer is smaller than on the first one. Therefore it is neglected here.

A general expression for the demagnetizing fields is also used, that exhibits the direct dependence of the demagnetizing field on the surface anisotropy due to one interface with the

MgO separating the first layer from the reference layer and to another interface on top of the structure :

$$H_d^{\mathrm{SL}} = M_S - \frac{K_1 + K_2}{\mu_0 M_S t} \qquad \begin{cases} H_{d2} &= M_S - \dfrac{K_2}{\mu_0 M_S t_2} \\ H_{d1} &= M_S - \dfrac{K_1}{\mu_0 M_S t_1} \end{cases}$$

With K_1 the surface anisotropy energy density due to the interface with the MgO and K_2 the one due to the top interface. Let I_0^{SyF} and I_0^{SL} be characteristic currents :

$$I_0^{\mathrm{SyF}} = \frac{2eS}{\hbar\eta_1}\alpha\frac{H_{d1} + H_{d2}}{2}M_S \times (2t_1)$$
$$I_0^{\mathrm{SL}} = \frac{2eS}{\hbar\eta_1}\alpha H_d^{\mathrm{SL}} M_S t$$

The notation $Q = Q' + j$ is used, so that for a single layer (SL) :

$$I_c^{\mathrm{SL}} = I_0^{\mathrm{SL}}(1/2 + Q')$$

For the critical current of the SyF, the asymmetry term in the numerator of eq. 3.24 is neglected, so that :

$$I_c^{\mathrm{SyF}} = I_0^{\mathrm{SyF}}\frac{1/2 + Q' + j}{1 + |\delta|}$$

Let τ be the adimensional thickness asymmetry :

$$t = t_2 + t_1 \qquad \tau = \frac{t_2 - t_1}{t_2 + t_1}$$

Notice that because $M_1 = M_2 = M_S$, $\tau = -\nu$.
According to the expressions of the demagnetizing fields, the ratio σ of the SyF and of the SL characteristic currents, $\sigma = I_0^{\mathrm{SyF}}/I_0^{\mathrm{SL}}$, is given by :

$$\sigma = 1 - \tau\frac{1 + \epsilon}{1 + \tau\epsilon}$$

Therefore, the critical current for a SyF MTJ is smaller than for a single layer MTJ if the following condition is fulfilled :

$$\sigma(\frac{1}{2} + Q' + j) < (\frac{1}{2} + Q')(1 + \delta)$$

This can be written as a maximum for the adimensional RKKY coupling energy J defined earlier :

$$2J < \frac{(1 + 2Q')(1 + \epsilon\tau)}{1 - \tau}\left(\tau\frac{J}{j}\frac{1 + \epsilon}{1 + \epsilon\tau} + \left|\epsilon + \kappa(1 + 2Q' + 2j)\right|\frac{1 + Q'/j}{\sqrt{\gamma_n}}\right)$$

Two particular cases are of interest :

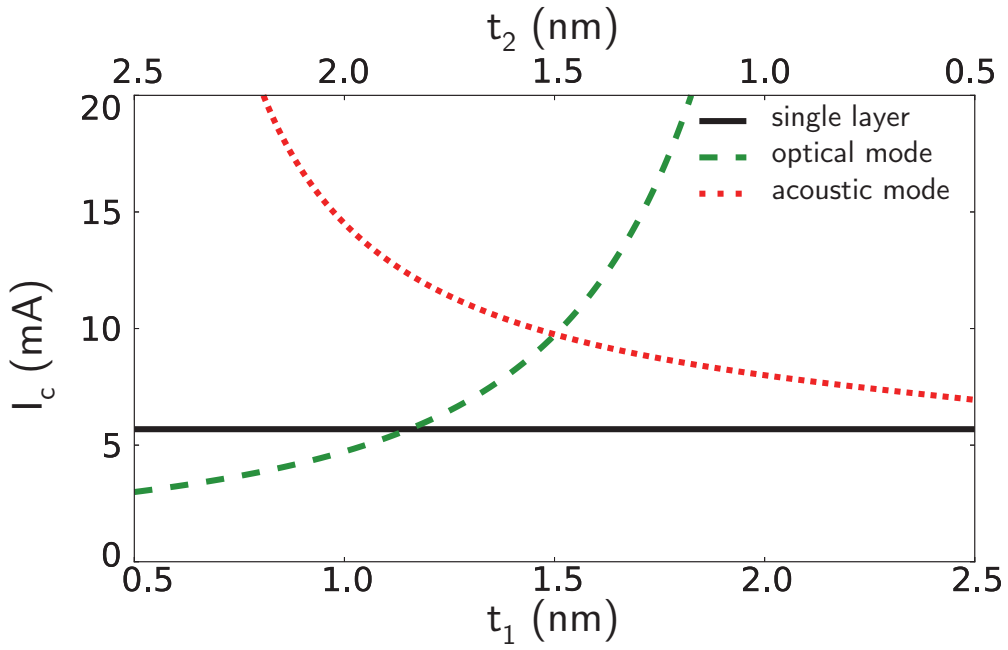

Figure 3.10 – Critical current versus thickness of the layer 1, t_1, for the same total thickness $t = 3$ nm.

- $\epsilon = 0 \quad \Longrightarrow \quad 2J < \dfrac{\tau}{1-\tau} C$
  with $C = 2$ or $C = -Q'/j$ if τ is positive or negative, respectively.
- $\tau = 0 \quad \Longrightarrow \quad 2J < |\epsilon| \Big(1 + 2Q'\Big)\Big(1 + Q'/j\Big)$

In this framework, where no spin-torque is acting on the second layer of the SyF, it appears that the critical current of a single layer can be reduced by making it a SyF with the same magnetic volume. The corresponding SyF must be strongly asymmetric, either due to the thickness difference between its two layers (Fig. 3.10), or due to an interfacial surface anisotropy (Fig. 3.11). For an asymmetric SyF, reducing the RKKY coupling energy reduces the critical current (Fig. 3.12).
However, these parameters also affect other properties of the SyF, like for instance the coercive field. As seen on Fig. 3.8.f, the coercive field for a SAF with asymmetric thicknesses, $t_1 = 1$ nm and $t_2 = 2$ nm, is much reduced compared to a symmetric SAF : 50 kA/m compared to 150 kA/m in the symmetric case. Therefore, the thickness asymmetry must not be too large, so that the MTJ has a large enough bistable region with respect to external field.
To realize memory cells, the stability factor has to be as large as possible. However, the dependence of the stability factor with the thickness asymmetry (and other parameters) is not clear. It was estimated by Taniguchi et al.[Taniguchi 2011], and was found independent of the RKKY coupling energy. They found that the stability factor of a SAF is the average of the stability factors of the two layers that compose the SAF. This point is discussed in Appendix A.

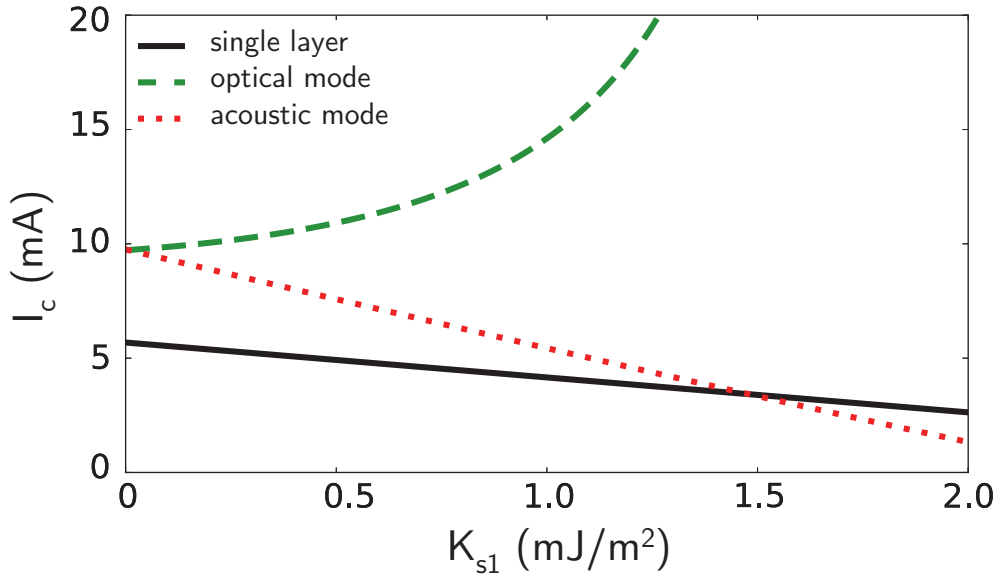

Figure 3.11 – Critical current versus interfacial surface anisotropy energy of the layer 1, K_{s1}.

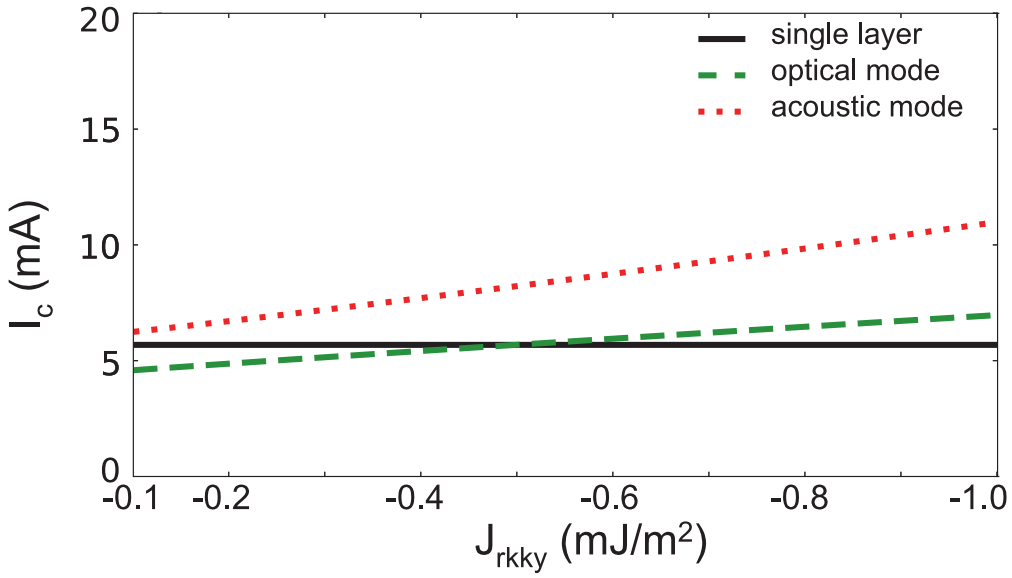

Figure 3.12 – Critical current versus RKKY coupling energy J_{RKKY} with a thickness asymmetry : $t_1 = 1.3$ nm, $t_2 = 1.7$ nm.

3.3.3 Stability analysis of an oscillator without reference layer

Unlike the previous sections, the system of interest here is a configuration without fixed polarizing layer ($\eta_1 = \eta_2 = 0$, so $i = 0$), with antiferromagnetic coupling between the layers ($n = -1$), and with mutual spin-torque between the layers. The layers magnetizations are

excited only by the mutual spin-torque between the layers. It also provides an extra coupling between the layers, in addition to the RKKY coupling. Some experimental results on this configuration were presented in [Seki 2010]. An experimental phase diagram is presented, for positive applied field, which shows that the self-sustained oscillations appear only for positive current. This feature can possibly be explained by the following analytical calculations of the critical current, because the two modes, acoustic or optical, are excited each for one polarity of the current. If only one of these modes is detected experimentally, it would explain why the excitations are only encountered for one current polarity. Moreover, the simulations show that it is possible to excite an optical-like mode in this structure. Since the optical mode has a larger frequency than acoustic mode usually encountered in conventional STO, such structure could extend the frequency range of STO.

In order to simplify the problem and try to focus on what makes this system special, the layers are supposed identical layers, hence $\epsilon = \nu = \zeta = \rho = 0$, and also $t_1 = t_2$, $j = J$. In addition, without applied field, $\kappa = 0$, and so the linewidths for the two modes, optical and acoustic, write :

$$\Delta\omega_{op/ac} = -\alpha\omega\left(1 + 2Q \mp \frac{2\beta_{IEC}\alpha^2 k^2}{j}(1 + 2Q - 2j)\right) \tag{3.25}$$

The equilibrium state becomes unstable when the linewidth becomes positive, and according to the previous equation, without applied field, this is possible only for the optical mode. Notice also that without spin-torque field-like term, or IEC, ($\beta_{IEC} = 0$), the linewidth is not modified by current in the symmetric case. Because k is proportional to the applied current I, increasing the current increases the acoustic mode linewidth in absolute value but it always remains negative. However, when increasing the current, the optical mode linewidth will eventually vanish. Fig. 3.13) represents the critical lines corresponding to $\Delta\omega_{op/ac} = 0$ versus applied current and applied field. Without applied field, only the optical mode can be excited. The final state of macrospin simulations are superposed to the critical lines and show a good agreement. The gray regions represent a final IPP steady state, while the white regions represent an equilibrium state, P as the initial configuration, or AP if one of the layer switched. The simulations were only performed between -50 and 50 kA/m.

The expressions of the critical lines are complicated with an applied field, however it is possible to obtain the expression of the critical current for $H_a = 0$.
Let I_m be a characteristic current amplitude, given by :

$$I_m = \alpha M_s t_1 \frac{2e\omega S}{\gamma\hbar}\frac{1 - \lambda_{21}}{\eta_{21}} \tag{3.26}$$

The critical current I_c^{op} of two identical layers with mutual spin-torque and without applied field is given by :

$$I_c^{op} = \frac{I_m}{\alpha}\sqrt{\frac{j}{2\beta_{IEC}}}\sqrt{\frac{1 + 2Q}{1 + 2Q - 2j}} \tag{3.27}$$

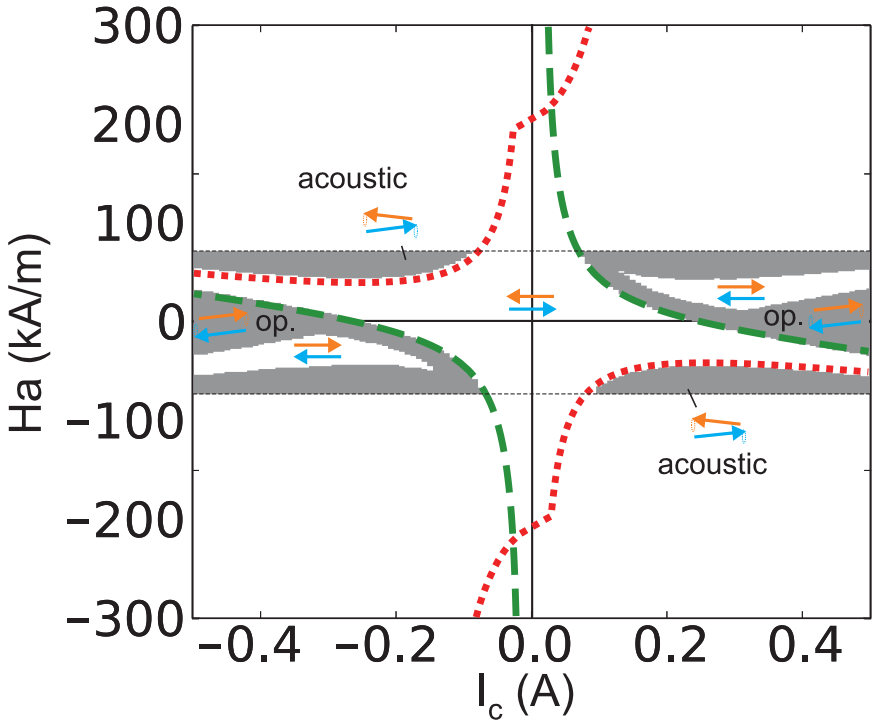

Figure 3.13 – Critical lines versus current and field without fixed polarizing layer and with mutual spin-torque between the layers. Red dotted-line, acoustic mode, green dashed-line, optical mode. From $H_a = -50$ kA/m to $H_a = 50$ kA/m, steady state from macrospin simulations : in-plane steady state (white region) and IPP (grey region). The SAF is initially in the P configuration (center), and reverses to AP in the top-right and bottom-left panel. The IPP is optical-like around zero field and close to the optical critical line, and acoustic-like otherwise. The layers are identical, with thicknesses $t_1 = t_2 = 1.5$ nm, $J_{\mathrm{RKKY}} = -10^{-3}$ J/m^2 and $\beta_{IEC} = 1$.

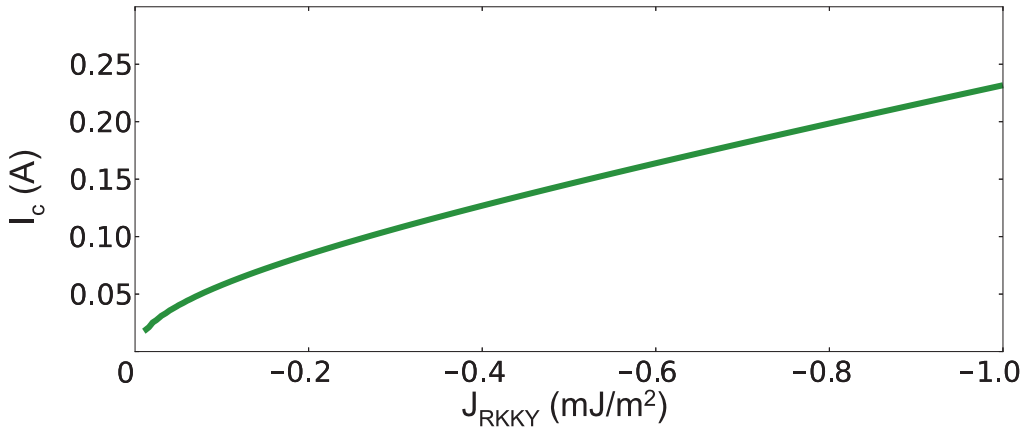

Figure 3.14 – Critical current versus RKKY coupling energy J_{RKKY} without fixed polarizing layer and with mutual spin-torque between the layers. The layers are identical, with thicknesses $t_1 = t_2 = 1.5$ nm and no applied field, $H_a = 0$.

Because j is proportional to the RKKY coupling energy per unit area J_{RKKY}, it appears that the critical current is proportional to the square root of the RKKY coupling constant for small coupling, as shown in Fig. 3.14. Notice that the RKKY constant is also included in Q, therefore for a large RKKY constant, namely $j > 1/2$, the critical current tends to be proportional to j.

3.4 Conclusion on the SyF structures

The STT-induced dynamics of a SyF free layer was studied for two magnetization directions of the polarizing layer. With a perpendicular polarizer, it was found that the SyF free layer behaves qualitatively and quantitatively like a single layer with the same magnetic volume, if the RKKY coupling field is larger than the anisotropy field, the so-called high-coupling regime. On the contrary, in the low-coupling regime, the two layers of the SyF are decoupled.
With an in-plane reference layer, the SyF free layer usually exhibits larger critical fields than the equivalent single layer with the same magnetic volume. In the case of a symmetric SyF, the critical fields are enhanced by the value of the RKKY coupling field. However, it was found that the critical field can be reduced with an asymmetric SyF. If the difference between the thicknesses of the two layers of the SyF is large enough, the critical current can be reduced below the critical current of the equivalent single layer. Qualitatively, the current-induced switching of a SyF free layer is similar to the switching of a single layer : above the critical current, the magnetization oscillates with increasing amplitude around the equilibrium until the reversal. For a SyF, though, the magnetization oscillation frequency can take two different values, depending if the destabilization is optical or acoustic.
Regarding the thermal stability factor of a SyF free layer, mentioned in Appendix A, it is the average of the thermal stability factors of the two layers taken separately, the RKKY coupling has no part in it, even if it increases the value of the coercive field. So there is no advantage of using a SyF free layer for the purpose of increasing the thermal stability.

For the comparison with a single layer free layer, it was found that, as far as the coupling between the two layers of the SyF is strong, the SyF behaves like a single layer free layer of equivalent magnetic volume, with enhanced critical fields and currents. Qualitatively, there is no difference between a SyF with strong coupling and a single layer. If the coupling field is of the same order of magnitude than the anisotropy field, the situation is more complicated, between a single layer and two independent layers.

In the rest of the theoretical analysis presented in this manuscript, the free layer is supposed to be a single layer, but changing it for a SyF with a strong coupling should not change drastically the outcome.

Chapter 4

Perturbation of the out-of-plane precession of an in-plane MTJ with a perpendicular polarizer

The OPP steady state of a single layer in-plane MTJ with a perpendicular polarizer could be solved analytically if only the demagnetizing field and the spin torque from the perpendicular polarizer were taken into account[Ebels 2008][Lee 2005] (see Chapter 2). Here, a perturbative approach is presented, which allows to estimate the effect of the applied field, the anisotropy field and the spin-torque from the reference layer on the OPP state. The change in frequency due to these perturbations and the critical current for the existence of the OPP steady state submitted to these perturbations were computed using this approach.

This approach is different from earlier studies of the STO dynamics[Slavin 2008, Slavin 2009, Kim 2008], for which the dynamical steady state was calculated as a small deviation from the equilibrium state. It differs also from the planar approximation[Bazaliy 2012] that is a general analysis in the assumption that the dynamics are almost in-plane. Here the dynamical steady state is a deviation from another limit cycle with a simpler expression.

This analysis will allow to understand how these different perturbations, anisotropy, external field and reference layer STT, perturb the self-oscillations of the free-layer with a perpendicular polarizer, in order to reduce these perturbations to realize improved STO, or on the contrary to enhance the perturbations so that the oscillations disappear, to realize memory cells.

4.1 Macrospin equation and solvable case

4.1.1 LLGS equation

The goal of this section is to start with the most simplistic model that describes OPP, and to add all other contributions perturbatively. The system eventually considered contains various terms, that are presented below.
The free layer energy E contains the terms due to the demagnetizing field H_d, the uniaxial

anisotropy field H_K and an external applied field in any arbitrary direction $\boldsymbol{H}_a$ (it can also include an exchange bias and a stray field) :

$$E = \frac{1}{2}\mu_0 V M_S^2 m_z^2 - \frac{1}{2}\mu_0 V M_S^2 m_x^2 - \mu_0 M_S V \boldsymbol{m}\cdot\boldsymbol{H}_a$$

V is the volume of the free layer, while M_S is its saturation magnetization.
The spin torque potential P contains the contributions due to the perpendicular polarizer (labeled $PERP$) and to the reference layer, which acts like a longitudinal polarizer (labeled $LONG$) :

$$P = -\frac{\hbar}{2e} I\eta_x \frac{\ln(1+\lambda_x \boldsymbol{m}_x\cdot\boldsymbol{m})}{\lambda_x} + \frac{\hbar}{2e} I\eta_z \frac{\ln(1+\lambda_z \boldsymbol{m}_z\cdot\boldsymbol{m})}{\lambda_z}$$

The current I is positive for electrons flowing from the perpendicular polarizer to the free layer, then to the reference layer. The current density J is defined as $I = JS$, where S is the area of the free layer cylindrical cross-section, and the free layer thickness is called t : $V = St$. The spin polarization and spin polarization asymmetry of the perpendicular polarizer (reference layer) are labeled η_z and λ_z (η_x and λ_x, resp.). Notice that the case of a unique polarizing layer with a tilted magnetization $\boldsymbol{m}_{pol} = \sin\theta_P \boldsymbol{u}_x + \cos\theta_P \boldsymbol{u}_z$ is consistent with this definition of the spin torque potential in the limit of $\lambda_z, \lambda_x \ll 1$. Let η_{pol} and λ_{pol} be the spin polarization and spin polarization asymmetry of the tilted polarizer. Thus, the spin torque potential i defined by the above expression, with $\eta_z = \cos\theta_P \eta_{pol}$, $\eta_x = -\sin\theta_P \eta_{pol}$ and $\lambda_{pol} = \lambda_x = \lambda_z$.

The free layer magnetization $\boldsymbol{m}$ is solution of the macrospin Landau-Lipschitz-Gilbert-Slonczewski (LLGS) equation, expressed in spherical coordinates :

$$\dot{\tilde{\boldsymbol{R}}} = \frac{\gamma}{M_S V}\left(\boldsymbol{\Omega_1}\partial_{\tilde{\boldsymbol{R}}}\mathcal{H} - \partial_{\tilde{\boldsymbol{R}}}\Gamma\right) \tag{4.1}$$

Let $\boldsymbol{\Omega_1}$ be the symplectic matrix : $\boldsymbol{\Omega_1} = \begin{pmatrix} 0 & -1 \\ 1 & 0 \end{pmatrix}$

Like in previous chapters, the notation $\dot{\tilde{\boldsymbol{R}}}$ stands for $(\dot\theta, \dot\phi\sin\theta)^\intercal$, where $\dot\theta = \frac{\mathrm{d}\theta}{\mathrm{dt}}$, and $\partial_{\tilde{\boldsymbol{R}}} = (\frac{\partial}{\partial\theta}, \frac{1}{\sin\theta}\frac{\partial}{\partial\phi})^\intercal$. The conservative and dissipative potentials $\mathcal{H}$ and Γ are defined by $\mathcal{H} = E + \alpha\beta_{IEC}P$ and $\Gamma = \alpha E - P$, respectively. α is the damping constant of the free layer and γ is the gyromagnetic ratio. In the following, $\beta_{IEC} = 1$, the IEC is only due to the transform of $\alpha\boldsymbol{m}\times\frac{\mathrm{dm}}{\mathrm{dt}}$ in the LLGS equation.

With the compact notation for the partial derivative of a potential f : $\frac{\partial f}{\partial\theta} = f_\theta$, the LLGS writes :

$$\begin{aligned}
\dot\theta &= \frac{\gamma}{M_S V}\left(-\frac{\mathcal{H}_\phi}{\sin\theta} - \Gamma_\theta\right) \\
\dot\phi\sin\theta &= \frac{\gamma}{M_S V}\left(\mathcal{H}_\theta - \frac{\Gamma_\phi}{\sin\theta}\right)
\end{aligned} \tag{4.2}$$

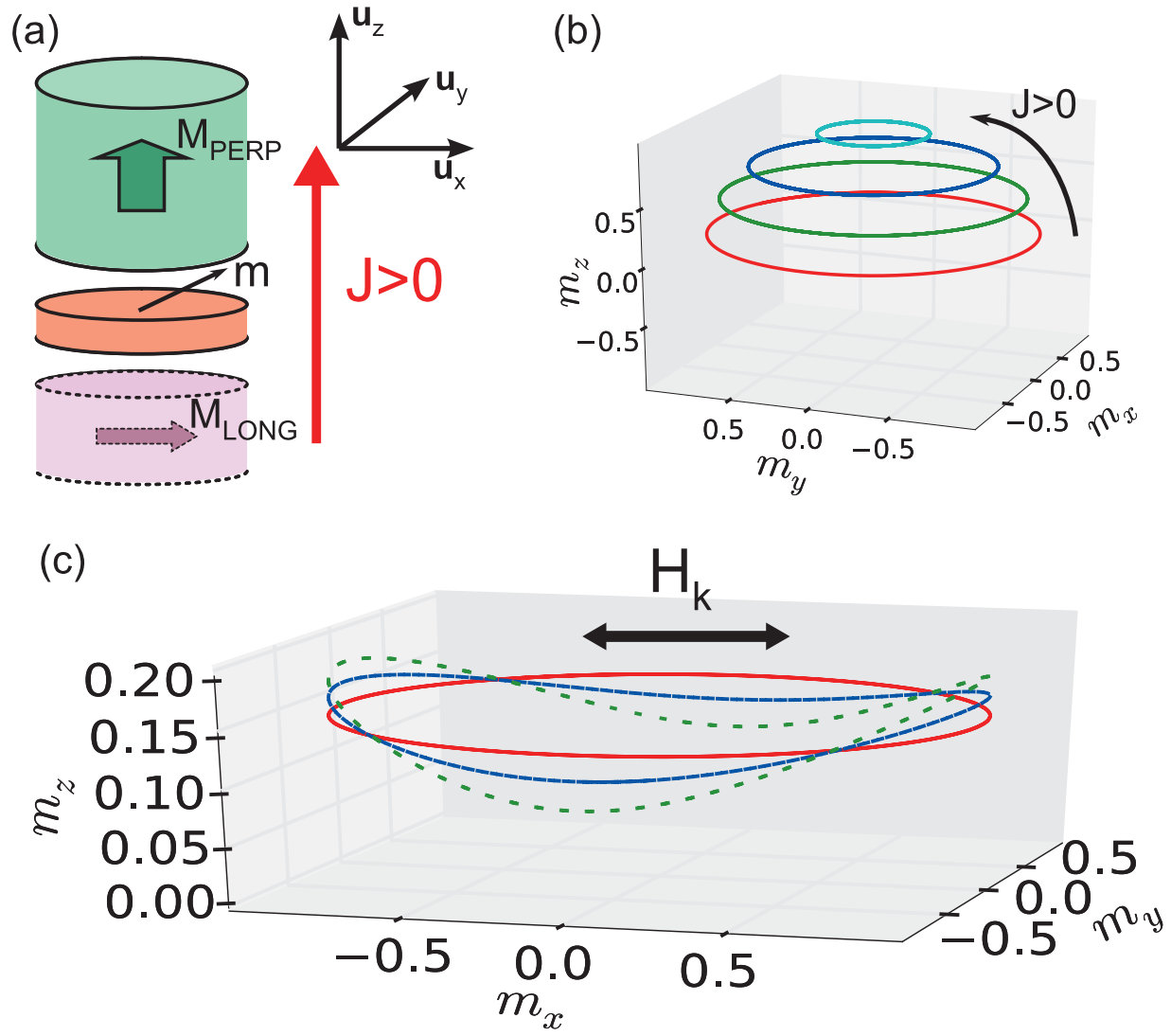

Figure 4.1 – (a) Schematics of the in-plane MTJ with a perpendicular polarizer. The spin torque from the reference layer is treated like a perturbation. (b) Unperturbed trajectory for different current densities J : 2, 6, 10 and 14 $\times 10^1 1$ A/m^2. (c) Perturbed trajectory for $J = 1.5e11$ A/m^2 and different anisotropy field H_k : 0, 24 and 48 kA/m.

The conservative and dissipative potentials defined above write in spherical coordinates :

$$\mathcal{H} = \mu_0 M_S V \Big(\frac{H_d}{2} \cos^2\theta - \frac{H_k}{2} \sin^2\theta \cos^2\phi - H_x \sin\theta\cos\phi - H_y \sin\theta\sin\phi - H_z\cos\theta + \frac{\alpha p_z}{\lambda_z} \ln(1+\lambda_z\cos\theta) - \frac{\alpha p_x}{\lambda_x} \ln(1+\lambda_x \sin\theta\cos\phi) \Big)$$

$$\Gamma = \mu_0 M_S V \Big(\frac{p_x}{\lambda_x} \ln(1 + \lambda_x \sin\theta\cos\phi) - \frac{p_z}{\lambda_z} \ln(1 + \lambda_z \cos\theta) + \alpha \frac{H_d}{2} \cos^2\theta - \alpha \frac{H_k}{2} \sin^2\theta \cos^2\phi - \alpha H_x \sin\theta\cos\phi - \alpha H_y \sin\theta\sin\phi - \alpha H_z \cos\theta \Big)$$

Here $p_x = \dfrac{\hbar}{2e} \dfrac{I\eta_x}{\mu_0 M_S V}$, $p_z = \dfrac{\hbar}{2e} \dfrac{I\eta_z}{\mu_0 M_S V}$ define spin torque "fields".

The demagnetizing energy is supposed, henceforth, to be the dominant term of the magnetic free energy. In fact, $H_d \gg H_k, H_a, p_x, p_z$ is assumed, which is generally the case for thin films in nanopillars. Therefore the dominant term of the conservative part $\mathcal{H}$ comes from the demagnetizing energy $\dfrac{H_d}{2}\cos^2\theta$. The dissipative term Γ is smaller compared to the conservative part, by a factor α, and it is dominated by the spin-torque $p_z\cos\theta/(1 + \lambda_z\cos\theta)$ and the damping of the demagnetizing field $\alpha\dfrac{H_d}{2}\cos^2\theta$. The uniaxial anisotropy field and the Zeeman field give smaller contributions. Therefore, the OPP trajectory of the free layer magnetization is dominated by the influence of the demagnetizing field and of the perpendicular polarizer spin torque.

As shown in Fig. 4.1.c, changing the anisotropy field, for instance, does not change much the magnetization trajectory. In fact, the trajectory of the dynamical system with a uniaxial anisotropy, an applied field or an analyzer spin-torque is very close to the trajectory with none of them. Hence it is reasonable to study first the simplest dynamical system describing a limit cycle, and then to treat the addition of other terms as perturbations around this limit cycle.

4.1.2 Unperturbed system

In a first attempt to describe the out-of-plane precession state of the free layer magnetization with a perpendicular polarizer, like in Chapter 2, only the demagnetization energy $\dfrac{H_d}{2}\cos^2\theta$ is considered in the total energy, and only the z-component of the spin-torque p_z in the particular case of a MTJ with $\lambda_z = 0$, is considered in the spin torque potential, so $P = p_z m_z$[Ebels 2008, Silva 2010]. Neglecting other terms, the trajectory is exactly circular (see Fig. 4.1(c)), and because they are the dominant terms, it is a good approximation of the complicated trajectory including all the terms. In this framework, the conservative and dissipative potentials have simple expressions :

$$\begin{cases} \mathcal{H} &= \mu_0 M_S V \left(\dfrac{H_d}{2}\cos^2\theta + \alpha p_z \cos\theta \right) \\ \Gamma &= \mu_0 M_S V \left(\alpha \dfrac{H_d}{2}\cos^2\theta - p_z \cos\theta \right) \end{cases}$$

The LLGS equation writes, with $\gamma_0 = \mu_0\gamma$:

$$\begin{cases} \dot\theta &= \alpha\gamma_0 H_d \cos\theta\sin\theta - \gamma_0 p_z \sin\theta \\ \dot\phi \ \sin\theta &= -\gamma_0 H_d \cos\theta\sin\theta - \alpha\gamma_0 p_z \sin\theta \end{cases} \tag{4.3}$$

Two characteristic quantities appear : $\omega_0 = \dfrac{\gamma_0 p_z}{\alpha}$ and $z_0 = \dfrac{p_z}{\alpha H_d}$

z_0 is the constant out-of-plane component of the magnetization in the OPP steady state, with a pulsation $\omega_0(1+\alpha^2)$. This is more obvious with the change of variables $z = \cos\theta$. Eq. 4.3 becomes :

$$\begin{cases} \dot{z} &= -\alpha\omega_0(1-z^2)(\frac{z}{z_0}-1) \\ \dot{\phi} &= -\omega_0(\frac{z}{z_0}+\alpha^2) \end{cases} \tag{4.4}$$

This equation can be solved explicitly for the variable z by separation of variables and using partial fraction decomposition :

$$\left|\frac{z-z_0}{z_i-z_0}\right| \left|\frac{(1+z)(1-z_i)}{(1-z)((1+z_i))}\right|^{z_0/2} \sqrt{\frac{1-z_i^2}{1-z^2}} = e^{-\beta_0\omega_0 t}$$

Here z_i and ϕ_i are the initial out-of-plane magnetization and in-plane phase. The initial time is taken to be zero. Let the relaxation parameter be $\beta_0 = \alpha(1-z_0^2)/z_0$, with the inverse relaxation time $\beta_0\omega_0 = \alpha H_d \gamma_0 (1-z_0^2)$ being always positive. As the left-hand side tends towards zero when time tends to infinity, the right-hand side must also tend towards zero. Except for the degenerate case of $z_i = \pm 1$, this condition means that $z \to z_0$ for long-term time. Therefore after a certain time the condition $|z - z_0| \ll 1$ will be fulfilled and an approximated equation for the out-of-plane magnetization z and the phase ϕ is derived :

$$\begin{aligned} z - z_0 &= (z_i - z_0)e^{-\beta_0\omega_0 t} \\ \phi - \phi_i &= -\omega_0(1+\alpha^2)t + \frac{z_i - z_0}{z_0\beta_0}\left(e^{-\beta_0\omega_0 t} - 1\right) \end{aligned} \tag{4.5}$$

Eq. 4.5 describes the unperturbed out-of-plane precession of the magnetization. In permanent regime the precession is characterized by a constant out-of-plane magnetization $m_z = z_0$ and a constant frequency f_0, which is proportional to the applied current I[Lee 2005] (see Fig. 4.1.b) :

$$f_0 = \frac{\omega_0(1+\alpha^2)}{2\pi} = \frac{\gamma\hbar\eta_z}{4\pi e\alpha M_S V} I \tag{4.6}$$

This trajectory is in fact an attractive limit-cycle of the dynamical system described by eq. 4.4, as it will be proven below. In general, the study of limit-cycle stability requires to define a Poincaré map but in the present case, where the geometrical space is 2-dimensional, one can directly extract the eigenvalue of the linearized Poincaré map, also known as multiplier, μ_1 :

$$\mu_1 = \exp\left\{\int_0^T \operatorname{div} \boldsymbol{F}(\boldsymbol{x}_0(t))dt\right\} \tag{4.7}$$

Where T is the period of the limit-cycle, $\boldsymbol{F}(x)$ is the vector field of the dynamical system $\dot{\boldsymbol{x}} = \boldsymbol{F}(\boldsymbol{x})$ and $\boldsymbol{x}_0(t)$ is a parametrization of the limit-cycle. Expressed in spherical coordinates,

eq. 4.7 can be simplified with the expression of the vector field taken from the left-hand side of eq. 4.2 :

$$\mu_1 = \exp\left\{ -\frac{\gamma}{M_S V}\int_0^T \Big(\Delta_R \Gamma(\boldsymbol{x}_0(t))\Big)dt \right\}$$

Where $\Delta_R\Gamma$ is the Laplacian in spherical coordinates of Γ, expressed by :

$$\Delta_R\Gamma = \cot\theta\,\Gamma_\theta + \Gamma_{\theta\theta} + \frac{\Gamma_{\phi\phi}}{\sin^2\theta}$$

Notice that only the dissipative term participates to the stability of the limit-cycle. In the simplified case of eq. 4.4, the time-parametrized spherical equation of the limit-cycle is $\boldsymbol{x}_0(t) = (\theta_0, -\omega_0(1+\alpha^2)t)$ ($z_0 = \cos\theta_0$). The expression of div $\boldsymbol{F}$ is then $-\gamma_0 p_z \frac{1+2z_0\cos\theta - 3\cos^2\theta}{z_0}$ and the period $T = 1/f_0 = \dfrac{2\pi}{\omega_0(1+\alpha^2)}$. The multiplier of the Poincaré map is then $\mu_1 = \exp\left\{-\dfrac{2\pi\beta_0}{1+\alpha^2}\right\}$. The multiplier is the relaxation rate towards the limit cycle from a state slightly deviated, for instance by thermal fluctuations[Silva 2010]. Because μ_1 is less than unity in absolute value, the limit-cycle is hyperbolically stable.

4.1.3 High-symmetry system

In addition to the previous simple case, some terms that present the same symmetry as the unperturbed equation may be added, like treated in previous papers [Ebels 2008, Silva 2010]. It means that only the terms independent of the in-plane angle ϕ are considered : the spin-torque amplitude is angle dependent ($\lambda_z \neq 0$) and there is an out-of-plane applied field H_z. The out-of-plane applied field can describe the stray field created by the perpendicular polarizer, or an external applied field. Eq. 4.2 is then :

$$\begin{cases} \dot{\theta} &= \alpha\gamma_0 H_d \cos\theta\sin\theta - \dfrac{\gamma_0 p_z \sin\theta}{1+\lambda_z\cos\theta} - \alpha\gamma_0 H_z \sin\theta \\ \dot{\phi}\ \sin\theta &= -\gamma_0 H_d \cos\theta\sin\theta - \dfrac{\alpha\gamma_0 p_z \sin\theta}{1+\lambda_z\cos\theta} + \gamma_0 H_z \sin\theta \end{cases} \tag{4.8}$$

As for the unperturbed system, the vector field is only θ-dependent, hence the system can be solved analytically. As at least one limit-cycle is expected to arise from the equations, we directly look for the permanent regime solution, with a constant angle θ. By changing the variables $z = \cos\theta$ and using the parameters ω_0, z_0 and $\nu_z = \gamma_0 H_z/\omega_0$, one can directly find the (non-trivial) solutions (z_+, z_-) of $\dot{z} = 0$:

$$z_\pm = -\frac{1-\lambda_z z_0 \nu_z}{2\lambda_z} \pm \frac{1}{2\lambda_z}\sqrt{(1+\lambda_z z_0\nu_z)^2 + 4\lambda_z z_0}$$

The positive solution z_+ tends toward z_0 when the parameters λ_z and ν_z tend toward zero: it is the perturbed solution. As only solutions with a small out-of-plane magnetization z are

considered for application in precessional switching, only the z_+ solution is interesting here. Notice that z_- does not always exist (if $|z_-|> 1$ for instance), and when it does, it does not always describe an attractive limit-cycle. With the constant out-of-plane magnetization z_+, the frequency of the precession is also changed compared to the unperturbed frequency $f_0 = \omega_0(1+\alpha^2)/(2\pi)$:

$$f = \frac{f_0}{1+\lambda_z z_+}$$

For a small λ_z parameter, the Taylor expansion gives an approximative frequency : $f = f_0[1 - \lambda_z z_0(1+\nu_z)]$. See Fig. 4.2 for comparison of the analytical expression of the frequency with $\lambda \neq 0$ and numerical simulations.

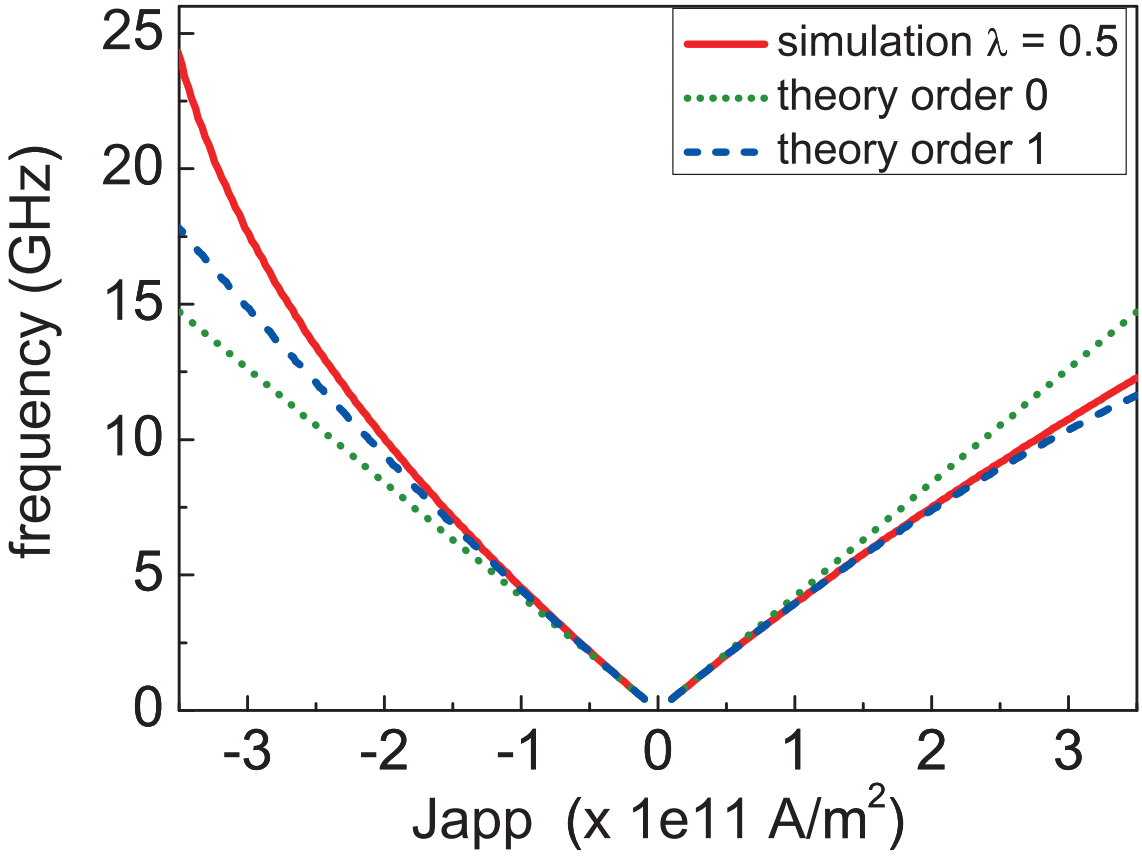

Figure 4.2 – Oscillation frequency versus applied current density J. Comparison between macrospin simulation with $\lambda_z = 0.5$ (red full-line) and analytical expressions at order 0 in λ_z (green dotted-line) and order 1 (blue dashed-line). The other simulation parameters are : $\alpha = 0.02$, $M_S = 1.2e6\,\mathrm{A/m}$, $\eta_{\mathrm{PERP}} = 0.6$, $t = 3\,\mathrm{nm}$ and $H_z = 0$.

The high-symmetry system is not of real interest for applications in precessional switching, as an important parameter is omitted, the uniaxial anisotropy. However, since the approximation

at order 1 for the spin polarization asymmetry is close to the exact solution, this gives credit to this approach and encourages the investigation of other additional perturbative terms.

The stability of the out-of-plane precession state (OPP) is insured by the condition $\mu_1 < 1$. It also means that if LLGS eq. 4.3 is slightly modified, for instance by adding the term associated with a uniaxial anisotropy, the OPP state will remain a limit-cycle, for small enough perturbations[Silva 2010]. In the following section, we will start from eq. 4.3, henceforth called the unperturbed case, and study the general case with the general assumption that the solutions are very close to the unperturbed case. The unperturbed dynamical system will be modified by perturbations, namely uniaxial anisotropy field, applied field and longitudinal polarizer.

4.2 Perturbation theory : Lindstedt's series

4.2.1 Uniaxial anisotropy

Compared to the previous case, including the uniaxial anisotropy term in eq. 4.2 makes the vector field not only θ-dependent but also ϕ-dependent. Exact analytical solutions are then much more difficult to obtain, so a perturbative approach is used to approximate the solution [Bertotti 2001], using a Lindstedt's expansion[Murdock 1991]. When a periodic dynamical system is perturbed, the perturbated solution will also be periodic, by continuity. The perturbated solution is approximated by a generalized asymptotic expansion that preserves the periodicity of the solution, the Lindstedt's series, for which the frequency is also expanded with respect to the perturbation parameter ϵ. The only assumption on the perturbation parameter is that it is small compared to the non-perturbated frequency, hence the equations are normalized to the frequency. Thus, the approximation's error is of order $\mathrm{O}(\epsilon)$ on a time-scale of $\mathrm{O}(1/\epsilon)$, which is sufficient if the functions are periodic with a normalized period of 1.

On top of the uniaxial anisotropy perturbation, all the following cases will also be solved using this approach. From the unperturbed equation 4.3, the uniaxial anisotropy term is added :

$$\begin{cases} \dot{\theta} &= \gamma_0\Big(\alpha H_d \cos\theta\sin\theta - p_z\sin\theta - \frac{H_k}{2}\sin\theta\sin(2\phi) + \alpha\frac{H_k}{2}\sin\theta\cos\theta\Big(1+\cos(2\phi)\Big)\Big) \\ \dot{\phi}\ \sin\theta &= \gamma_0\Big(- H_d\cos\theta\sin\theta - \alpha\frac{H_k}{2}\sin\theta\sin(2\phi) - \alpha p_z\sin\theta - \frac{H_k}{2}\sin\theta\cos\theta\Big(1+\cos(2\phi)\Big)\Big) \end{cases} \tag{4.9}$$

The characteristic quantities ω_0 and z_0 are used again. The perturbation parameter ϵ is defined below. For clarity, the time variable is also changed to τ :

$$\epsilon = \frac{H_k}{\omega_0(1+\alpha^2)} = \frac{\alpha}{1+\alpha^2}\frac{H_k}{2p_z}$$

$$\tau = \omega_0(1+\alpha^2)t$$

The time derivative $\dot{X}$ is also changed to X', which means a derivative with respect to τ.

Let $r_0 = \sqrt{1-z_0^2}$ and $\beta = \alpha r_0^2/(z_0(1+\alpha^2))$ be the norm of the in-plane projection of the magnetization and the relaxation parameter, respectively. As $\alpha \ll 1$, the parameter β is very close to β_0 previously defined. For commodity, the following functions are introduced :

$$\begin{aligned} g_\theta(\theta) &= \frac{\alpha}{1+\alpha^2}\sin\theta\left(\frac{\cos\theta}{z_0}-1\right) \\ h_\phi(\theta) &= -\frac{\cos\theta + z_0\alpha^2}{z_0(1+\alpha^2)}\sin\theta \end{aligned} \tag{4.10}$$

Two perturbation functions are also introduced, which in the case of the uniaxial anisotropy, write :

$$\begin{aligned} f_\theta^\epsilon(\theta,\phi) &= -\sin\theta\sin(2\phi) + \alpha\sin\theta\cos\theta\Big(1+\cos(2\phi)\Big) \\ f_\phi^\epsilon(\theta,\phi) &= -\sin\theta\cos\theta\Big(1+\cos(2\phi)\Big) - \alpha\sin\theta\sin(2\phi) \end{aligned} \tag{4.11}$$

Hence equation 4.9 takes the simplified form :

$$\begin{cases} \theta' &= g_\theta(\theta) + \epsilon f_\theta^\epsilon(\theta,\phi) \\ \phi'\sin\theta &= h_\phi(\theta) + \epsilon f_\phi^\epsilon(\theta,\phi) \end{cases} \tag{4.12}$$

To solve this sytem, the following assumptions are made : (i) $\epsilon \ll 1$, the perturbation is smaller than the oscillation frequency, (ii) the functions $\theta(\tau)$ and $\phi(\tau)$, solutions of eq. 4.12, are written as a power series of the parameter ϵ. In the framework of the Lindstedt's series, it is assumed that the period of the limit-cycle can be written as a power series of ϵ, to get rid of the secular terms.

If the time variable is changed to $\tau' = \omega\tau$, the frequency and angles of the OPP, ω, θ and ϕ, will be written (up to the second order) as :

$$\begin{cases} \theta = \theta_0 + \epsilon\theta_1 + \epsilon^2\theta_2 + \dots \\ \phi = \phi_0 + \epsilon\phi_1 + \epsilon^2\phi_2 + \dots \\ \omega = 1 + \epsilon f_1 + \epsilon^2 f_2 + \dots \end{cases}$$

The development of the calculations is made in Appendix 4.5. For the uniaxial anisotropy, the trajectory of the perturbed OPP is defined up to first order by :

$$\theta_0(\tau') = \arccos(z_0) \qquad \phi_0(\tau') = -\tau' \tag{4.13}$$

$$\begin{aligned} \theta_1(\tau') &= a_0 + a_2\cos(2\tau') + b_2\sin(2\tau') \\ \phi_1(\tau') &= c_2\cos(2\tau') + d_2\sin(2\tau') \end{aligned} \tag{4.14}$$

$$\text{with} \quad \begin{cases} a_0 = (1+\alpha^2) z_0^2 / r_0 \\ a_2 = \dfrac{r_0}{4+\beta^2}(\alpha\beta z_0 - 2) \\ b_2 = \dfrac{r_0}{4+\beta^2}(2\alpha z_0 + \beta) \\ c_2 = -\dfrac{(1+\alpha^2)\beta^2/2 + \alpha\beta z_0 + 2\alpha^2}{\alpha(4+\beta^2)} \\ d_2 = -\dfrac{2\alpha z_0 + \beta}{\alpha(4+\beta^2)} \end{cases}$$

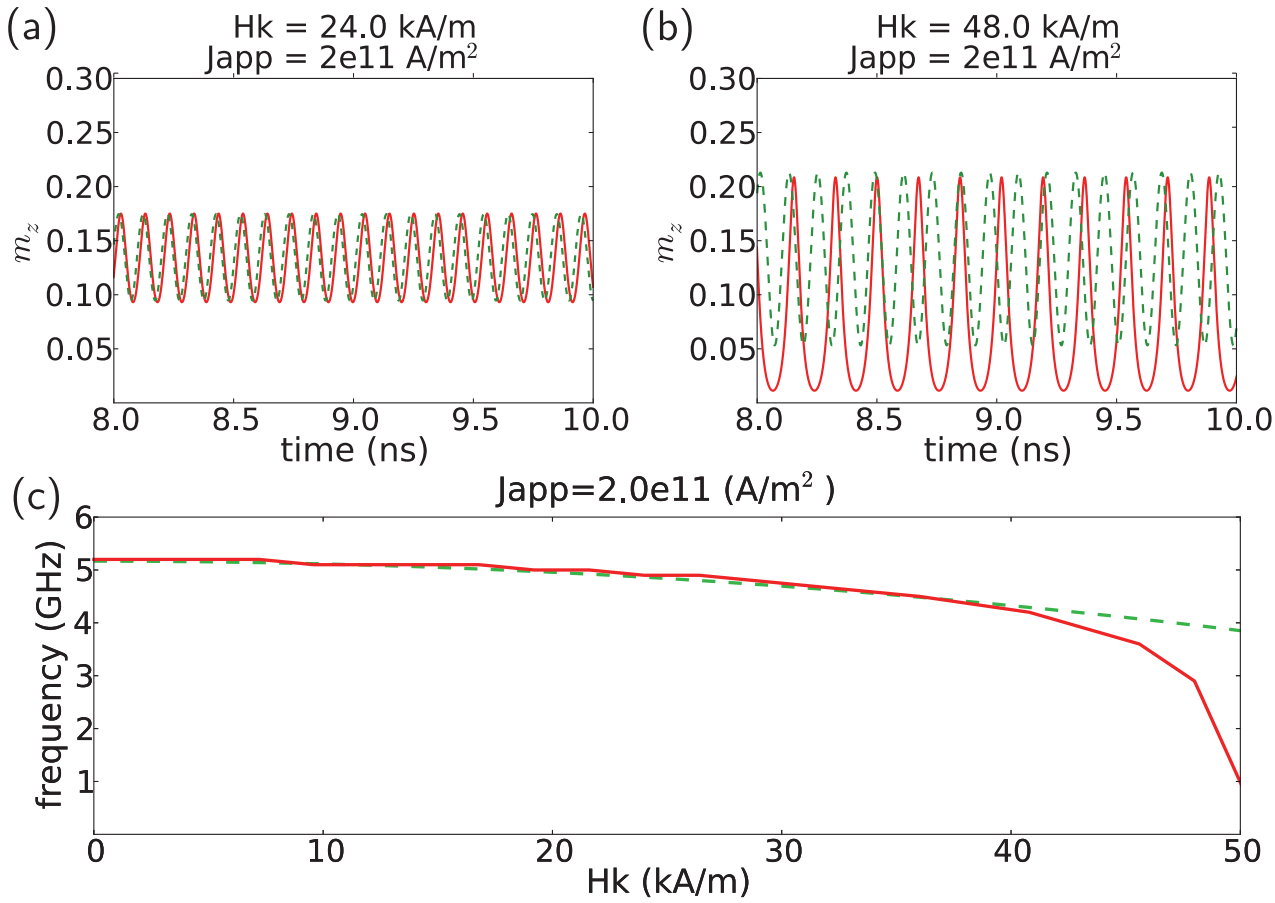

Figure 4.3 – Macrospin simulation (red full-line) and analytical expression at first order in ϵ (green dashed-line). **(a-b)** Out-of plane component of the magnetization m_z versus time, with applied current density of $J_{app} = 2\text{e}11\ \text{A/m}^2$ and with **(a)** $H_k = 24\,\text{kA/m}$ and **(b)** $H_k = 48\,\text{kA/m}$. **(c)** Frequency of the in-plane component m_x versus anisotropy field H_k with applied current density of $J_{app} = 2\text{e}11\ \text{A/m}^2$. The other used parameters are given in the text.

The frequency f of the periodic orbit is changed only at the second order in the parameter

ϵ :

$$f_1 = 0 \qquad f_2 \approx -\frac{1+4z_0^2}{8z_0^2+2\alpha^2} \tag{4.15}$$

With the expression of the unperturbed frequency f_0 found in eq.4.6, the perturbed frequency writes :

$$f = f_0\Big(1-\epsilon^2\frac{1+4z_0^2}{8z_0^2+2\alpha^2}\Big) \tag{4.16}$$

These analytical expressions were compared to the results of 10 ns-long macrospin simulations. For the simulations, $\alpha = 0.02$, $M_S = H_d = 1.2e6$ A/m, $t = 3e-9\,nm$ and $\eta_{\text{PERP}} = 0.2$. Fig. 4.3 (a-b) shows the out-of-plane component of the free layer magnetization m_z in the permanent regime (8 ns after the application of the current pulse) for an applied current density of $J_{\text{app}} = 2e11$ A/m^2. The macrospin simulations in red full-line are compared with the analytical expression at first order in ϵ, in green dashed-line. In Fig. 4.3 (a), for $H_k = 24$ kA/m, corresponding to $\epsilon = 0.05$, the analytical expression is very similar to the macrospin simulations. The phase shift with the simulation is due to the transient regime that is not taken into account in the analytical expression. However in Fig. 4.3 (b), for $H_k = 48$ kA/m, and so $\epsilon = 0.1$, the trajectory from the macrospin simulation is not exactly sinusoidal and it cannot be described by the first order approximation only. As seen also in Fig. (c), for larger value of the perturbation H_k, the frequency change is not well described by the second order approximation anymore. Notice that the anisotropy induces a perturbation of twice the natural frequency because of the symmetry of the anisotropy term. The applied field and analyzer spin-torque induce a perturbation at the natural frequency.

The trajectory of the magnetization is very close to the trajectory of the unperturbed system, as shown in Fig. 4.1.c. It validates the use of a perturbation expansion. The perturbed trajectory has a larger out-of-plane component m_z close to the easy-axis $\pm\boldsymbol{u}_x$ directions, and m_z is smaller close to the hard-axis directions $\pm\boldsymbol{u}_y$. It appears that the magnetization speed is proportional to the out-of-plane component m_z, like the frequency of the unperturbated trajectory is proportional to m_z. Therefore, the magnetization spends more time along the hard $\boldsymbol{u}_y$ axis than along the easy $\boldsymbol{u}_x$ axis.

The magnetoresistive signal that can be measured with an in-plane analyzer depends on $m_x = \sin\theta\cos\phi$. Therefore, the signal has a fundamental frequency and higher order harmonics, of which the amplitude can be estimated :

$$\begin{aligned} m_x &= \sin(\theta_0+\epsilon\theta_1)\cos(-\tau+\epsilon\phi_1) \\ m_x &\approx r_0\cos\tau + \epsilon\Big(z_0\theta_1\cos\tau + r_0\phi_1\sin\tau\Big) \end{aligned}$$

Because θ_1 and ϕ_1 oscillate at twice the fundamental frequency, the second harmonic vanishes.

4.2.2 Applied field

We next discuss the perturbative effect of the applied field along the easy axis H_x and along the in-plane hard axis H_y. They are treated in the same section because they yield similar results. However the respective perturbative developments were done separately.

Let the dimensionless variables be introduced :

$$\nu_x = \frac{\alpha}{1+\alpha^2}\frac{H_x}{p_z} \qquad \nu_y = \frac{\alpha}{1+\alpha^2}\frac{H_y}{p_z}$$

The perturbation functions on the angles θ and ϕ are respectively :

$$\begin{aligned} f_\theta^{\nu_x}(\theta,\phi) &= \alpha\cos\theta\cos\phi - \sin\phi \\ f_\phi^{\nu_x}(\theta,\phi) &= -\alpha\sin\phi - \cos\theta\cos\phi \\ \\ f_\theta^{\nu_y}(\theta,\phi) &= \alpha\cos\theta\sin\phi + \cos\phi \\ f_\phi^{\nu_y}(\theta,\phi) &= \alpha\cos\phi - \cos\theta\sin\phi \end{aligned} \tag{4.17}$$

After solving the system up to second order, the expressions of the perturbed frequencies and the perturbed trajectories for the two directions of the applied field are found to be :

$$\text{In both cases :} \quad f_1 = 0 \qquad f_2 = -\frac{(1+\alpha^2)^2}{2z_0^2+2\alpha^2} \tag{4.18}$$

$$\begin{aligned} \theta_1^i(\tau') &= a_1^i\cos\tau' + b_1^i\sin\tau' \\ \phi_1^i(\tau') &= c_1^i\cos\tau' + d_1^i\sin\tau' \end{aligned} \tag{4.19}$$

$$\begin{cases} a_1^x = -\dfrac{1-\alpha\beta z_0}{1+\beta^2} \\ b_1^x = \dfrac{\beta+\alpha z_0}{1+\beta^2} \\ c_1^x = -\dfrac{\alpha\beta z_0 + \beta^2(1+\alpha^2)+\alpha^2}{\alpha r_0(1+\beta^2)} \\ d_1^x = -\dfrac{\beta+\alpha z_0}{\alpha r_0(1+\beta^2)} \end{cases} \qquad \begin{cases} a_1^y = \dfrac{\beta+\alpha z_0}{1+\beta^2} \\ b_1^y = \dfrac{1-\alpha\beta z_0}{1+\beta^2} \\ c_1^y = -\dfrac{\beta+\alpha z_0}{\alpha r_0(1+\beta^2)} \\ d_1^y = \dfrac{\alpha\beta z_0 + \beta^2(1+\alpha^2)+\alpha^2}{\alpha r_0(1+\beta^2)} \end{cases}$$

Fig. 4.4 shows the comparison with macrospin simulations using the same numerical values as previously, except that $J_{\text{app}} = 3.1e11$ A/m^2 and with an in-plane applied field along $\boldsymbol{u}_x$. Fig. 4.4 (a) and 4.4 (b) represent the out-of-plane component of the magnetization m_z after the transitory regime, for $H_x = 10$ kA/m ($\nu_x = 0.044$) and $H_x = 20$ kA/m ($\nu_x = 0.088$) respectively. In both cases the analytical expression is in good agreement with the simulations. The frequency versus applied field, on Fig. 4.4(c), shows also a good agreement between the simulations and the approximation at second order in ν_x up to $H_x = 20$ kA/m.

Concerning the harmonics of the magnetoresistive signal, the second harmonic has a non-vanishing amplitude, using the formula of the previous section. Here, the applied current density is assumed to be large enough so that $\beta \ll 1$, and small enough so that $z_0^2 \ll 1$. For $i = (x, y)$ the two directions of the in-plane applied field :

$$m_x = r_0\cos\tau + \frac{\nu_i}{2}\Big((z_0a_1^i - r_0d_1^i)\cos(2\tau) + (z_0b_1^i + r_0c_1^i)\sin(2\tau)\Big)$$

Let ψ be a constant phase. The in-plane component m_x is approximately given by :

$$m_x \approx r_0\cos\tau + \frac{\nu_i}{2z_0}\cos(2\tau+\psi)$$

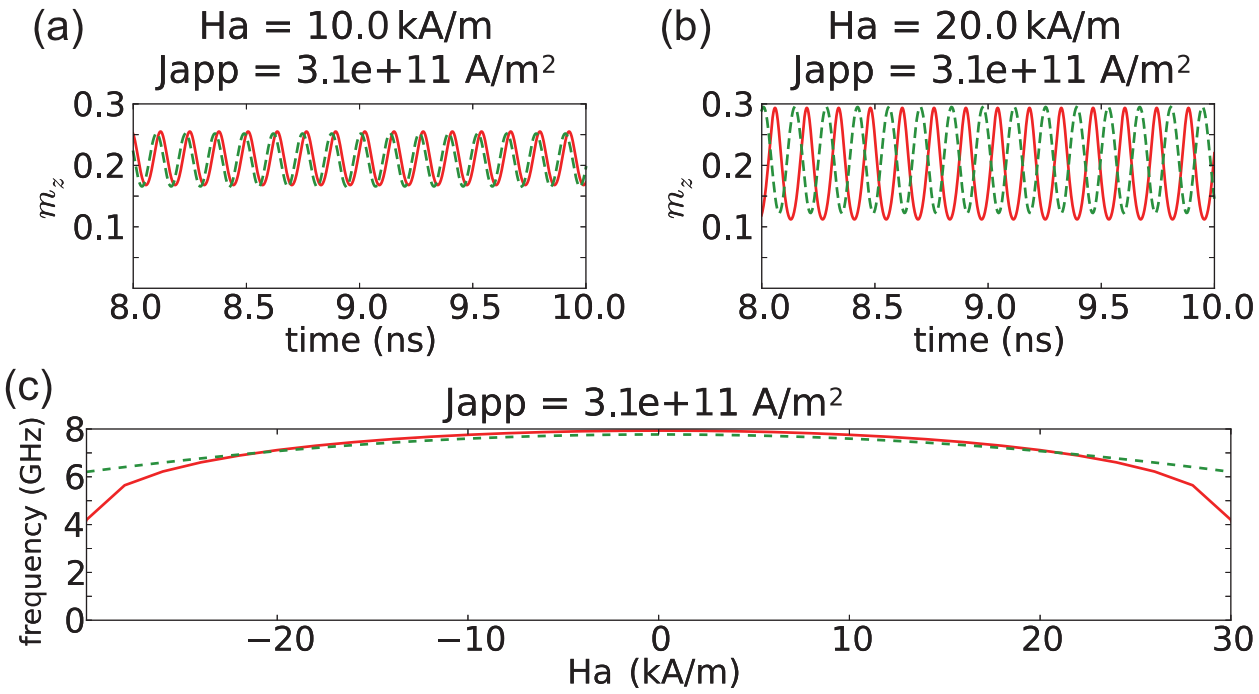

Figure 4.4 – Macrospin simulation (red full-line) and analytical expression at first order in ν_x (green dashed-line). **(a-b)** Out-of plane component of the magnetization m_z versus time, with applied current density of $J_{app} = 3.1\text{e}11$ A/m^2 and with applied field **(a)** $H_x = 10$ kA/m and **(b)** $H_x = 20$ kA/m. **(c)** Frequency of the in-plane component m_x versus applied field H_x with applied current density of $J_{app} = 3.1\text{e}11$ A/m^2.

4.2.3 Spin torque from the reference layer

In this section, we focus on the perturbation due to the spin torque of the longitudinal polarizer, initially with $\lambda_x = 0$. Let the perturbation parameter be :

$$\xi = \frac{\alpha}{1+\alpha^2}\frac{p_x}{p_z}$$

The associated perturbation functions are given by :

$$\begin{aligned} f^{\xi}_{\theta}(\theta,\phi) &= -\cos\theta\cos\phi - \alpha\sin\phi \\ f^{\xi}_{\phi}(\theta,\phi) &= +\sin\phi - \alpha\cos\theta\cos\phi \end{aligned} \tag{4.20}$$

In experiments, the reference layer is most often separated from the free layer by a tunnel barrier, whereas the perpendicular polarizer is separated by a metallic barrier[Liu 2010, Marins de Castro 2012]. This choice is made in order to maximize the amplitude of the output TMR signal. Consequently the ratio $r = p_x/p_z$ is greater than unity. The variable ξ can only be treated as a perturbation because of the α coefficient. Therefore the effect of the longitudinal

polarizer on the OPP state is stronger than for other contributions. The solutions are given by :

$$f_1 = 0 \qquad f_2 = \frac{(1+\alpha^2)^2 z_0^2}{2(1+\alpha^2 z_0^2)} \tag{4.21}$$

$$\begin{aligned} \theta_1(\tau') &= a_1 \cos\tau' + b_1 \sin\tau' \\ \phi_1(\tau') &= c_1 \cos\tau' + d_1 \sin\tau' \end{aligned} \tag{4.22}$$

$$\begin{cases} a_1 = -\dfrac{\alpha+\beta z_0}{1+\beta^2} \\ b_1 = \dfrac{\alpha\beta - z_0}{1+\beta^2} \\ c_1 = \dfrac{\alpha+\beta z_0}{\alpha r_0(1+\beta^2)} \\ d_1 = -\dfrac{\alpha\beta + \alpha^2 z_0 + z_0\beta^2(1+\alpha^2)}{\alpha r_0(1+\beta^2)} \end{cases}$$

The comparison with macrospin simulations with $J_{\text{app}} = 1e11$ A/m^2 is shown in Fig. 4.5. The analyser spin polarization η_{LONG} is to $\eta_{\text{LONG}} = r \times \eta_{\text{PERP}} = 0.2r$, where r is the ratio p_x/p_z that varies from 0 to 80 in the simulations. This should give values of η_{LONG} larger than 1 that are unphysical, but they correspond to physical situations by rescaling the applied current density. Hence the absolute value of η_{LONG} is not so important, and only r matters. Fig. 4.5 (a) and Fig. 4.5 (b) show m_z versus time for $r = 10$ ($\xi = 0.2$) and $r = 20$ ($\xi = 0.4$) respectively. For $r = 10$, the analytical expression is offset compared to the simulations, showing that there must be a constant term arising from the second order development that is not taken into account here. For $r = 20$, the simulated m_z is not sinusoidal, giving rise to a frequency mismatch with the first order analytical expression. The frequency change versus ratio r shown in Fig. 4.5 (c) shows that it is at least a third order perturbation, as second order frequency change cannot explain the frequency drop for large r.

Because the perturbation in first order has a frequency that is the fundamental frequency, like for the applied field, the second harmonic amplitude is non-zero :

$$m_x \approx r_0 \cos\tau + 2\xi \cos(2\tau + \psi')$$

Here, $\beta \ll 1$ and $z_0^2 \ll 1$ were assumed and ψ' is a constant phase.

4.2.4 Interplay of two contributions

The power series expansion was only carried up to second order, because of the difficulty of developing further the analytical solutions and also because second-order is sufficient regarding the negligible size of other terms. So far only one contribution was considered at a time, but if two contributions are considered simultaneously, the perturbed expressions change. In first order, the influence of the different contributions can be added directly to determine the

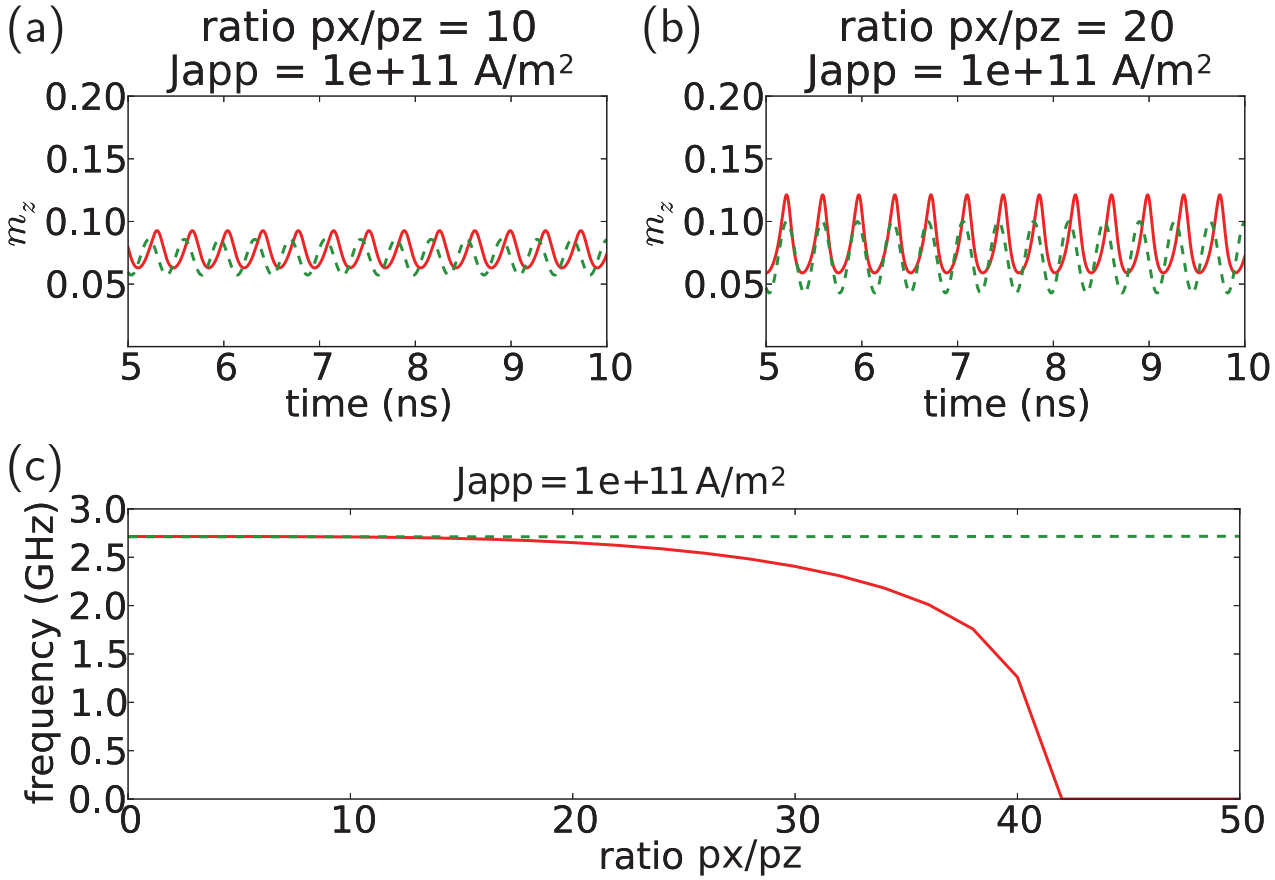

Figure 4.5 – Macrospin simulation (red full-line) and analytical expression at first order in ξ (green dashed-line). **(a-b)** Out-of plane component of the magnetization m_z versus time, with applied current density of $J_{app} = 1\text{e}11$ A/m^2 and with a ratio $r = p_x/p_z$ **(a)** $r = 10$ and **(b)** $r = 20$. **(c)** Frequency of the in-plane component m_x versus ratio p_x/p_z with applied current density of $J_{app} = 1\text{e}11$ A/m^2.

analytical expression for the angle θ and ϕ, there is no interaction between the contributions. However, at second order, the different contributions do not simply add together; there is also an additional term of interaction. Sometimes the interaction term vanishes, for instance with the uniaxial anisotropy combined with the longitudinal spin-torque or the applied field. However if the longitudinal spin torque p_x and the applied field H_x (similar for H_y) are taken into account, an interaction term is added to the perturbed frequency.

We perform an expansion by setting $\varsigma = \dfrac{H_x}{p_x}$ and expanding with respect to ξ. The frequency correction is given by the term coming from H_x alone multiplied by ν_x^2, the term coming from p_x alone multiplied by ξ^2, plus the interaction term, multiplied by $\xi\nu_x$:

$$f_2 = -\frac{(1+\alpha^2)^3 z_0^2}{\alpha(1+\alpha^2 z_0^2)(\alpha^2+z_0^2)}$$

We can also treat the case of an angle dependant spin torque amplitude with uniaxial anisotropy. First, p_z is replaced by $p_z/(1+\lambda_z\cos\theta)$, and λ_z is treated as a perturbative parameter. Without any other perturbation, the variation of the frequency was derived exactly in the high-symmetry case, $f = f_0/(1+\lambda_z z_+)$, and its Taylor expansion versus λ_z corresponds to the terms derived by the technique used here. However there is an interaction with the uniaxial anisotropy term at the second order. On top of the uniaxial anisotropy term only, and the spin-torque assymetry term, $2\lambda_z^2 z_0^2$, there is an interaction term multiplied by $\lambda_z\epsilon$:

$$f_2 = z_0^2(1+\alpha^2)$$

Finally, we study the case of an angle-dependent spin-torque along the x-axis. There is an interaction between the angle-independant term p_x and the assymetry parameter λ_x. For this, the full expression $\dfrac{p_x\sin\theta\cos\phi}{1+\lambda_x\sin\theta\cos\phi}$ is Taylor expanded with respect to the parameter λ_x. The perturbation approximation is then computed by expanding with the parameter ξ, and with λ_x if necessary. The frequency change is given by the term on ξ only, plus a first order and a second order term depending on λ_x also :

$$f \approx f_0\left[1+\xi\lambda_x\frac{z_0}{2\alpha}(1+\alpha^2)+\xi^2\lambda_x^2\frac{z_0^2}{4\alpha^2}(1+\alpha^2)^2+\xi^2\frac{(1+\alpha^2)^2z_0^2}{2(1+\alpha^2z_0^2)}\right]$$

4.3 Critical currents

4.3.1 Stability criterion

The expressions of the OPP trajectory with perturbation up to first order define a stability criterion for these trajectories. Regarding the Poincaré's map multiplier for the trajectories up to first order, $|\mu_1|<1$ for all the perturbations treated in this paper, regardless of the amplitude of the perturbation. It means that the corrected trajectories are stable to sufficiently small thermal fluctuations. However the multiplier does not give any information on the maximum amplitude of the perturbations until which the out-of-plane precession is maintained.

For this, the Melnikov function is used[Ebels 2008][Bazaliy 2007]. This function can be extracted from the equation of motion 4.2. By operating the scalar product of this equation with $\mathbf{\Omega_1}\mathrm{d}\tilde{\mathrm{R}}$, with $\mathrm{d}\tilde{\mathrm{R}} = (\mathrm{d}\theta, \sin\theta\mathrm{d}\phi)^\intercal$, then :

$$\mathrm{d}\tilde{\mathrm{R}}\cdot(\partial_{\tilde{\mathrm{R}}}\mathcal{H}+\Omega_1\partial_{\tilde{\mathrm{R}}}\Gamma)=0$$

If the trajectory $\mathcal{C}_0$ of the system is periodic, the closed integral of the conservative part of the previous expression vanishes, namely :

$$\oint_{\mathcal{C}_0}\partial_{\tilde{\boldsymbol{R}}}\mathcal{H}\cdot\mathrm{d}\tilde{\mathrm{R}}=0$$

Only the second part of the expression remains, $\oint \partial_{\tilde{\boldsymbol{R}}} (\boldsymbol{\Omega}_1 \Gamma) \cdot \mathrm{d}\tilde{\mathrm{R}} = 0$. The previous integral relation is true only along the exact periodic trajectory $\mathcal{C}_0$. Using the expression of $\mathrm{d}\tilde{\mathrm{R}}$ from the equation of motion, the Melnikov function is introduced for an arbitrary path $\mathcal{C}$[1] :

$$\mathcal{M}(\mathcal{C}) = \oint_{\mathcal{C}} \partial_{\tilde{\boldsymbol{R}}} \mathcal{H} \cdot \partial_{\tilde{\boldsymbol{R}}} \Gamma \, \mathrm{dt} \tag{4.23}$$

If the path $\mathcal{C}$ follows a the periodic orbit solution of the equation of motion, then the Melnikov function vanishes. In the framework of weakly perturbed time periodic Hamiltonian systems, the Melnikov function is assumed to vanish (in first order) if the closed loop integral is taken over the trajectory $\tilde{\mathcal{C}}$ of the unperturbed system ($\Gamma = 0$) with constant energy w. The condition that the Melnikov function must vanish for the trajectory of constant energy gives a constraint on the parameters of the system, namely on the applied current I.

The issue of calculating the critical parameters until which the periodic orbit is maintained has already been addressed by Ebels et al.[Ebels 2008] in the case of a free layer with a perpendicular polarizer and an applied field along the easy axis (x-axis). They use a similar technique, of zeroing the Melnikov function, to obtain the critical current I_{c4} below which no periodic orbit is possible. They extracted numerical data for the critical current Is_{c4} with respect to the applied field, the anisotropy field H_k (named H_u in ref.[Ebels 2008]), the saturation magnetisation M_S (equal to the demagnetizing field in $\mathcal{C}_0$) and the damping constant α. Unfortunately no analytical expression was found.

Critical currents for stability of the periodic out-of-plane precession can also be approximated using the expressions computed in the previous section. Using the expressions of the angles θ and ϕ at first order in the perturbation parameter, one can check that the in-plane angle variation $\dot{\phi}$ never vanishes. Otherwise, the precessional motion would be stopped.

Using this criterion, critical spin torque amplitudes were computed, with only one perturbation at a time. The critical currents I_{c4} are proportional to the critical spin-torque amplitudes p_{z_c}. The critical spin torque amplitudes are given beneath for the different perturbation cases, respectively, uniaxial anisotropy, in-plane applied field (there is no distinction between H_x and H_y direction, so H_a is used, pointing in any arbitrary in-plane direction) and spin torque from the longitudinal polarizer. Here, the case $\alpha^2 \ll (H_a/H_d, H_k/H_d)$ is considered, which is realistic approximation in experiments, so that $\beta \ll 1$ and the expression are simplified.
For the uniaxial anisotropy and the applied field, the out-of-plane precessional state is allowed as long as $p_z > p_{z_c}$. For these two perturbations the stability criterion defines a minimal spin torque amplitude for the existence of the precessional state :

$$\text{anisotropy :} \quad p_{z_c} = \frac{\alpha}{2}\sqrt{H_k H_d} \tag{4.24}$$

$$\text{in-plane applied field :} \quad p_{z_c} = \alpha\sqrt{H_a H_d} \tag{4.25}$$

[1] In Cartesian coordinates, the Melnikov function writes $\mathcal{M}(\mathcal{C}) = \oint_{\mathcal{C}} (\nabla_{\boldsymbol{m}}\mathcal{H} \cdot \nabla_{\boldsymbol{m}}\mathcal{G} - (\boldsymbol{m} \cdot \nabla_{\boldsymbol{m}}\mathcal{H})(\boldsymbol{m} \cdot \nabla_{\boldsymbol{m}}\mathcal{G})) \, \mathrm{dt}$

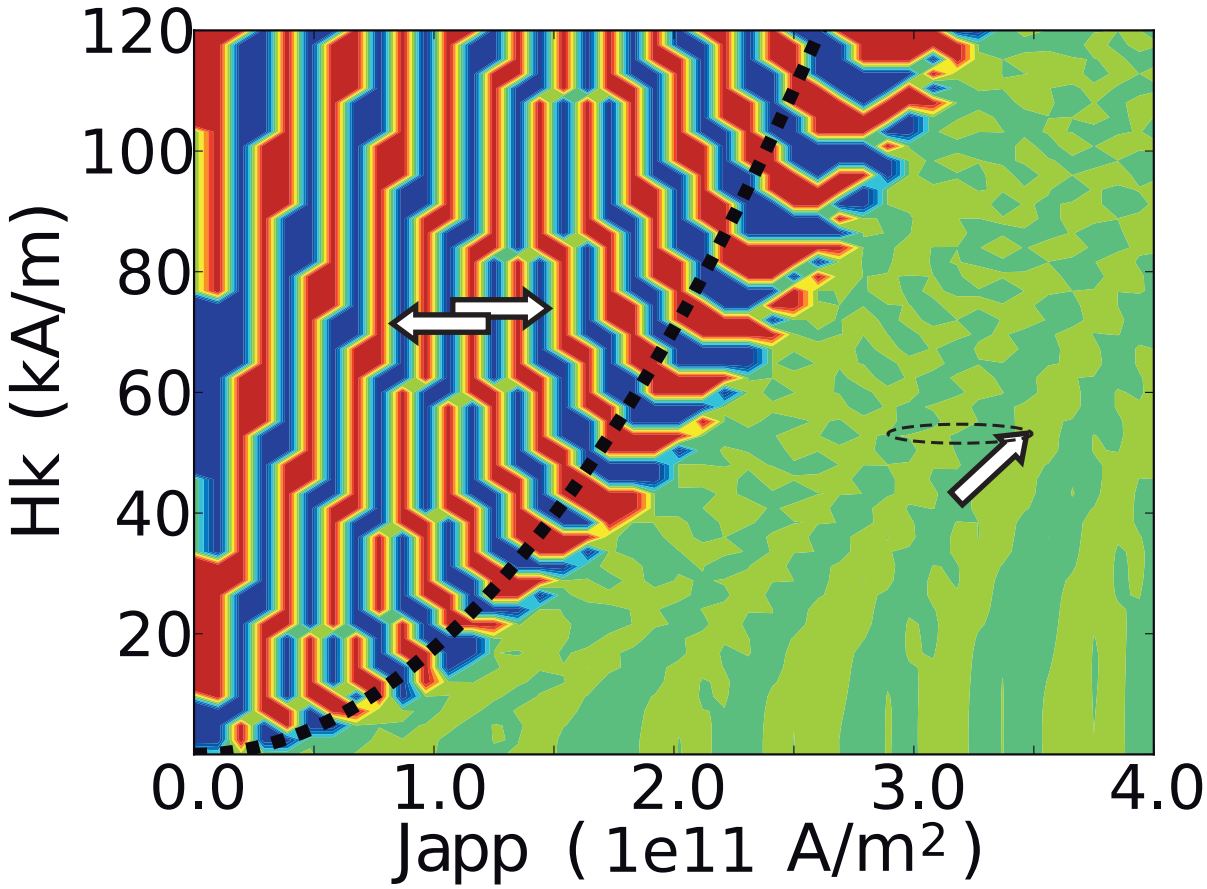

Figure 4.6 – From macrospin simulations, average in-plane component m_x of the magnetization in permanent regime versus applied current density and anisotropy field. Dark blue and red colors correspond to the equilibrium states $\langle m_x \rangle = \pm 1$, respectively. Light green color corresponds to $\langle m_x \rangle = 0$, the out-of-plane precessional steady state. The analytical critical current is represented by the black dashed line.

Fig. 4.6 and 4.7 represent the average in-plane component m_x of the free layer magnetization with an applied current pulse of 10 ns from macrospin simulations. The average is taken between 8 and 10 ns to avoid the transient regime. The magnetization is initially almost completely out-of-plane ($m_z \approx 1$) to favor the OPP steady state that appears when the magnetization relaxes towards the plane. The average magnetization is represented versus the applied current density and, the anisotropy field in Fig. 4.6 and the in-plane applied field along $\boldsymbol{u}_x$ in Fig. 4.7. The blue and red colors correspond to an average magnetization in equilibrium in the plane, $\langle m_x \rangle = \pm 1$, respectively. The light green color corresponds to $\langle m_x \rangle = 0$, representative of the OPP steady state. The critical current I_{c4}, or the critical current density, is extracted from the boundary between the light green and dark blue/red regions. The analytical critical line from expressions 4.25 are represented in black dashed line. For the highest value of anisotropy field and applied field used in the simulations, the analytical critical current differs from the simula-

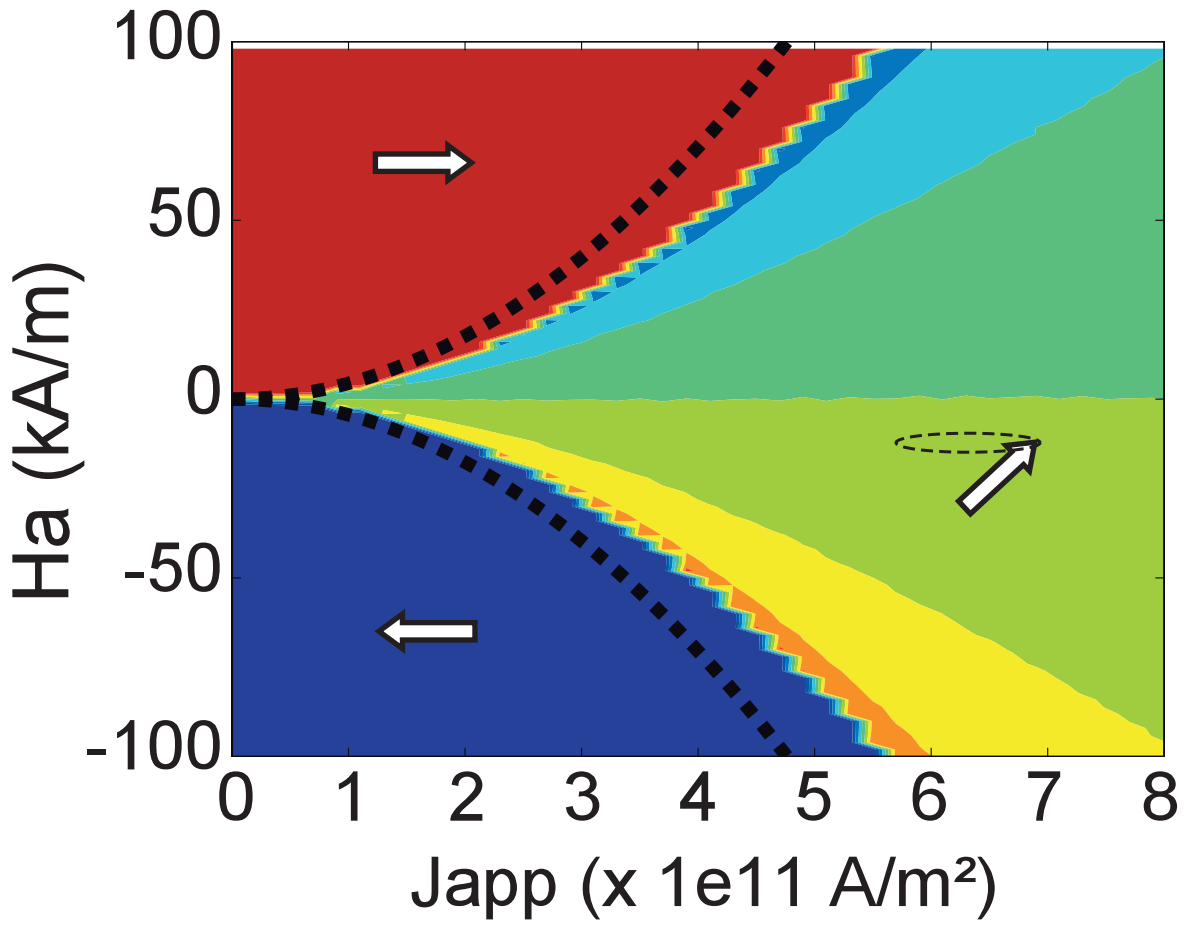

Figure 4.7 – Same as Fig. 4.6 with the applied field along $\boldsymbol{u}_x$.

tions value by 20% and 10% respectively. Notice that for the anisotropy figure, the equilibrium region is not uniformly colored and presents blue and red stripes because depending on where the OPP is stopped, the magnetization relaxes to $m_x = -1$ or $m_x = 1$. The final states actually depend on the transient regime, they are of little interest here. The critical currents obtained by finding numerically the root of the Melnikov function, as in Ebels et al.[Ebels 2008], are also in agreement with the analytical expressions. In fact they match with an error of less than 10% as seen on Fig. 4.8, which represents the critical spin torque amplitude found by numerical method, normalized by the analytical expression, versus applied field.

For the analyser spin torque, the same criterion used for anisotropy and applied field defines a maximal spin-torque amplitude for which the periodic orbit exists. The critical current density

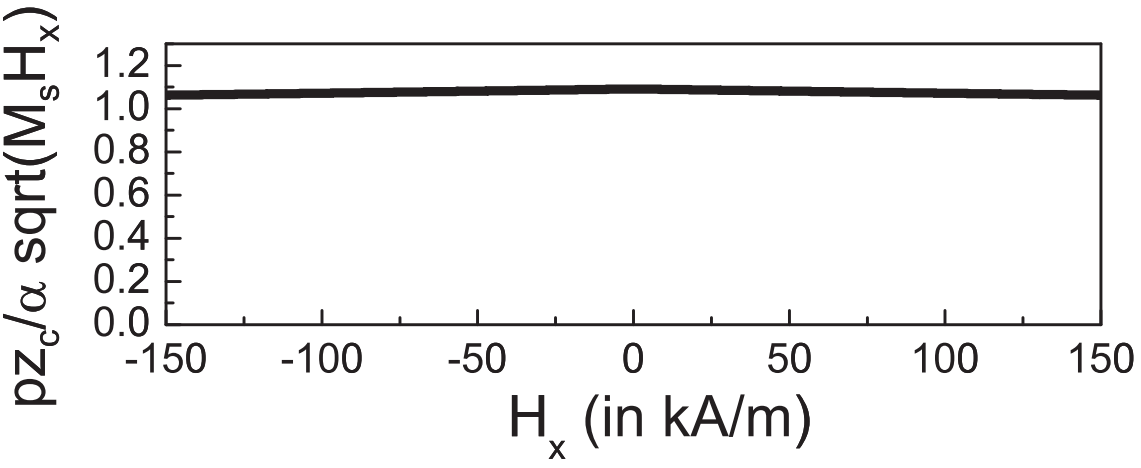

Figure 4.8 – Critical spin torque amplitude computed with the Melnikov function, versus applied field H_x along $\boldsymbol{u}_x$. The critical spin torque amplitude is normalized by the analytical expression.

depends on the ratio $r = p_x/p_z$ of the two spin-torque contributions :

$$\begin{cases} p_{z_c} = \alpha H_d \left(1 - \alpha^2 r^2\right) & \text{for } 2\alpha r < 1 \\ p_{z_c} = \dfrac{\alpha^2 H_d}{\sqrt{4\alpha^2 r^2 - 1}} & \text{for } 2\alpha r > 1 \end{cases} \tag{4.26}$$

The phase diagram of Fig. 4.9 represents the average of the in-plane magnetization m_x from macrospin simulations with different applied current density and ratio $r = px/pz$. The analytical expression for the critical current density is drawn in black dashed-line. The analytical critical line corresponds qualitatively to the region boundary of the diagram. However, for a given current density, the corresponding critical ratio is 35% smaller with the analytical expression than found by macrospin simulations. On the critical line, the ratio is around 40, giving a perturbation parameter $\xi = 0.8$. In this range, we should consider higher orders to obtain a better accuracy on the critical current.

4.4 Discussion

The perturbative approach developed here shows good agreement with macrospin simulations even at low order. For the anisotropy field and the applied field, we were able to calculate the frequency change due to these perturbations, except close to the range where the frequency vanishes. For these perturbations, we were also able to give a good approximation of the critical current J_{c4} at which the OPP state disappears. In fact, the perturbation parameter, for instance ϵ, is more or less inversely proportional to the frequency of the OPP, so it is clear that the perturbative expansion is less precise when the frequency vanishes, or close to the critical current, which is determined by this same criterion. Another limit is when the applied

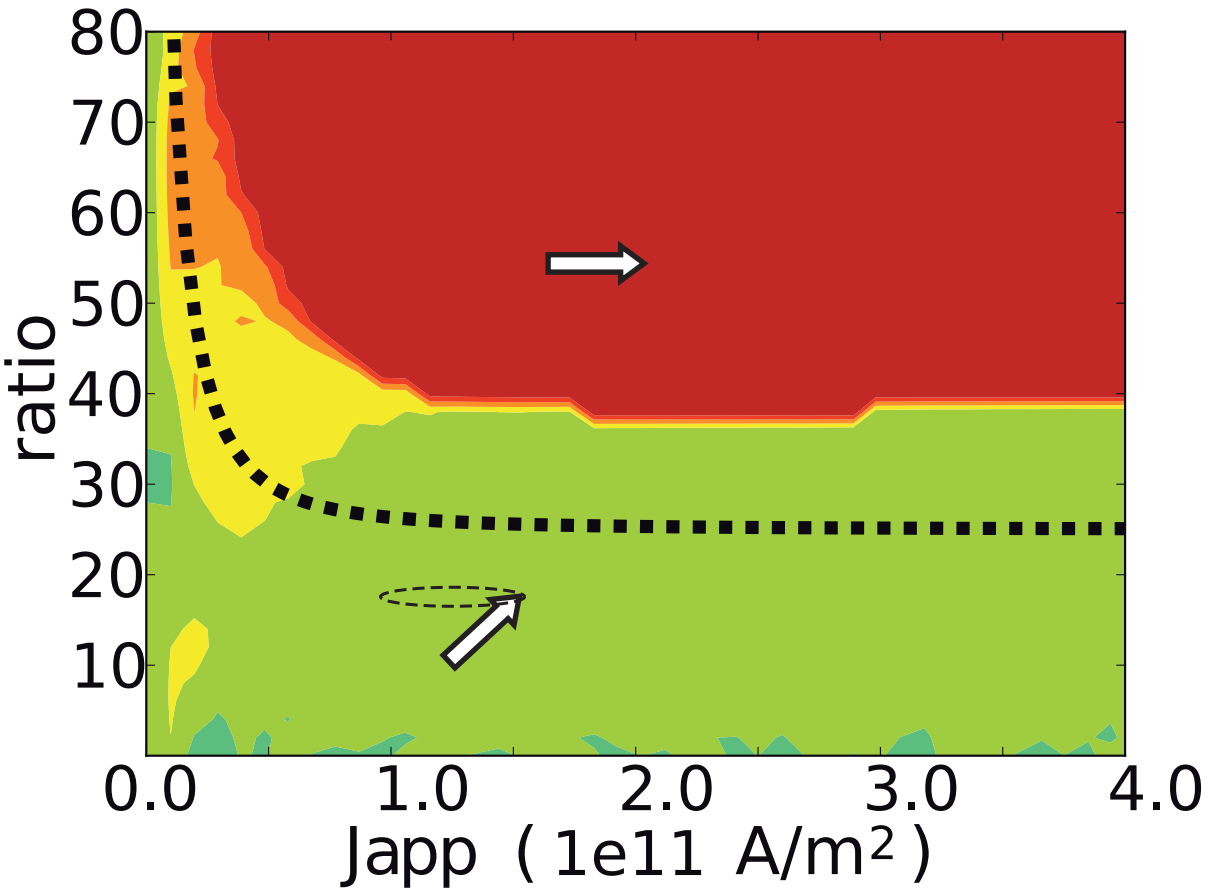

Figure 4.9 – Same as Fig. 4.6 with the ratio $r = p_x/p_z$.

current density tends towards zero, that corresponds also to a vanishing frequency. However this limit is not very relevant physically as the dynamical system studied here presents another critical current density, usually called J_{c1}, below which the magnetization remains in static equilibrium in-plane. So the dynamical system presents a bifurcation between an equilibrium and a limit cycle not associated with this equilibrium, and the frequency is non-vanishing close to the critical current J_{c1}.

This study has been carried out for an in-plane magnetized MTJ with additional perpendicular polarizer. The same perturbation expansion could also be done with a MTJ with in-plane precession (IPP) steady state. A good starting point to treat this case would be to consider the Landau-Lifshitz-Gilbert equation in complex numbers as described by the Kim, Tiberkevich and Slavin (KTS) theory[Slavin 2008][Slavin 2009][Kim 2008] : If we write the complex differential equation as a couple of differential equations for the amplitude and the phase, the amplitude would play the role of θ here, and the phase the role of ϕ. By rescaling the time with the eigenfrequency ω_0 corresponding to the FMR frequency, we expect to carry out the

Lindstedt's series expansion of the trajectory with constant energy, considering α as a small parameter. It should give a good approximation of the non-linear parameters modifying the frequency and the linewidth, and also the relative amplitude of the second harmonics, which are not treated by the present KTS theory.

Summary of results

Let $z_0 < 1$ be the average out-of-plane angle of the free layer magnetization, which is proportional to the applied current I : $z_0 = \frac{\hbar}{2e}\frac{\eta_{\mathrm{PERP}} I}{\alpha\mu_0 M_s^2 V}$. The main results of this chapter are summarized in the table below : the frequency change from the unperturbed frequency f_0, the amplitude of the second harmonic and the critical current I_{c4}, lower boundary for the existence of OPP, with respect to the perturbation due to an in-plane applied field, H_x or H_y, due to the in-plane uniaxial anisotropy field H_k and due to the STT of the reference layer p_x :

	H_x,H_y	H_k	p_x
$(f-f_0)/f_0$	$-\frac{1}{2z_0^4}\left(\frac{H_{x/y}}{M_S}\right)^2$	$-\frac{1}{32z_0^4}\left(\frac{H_k}{M_S}\right)^2$	$\frac{1}{2}\left(\frac{p_x}{M_S}\right)^2$
2nd harmonic	$H_{x/y}/z_0^2$	0	p_x/z_0
$I_{c4} \sim \cdots$	$\alpha\sqrt{H_{x/y}M_s}$	$\alpha\sqrt{H_k M_s}$	0

4.5 Annexe : Lindstedt's series expansion

The Lindstedt'series expansion is a method used to obtain an approximation of the solution of a dynamical system (S) with a small perturbation, by using the solution of an unperturbed system (S_0). Let (S) and (S_0) be the following formal systems, and $\boldsymbol{X}_0$ be the solution of (S_0) :

$$\begin{aligned}(S): &\quad \dot{\boldsymbol{X}} = \boldsymbol{F}(\boldsymbol{X}) + \epsilon \boldsymbol{G}(\boldsymbol{X}) \\ (S_0): &\quad \dot{\boldsymbol{X}}_{\boldsymbol{0}} = \boldsymbol{F}(\boldsymbol{X}_0)\end{aligned}$$

In order to find the solution of (S), we suppose that the solution $\boldsymbol{X}$ of (S) can be written as a power series of the small parameter ϵ :

$$\boldsymbol{X} = \boldsymbol{X}_0 + \epsilon \boldsymbol{X}_1 + \epsilon^2 \boldsymbol{X}_2 + \ldots$$

We can then replace $\boldsymbol{X}$ by this power series in the system (S) :

$$\dot{\boldsymbol{X}}_0 + \epsilon\dot{\boldsymbol{X}}_1 + \epsilon^2\dot{\boldsymbol{X}}_2 + \ldots = \boldsymbol{F}(\boldsymbol{X}_0 + \epsilon\boldsymbol{X}_1 + \epsilon^2\boldsymbol{X}_2 + \ldots) + \epsilon\boldsymbol{G}(\boldsymbol{X}_0 + \epsilon\boldsymbol{X}_1 + \epsilon^2\boldsymbol{X}_2 + \ldots)$$

Then the perturbed dynamical system (S) becomes (S_1) at the first order in ϵ :

$$(S_1): \quad \dot{\boldsymbol{X}}_0 + \epsilon \dot{\boldsymbol{X}}_1 = \boldsymbol{F}(\boldsymbol{X}_0) + \epsilon \, \mathrm{d}\boldsymbol{F}(\boldsymbol{X}_0)[\boldsymbol{X}_1] + \epsilon \boldsymbol{G}(\boldsymbol{X}_0)$$

Here $\mathrm{d}\boldsymbol{F}(\boldsymbol{X}_0)$ is the differential of the vector field $\boldsymbol{F}$ evaluated at $\boldsymbol{X}_0$. By identification, two differential equations are obtained, where the first one is the unperturbed system (S_0) :

$$\begin{aligned} \dot{\boldsymbol{X}}_0 &= \boldsymbol{F}(\boldsymbol{X}_0) \\ \dot{\boldsymbol{X}}_1 &= \mathrm{d}\boldsymbol{F}(\boldsymbol{X}_0)[\boldsymbol{X}_1] + \boldsymbol{G}(\boldsymbol{X}_0) \end{aligned}$$

This method theoretically allows to calculate the solution up to any order. However if the solution $\dot{\boldsymbol{X}}_k$ at order k is periodic, the resolution of the dynamical system at order $k+1$ may give rise to non-periodic secular terms, often $t\cos(\omega_0 t)$ terms, or, for the equation addressed in this paper, t terms. In order to get rid of the secular terms, the angular frequency is also written as a power series of ϵ : $\omega = \omega_0 + \epsilon\omega_1 + \epsilon^2\omega_2 + \ldots$ By rescaling time with the change of variables $\tau = \omega t$, system (S) rewrites :

$$\begin{aligned} \left(\omega_0 + \epsilon\omega_1 + \epsilon^2\omega_2 + \ldots\right)\left(\dot{\boldsymbol{X}}_0 + \epsilon\dot{\boldsymbol{X}}_1 + \epsilon^2\dot{\boldsymbol{X}}_2 + \ldots\right) & \\ = \boldsymbol{F}(\boldsymbol{X}_0 + \epsilon\boldsymbol{X}_1 + \epsilon^2\boldsymbol{X}_2 + \ldots) & \\ + \epsilon\boldsymbol{G}(\boldsymbol{X}_0 + \epsilon\boldsymbol{X}_1 + \epsilon^2\boldsymbol{X}_2 + \ldots) & \quad (4.27) \end{aligned}$$

Henceforth $\dot{\boldsymbol{X}}$ denotes a derivation with respect to τ. The first order sytem becomes :

$$\dot{\boldsymbol{X}}_1 + \omega_1\dot{\boldsymbol{X}}_0 = \mathrm{d}\boldsymbol{F}(\boldsymbol{X}_0)[\boldsymbol{X}_1] + \boldsymbol{G}(\boldsymbol{X}_0)$$

The value of ω_1, and higher order terms ω_k, is set so that secular terms are cancelled. In the majority of the cases treated in this paper, it appears that $\omega_1 = 0$ because no secular terms appear at order 1. However at order 2, in order to cancel the secular terms, ω_2 needs to be non-zero.

However, this way of solving the perturbed system does not account for an additional temporal dephasing between the angles θ and ϕ. According to the exact solutions of eq. 4.5, the second term of the right-hand-side from the expression of ϕ is a dephasing term that accounts for the initial condition z_i. In this particular case, the angle θ is constant in the permanent regime so this dephasing has no effect. However solving a perturbed system gives rise to oscillating terms on the angle θ, for which the exact dephasing with the angle ϕ is important, specially for second-order terms. In fact the second order terms partly accounts for an interaction between θ and ϕ harmonics. In order to solve this issue, the equation of the angle θ with respect to ϕ is computed first, then the expression of $\theta(\tau)$ and $\phi(\tau)$ are obtained. By dividing the first equation of eq. 4.12 by the second equation, the differential equation governing $\theta(\phi)$ is derived :

$$\frac{\mathrm{d}\theta}{\mathrm{d}\phi} = \sin\theta \frac{g_\theta(\theta) + \epsilon f_\theta^\epsilon(\theta,\phi)}{h_\phi(\theta) + \epsilon f_\phi^\epsilon(\theta,\phi)} \tag{4.28}$$

Both sides of this equation can be Taylor expanded with respect to ϵ by using the expressions for θ and ϕ from eq. 4.2.1. Hence the expression of θ with respect to ϕ is computed up to any given order k. The assumption that $\epsilon \ll 1$, or that the perturbation is small compared to the non-perturbated frequency, is critical here.

Thereafter, the expression of $\theta(\phi)$ at order k is injected in the differential equations 4.12 of θ and ϕ versus time τ to obtain the precession harmonics and the frequency changes, using the Lindstedt's series.

The results of this section were obtained with the computer algebra system Maxima[2], by differentiating eq. 4.27 with respect to ϵ to get the equations at the different orders in ϵ. At order 2, the solutions already hold a lot of terms that are not shown here because we were only concerned about the frequency change. The computation of higher order terms is rather complicated.

[2] http://maxima.sourceforge.net/

Part III

Theoretical and experimental study of STT-induced dynamics in the free layer of an in-plane magnetized MTJ with additional perpendicular polarizer

Chapter 5

Influence of the anisotropy on the reversal

The previous Part presented analytical and simulation results in order to understand and describe some aspect of the dynamics of a real system comprising an in-plane MTJ with an in-plane reference layer and a perpendicular polarizer. In Chapter 4, the configuration with two polarizing layers was analyzed from the "oscillator" point of view, i.e. the free layer was supposed to be oscillating due to the STT from the perpendicular polarizer, and the in-plane STT was only slightly perturbating the oscillation. Even if critical currents for the existence of OPP were extracted from this analysis, it is interesting to try to solve the problem of the two polarizers from the "memory" side.

In this chapter, the phase diagram of the orthogonal STTRAM is computed. It gives the current range for which the free layer oscillates or is reversed. The latter situation is called bipolar switching because the free layer is in equilibrium in the P or AP configuration, depending on the polarity of the applied current pulse. It is obvious that without the reference layer STT, the free layer is in OPP under applied current; without the perpendicular polarizer STT, it is in the bipolar switching regime. The cross-over between the two regimes is presented in this chapter.

Finally, the analytical predictions are tested experimentally, using a real-time measurements setup. The real-time measurements give important information about the stochasticity of the reversal and about the incubation time, in order to evaluate if the addition of a perpendicular polarizer really improves the switching.

5.1 Qualitative argument

In the orthogonal STT geometry, described in Fig. 5.1.(a), the free layer (FL) senses two STT contributions, which have different effects on the FL magnetization dynamics. On the one hand, the STT contribution from the perpendicular polarizer pulls the free layer magnetization out-of-plane (Fig. 5.1.(c)), then due to the strong demagnetizing field, the FL magnetization precesses around the out-of-plane axis at gigahertz frequency. By tailoring the current pulse width, it is possible to stop the FL magnetization precession after half a precession, hence

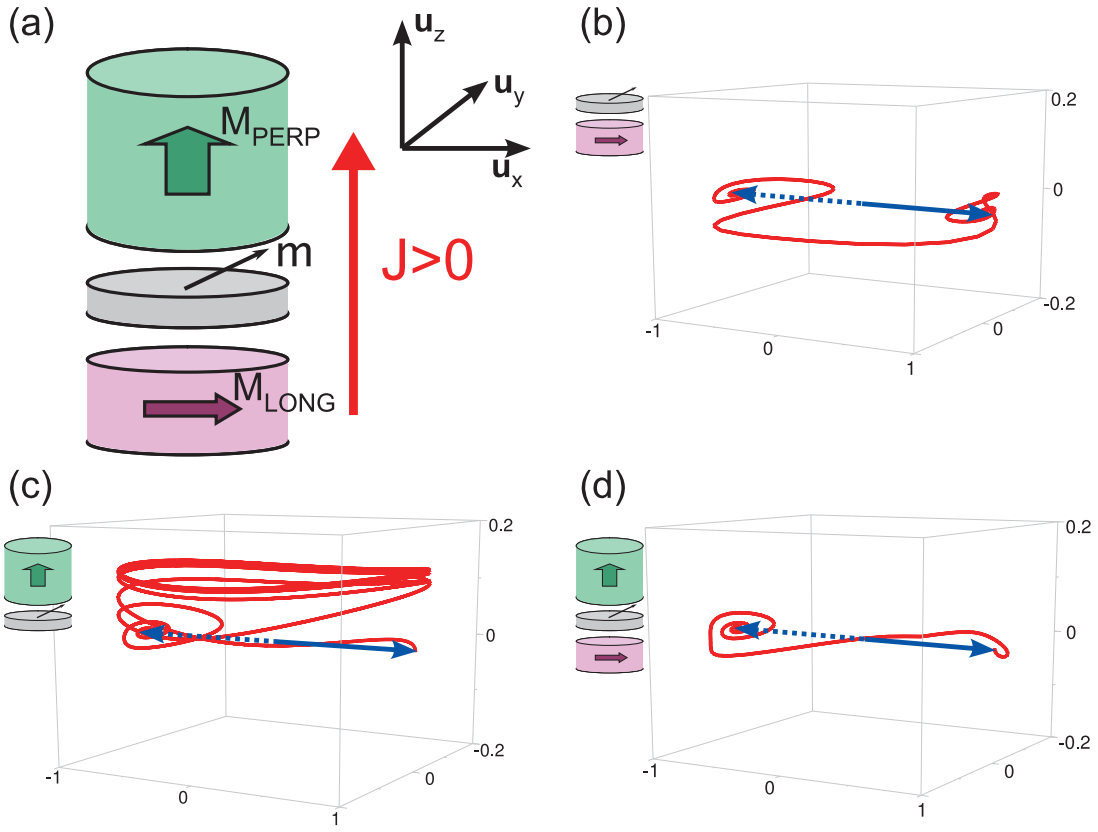

Figure 5.1 – (a) Geometry of the nanopillars with elliptical cross-section. (b)-(d), magnetization dynamics during the reversal of the free layer in three configurations : (b) with an in-plane reference layer, (c) with a perpendicular polarizer and (d) with the two polarizing layers. The magnetization is initially in the parallel (P) configuration (blue full-arrow), and relaxes in the anti-parallel (AP) state (blue dotted-arrow).

reversing the magnetization direction and switching the device. However this requires to send current pulses of very well controlled duration (typically 200 ps ±40 ps), which is possible in a laboratory experiment on a single cell, but much more complicated to implement at chip level with millions of cells (deformation of the current pulse during their propagation along the bit and word line). On the other hand, the STT contribution from the analyzer provokes a bipolar switching of the FL magnetization (Fig. 5.1.(b)). Depending on the polarity of the current, one of the two stable configurations, parallel (P) or antiparallel (AP) is favored, allowing to control the final state by the current polarity.

The second regime, bipolar switching, is particularly interesting for MRAM application, but one requires a significant effect of the perpendicular polarizer in order to reduce the stochasticity and achieve subnanosecond switching (Fig. 5.1.(d)).

In-plane MTJ with analyzer (or reference layer) and in-plane MTJ with perpendicular polarizer have been presented in Chapter 2. These analyses already give qualitative arguments for the behavior of the in-plane MTJ with the two polarizing layers. In the presence of a per-

pendicular polarizer alone, the free layer magnetization oscillates around the out-of-plane axis when the applied current is larger than the critical current I_c^{PERP} :

$$I_c^{\mathrm{PERP}} = \frac{2e}{\hbar}\frac{\mu_0 M_s V}{\eta_{\mathrm{PERP}}}\frac{H_k}{2} \tag{5.1}$$

For in-plane MTJ with analyzer, the expression of the critical current I_c^{LONG} above which the free layer magnetization switches comes out from the study of the equilibrium stability :

$$I_c^{\mathrm{LONG}} = \frac{2e}{\hbar}\frac{\mu_0 M_s V}{\eta_{\mathrm{LONG}}}\alpha\left(\frac{H_d}{2} + H_k\right) \tag{5.2}$$

Here, $V = St$ is the volume of the free layer, with thickness t and elliptical cross-section of area S. M_S is its saturation magnetization, H_k the anisotropy field and H_d the demagnetizing field. α is the Gilbert damping constant. η_{LONG} and η_{PERP} are the spin polarizations of the reference layer and of the perpendicular polarizer. The spin polarization asymmetry of the two spin torque contributions was neglected.

In order to achieve a bipolar switching of an MTJ with the two STT contributions, the comparison of these two critical currents gives a good qualitative argument. If the critical current for bipolar switching is smaller than the critical current for the OPP, three regimes are expected as the applied current is increased : (i) below I_c^{LONG}, the magnetization remains in the initial configuration, no switching occurs; (ii) between I_c^{LONG} and I_c^{PERP}, bipolar switching regime; (iii) above I_c^{PERP}, oscillatory regime. It appears that the critical current that controls the onset of the oscillations I_c^{PERP}, is controlled by the uniaxial anisotropy field H_k : if H_k is increased, I_c^{PERP} is also increased. On the other hand, the critical current for bipolar switching, I_c^{LONG}, is barely affected by a change of the uniaxial anisotropy, given that generally $H_k \ll H_d$ in thin films.

According to this qualitative analysis, it appears that increasing the anisotropy field H_K favors the bipolar switching over the oscillatory regime. The uniaxial anisotropy field H_K is mainly due to shape anisotropy in these structures. It is vanishing for a circular sample and it increases with the aspect ratio of the nanopillar elliptical cross-section.
This intuitive consideration will be first confirmed by analytical study of the system with two polarizers in the macrospin approach. It is also supported by numerical simulations, both in macrospin and micromagnetics. At last, it is experimentally confirmed on samples realized in the laboratory.

5.2 Analytical state diagram

The previous argument is only qualitative but it is possible to obtain a similar conclusion by studying the equilibrium state of an in-plane MTJ with the STT contributions of an analyzer and a perpendicular polarizer in the macrospin model. As previously, the free layer magnetization dynamics is modeled by the LLGS equation with the two STT contributions. Without applied current, two stable equilibrium states exist, the parallel and antiparallel states. When a current is applied, there are two equilibrium states, if they exist, but they are different from P or AP (like with a perpendicular polarizer alone, but unlike the case with the analyzer alone for which the equilibrium states are P and AP whatever the current). However, for specific values of the anisotropy factor $Q = H_k/M_S$, of the ratio $r = \eta_{\mathrm{LONG}}/\eta_{\mathrm{PERP}}$ and of the applied current I (or equivalently, of the applied current density J, $I = JS$), no equilibrium state exists. For such a choice of parameters the free layer magnetization is actually oscillating because no equilibrium state is available.

We consider the Landau-Lifshitz-Gilbert-Slonczewski (LLGS) equation describing the dynamics of a magnetic layer submitted to the two spin-transfer-torque contributions originating from the perpendicular polarizer and the reference layer. The free energy E contains the demagnetizing energy and the uniaxial anisotropy, the applied fields and stray fields are neglected :

$$E = \frac{1}{2}\mu_0 M_S^2 V\Big(N_z m_z^2 - Q m_x^2\Big) \tag{5.3}$$

The demagnetizing N_z and anisotropy Q factors are the dimensionless quantities associated to the demagnetizing field, $H_d = N_z M_S$, and the anisotropy field, $H_k = Q M_S$.

The spin torque potential P includes the two contributions to the spin torque :

$$P = +I\frac{\hbar}{2e}\eta_{\mathrm{PERP}} m_z - I\frac{\hbar}{2e}\eta_{\mathrm{LONG}} m_x = \mu_0 M_S^2 V\Big(i_z m_z - i_x m_x\Big) \tag{5.4}$$

The current I is positive for electrons flowing from the perpendicular polarizer to the free layer, then to the reference layer. η_{LONG} and η_{PERP} are the spin polarizations from the reference layer and from the perpendicular polarizer, respectively. The spin polarizations asymmetry are set to zero, for both contributions. $i_x = \frac{\hbar}{2e}\frac{\eta_{\mathrm{LONG}} I}{\mu_0 M_S^2 V}$ and $i_z = \frac{\hbar}{2e}\frac{\eta_{\mathrm{PERP}} I}{\mu_0 M_S^2 V}$ are the dimensionless quantities associated to the two spin torque contributions.

The conservative and dissipative potentials are defined by $\mathcal{H} = E$ and $\Gamma = \alpha E - P$. The conservative potential only depends on the energy, the IEC is neglected. The demagnetizing factor is assumed to be the dominant parameter at the second order, $N_z^2 \gg Q^2, i_x^2, i_z^2$. It is completely justified for thin films, nevertheless if the demagnetizing field is reduced due to interface anisotropy, it should still be relatively large for the further analysis to hold.
The magnetization is expressed in spherical coordinates, and the LLGS writes :

$$\begin{cases} m_x = \sin\theta\cos\phi \\ m_y = \sin\theta\sin\phi \\ m_z = \cos\theta \end{cases} \qquad \begin{cases} \dfrac{M_S V}{\gamma}\dfrac{\mathrm{d}\theta}{\mathrm{dt}} = -\dfrac{1}{\sin\theta}\dfrac{\partial E}{\partial\phi} - \dfrac{\partial\Gamma}{\partial\theta} \\ \dfrac{M_S V}{\gamma}\sin\theta\dfrac{\mathrm{d}\phi}{\mathrm{dt}} = +\dfrac{\partial E}{\partial\theta} - \dfrac{1}{\sin\theta}\dfrac{\partial\Gamma}{\partial\phi} \end{cases}$$

First, the equilibrium configurations of the dynamical system are computed. The equilibrium in-plane and out-of-plane angles are noted ϕ and θ, without distinction with their non-equilibrium values, not to overload the notations. They are solution of :

$$\begin{cases} 0 = -\dfrac{Q}{2}\sin\theta\sin(2\phi) - i_z\sin\theta - i_x\cos\theta\cos\phi \\ 0 = -\sin\theta\cos\theta(N_z + Q\cos^2\phi) + i_x\sin\phi \end{cases} \tag{5.5}$$

The expression of the out-of-plane angle θ at equilibrium with respect to the angle ϕ is computed from the second equation :

$$\sin(2\theta) = \frac{2i_x\sin\phi}{N_z + Q\cos^2\phi} \tag{5.6}$$

For clarity, let $A = \dfrac{2i_x\sin\phi}{N_z + Q\cos^2\phi}$. $A^2 \ll 1$ from the assumption that the demagnetizing is dominant at second order. From eq. 5.6, the two possible values of the cotangent of θ are given by :

$$\cot(\theta)_\pm = \frac{1}{A}\left(1 \pm \sqrt{1 - A^2}\right)$$

The two solutions describe an in-plane (IPS) equilibrium and an out-of-plane equilibrium (OPS), for which $\cos\theta \approx A/2$ and $\sin\theta \approx A/2$, respectively. Replacing $\cos\theta$ and $\sin\theta$ in the first equation of eq. 5.5, the expression of the in-plane angle ϕ at equilibrium is obtained for the IPS and OPS equilibriums :

$$\text{(OPS)}: \quad \cot\phi = \frac{-i_z}{N_z + Q} \qquad\qquad \text{(IPS)}: \quad \sin(2\phi) = \frac{-2i_z}{Q + \dfrac{i_x^2}{N_z + Q/2}} \tag{5.7}$$

The OPS equilibrium is always defined. However, the IPS equilibrium is defined only if the right-hand-side in the previous expression of ϕ is smaller than unity in absolute value, i.e. :

$$2|i_z| < Q + \frac{i_x^2}{N_z} \tag{5.8}$$

From the expressions of i_x and i_z, let $I_0 = \dfrac{2e}{\hbar}\mu_0 M_s^2 V$ be a characteristic current. The criterion for the existence of an IPS equilibrium becomes :

$$\eta_{\text{PERP}} < \frac{QI_0}{2I} + \frac{\eta_{\text{LONG}}^2 I}{2I_0(N_z + Q/2)} \tag{5.9}$$

The right-hand-side defines a function of the applied current : if the function's graph is below the horizontal line $y = \eta_{\text{PERP}}$, no IPS equilibrium can exist at this given applied current. As this function of I is decreasing for small current and increasing for large currents, it goes through a minimum. If η_{PERP} is smaller than the minimum of this function, then the criterion for the existence of the IPS equilibrium is always verified. After computing the value of the minimum

of the function of I, it appears that for the IPS equilibrium to be defined for any current, the ratio of the two spin polarizations must satisfy the criterion :

$$\frac{\eta_{\mathrm{PERP}}}{\eta_{\mathrm{LONG}}} < \sqrt{\frac{Q}{N_z}}$$

This relation defines a critical spin polarization of the perpendicular polarizer, $\eta^c_{\mathrm{PERP}} = \eta_{\mathrm{LONG}}\sqrt{\frac{Q}{N_z}}$.
If the spin polarization η_{PERP} has a value above this critical value, then the IPS equilibrium exists for small current and for large current, and there is a range of current for which no IPS equilibrium exists.
Nonetheless, even if the IPS and OPS equilibriums exist, it does not mean that they are stable equilibriums. To check the stability of the IPS and OPS equilibriums, one must compute the dynamical matrix, evaluated at the equilibrium configuration. As it was shown in Chapter 1, the conservative part is the dominant term in the expression of the eigenvalues of the dynamical matrix. Therefore, if the equilibrium is stable, the eigenvalues $\lambda_\pm$ are complex conjugates (with the imaginary unit i, $i^2 = -1$) :

$$\lambda_\pm \approx \frac{\Delta\omega}{2} \pm i\omega_0 \tag{5.10}$$

The definitions of the linewidth $\Delta\omega$, using the Laplacian of Γ, $\Delta_R\Gamma$, and of the FMR frequency ω_0 are recalled here :

$$\Delta\omega = -\frac{\gamma}{M_S V}\Delta_R\Gamma = -\frac{\gamma}{M_S V}\left(\Gamma_{\theta\theta} + \cot\theta\ \Gamma_\theta + \frac{\Gamma_{\phi\phi}}{\sin^2\theta}\right)$$
$$\omega_0^2 = \left(\frac{\gamma}{M_S V}\right)^2\left[E_{\theta\theta}\left(\frac{E_{\phi\phi}}{\sin^2\theta} + \cot\theta\ E_\theta\right) - \left(\frac{E_{\theta\phi}}{\sin\theta} - \cot\theta\ \frac{E_\phi}{\sin\theta}\right)^2\right]$$

After some calculations and if the prefactors are omitted, the linewidth writes : $\Delta\omega \sim 2i_x\cos\phi\sin\theta - 2i_z\cos\theta - \alpha N z\,(1-3\cos^2\theta) + \alpha Q\,(1-3\cos^2\phi\sin^2\theta)$.
Also, $\omega_0^2 \sim N_z^2\cos(2\theta)\cos^2\theta + (QN_z - Q^2\sin^2\theta\cos^2\phi)\,(\cos^2\theta - \cos(2\phi)\sin^2\theta)$. Therefore, the FMR frequency takes different values for the IPS and the OPS equilibrium :

$$\text{OPS, } \sin^2\theta \ll 1 : \qquad \omega_0^2 = N_z(N_z+Q) \tag{5.11}$$
$$\text{IPS, } \cos^2\theta \ll 1 : \qquad \omega_0^2 = \cos(2\phi)Q(N_z + Q\cos^2\phi) \tag{5.12}$$

Because its FMR frequency never vanishes, the stability of the OPS equilibrium is determined by the linewidth : for $i_z < \alpha(N_z + Q/2)$, the OPS equilibrium is unstable; it is stable for $i_z > \alpha(N_z + Q/2)$.
For the IPS equilibrium, the FMR frequency vanishes for $\cos(2\phi) = 0$, or $\sin(2\phi) = \pm 1$, which was already the criterion for the existence of the IPS equilibrium. Therefore the stability of the IPS equilibrium is also determined by the linewidth. If we suppose that $\sin^2(2\phi) \ll 1$ (the IPS equilibrium is far from the critical in-plane angle), the IPS equilibrium is stable for $|i_x| < \alpha(\frac{N_z}{2} + Q)$, unstable otherwise.

5.5.2 Analytical state diagram

Finally the stability diagram of the in-plane free layer with two polarizers has been established. There are three critical currents, or more precisely critical lines :

(i) The critical line for the existence of an IPS equilibrium, defined by eq. 5.9. It strongly depends on the anisotropy factor Q, and it corresponds, for small currents, to the critical current for the bifurcation IPS/OPP of the system with a free layer and the perpendicular polarizer alone.

(ii) The critical line for the destabilization of the IPS, defined by $|i_x| = \alpha(\frac{N_z}{2} + Q)$. It corresponds to the critical current of a free layer with the in-plane reference layer. Depending on the initial magnetization configuration, P or AP, positive or negative currents destabilize the IPS equilibrium. It is not strongly dependent on the anisotropy factor.

(iii) The critical line for the stabilization of the OPS equilibrium, defined by $i_z = \alpha(N_z + Q/2)$. It corresponds to the bifurcation OPP/OPS with the perpendicular polarizer alone and does not depend strongly on the anisotropy factor.

Only five parameters appear in the expressions of the critical lines, N_z, Q, i_x, i_z and α. However, there are three critical lines, therefore the system can be described by three parameters with an appropriate rescaling. Here we choose to represent the state diagram using the anisotropy factor Q (or the anisotropy field), the applied current I (or the current density J) and the ratio between the two spin polarizations, $r = \eta_{\mathrm{LONG}}/\eta_{\mathrm{PERP}}$ (or the spin polarization of the perpendicular polarizer, giving the spin polarization of the reference layer a fixed value), that was already defined in Chapter 4.

Fig. 5.2 shows the phase diagram for a given $Q = 0.01$ versus current density J and η_{PERP}, the polarization of the perpendicular polarizer. Here we set $\eta_{\mathrm{LONG}} = 0.3$, $\alpha = 0.02$ and $N_z = 1$. The diagram is separated in four regions : (A) the oscillating region for which no equilibrium state exists, labeled OPP; (B) the stable state region, characterized by a stability of the initial equilibrium state, labeled AP/P; (C) the bipolar reversal region, for which the initial equilibrium state is not stable but the other equilibrium state is stable, resulting in a switching of the free layer magnetization, labeled AP or P depending on the current polarity; (D) the OPS region, for which the out-of-plane precessions are not stable and the OPS equilibrium is stable.

Among the three critical lines, the bistable/monostable line (between the B and C regions) and the OPP/OPS line (between the A and D regions) do not depend on the anisotropy field, but on the damping constant α. On the contrary, the IPS/OPP line (between the B/C and A regions) depends on the anisotropy field : if the anisotropy increases the line is moved upward. Therefore, by increasing the anisotropy field, the bipolar switching region (C) area increases to the detriment of the OPP region (A). Thus the current density range for bipolar switching is increased.

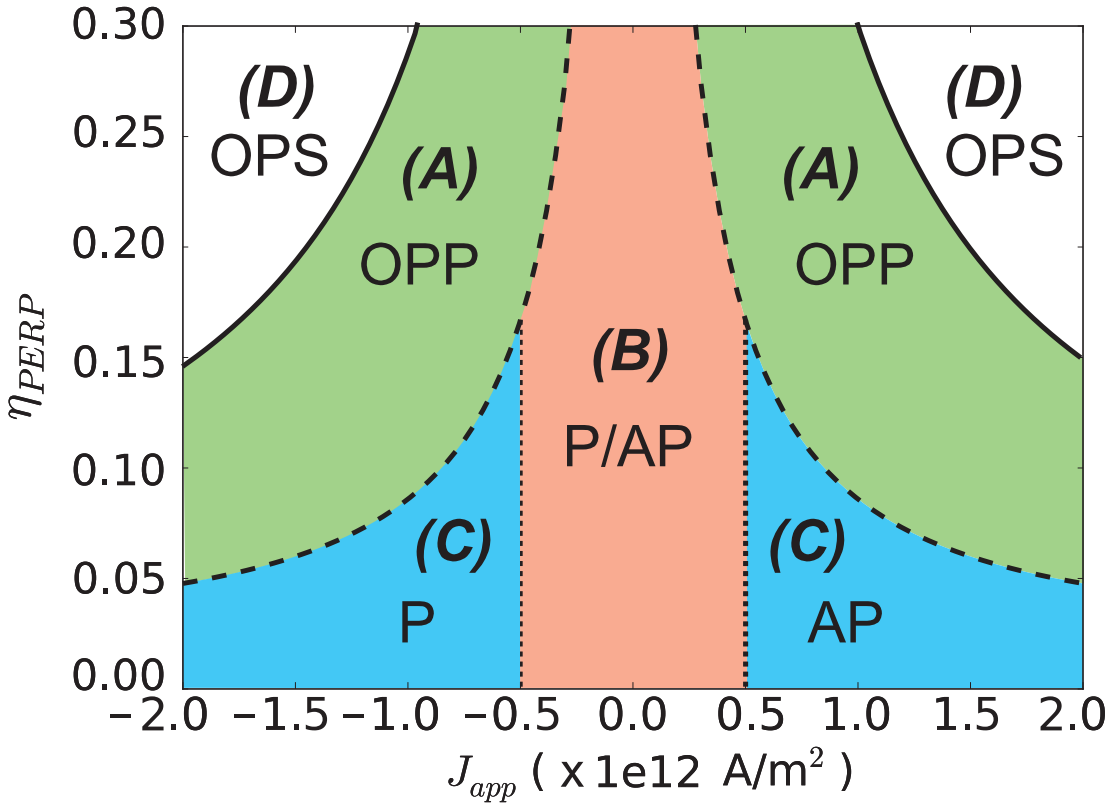

Figure 5.2 – Analytical phase diagram of the available equilibrium for $Q = 0.01$, $\alpha = 0.02$ and $\eta_{\text{LONG}} = 0.3$. (A) OPP region (in green), no equilibrium state is available for such choice of parameters (J, Q, r). (B) bistable P/AP region (in red), both in-plane equilibriums P and AP are available. (C) stable P or AP region (in blue), only one equilibrium state, P or AP, is stable depending on the current polarity. (D) OPS region, the OPP are unstable and the OPS equilibrium is stable.

5.3 Macrospin and micromagnetics simulations

5.3.1 Comparison of macrospin simulations with the analytical state diagram

We performed macrospin simulations with different anisotropy field H_k and polarization of the perpendicular polarizer η_{PERP} to validate the analytical critical lines. The parameters of the macrospin simulations are :

Saturation magnetization	M_S	1.2e6 A/m
Thickness	t	3 nm
Nanopillar area	S	10^{-14} m^2
Damping constant	α	0.02
Demagnetizing factor	$N_z = H_d/M_S$	1
Spin polarization of the ref. layer	η_{LONG}	0.3

The magnetization is initially in the P state ($m_x = 1$). The average in-plane magnetization component m_x in the permanent regime is calculated for different values of applied current density J_{app} and polarization η_{PERP} and represented in Fig. 5.3, for two different values of the anisotropy field : (a) $H_k = 6$ kA/m ($Q = 0.005$) and (b) $H_k = 24$ kA/m ($Q = 0.02$). These anisotropy fields are calculated from the shape anisotropy for free layer sizes of 105x95x3 nm and 180x60x3 nm, respectively. The diagrams show three regions (the OPS region is indiscernible from the OPP one because they are both characterized by an average m_x being zero, $\langle m_x \rangle = 0$) :

(Red region) : The final state is the same as the initial P state, the free layer has not switched.

(Blue region) : The final state is the AP equilibrium, the free layer has switched.

(Green region) : The free layer is in OPP steady state (or OPS), the final state depends on the current density pulse duration, as described in Chapter 2.

The analytical critical lines obtained in the last section were reported on the figure. Moreover, the critical lines calculated in Chapter 4 for the existence of the OPP steady state with an anisotropy field and the STT of the reference layer were included in the figure :

(Black dotted-line) : Critical line for the instability of the P equilibrium.

(Black dashed-line) : Disappearance of the two IPS equilibriums. Above this critical line, only the OPP and OPS steady states exist.

(Black full-line) : Critical line for Andronov-Hopf bifurcation OPP/OPS.

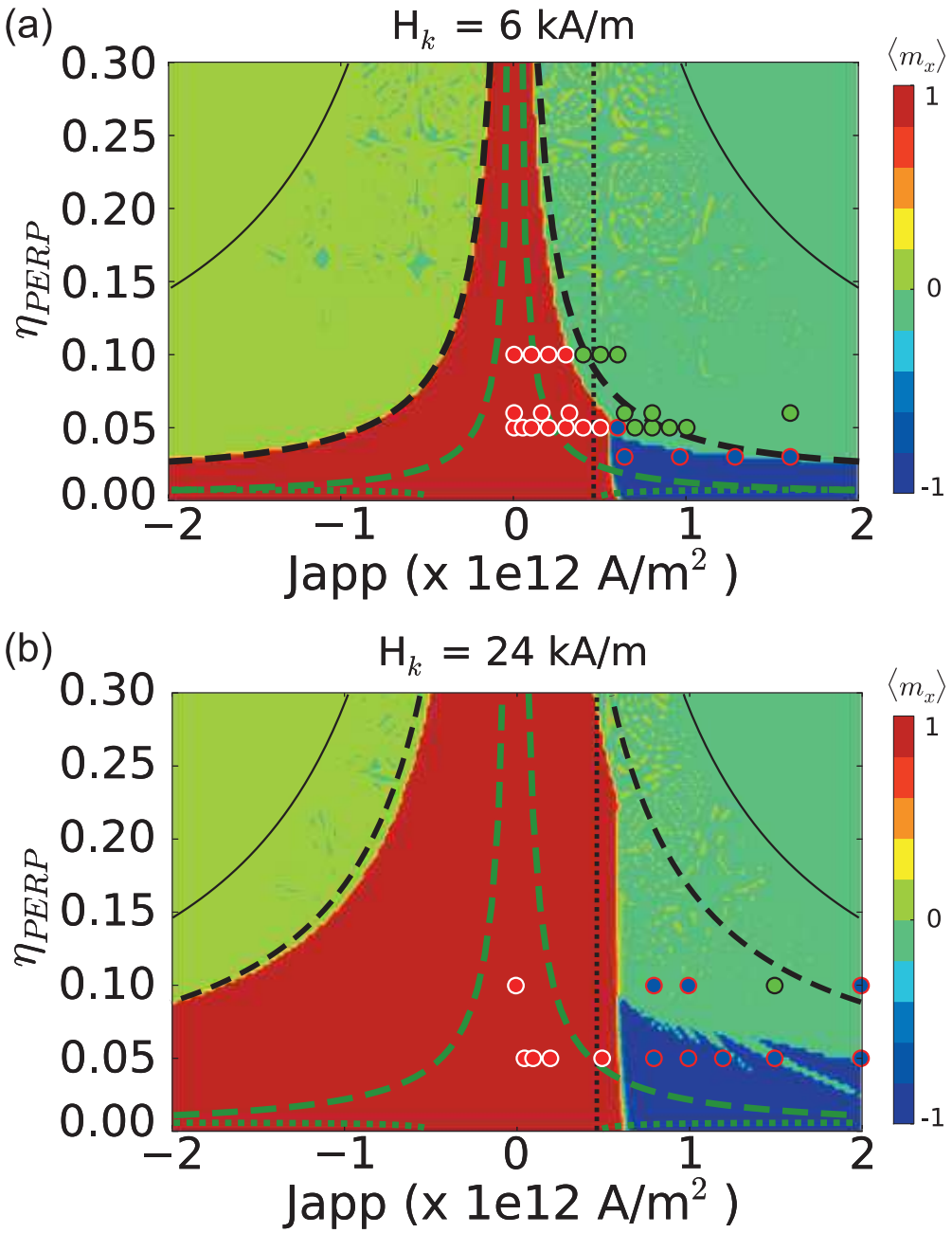

Figure 5.3 – Macrospin simulation of the average in-plane magnetization m_x, versus current density and polarization of the perpendicular polarizer, for different anisotropy field (a) 6 kA/m and (b) 24 kA/m. The magnetization is initially in the P configuration. There are three final steady states : (i) in red, P final state, no switching. (ii) in blue, AP final state, switching of the free layer magnetization. (iii) in green, the average in-plane component of the magnetization vanishes, corresponding to an OPP steady state or OPS (the two steady states are indiscernible here). Black dotted-line : instability of the P equilibrium. Black dashed-line : disappearance of the two IPS equilibriums. Black full-line : transition between OPP and OPS. Green dashed-line : critical line of the disappearance of OPP due to the reference layer STT. Green dotted-line : disappearance of the OPP due to the anisotropy field. The circle symbols represent the final steady state from micromagnetic simulations : P final state (orange), AP final state (blue), and OPP (green). Micromagnetics simulations run by L. Buda-Prejbeanu.

(Green dotted-line) : Critical line for the existence of OPP due to the STT of the reference layer. Below this line, the OPP do not exist.

(Green dashed-line) : Critical line for the existence of OPP due to the anisotropy field. Below this line, the OPP do not exist.

The borders between the OPP (green) region and the P (red) region for negative current corresponds to the IPS/OPP analytical critical line. For positive currents, the border of the P (red) region with the AP (blue) region is in agreement with the instability line of the P equilibrium. The border between the P (red) region and OPP (green) region also corresponds to the IPS/OPP critical line. However, the border between the AP (blue) region and the OPP (green) region does not correspond to any analytical critical line : it is set between the black dashed-line, above which only the OPP state exists, and the green dashed-line, below which the OPP do not exist. The region between these two critical line is a bistable region, OPP/AP. Because the two steady states are available in this region, the final state depends on the dynamics. If the magnetization is initially in the P equilibrium, the dynamics in this region, where P is unstable are complicated, and either the magnetization is reversed and the final state is the equilibrium AP state, or the magnetization ends in the OPP dynamic state.

In Fig. 5.3.b, for $H_k = 24$ kA/m or $Q = 0.02$, around the OPP/AP border, the simulations exhibit some "tongues" of OPP (green) inside the AP (blue) region. These are an example that the final state in the bistable OPP/AP region is complicated and depends on the dynamics. It was found that these "tongues" disappear when non-crucial parameters are changed, like the time that the current reaches its nominal value in the current ramp, or the angle between the initial magnetization and the x-axis. On the other hand, the rest of the border between OPP/AP is not changed much by these parameters. As they are very sensitive to small changes of parameters, the "tongues" should not survive in more accurate description of the system, like in micromagnetics simulations, or with the addition of stochastic thermal effects.

Even if the reversal region is not fully described by the analytical study, the effect of the anisotropy was confirmed by the simulations : if the anisotropy field is increased, the range of bipolar switching (blue region) is increased. For instance, if the polarization of the perpendicular polarizer is 0.05, for an almost circular nanopillar with $H_k = 6\,\mathrm{kA/m}$, no bipolar switching is observed in the simulations, only an oscillatory behaviour. However if the nanopillar elliptical cross-section has an aspect ratio of 3, with $H_k = 24\,\mathrm{kA/m}$, it is possible to reverse the magnetization by applying a current density between 5 and 15 $\times 10^{11}$ A/m^2. Interestingly, for large currents, the final state is the OPP steady state.

5.3.2 Micromagnetics simulations

The impact of the anisotropy on the reversal was also confirmed with micromagnetic simulations including an applied current and the two polarizing layers. The free layer is taken cylindrical with an elliptical section of dimensions $105 \times 95 \times 3$ nm^3, that corresponds to $H_k = 6\,\mathrm{kA/m}$, and

$180 \times 60 \times 3$ nm^3, to $H_k = 24$ kA/m. The exchange stiffness constant is set to $1.6{\times}10^{-11}$ J/m, all the other parameters are the same as for the macrospin simulations. The final state after 10 ns is reported on Fig. 5.3 by the symbols. The boundary for the stability of the initial P equilibrium is the same in micromagnetics as in the macrospin model, the orange squares are situated in the red region. This is probably due to the fact that the initial micromagnetic configuration is uniformly magnetized along the x-axis (except at the edges), so the initial micromagnetic configuration is almost macrospin. However the boundary between the bipolar reversal and the precessional state (between AP and OPP) differs in the micromagnetics simulations. It was already mentioned that this region is bistable OPP/AP and that the final state depends entirely on the dynamics. It appears that the OPP steady state is less stable in micromagnetics, principally because the precession is not uniform, so the macrospin picture is not valid anymore. This is illustrated in Fig. 5.4, showing (a,c) the switching and (b,d) the OPP of the free layer for $\eta_{\mathrm{PERP}} = 0.05$ and $\eta_{\mathrm{PERP}} = 0.10$ respectively, with the same aspect ratio of $180 \times 60 \times 3$ nm, corresponding to an anisotropy field of $H_K = 24$ kA/m and an applied current density of J =1e12 A/m^2.
For $\eta_{\mathrm{PERP}} = 0.05$, the reversal of the free layer magnetization is not uniform. Two domains appear in the right and left edges of the sample. The domain formation is rather due to the elliptical shape of the sample, than to the perpendicular polarizer STT, because the domain nucleation also appears without perpendicular polarizer. The reversal occurs in 2 ns.
For $\eta_{\mathrm{PERP}} = 0.10$, the free layer eventually switches, but after an oscillatory phase of 5 ns. The oscillatory phase is not particularly uniform, therefore it seams the oscillation is destroyed because the oscillation becomes more and more spatially incoherent.

As a result, the bipolar switching is favored according to micromagnetics simulations. For large current densities and large perpendicular polarizer spin polarization η_{PERP}, though, a non-uniform, large amplitude out-of-plane precessional motion was observed, in agreement with the macrospin analysis (except for the fact that the precession is non-uniform). Like in the macrospin approximation, a larger anisotropy field favors bipolar switching.

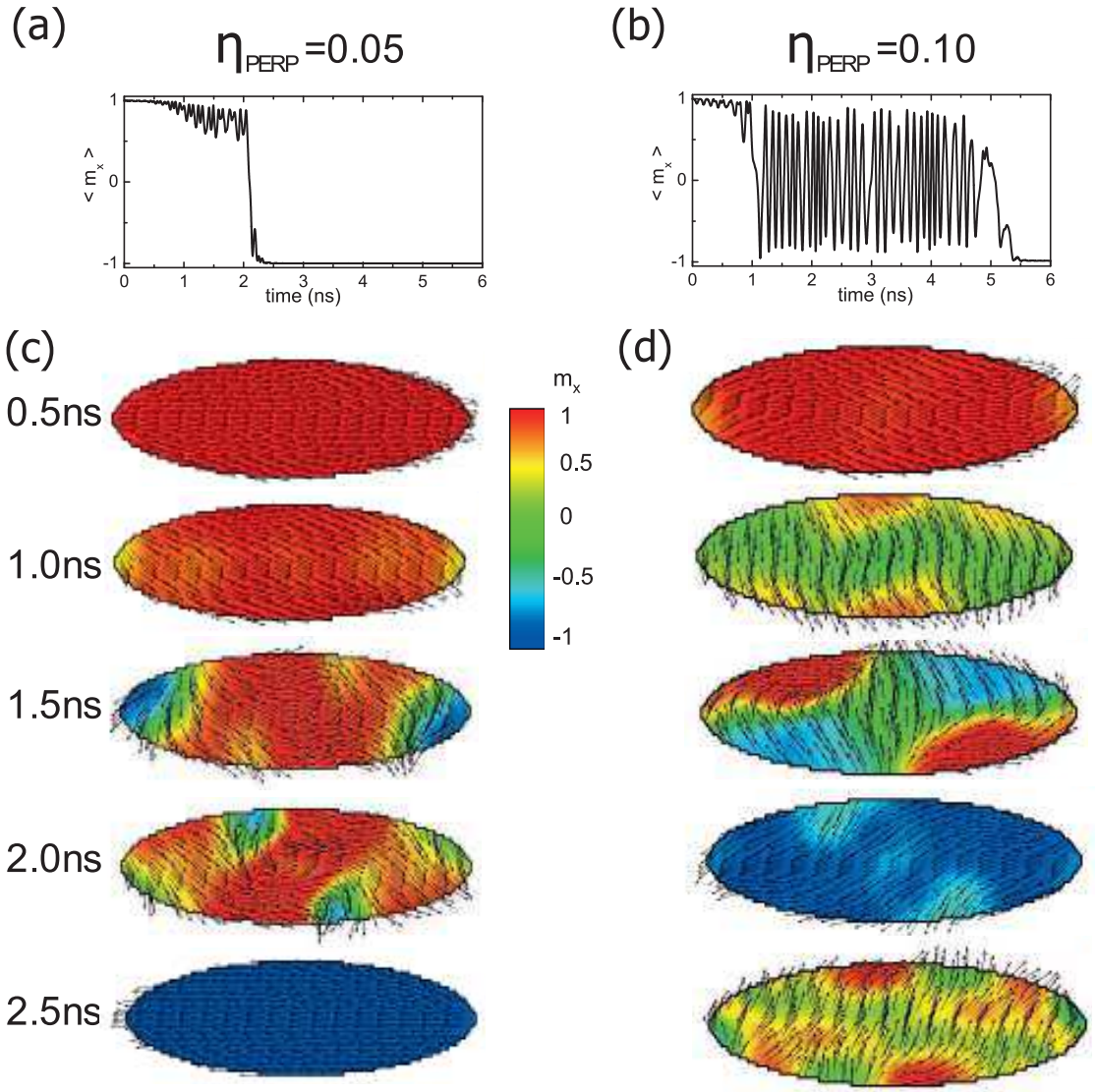

Figure 5.4 – Micromagnetic simulation on a $180 \times 60 \times 3$ nm^3 elliptical sample, corresponding to a shape anisotropy field of $H_k = 24$ kA/m, with an applied current density of J =1e12 A/m^2. The spin polarization of the reference layer is constant $\eta_{\mathrm{LONG}} = 0.3$, and the spin polarization of the perpendicular polarizer is (a,c) $\eta_{\mathrm{PERP}} = 0.05$ and (b,d) $\eta_{\mathrm{PERP}} = 0.10$. (a-b) Average in-plane component of the magnetization along the easy axis, $\langle m_x \rangle$. (c-d) Mapping of the local magnetization at different times. A blue color represents a local P alignment ($m_x = 1$), and a red color a local AP alignment ($m_x = -1$). The arrows represent the magnetization direction. Micromagnetics simulations run by L. Buda-Prejbeanu.

5.4 Experimental results

5.4.1 Description of the samples

In order to demonstrate the impact of the aspect ratio on the switching, we realized in-plane MTJ stacks with a perpendicular polarizer, with different aspect ratios of the ellipse of the nanopillar. Then, the resistance change in the junction was measured in real-time, while a voltage pulse is applied. The samples were realized by M. Marins de Castro and are described in [Marins de Castro 2012]. They consist of, from bottom to top :

Perpendicular polarizer Ta 3/Pt 5/[Co 0.5/Pt 0.4]x5/Co 0.5/Ru 0.9/[Co 0.5/Pt 0.4]x3/Co 0.5/$Co_{60}Fe_{20}B_{20}$ 1 nm

Metallic spacer Cu 3 nm

Free layer $Co_{60}Fe_{20}B_{20}$ 1.3/Ru 0.9/$Co_{60}Fe_{20}B_{20}$ 1.7 nm

Tunnel barrier Mg 0.8 + 10 s natural oxidation at 160 mbar of oxygen pressure /Mg 0.5 nm

Reference layer $Co_{60}Fe_{20}B_{20}$ 3/Ru 0.9/Co 2/IrMn 7 nm

All the layers are synthetic antiferromagnets so that the stray field from one layer to another is much reduced. Therefore the layers can be considered independent from each other from a magnetostatic point of view. The reference layer and perpendicular polarizer are also more stable and stiffer. The perpendicular polarizer is composed of a multilayer of Pt and Co, which perpendicular anisotropy is provided by the [Pt/Co] interfaces.
After deposition, the samples were annealed at 300°C for 90 min under an in-plane magnetic field of 0.23 T. Then the samples were patterned in nanopillars with elliptical cross-section of various aspect ratios. The average TMR signal was found to be about 70% and the RxA product of 17 $\Omega \cdot \mu m^2$ in average. Due to a residual stray field, the antiparallel (AP) alignment is favored in the samples.

The spin polarization of the reference layer and perpendicular polarizer are difficult to estimate. From the TMR value and the formulas of Chapter 1, the spin polarization of the reference layer is estimated around $\eta_{\text{LONG}} = 0.6$ (using the formula for symmetric magnetic electrodes). The reference layer is separated from the free layer by a tunnel barrier, whereas the perpendicular polarizer is separated by a metallic spacer. The TMR and spin polarization of a layer separated by a metallic spacer are smaller than for a tunnel barrier, therefore the spin polarization of the perpendicular polarizer is estimated to be around $\eta_{\text{PERP}} = 0.2 - 0.3$. So the ratio of the two spin polarization should dwell roughly in the region on Fig. 5.3 that is bistable OPP/AP, where the anisotropy field of the layer and its aspect ratio can change the dynamics.

The macrospin (and micromagnetic) simulations presented in this chapter concern almost exclusively single layer free layers, nonetheless the free layer is a SAF in the experimental stack. According to Chapter 3, the SyF free layer behaves qualitatively like a single layer free layer in the high-coupling regime, with the STT of the reference layer (RL) and of the perpendicular

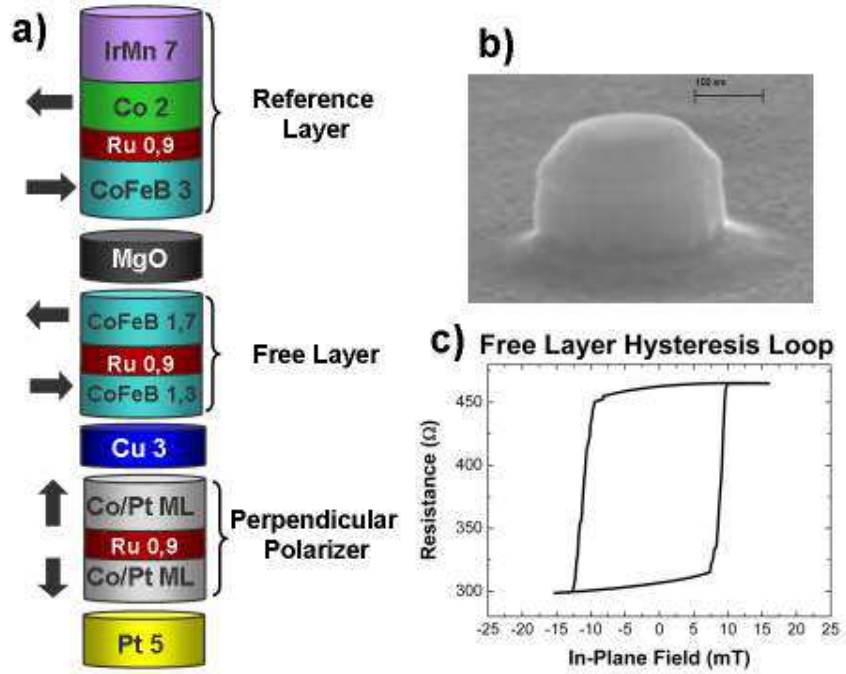

Figure 5.5 – (a) Description of the magnetic stack, comprising an in-plane reference layer, an in-plane free layer and a perpendicular polarizer, from top to bottom. (b) MeB image of one nanopillar. (c) Typical hysteresis loop of the nanopillars. The residual stray field favors the AP alignment.

polarizer (PP) taken separately. Here, the RKKY coupling is larger than 1e-4 J/m^2, from the hysteresis loops measured on a stack comprising only the free layer, so $K \ll 1$ with the definition of Chapter 3. The assumption of high-coupling regime is justified. The critical current I_{c1}^{PERP} for the bifurcation IPS/OPP for a SAF free layer corresponds to the critical current of a single layer of same magnetic volume. The critical current I_c^{LONG} for the instability of the P configuration of a SAF free layer corresponds to the critical current of a single layer with the same magnetic volume, but with the demagnetizing field enhanced by the RKKY field. Therefore, the SAF free layer with the two polarizers is expected to show a similar behavior than a single layer free layer.
On the other hand, the SAF free layer has a reduced stray field, so the other layers are less affected by its presence. It is especially critical for the perpendicular polarizer, which could become magnetized in plane due to the stray field of the free layer.

5.4.2 Experimental setup

The magnetic junctions are connected to a resistance-versus-field measurement bench. In parallel to this setup, at any given field, it is possible to send a voltage pulse of 10 ns width through the nanopillar and measure the transmitted voltage with an oscilloscope in real-time. For our purpose, the pulse is sent in the bistable region, namely in the center of the hysteresis loop. The hysteresis loop is shifted because of the stray fields from other layers, so the center of the

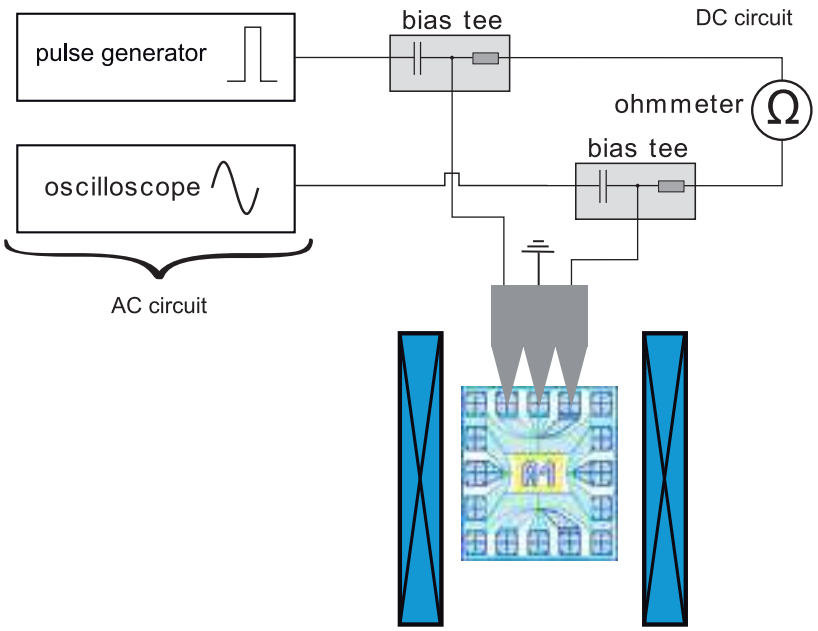

Figure 5.6 – Schematics of the electrical circuit. The two circuits, DC and AC are in parallel : DC for the resistance measurement and AC for the real-time measurement of the transmitted pulse.

hysteresis loop is not exactly zero. The current pulse is sent at the field that compensates the stray field. This field is called the write-field because it is the field at which the memory cell is written. The experiment is to mimic the write-sequence of a memory cell, which is realized without applied field ideally. By optimization of the structure (for instance by changing the layer thicknesses), the stray field may be further reduced, and the hysteresis loop become centered around zero field. Therefore, the magnetization is reversed or not, depending on the current polarity, by the current (or voltage) pulse.
An experiment at constant field could also be realized, however the hysteresis loop gives information about domain formation, reversal of the reference layer, etc... Therefore, it is interesting to measure it. Moreover, the free-layer magnetization must be saturated in the P or AP configuration before sending the current pulse. This is realized when the hysteresis loop is measured. The measure is done sequentially as follows (see also Fig. 5.7.b and c) :

1. The field is incremented, the DC resistance is measured and the field incremented again, until the value of the write-field is reached.

2. At the write-field value, and after the field is set, a voltage pulse is sent in the junction.

3. The transmitted pulse is recorded on the oscilloscope.

4. The DC resistance is measured. Then the field is incremented until all the hysteresis loop is captured.

The switching probabilities versus pulse duration are obtained using the hysteresis loops. The DC resistance measured after the pulse application is compared to the resistance of the

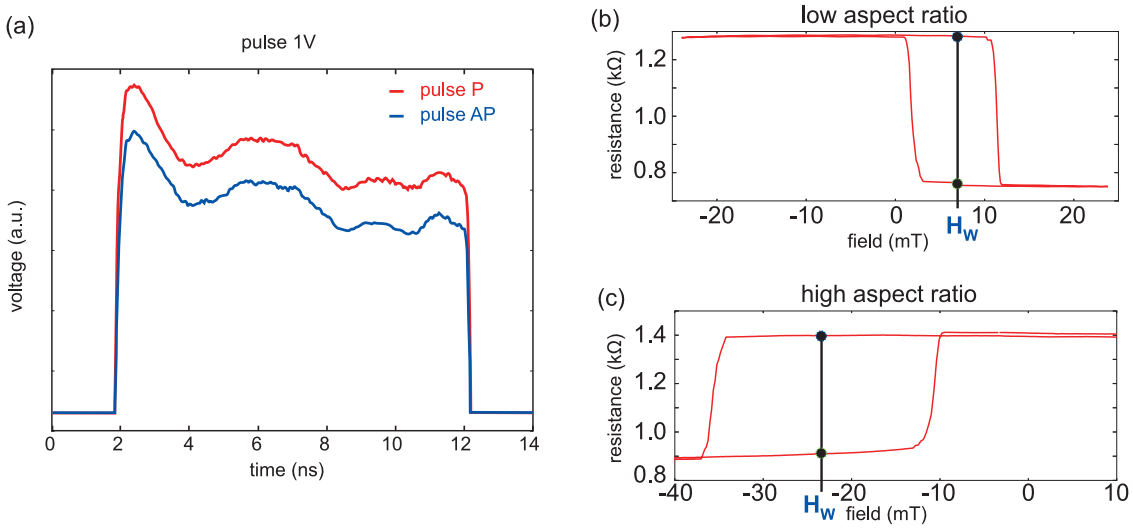

Figure 5.7 – (a) Transmitted pulse with a 10 ns applied pulse of 1 V, with the junction saturated with an external field in the P (red) and AP (blue) configurations. (b) and (c) Hysteresis loops of samples with low and high aspect ratio, respectively. The field scale (x-axis scale) is the same on both figures for comparison. The voltage pulse is sent at the write-field H_W, when the field is increasing or decreasing, corresponding to an initial P or AP state.

junction before the pulse. By repeating several times the measurement of the hysteresis loop with the pulse sent at the same write-field, the probability of switching with a particular current polarity, current amplitude, pulse duration and write-field is obtained. The pulse width ranges from 100 ps to 10 ns typically. This measurements is even closer to nominal MRAM working conditions, however it does not catch the magnetization dynamics during the application of the pulse.

This information is extracted from the transmitted pulse recorded on the oscilloscope. If the magnetization switches during the pulse application, the resistance of the junction will change and the transmitted pulse amplitude also. We recall that the resistance of the junction and the TMR depend on the projection of the magnetization along the x-axis, which is the orientation axis of the reference layer magnetization.
The TMR depends on the voltage set on the junction (see Fig. 1.4), so the resistances in the P and AP configuration must be measured for every particular amplitude of the voltage pulse. For that purpose, the MTJ is saturated beforehand with an external magnetic field in the parallel (P) configuration, several pulses are sent and the average transmitted voltage is saved for reference. The same procedure is applied in the antiparallel (AP) configuration. Because of the external field, the magnetization of the free layer remains fixed during the pulse application. These two measurements serve as reference for the value of the resistances in P and AP state under an applied pulse. Namely, the saturated pulse in the AP state is subtracted from the transmitted pulses measured at the write-field. The transmitted pulses in the two saturated states, P and AP, are shown on Fig. 5.7.a, with an applied pulse of 1 V and 10 ns duration.

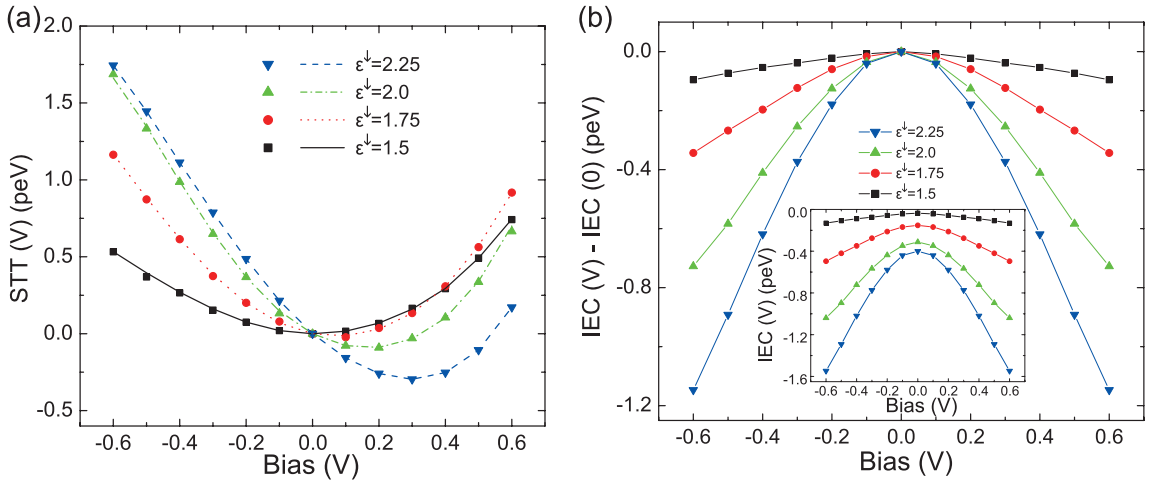

Figure 5.8 – Bias dependence of (a) STT and (b) IEC for an angle between the free and reference layer of $\pi/2$. The different symbols and colors represent different values of the spin-splitting $\Delta = \epsilon^{\uparrow} - \epsilon^{\downarrow}$ in the ferromagnetic materials, with $\epsilon^{\uparrow} - E_F = 1.2$ eV. From [Theodonis 2006].

The transmitted pulse is almost rectangular, with an overshoot at the rising edge and small oscillations in the high voltage state. Despite these two anomalies, the difference between the two configurations, P and AP, is constant in the high level, so the difference of the two signals is a rectangular pulse.

As already mentioned (see Fig. 5.7.b and c), the AP state is favored. And even if an in-plane field is applied along the easy axis to compensate for the stray field, it is still very difficult to see any switching or oscillations of the resistance when the magnetization is initially in the AP configuration. In the following, the experiments shown are for the magnetization initially in the P state. Additionally, only one polarity of the current is shown, the polarity that triggers the switching from P to AP. With the other polarity, the effects are less pronounced.
The asymmetry between the P and AP initial configuration may also reflect an influence of the spin polarization asymmetry λ_{LONG}, which is not included in the macrospin analysis. Another possible cause of the asymmetry between the two current polarities lies in the IEC, or field-like, term, b_J, which was not taken into account in the simulations either. According to recent publications[Theodonis 2006, Oh 2009], the IEC torque is quadratic with respect to the applied current in symmetric MTJ, whereas the STT is linear, as shown on Fig. 5.8. Thus, the two current polarities contribute identically to the IEC, whereas they have an opposite effect on the STT, that is responsible for the bipolar switching of MTJ due to an applied current. In fact, the IEC favors the AP configuration, independently of the current polarity. The IEC favors the switching from P to AP, but it is detrimental to the switching from AP to P.

For a more precise description of the experimental results with the other polarity and switching direction, refer to [Marins de Castro 2011], although only statistics of switching are shown, no real-time measurements.

5.5 Experiments low AR

5.5.1 Oscillation of the resistance

In this section, samples with an elliptical cross-section of low aspect ratio are measured. The aspect ratio is around 2:1, with nominal sizes of 170x70x3 nm (140:40). The coercive field is measured from the hysteresis loops to be around 3 kA/m (see Fig. 5.7.b). The coercive field is a low estimate of the anisotropy field, which is then considered small in this series of samples. In these samples the effect of the perpendicular polarizer is dominant, so an oscillation of the free layer magnetization around the out-of-plane axis is expected.
From macrospin simulations for $H_k = 6$ kA/m and $\eta_{\mathrm{PERP}} = 0.05$, the diagram of the final state, with an initial P alignment, versus pulse duration and current density is expected to show alternating P and AP regions, or more precisely switching and no-switching alternating regions, as shown on Fig. 5.9.a. Above the critical current, the magnetization of the free layer is expected to oscillate, so the resistance of the junction will also oscillate around its P and AP values, as shown on Fig. 5.9.b. The frequency of the oscillations should increase with increasing current.

Fig. 5.10 shows the transmitted voltage when sending a pulse of 10 ns at different voltages : 1.0V, 1.12V, 1.26V and 1.42V, through the MTJ. The reference signal in AP state was subtracted from the data. In these voltages range, the magneto-resistance oscillates between the two values corresponding to AP and P resistance level (black curve). This large amplitude oscillation is characteristic of the action of the perpendicular polarizer. Moreover, the increase of the oscillation frequency with the increase of the pulse amplitude is characteristic of OPP. However, the oscillations exhibit a high noise level. Indeed, the oscillation period varies with time on the single-shot traces (green curve), and sometimes, one oscillation is "missing", like for instance between 8 and 10 ns at 1.26 V on Fig. 5.10. The oscillation decoherence is responsible

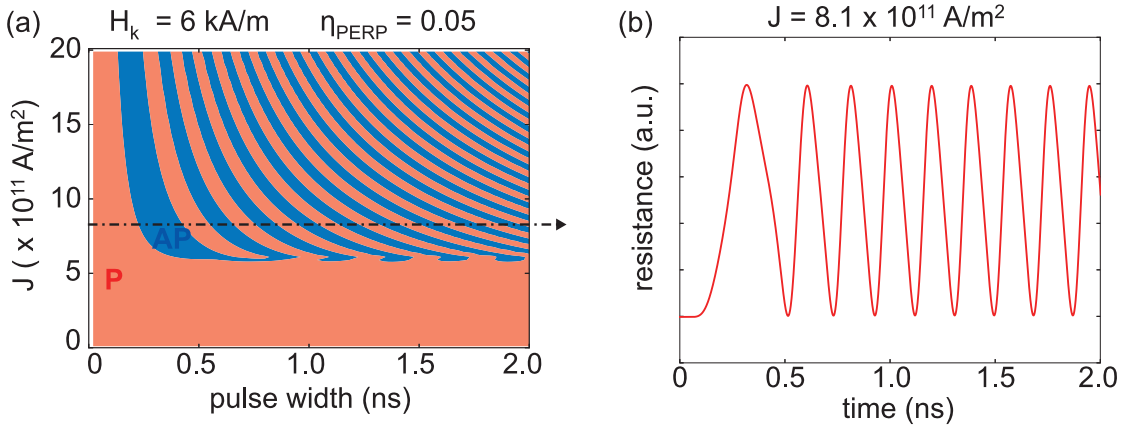

Figure 5.9 – Macrospin simulations for $H_k = 6$ kA/m and $\eta_{\mathrm{PERP}} = 0.05$, in the initial P configuration. (a) Final state versus pulse duration and current density. Alternating P (red), switching, and AP (blue), no-switching. (b) Resistance versus time for a current density of $J = 8.1\mathrm{e}11$ A/m^2.

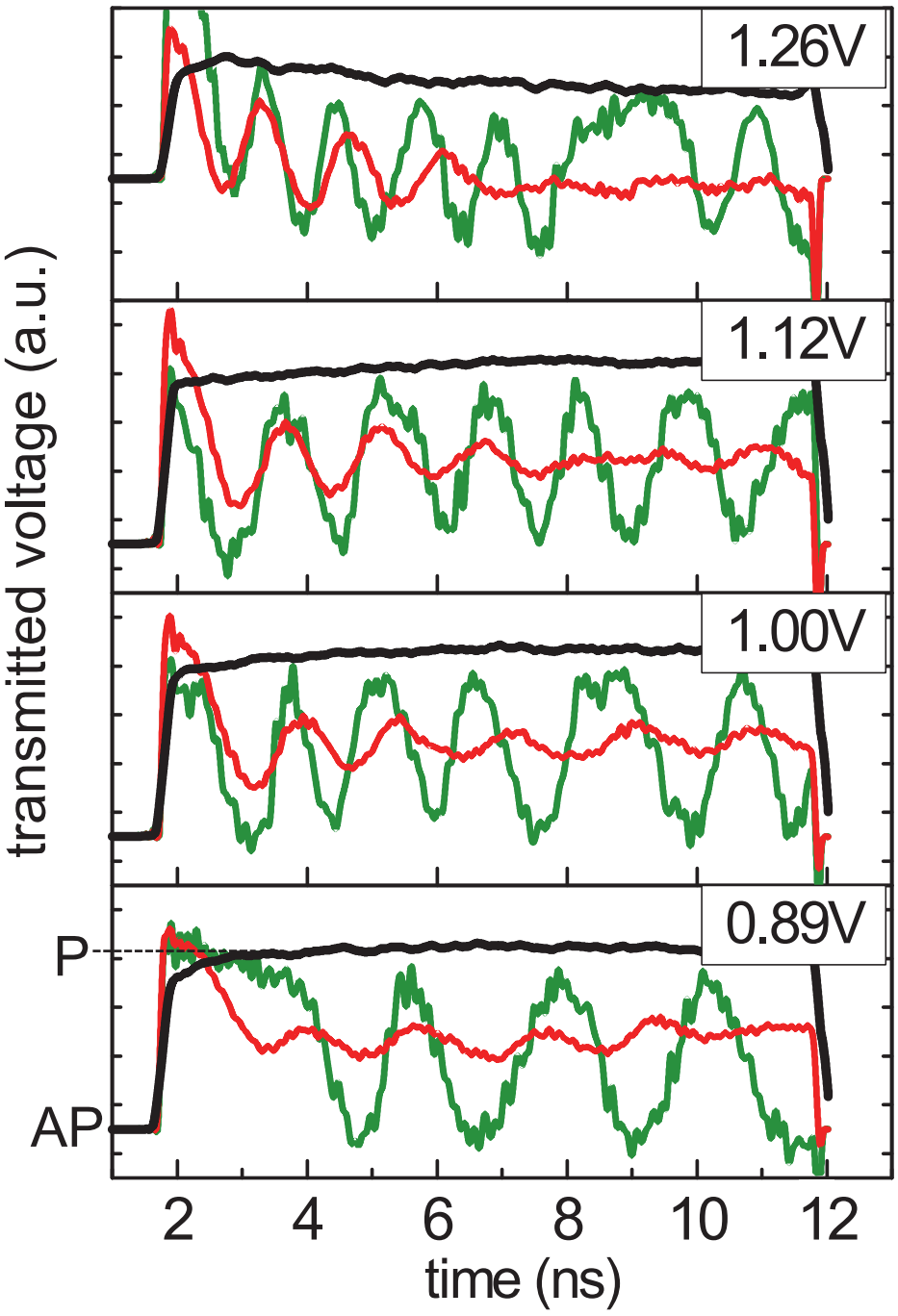

Figure 5.10 – Low aspect ratio MTJ. Transmitted voltage with an applied voltage pulse of 0.89 V, 1.00 V, 1.12 V and 1.26 V (from bottom to top). The MTJ is initially in P state. In green, a single-shot trace. In red, average of 50 traces. In black, difference of resistance between the AP and the P state saturated with an external field, for reference. The low level corresponds to the AP state, the top level to the P state.

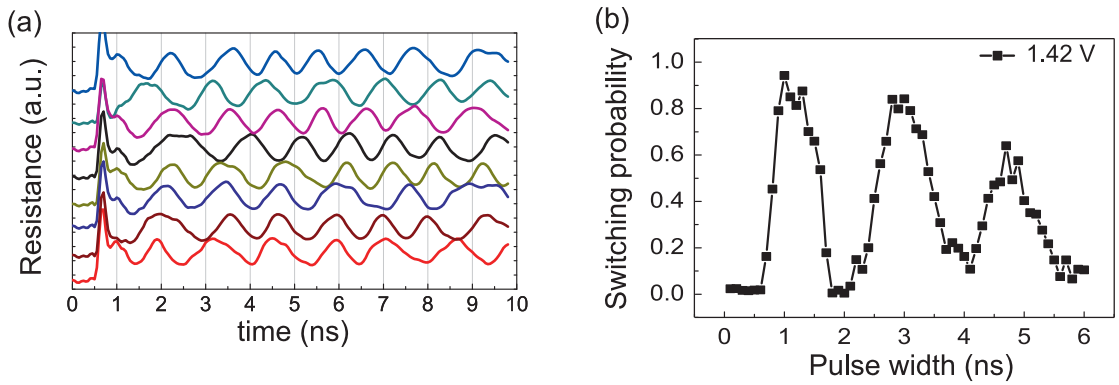

Figure 5.11 – Low aspect ratio MTJ at room temperature. (a) Single-shot traces for the same applied voltage pulse of 1.42 V. A low-pass filter at 3 GHz was applied. (b) Switching probability of an MTJ initially in P state versus applied voltage pulse width. The pulse amplitude is constant and set to 1.42 V.

for the damped oscillation of the average trace over 50 single-shots (red curves).
In order to study the oscillation decoherence, several single-shots at the same pulse amplitude of 1.42 V are compared in Fig. 5.11.a. From this figure, we conclude that the oscillation is not coherent, the frequency is not well defined and the single-shot signals are phase shifted, likely due to thermal fluctuations. Therefore, the oscillation of the magneto-resistance is attenuated on the average trace of 50 single-shots shown in Fig. 5.10 (red color). Because the oscillations are not very coherent, a decay is also observed on the amplitude of the switching probability. In Fig. 5.11.b, the switching probability from P to AP is shown for a voltage pulse of 1.42 V with different pulse width, from 10 ps to 6 ns. Because the magnetization is oscillating between the P and AP state during the pulse application, the final state will depend on the pulse width. We observe an oscillation of the switching probability, with a decay of the oscillation amplitude due to decoherence.

5.5.2 Temperature dependence

In order to investigate the origin of the decoherence, the same experiment was realized at different temperatures, down to 80 K. This experiments were realized at *Institut d'électronique fondamentale* in Orsay, in collaboration with T. Devolder.

The transmitted voltage of an applied pulse of 1 V, 1.12 V, 1.26 V and 1.42 V was recorded at different temperature : 80 K, 160 K, 240 K, 300 K and 400 K (with a risk of breaking the junction at this temperature).
Fig. 5.12.a shows a single-shot for an applied pulse of 1.26 V at the different temperatures. Although the frequency is the same whatever the temperature, there are more oscillation failures at high temperature. In fact, the average of one hundred single-shots shows no oscillations, except at 80 K, because of the high decoherence due to the thermal fluctuations.
The frequency of the oscillations depends linearly on the applied voltage, as shown in Fig. 5.12.b, and the slope is the same at all the measured temperatures. The expression of the OPP

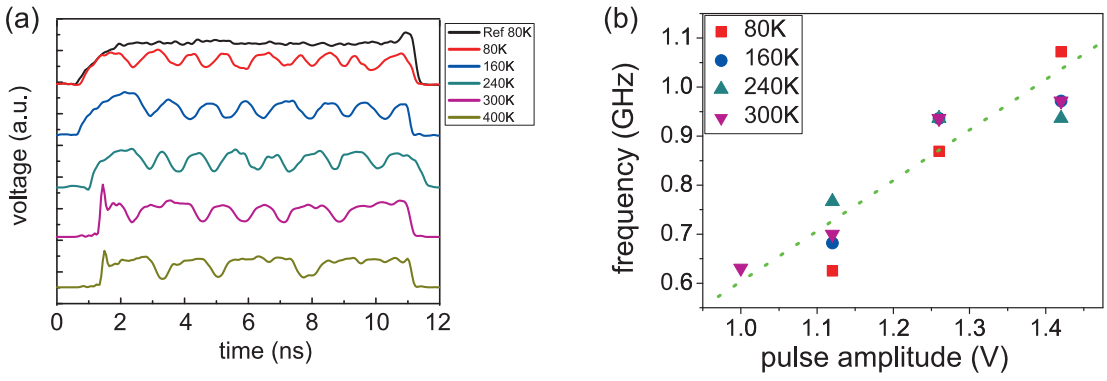

Figure 5.12 – Low aspect ratio MTJ. (a) Single-shot transmitted voltage with a pulse of 1.26 V at different temperature (from top to bottom) : 80 K, 160 K, 240 K, 300 K and 400 K. The P reference voltage is shown at 80 K (black line). (b) Oscillation frequency versus applied voltage pulse at different temperatures. The dependency is almost linear. Measurements realized with T. Devolder in *IEF*, Orsay.

frequency f_0 with a perpendicular polarizer was given in Chapter 2 and is recalled here :

$$f_0 = I\frac{\hbar}{2e}\frac{\gamma}{2\pi V}\frac{\eta_{\mathrm{PERP}}}{\alpha M_S} \tag{5.13}$$

The fact that the slope is the same for every temperature could be interpreted by an analogous temperature dependence of the saturation magnetization and of the spin polarization of the perpendicular polarizer, if the damping constant and the junction resistance temperature dependence are supposed to be negligible. However, given the uncertainty on the value of the frequency and the fact that the macrospin model with the STT from the perpendicular polarizer alone, is a crude approximation of the actual physical system, no definite conclusion is held.

The precession coherence is largely affected by temperature. In fact, the thermal fluctuations are responsible for the broad linewidths encountered in spin-torque nano-oscillators, which were presented in Chapter 2. Fig. 5.13.a shows the frequency spread for different applied currents from a spectrum analyzer. This experiment was realized on in-plane spin-valves with a perpendicular polarizer from [Houssameddine 2007]. Fig. 5.13.b is the windowed fast-Fourier transform of the oscillating voltage at different times (on the y-axis). It shows that the instantaneous frequency is not constant in the time.
From Fig. 5.11.b, the linewidth is estimated by the relaxation time of the switching probability oscillations to be around 100 MHz. It is of the same order of magnitude as the linewidth obtained is spin-valves, from the width of the Lorentzian spectrum in Fig. 5.13.a.

5.5.3 Influence of an in-plane transverse field

The precession is affected by an external field. The experimental setup allows to send the pulse at any given field. This allows to study the effect of an external field applied along the easy axis ($\boldsymbol{u}_x$). In fact, the effect of a field along the easy axis on the OPP of an in-plane free layer

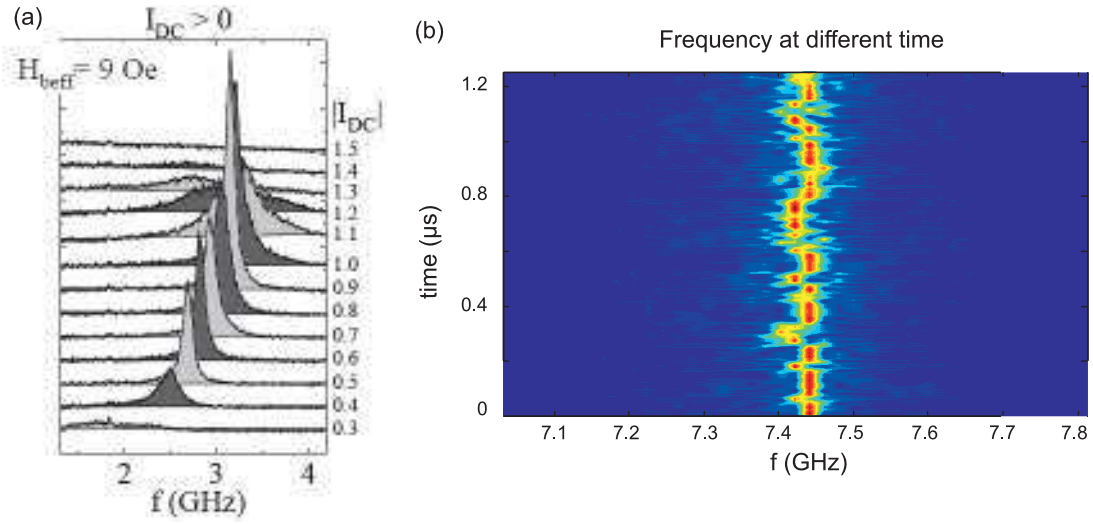

Figure 5.13 – (a) Spectrum analysis of an in-plane spin-valve with a perpendicular polarizer at different applied currents. (b) Spectrum analysis at different time for the same applied current. From [Houssameddine 2007].

with a perpendicular polarizer, and more particularly its effect on the critical current I_{c1}, are described in [Ebels 2008], and was reported in the state diagram of Fig. 2.7.c. The critical current I_{c1} depends linearly on the applied field.
In this section, we are considering a field applied in-plane in the transverse direction, along the hard axis $\boldsymbol{u}_y$, and we are studying its influence on the precession, both theoretically and experimentally.

To start with, the effect of the in-plane transverse field on the dynamics of a single layer free layer with a perpendicular polarizer only (no STT from the reference layer) is studied analytically.
The influence of a transverse applied field on the out-of-plane precessional motion induced by a perpendicular polarizer can be treated in a similar way as for an applied field along the easy axis as described in the paper [Ebels 2008].
Using the same formalism and expressing the magnetization in spherical coordinates, we obtain a couple of equations that describe the in-plane steady state (IPS), like eq. 2.11 in Chapter 2 :

$$\cos\theta_0 = 0 \qquad \text{and} \qquad -\frac{H_K}{2}\sin(2\phi_0) + H_y\cos\phi_0 = \bar{\eta}I \tag{5.14}$$

where (θ_0, ϕ_0) are the angles in spherical coordinates of the equilibrium free layer magnetization, H_k is the uniaxial anisotropy field, H_y is the transverse applied field along the hard axis (y-axis), I is the applied current and $\bar{\eta} = \dfrac{\hbar}{2e}\dfrac{\eta_{\mathrm{PERP}}}{\mu_0 M_S V}$ is proportional to the spin polarization of the perpendicular polarizer η_{PERP}.

The critical current for the existence of the IPS equilibrium is computed by finding the

extrema of the left-hand side of the second expression with respect to ϕ_0. The extrema is computed by derivation with respect to ϕ_0 :

$$\frac{d}{d\phi_0}\left(-\frac{H_K}{2}\sin(2\phi_0)+H_y\cos\phi_0\right)=0 \tag{5.15}$$

The solution of this equation is given in terms of $\cos(2\phi_0)$, because without transverse field $\cos(2\phi_0)$ is vanishing for the value of the critical current according to the results of Chapter 2, and because without applied current, the initial in-plane angle ϕ_i is 0 in the P configuration, or π in the AP configuration, so that $\cos(2\phi_i)$=1. Hence, without applied field, $\cos(2\phi)$ goes from 1 to 0 when the current is increased. For a small applied transverse field, namely $H_y \ll H_k$, $\cos(2\phi)$ is also expected to decrease from 1 to almost 0.
From the previous equation, the extremal value of $\cos(2\phi)$ is :

$$\cos(2\phi_0)=\left(\frac{H_y}{2H_k}\right)^2\left[\pm\sqrt{2+\left(\frac{H_y}{2H_k}\right)^2}-1\right] \tag{5.16}$$

There are two solutions for $\cos(2\phi_0)$. However, because the in-plane angle in the initial configuration verifies $\cos(2\phi_i)=1$, the extremal value of $\cos(2\phi)$ of interest here is the positive solution of $\cos(2\phi_0)$ because it will be the first reached when the current is increased. Moreover, small transverse fields are considered, so $\cos(2\phi_0)\approx\left(\frac{H_y}{2H_k}\right)^2\left(\sqrt{2}-1\right)$.

The value of the extremal in-plane angle is injected in eq. 5.14, so the value of the critical current for small transverse fields ($H_y \ll H_k$) is given by :

$$I_{c1}^{PERP}=\frac{2e}{\hbar}\frac{\mu_0 M_S V}{\eta_{\mathrm{PERP}}}\frac{H_K}{2}\left(1+\ell\sqrt{2}\frac{H_y}{H_k}\right) \tag{5.17}$$

Where ℓ is the sign of $-\sin\phi_0$, which is also given by $\ell=\mathrm{sign}(I)\,\mathrm{sign}(\cos\phi_i)$. For instance, for positive currents with an initial P configuration ($\cos\phi_i=1$), the critical current for the IPS/OPP transition is enhanced by a positive transverse field.

This expression can be easily obtained for the case of a single-layer free layer with only the STT from the perpendicular polarizer. The samples used for the measurements are composed of a SAF free layer and contain a reference layer, though, for which such an analytical expression is more complicated to derive.

Instead, numerical simulations of the system using the macrospin model were performed. The free layer is composed of two layers, respectively 2nm and 1nm thick, antiferromagnetically coupled by an RKKY interaction of amplitude $J_{int}=10^{-4}$ J/m^2. The spin polarization of the reference layer is $\eta_{\mathrm{LONG}}=0.3$. The saturation magnetization of both layers is the same, M_S=1.2e6 A/m, as well as the Gilbert damping parameter α=0.02. The uniaxial anisotropy field is of 6 kA/m and the spin polarization from the perpendicular polarizer is $\eta_{\mathrm{PERP}}=0.05$. The initial free layer magnetization is set in the P configuration. Fig 5.14.a shows a calculated

state diagram representing the state of the system in the permanent regime versus an applied current density J and a transverse applied field H_y. The diagram shows three regions. The P-IPS (AP-IPS) region corresponds to an in-plane static state in an almost parallel (antiparallel) configuration. The OPP region corresponds to the out-of-plane precession. With no applied field, there is a bifurcation at around 3e11 A/m^2 between the equilibrium state (P-IPS) and the precessional state. The AP-IPS region corresponds to a reversal of the magnetization. Notice that the diagram is similar for a single layer free layer without STT from the reference layer. Hence the existence of the three regions is only due to the transverse field.
For small applied fields, the critical current between the P-IPS and OPP region is linear with respect to H_y, similarly to the analytical expression found above for a single-layer free layer.

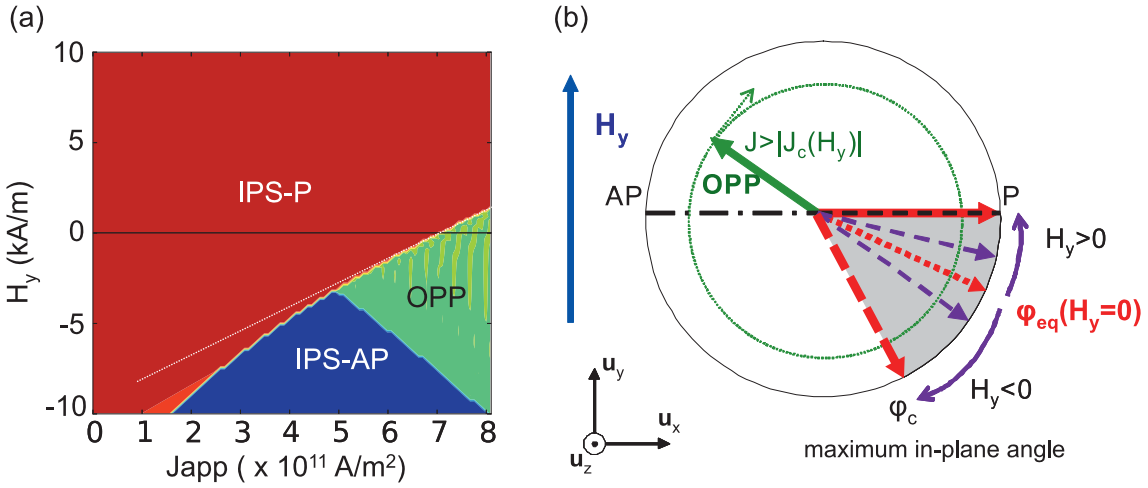

Figure 5.14 – a) State diagram with critical lines and regions representing the three possible steady states of the system with an initial P configuration : P-IPS and AP-IPS region for the in-plane steady state in canted parallel, or antiparallel respectively, equilibrium; OPP for the region of out-of-plane precession. (b) Schematic of the P-IPS and OPP steady states. OPP : without transverse applied field and for current densities larger than the critical current density J_{c1}, the magnetization rotates around the z-axis (green dotted-circle). P-IPS : without transverse applied field, when increasing the applied current density from zero (red full-arrow) to J_{c1} (red dashed-arrow), the magnetization relaxes to an equilibrium in-plane configuration (red dotted-arrow), characterized by the in-plane angle φ_{eq}. This equilibrium exists as long as φ is smaller than the critical angle φ_c. For a given applied current density (red-dotted arrow), a positive transverse applied field shifts the equilibrium towards the AP state and a negative field shifts it towards the critical angle φ_c (both purple dashed-arrows).

The effect of an in-plane transverse field on the IPS state is synthetized in Fig 5.14.b. For a given current density for which the system is in IPS for zero field, a positive transverse field brings the magnetization equilibrium closer to the AP state along the easy axis. A negative transverse field brings the magnetization closer to the critical in-plane equilibrium angle, and for large enough field the magnetization exceeds the critical angle and enters the OPP state. For instance, with an applied current density of 7.5e11 A/m^2, the free layer magnetization is in OPP state for no applied transverse field. If a hard axis positive field of more than

+2 kA/m is applied, the magnetization remains in a steady state slightly canted with respect to the parallel configuration. If a negative hard axis field of more than -9 kA/m is applied, the magnetization switches from the parallel to another configuration slightly canted from the antiparallel configuration.

The influence of the transverse applied field appears also in the time-evolution of the magnetoresistance, in the simulations and experimentally, as seen in Fig. 5.15. In Fig. 5.15.a the time-traces are calculated for the same same applied current density of 7.5e11 A/m and at different fields. These simulations correspond to moving on the same vertical line at $J = 7.5e11$ A/m^2 in Fig 5.14.a. Fig 5.15.b shows experimental time-traces measured for the same 10 ns pulse of 1.26 V. Both figures show the same behavior when applying a transverse field. With no hard axis applied field, the free layer magnetization precesses around the out-of-plane axis. By applying a positive field, the appearance of the precessions is hindered. And if the positive applied field is large enough, the free layer magnetization does not precess and stays in the parallel configuration. On the contrary, with a negative field, the precession appears faster. In the simulation, at -10 kA/m, there is an ultra-fast reversal of the magnetization which takes place within 200 ps. Experimentally, this threshold was above the maximum applicable field.

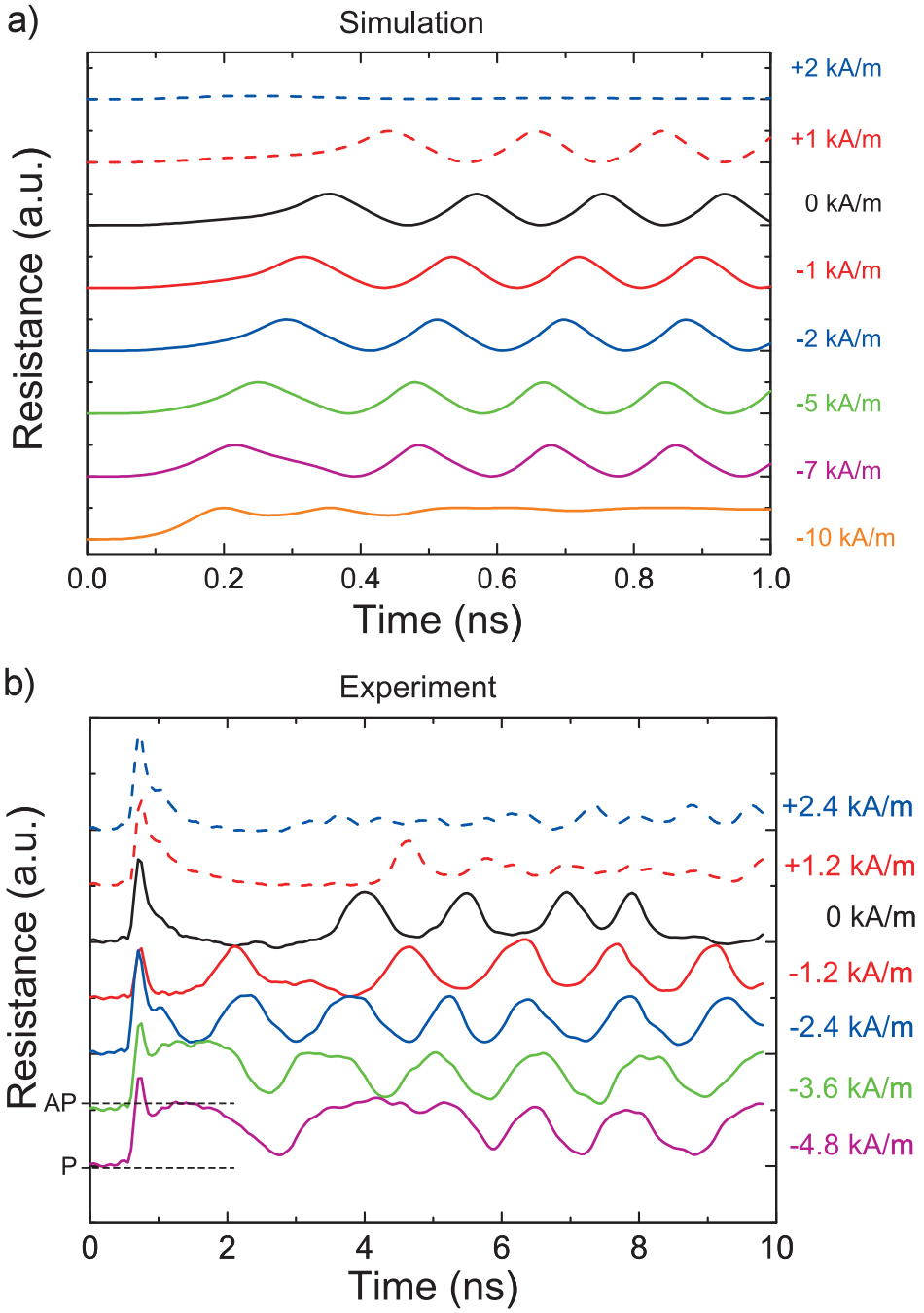

Figure 5.15 – Resistance of the junction versus time for different in-plane transverse fields : (a) From macrospin simulations with a fixed current density of 7.5e11 A/m^2. The magnetization is initially in the P state, corresponding to a low resistance; b) From experimental data obtained with the time-resolved transmission setup with an applied pulse of 1.26 V. For a positive transverse field, the out-of-plane precessions (OPP) are suppressed, and for negative fields the system reaches the OPP state faster. The initial peak is an artefact due to the substraction with the saturated P resistance. The different curves are offset for clarity. Real-time measurements realized with T. Devolder in *IEF*, Orsay.

5.6 Experiments high AR

According to the different results on the decoherence of the oscillations, it seems difficult to achieve accurate precessional switching with a half-precession, because the pulse width has to be tuned with 100 ps precision due to the stochasticity of the oscillation frequency and phase. To realize a bipolar switching independently of the pulse width, it is important to increase the influence of the reference layer, for instance by increasing the aspect ratio of the ellipse of the nanopillars.

5.6.1 Magnetization reversal

Consequently, we measured samples with a higher aspect ratio of 4:1, with nominal sizes of 260x70x3 nm (230:40). The in-plane anisotropy field is estimated by measuring the coercive field, which was found to be around 10 kA/m (see Fig. 5.7.c). The anisotropy field is thus considered large in these samples.

From the macrospin simulations, the diagram of the final state when the magnetization is initially in P state, and after applying a pulse, is plotted versus the pulse width and the pulse amplitude in Fig. 5.16.a. For these simulations, the spin polarizations of the reference layer and of the perpendicular polarizer are respectively of $\eta_{\mathrm{LONG}} = 0.3$ and $\eta_{\mathrm{PERP}} = 0.05$. The anisotropy field is set to $H_k = 24$ kA/m. The other parameters are the same as previously, with a single layer 3 nm thick free layer. The critical current density for bipolar switching is around 8e11 A/m^2. From 8 to 18e11 A/m^2, the junction is reversed if the pulse width is large enough. The higher the applied current, the faster the magnetization is reversed. Above 18e11 A/m^2, the free layer magnetization oscillates, like for the previous case of a low aspect

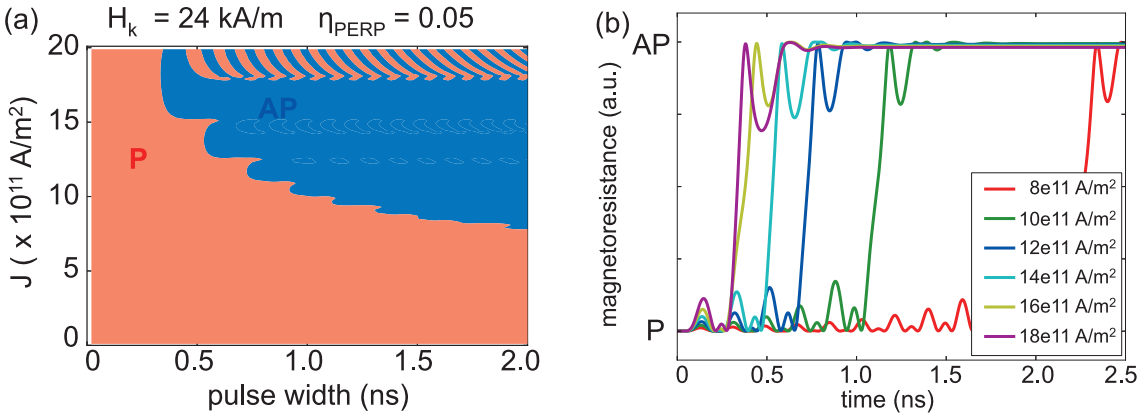

Figure 5.16 – Macrospin simulations for $H_k = 24$ kA/m and $\eta_{\mathrm{PERP}} = 0.05$, in the initial P configuration. (a) Final state versus pulse duration and current density. Alternating P (red), switching, and AP (blue), no-switching. (b) Resistance versus time for different current densities, from 8 to 18 $\times$ 10^{11} A/m^2. The resistance oscillates for higher current densities.

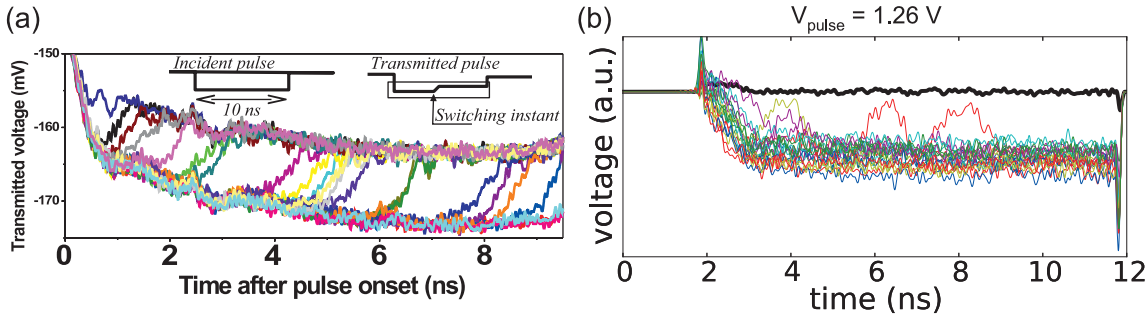

Figure 5.17 – (a) Transmitted voltage with an applied pulse through an in-plane MTJ without perpendicular polarizer. From [Devolder 2008]. (b) Transmitted voltage, with an applied pulse of 1.26 V, on an in-plane MTJ with perpendicular polarizer and a large aspect ratio.

ratio. The "tongues" of OPP from the diagram of Fig. 5.3 are visible in this diagram also.
The magnetization reversal for different applied current densities is shown on Fig. 5.16.b. The oscillatory regime at high current is not shown. Compared with simulations without perpendicular polarizer ($\eta_{\mathrm{PERP}} = 0$), the switching time is decreased by a factor 2. The reversal occurs after some oscillations around the equilibrium configuration, like without perpendicular polarizer, however these initial oscillations have larger amplitudes and the magnetization reaches the saddle-point faster.

Thus, the perpendicular polarizer allows a faster switching, and because the torque it generates on the free layer magnetization is orthogonal to the equilibrium configuration, the reversal is more deterministic than without the polarizer. This was confirmed by measurements on the samples with a high aspect ratio.
Fig. 5.17.a represents single-shots of the transmitted voltage after applying a pulse through an in-plane MTJ without perpendicular polarizer, from [Devolder 2008]. The reversal occurs at different times, between 1 ns and 9 ns : the reversal depends strongly on thermal fluctuations. Even if the reversal itself last less than 500 ps, the incubation time can be up to 10 ns. For the fabrication of memories, it is necessary to send pulses of at least 10 ns to be sure (or at least with a small error rate) that the magnetization is reversed.
On the contrary, single-shots of the reversal of an in-plane junction with a perpendicular polarizer is shown on Fig. 5.17.b. The reversal is initiated as soon as the pulse is applied, resulting in a fast and coherent reversal. Indeed, the magnetization was reversed in 1 ns for 17 single-shots out of 20. For the last three attempts, the magnetization had one or two extra precessions, or back-hopping, before settling in the AP configuration.

The transmitted voltage for different applied pulse amplitude of 0.89 V, 1.0 V, 1.12 V and 1.26 V, is displayed in Fig. 5.18. The reference signal in the P configuration is shown in black. A single-shot for each voltage pulse is shown (green line), as well as the average of 50 single-shots (red line). Close to the critical current (0.89 V), the magnetization switches in 4 ns in average. The switching time is decreased to 1 ns at 1.26 V. However, at this pulse amplitude,

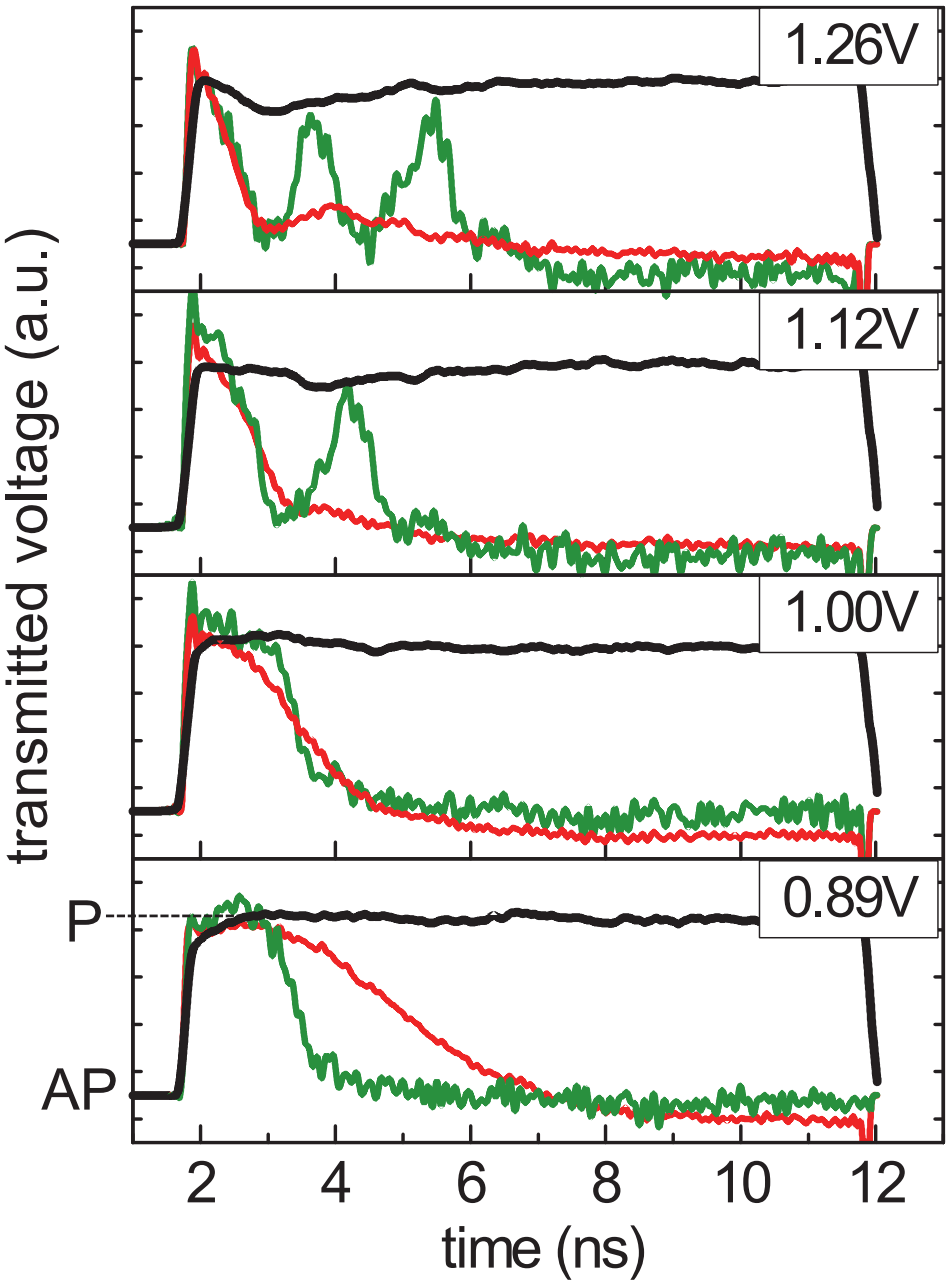

Figure 5.18 – High aspect ratio MTJ. Transmitted voltage with an applied voltage pulse of 0.89 V, 1.00 V, 1.12 V and 1.26 V (from bottom to top). The MTJ is initially in P configuration. In black, reference resistance in the P state taken with an external field to saturate the junction. In green, a single-shot trace. In red, average of 50 traces.

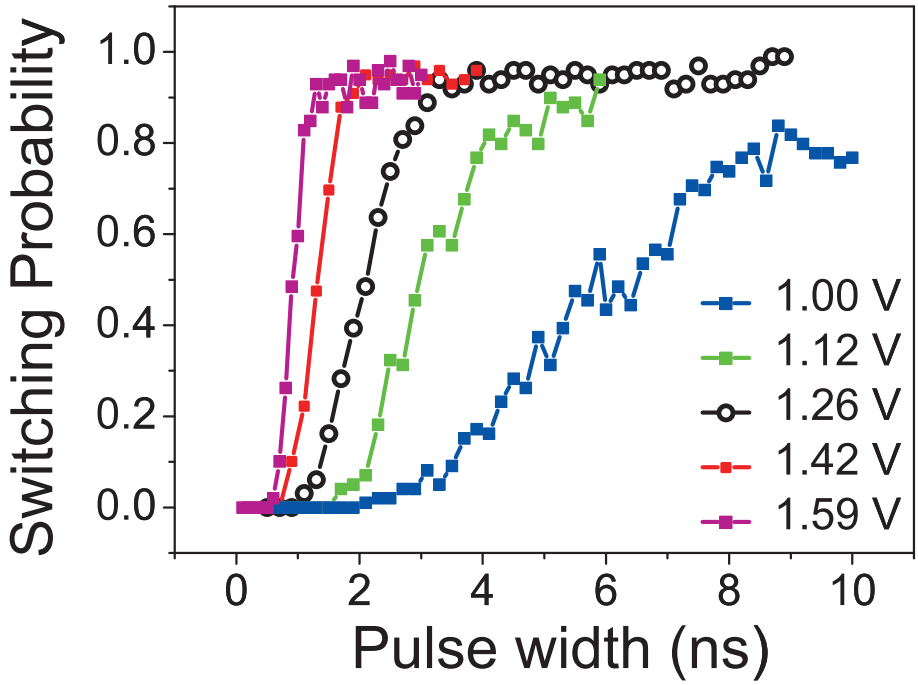

Figure 5.19 – High aspect ratio MTJ. Switching probability of an MTJ initially in P state versus applied voltage pulse width. The pulse amplitude varies from 1.0V to 1.59V.

back-hopping occurs : the applied current is close to the critical current of appearance of the OPP.
Regarding the switching probability versus pulse width, shown in Fig. 5.19, the same trend is observed : the switching time, with more than 90% of probability, is reduced to 1 ns for an applied pulse of 1.59 V.

The integration of a perpendicular polarizer with an in-plane MTJ allows to realize a bipolar deterministic reversal of the free layer magnetization. Because the stochasticity was reduced, we could measure reversals in less than 1 ns. The drawback of the perpendicular polarizer contribution to the spin torque is that it induces a precession of the magnetization, that in the best cases, materializes in back-hopping. In order to inhibit these back-hopping, it is important to realize an MTJ with a large aspect ratio of the elliptical cross-section of the nanopillars, in order to increase the anisotropy field. On top of improving the stability factor, we showed that a large anisotropy field favors bipolar switching over precessional motion. Therefore, high anisotropy structures are a good candidate for realizing fast MRAM for SRAM type of applications.

5.6.2 Switching time : macrospin simulations

The purpose of adding a perpendicular polarizer to a classical in-plane MTJ is to decrease the write-time of the MRAM cell, ideally below 1 ns. In the last sections, we presented the conditions to fulfill so that an in-plane MTJ with a perpendicular polarizer has a bipolar switching behavior, and how to avoid the appearance of oscillations. The influence of the anisotropy (and of the aspect ratio) was found decisive. In this section, we study specifically the switching time, under the assumption that the free-layer will not undergo out-of-plane oscillations. For this, the free layer needs a large anisotropy field, or anisotropy factor Q, and the perpendicular polarizer spin polarization η_{PERP} needs to be small. The effect of a perpendicular surface anisotropy that decreases the demagnetizing field will also be studied. In-plane structures with low demagnetizing field exhibit a lower critical current, as it is proportional to the demagnetizing factor N_z. Therefore, such structures are interesting for applications as low-consumption MRAM[Khalili Amiri 2011].

The switching time is studied through macrospin simulations. To start with, the phase diagram of Fig. 5.3.b is redrawn (only the positive currents) to represent the switching time in color scale, instead of the final state. The switching time is defined as the time when the magnetization component along the easy axis m_x vanishes. If this components vanishes several times, typically if the free layer magnetization is in OPP, it is not counted as a switching behavior. Thus, only the region of switching (in blue) has a non-vanishing switching time. For this simulations, $Q = 0.02$ ($H_k = 24$ kA/m) and $N_z = 1$ ($H_d = 1.2$e6 A/m). The other parameters are similar to the previous simulations : $\alpha = 0.2$, $\eta_{\mathrm{LONG}} = 0.3$, $t = 3$ nm and $S = 1$e-14 m^2. The diagram of switching time in logarithmic scale is shown in Fig. 5.20.a, versus applied current density and η_{PERP}. Only switching times between 0.1 ns and 10 ns are represented. Close to the critical current density, $J_c = 6$e11 A/m^2, the free layer takes time to reverse, around 10 ns. For relatively large perpendicular polarizer spin polarization $\eta_{\mathrm{PERP}} \approx 0.05$, the free layer is reversed in 1 ns at twice the critical current, but without perpendicular polarizer ($\eta_{\mathrm{PERP}} = 0$), it happens at almost thrice the critical current. The perpendicular polarizer really decreases the switching time. In Fig. 5.20.b, the inverse switching time versus current density is plotted for different anisotropy fields corresponding to Q =0.005, 0.01 and 0.02. $N_z = 1$ and $\eta_{\mathrm{PERP}} \approx 0.03$, so that the free layer is not in OPP for a small anisotropy fields. It appears that the switching time increases when the anisotropy increases. Therefore, a large anisotropy decreases the chance of resulting in OPP of the free layer, however the reversal is slowed down. The switching times in the macrospin simulations are only qualitatively correct, as they depend on the angle between the initial magnetization and the x-axis, which is arbitrary, typically of 0.035 rad. It is the same for all simulations, though.

The effect of the demagnetizing field is presented in Fig. 5.20.c, representing the inverse switching time versus applied current density J_{app} for different demagnetizing factors $N_z = H_d/M_S$: $N_z = 1$, $N_z = 0.8$ and $N_z = 0.5$. The anisotropy factor is the same for all curves, $Q = 0.02$, which corresponds to $H_k = 24$ kA/m. The perpendicular polarizer spin polarization is set to $\eta_{\mathrm{PERP}} = 0.05$.

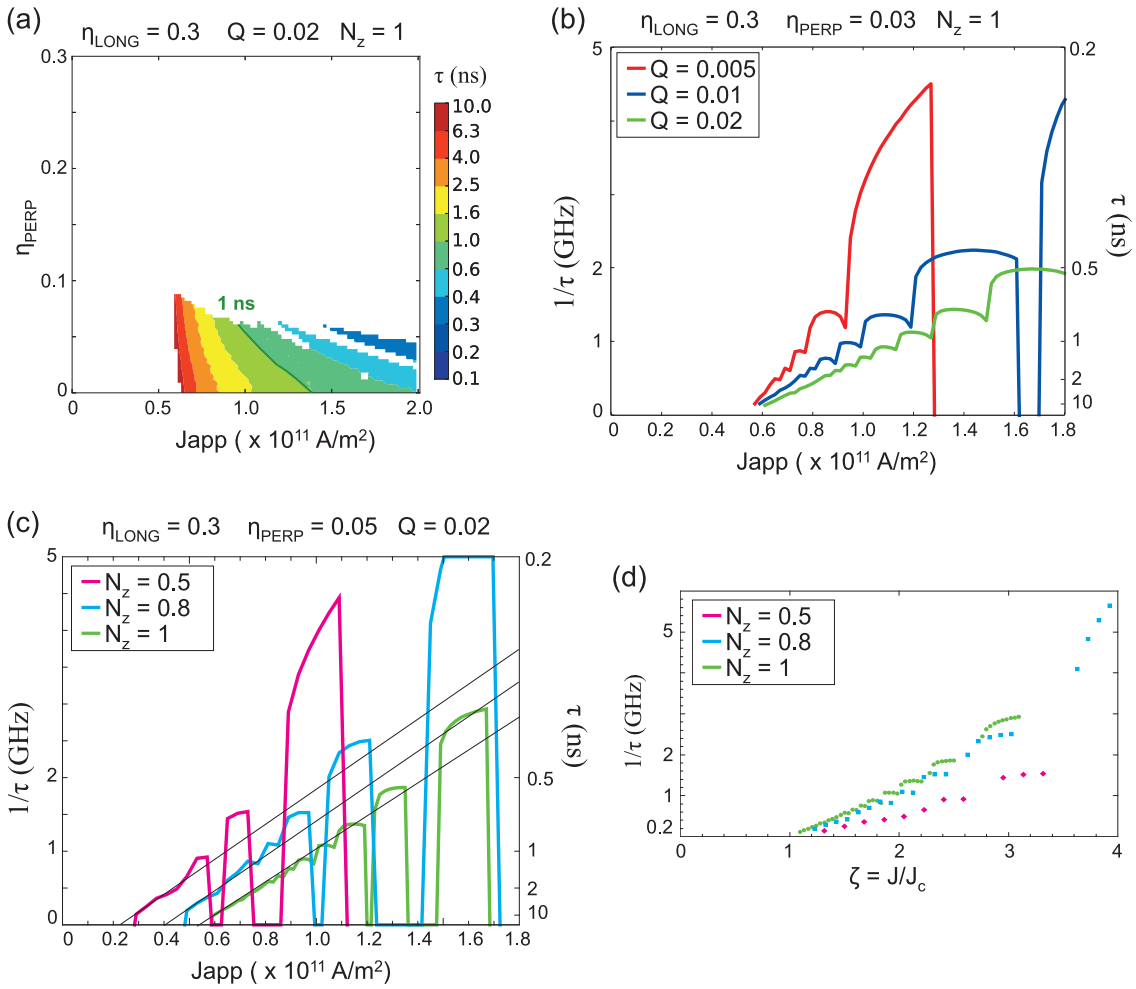

Figure 5.20 – (a) Diagram of the switching time in logarithmic scale versus applied current density J_{app} and spin polarization of the perpendicular polarizer η_{PERP}. $\eta_{\mathrm{LONG}} = 0.3$, $Q = 0.02$ and $N_z = 1$. (b) Inverse switching time versus applied current density J_{app} for different anisotropy factor $Q = H_k/M_S$: $Q = 0.005$, $Q = 0.1$ and $Q = 0.02$. $\eta_{\mathrm{LONG}} = 0.3$, $\eta_{\mathrm{PERP}} = 0.03$ and $N_z = 1$. (c) Inverse switching time versus applied current density J_{app} for different demagnetizing factor : $N_z = 1$, $N_z = 0.8$ and $N_z = 0.5$. $\eta_{\mathrm{LONG}} = 0.3$, $\eta_{\mathrm{PERP}} = 0.05$ and $Q = 0.02$. (d) Inverse switching time versus current density normalized to the critical current $\zeta = J_{app}/J_c$, for different demagnetizing factors.

The critical current J_c is reduced proportionally to the demagnetizing factor. Therefore, for the same applied current density, the switching time is reduced when the demagnetizing factor is reduced. However, if the inverse switching time is plotted versus the reduced current $\zeta = J_{app}/J_c$, like in Fig. 5.20.d, the trend is inverted. The structure with a low demagnetizing factor of $N_z = 0.5$ switches more slowly than the other ones, for the same reduced current ζ. For instance, at twice the value of the critical current, the structure with $N_z = 0.5$ is reversed in 2 ns, compared to 800 ps for $N_z = 1$.

The slopes of the inverse switching time versus current density of Fig. 5.20.c are almost the same for all the values of the demagnetizing factor, whereas they are different when the anisotropy is changed. This suggests that the switching time depends strongly on the anisotropy field, but only slightly or even not on the demagnetizing field. Hence, contrary to what was supposed in Chapter 2, the switching mechanism is more likely to be an exit of a potential well of height H_k, that is driven by the damping or dissipative term, and therefore that depends also on the damping constant α, than a real precessional switching, driven by the conservative torque of the demagnetizing field.
Although the switching mechanism may not be precessional, the advantages due to the perpendicular polarizer are still visible : the perpendicular polarizer STT decreases the switching time and also the stochasticity of the reversal, resulting in a reduced experimental switching time.

The increase of switching time with the anisotropy may be detrimental for the elaboration of ultra-fast MRAM. But it is not the only problem faced by high anisotropy samples or, more precisely, samples with an elliptical cross-section with a large aspect ratio. Indeed, micromagnetic simulations show that domains start forming for large aspect ratio, and the reversal in not single-domain anymore, but by nucleation and domain wall propagation, which are not described by the macrospin theory presented here. The multi-domain structures have a less sharp hysteresis loop that is detrimental for reading the memory cell. They also present intermediate resistance states, also problematic for memory applications.
Hence, the increase of the anisotropy is not a perfect solution, but coupled with a small enough perpendicular polarizer spin polarization, it guarantees a deterministic switching of around 1 ns, which is a real improvement compared to the STT-MRAM without perpendicular polarizer and their 10 ns switching times.

Conclusion and perspectives

In the experimental part of this thesis, we showed that, depending on the relative amplitude of the STT from the perpendicular polarizer and from the reference layer, the stack comprising an in-plane MTJ with a perpendicular polarizer exhibits two different behaviors. When the STT from the perpendicular polarizer dominates, the magnetization of the free layer oscillates under applied current. On the contrary, if the STT from the reference layer dominates, the free layer switches to the P or AP configuration, depending of the current polarity. Interestingly, we found that the anisotropy field also affects the regime in which the MTJ functions : a large anisotropy field favors the bipolar switching. This provides a way to control the switching dynamics in MTJ with orthogonal polarizers to achieve a controlled deterministic switching in less than 1 ns.
Reducing the demagnetizing field with the perpendicular anisotropy from interface with the MgO layer leads to in-plane magnetized MTJ with significantly reduced critical currents. Stacks with reduced demagnetizing fields are thus quite interesting for application in low consumption memory. However, the downsize scalability of these structures is limited to dimensions of the order of 150nm*60nm due to the limitation in thermal stability of in-plane magnetized storage layer.

From a theoretical point of view, the results of Part II are encouraging.
First, we presented a stability analysis of SyF free layers under applied current. The critical current was computed and asymmetric SyF were found to exhibit decreased critical currents. The mode of destabilization was also found to be either acoustic or optical, and ways of adjusting the parameters of the SyF to select one or the other mode were given.
However, the linear analysis of this chapter was not sufficient to predict the existence of self-sustained oscillations of the magnetization. This would be of primary interest in order to incorporate SyF free layers in STT nano-oscillators. One extension of the linear analysis would be to use the same formalism as in the KTS theory, in order to extract the non-linear parameters of a SyF.
The second achievement of this part was the perturbative treatment of the external field, anisotropy field and STT influence from the reference layer on the precessional motion of the magnetization of an in-plane magnetized free layer with a perpendicular polarizer. These perturbations were found to change the trajectory, otherwise circular, of the free layer magnetization under applied current. The perturbed trajectories were successfully computed and the associated change of frequency was quantified. The frequency changes should be measured experimentally for comparison. The critical currents due to these perturbations were also extracted from this analysis.
These results apply to STT oscillators with a perpendicular polarizer, but STO are usually based on in-plane magnetized layers, with in-plane precessions instead of out-of-plane precessions. Therefore, it would be of great interest for application to adapt this perturbative approach to in-plane precession. The most convenient formalism to achieve that seems to be, once again, the KTS theory. Regarding the large amount of theoretical and experimental research on in-plane STO, these results on the out-of-plane precession present a real interest.

Appendix A

Thermal stability

The Landau-Lifshitz-Gilbert-Slonczewski (LLGS) equation describes the evolution of the macrospin magnetization at zero temperature. In order to describe more precisely real devices, especially for memory application, it is important to include temperature effects. With finite temperature, a stochastic term has to by added to the LLGS equation. This term accounts for the small fluctuations due to temperature around the otherwise well-defined magnetization.
In in-plane (or out-of-plane) MTJ with a reference layer, if the magnetization of the free layer and of the reference layer are perfectly aligned, the STT vanishes and no switching can occur. Thermal fluctuations have to be somehow included to explain the switching observed in experiment. A simple idea consists in considering that the two magnetizations are never perfectly aligned. Instead the free layer is considered slightly canted with an angle equal to the RMS value of the angle distribution around the equilibrium due to thermal fluctuations. In practice, the initial configurations of the macrospin simulations presented in this thesis are slightly canted from the equilibrium.
However, this approach is not sufficient to explain, for instance, the write error rate in MRAM or the linewidth of self-sustained oscillators. For this, a stochastic LLGS equation has to be simulated. In this chapter, we present the general formalism used to solve the stochastic LLGS equation. As the equation involved in the general case are complicated, the solvable case of the perpendicular-to-plane MTJ is presented. The extension to in-plane MTJ is done by analogy. In particular, the expression for the probability of switching is given in two cases : for a large barrier height and a small applied current, and for currents larger than the critical current.

A.1 The Fokker-Planck equation

In the form of eq. 1.37, the LLGS equation does not take into account thermal fluctuations. In order to render the effect of temperature on the dynamics, one ought to transform the deterministic LLGS equation in a stochastic differential equation, also called a Langevin equation :

$$\dot{\boldsymbol{m}} = \frac{\gamma}{M_S V}\boldsymbol{m} \times \partial_{\boldsymbol{m}}\mathcal{H} + \frac{\gamma}{M_S V}\boldsymbol{m} \times \Big(\boldsymbol{m} \times \partial_{\boldsymbol{m}}\Gamma\Big) + \sqrt{2D}\, \boldsymbol{m} \times \boldsymbol{\eta} \tag{A.1}$$

Where $\mathcal{H} = E + \alpha\beta_{IEC}P$ is the conservative potential, $\Gamma = \alpha E - P$ is the dissipative potential, E and P are the free energy and spin torque potential respectively. D is the diffusion coefficient, that is supposed independent of $\boldsymbol{m}$. It will be determined later. $\boldsymbol{\eta}$ is a Gaussian white noise vector, with correlation function :

$$\langle \eta_i(t)\eta_j(t')\rangle = \delta_{ij}\delta(t-t') \tag{A.2}$$

This noise vector has the simplest form possible to include random processes in the dynamics. Fortunately, this formalism gives an equilibrium distribution that is the Gibbs distribution, in agreement with thermodynamical considerations.

The previous equation is stochastic. It is possible to transform it in a deterministic equation, the Fokker-Planck equation using Itō's lemma. Given the general stochastic differential equation :

$$\dot{\boldsymbol{X}}_t = \boldsymbol{\mu}_t + \boldsymbol{\sigma}_t\boldsymbol{\eta}_t \tag{A.3}$$

$\boldsymbol{\mu}_t$ is the drift vector, $\boldsymbol{\sigma}_t$ is the diffusion matrix and $\boldsymbol{\eta}_t$ is the Gaussian white noise defined earlier. The differential equation of any observable $\mathcal{O}$, or any function of $\boldsymbol{X}_t$, is defined by the chain rule with stochastic processes, given by :

$$\dot{\mathcal{O}}(\boldsymbol{X}_t) = \dot{\boldsymbol{X}}_t \cdot \nabla_{\boldsymbol{X}_t}\mathcal{O} + \frac{1}{2}\,\mathrm{Tr}(\boldsymbol{\sigma}^\intercal\,\mathbf{Hess}[\mathcal{O}]\boldsymbol{\sigma}) \tag{A.4}$$

Where $\nabla_{\boldsymbol{X}_t}\mathcal{O}$ is the gradient of $\mathcal{O}$ with respect to the variable $\boldsymbol{X}_t$, Tr is the trace operator, and $\mathbf{Hess}[\mathcal{O}]$ is the Hessian of $\mathcal{O}$, as defined in Chapter 1. For the LLGS equation, this leads to :

$$\dot{\mathcal{O}}(\boldsymbol{m}_t) = \nabla_{\boldsymbol{m}}\mathcal{O}\cdot\left(\frac{\gamma}{M_S V}\boldsymbol{m}\times\nabla_{\boldsymbol{m}}\mathcal{H} + \frac{\gamma}{M_S V}\boldsymbol{m}\times\left(\boldsymbol{m}\times\nabla_{\boldsymbol{m}}\Gamma\right)\right) + D\Delta_{\boldsymbol{m}}\mathcal{O} \tag{A.5}$$

$$+\nabla_{\boldsymbol{m}}\mathcal{O}\cdot\left(\sqrt{2D}\;\boldsymbol{m}\times\boldsymbol{\eta}\right) \tag{A.6}$$

Here $\Delta_{\boldsymbol{m}}\mathcal{O}$ is the Laplacian of $\mathcal{O}$. Let $\mathcal{L}$ be the generator of the drift-diffusion process :

$$\mathcal{L} = \left(\frac{\gamma}{M_S V}\boldsymbol{m}\times\nabla_{\boldsymbol{m}}\mathcal{H} + \frac{\gamma}{M_S V}\boldsymbol{m}\times\left(\boldsymbol{m}\times\nabla_{\boldsymbol{m}}\Gamma\right)\right)\cdot\nabla_{\boldsymbol{m}} + D\;\Delta_{\boldsymbol{m}} \tag{A.7}$$

Let $\rho(t,\boldsymbol{m})$ be the probability density function (PDF) of orientations of the magnetization. The PDF measures the probability that the magnetization is in the configuration $\boldsymbol{m}$ at time t. Its integral over all available configurations should be unity :

$$\int \rho(t,\boldsymbol{m})\mathrm{dm} = 1 \qquad \text{where dm spans all of the unit 2-sphere.}$$

The average of any observable $\mathcal{O}$ is defined by the scalar product of $\mathcal{O}$ and the PDF :

$$\langle\mathcal{O}\rangle(t) = \int \mathcal{O}(\boldsymbol{m})\rho(t,\boldsymbol{m})\mathrm{dm}$$

Therefore, there are two ways to write the derivative of the observable $\mathcal{O}$ average :

$$\begin{aligned}\langle\dot{\mathcal{O}}\rangle &= \int \mathcal{O}(\boldsymbol{m})\frac{\partial}{\partial t}\rho(t,\boldsymbol{m})\mathrm{dm} \\ &= \langle\mathcal{L}\mathcal{O}\rangle + \langle\nabla_{\boldsymbol{m}}\mathcal{O}\cdot\Big(\sqrt{2D}\;\boldsymbol{m}\times\boldsymbol{\eta}\Big)\rangle = \int \mathcal{L}[\mathcal{O}(\boldsymbol{m})]\rho(t,\boldsymbol{m})\mathrm{dm} = \int \mathcal{O}(\mathrm{m})\mathcal{L}^*[\rho(\mathrm{t},\mathrm{m})]\mathrm{dm}\end{aligned}$$

So the PDF is solution of the forward Kolmogorov equation or Fokker-Planck equation :

$$\frac{\partial}{\partial t}\rho(t,\boldsymbol{m}) = \mathcal{L}^*[\rho(t,\boldsymbol{m})] \tag{A.8}$$

Where $\mathcal{L}^*$ is the adjoint of the generator in the L^2 norm of functions that take value on the 2-sphere, defined by the integration by parts of $\mathcal{L}$:

$$\frac{\partial\rho}{\partial t} = -\nabla_{\boldsymbol{m}}\cdot\left(\rho\left(\frac{\gamma}{M_S V}\boldsymbol{m}\times\nabla_{\boldsymbol{m}}\mathcal{H} + \frac{\gamma}{M_S V}\boldsymbol{m}\times\Big(\boldsymbol{m}\times\nabla_{\boldsymbol{m}}\Gamma\Big)\right)\right) + \Delta_{\boldsymbol{m}}(D\rho) \tag{A.9}$$

In order to simplify the Fokker-Planck equation, it is expressed in spherical coordinates. In this system of coordinates, the integration over the sphere is more straightforward. The PDF defines the probability that the magnetization angles are (θ,ϕ) at time t, and :

$$\int \rho(t,\theta,\phi)\sin\theta\mathrm{d}\phi\mathrm{d}\theta = 1 \tag{A.10}$$

$$\frac{\partial\rho}{\partial t} = -\operatorname{div}\left(\frac{\gamma}{M_S V}\rho\Big(\Omega_1\boldsymbol{\nabla}_{\tilde{\boldsymbol{R}}}\mathcal{H} - \boldsymbol{\nabla}_{\tilde{\boldsymbol{R}}}\Gamma\Big)\right) + D\Delta\rho \tag{A.11}$$

Where div and Δ are the divergence and Laplacian operator in spherical coordinates, and $\boldsymbol{\nabla}_{\tilde{\boldsymbol{R}}} = (\frac{\partial}{\partial\theta}, \frac{1}{\sin\theta}\frac{\partial}{\partial\phi})$.
Given that :

$$\operatorname{div}\Big(\Omega_1\boldsymbol{\nabla}_{\tilde{\boldsymbol{R}}}\mathcal{H}\Big) = 0 \qquad\qquad \Big(\Omega_1\boldsymbol{\nabla}_{\tilde{\boldsymbol{R}}}\mathcal{H}\Big)\cdot\boldsymbol{\nabla}_{\tilde{\boldsymbol{R}}}\rho = -\boldsymbol{\nabla}_{\tilde{\boldsymbol{R}}}\mathcal{H}\;\Omega_1\boldsymbol{\nabla}_{\tilde{\boldsymbol{R}}}\rho \tag{A.12}$$

The simplification follows :

$$\frac{\partial\rho}{\partial t} = \frac{\gamma}{M_S V}\boldsymbol{\nabla}_{\tilde{\boldsymbol{R}}}\mathcal{H}\;\Omega_1\boldsymbol{\nabla}_{\tilde{\boldsymbol{R}}}\rho + \operatorname{div}\left(\frac{\gamma}{M_S V}\rho\boldsymbol{\nabla}_{\tilde{\boldsymbol{R}}}\Gamma + D\boldsymbol{\nabla}_{\tilde{\boldsymbol{R}}}\rho\right) \tag{A.13}$$

This equation describes the magnetization dynamics in the macrospin model at any temperature T. Unfortunately it is not possible to solve it in the general case. In fact, the time dependent problem is not exactly solvable even in the easiest case that is mentioned later. Therefore, let's first focus on solving the long-time problem, i.e. finding the equilibrium PDF, noted $\rho_0(\theta,\phi)$. As it appears, the equilibrium PDF gives also some information about switching times.
The equilibrium PDF ρ_0 is solution of :

$$0 = \frac{\gamma}{M_S V}\boldsymbol{\nabla}_{\tilde{\boldsymbol{R}}}\mathcal{H}\;\Omega_1\boldsymbol{\nabla}_{\tilde{\boldsymbol{R}}}\rho_0 + \operatorname{div}\left(\frac{\gamma}{M_S V}\rho_0\;\boldsymbol{\nabla}_{\tilde{\boldsymbol{R}}}\Gamma + D\boldsymbol{\nabla}_{\tilde{\boldsymbol{R}}}\rho_0\right) \tag{A.14}$$

A.2 Gibbs equilibrium distribution

Let $\mathcal{P}$ be a potential that accounts for the "interaction" between the conservative and the dissipative part :

$$\mathcal{P} = \left(\frac{\gamma}{DM_S V}\right)^2 \boldsymbol{\nabla}_{\tilde{\boldsymbol{R}}}\mathcal{H}\ \Omega_1 \boldsymbol{\nabla}_{\tilde{\boldsymbol{R}}}\Gamma$$

If $\mathcal{P}$ vanishes then the equilibrium PDF is rather straightforward :

$$\rho_0(\theta,\phi) = Z^{-1}\exp\left(-\frac{\gamma}{DM_S V}\Gamma(\theta,\phi)\right) \tag{A.15}$$

Where Z is the partition function, a normalization constant. This expression of ρ_0 is, indeed, solution of eq. A.14, in the case of $\mathcal{P} = 0$.
One very important case for which $\mathcal{P}$ vanishes is the case without applied current. Hence the conservative potential $\mathcal{H}$ is equal to the free energy E and the dissipative potential Γ is proportional to $\mathcal{H}$, $\Gamma = \alpha E$. Because Γ is a function of $\mathcal{H}$, $\mathcal{P}$ vanishes and the equilibrium PDF is given by :

$$\rho_0(\theta,\phi) = Z^{-1}\exp\left(-\frac{\alpha\gamma E}{DM_S V}\right) \tag{A.16}$$

However, the equilibrium distribution is known from thermodynamics to be the Gibbs distribution, its logarithm should be $-\dfrac{E}{k_B T}$, where $k_B T$ is the Boltzmann constant and T the temperature. Therefore, the value of the diffusion constant D without applied current is given by :

$$D = \frac{\alpha\gamma}{M_S V}k_B T$$

This is also a result of the fluctuation-dissipation theorem, that states that the fluctuations ("T") and the force that drags the magnetization to its equilibrium ("α") have the same origin.

A.3 The 1-dimensional case : high-symmetry configuration

Knowing the equilibrium distribution without STT leads to know the value of the diffusion constant D, that is supposed to remain the same when a current is applied. However the equilibrium distribution without STT has two limitations :

- We are interested in probability of switching *with* applied current, for application in MRAM.
- The thermal stability of this system cannot be evaluated, i.e. the average time for which the magnetization, initially in P state, reverse in the AP state due to thermal fluctuations is not known.

Fortunately, both questions can be answered in one specific configuration, the so-called high symmetry case, where the energy and spin torque potential depend only on one parameter, say the out-of-plane angle θ. This is typically the case for a perpendicular-to-plane free layer with a reference layer also out-of-plane. Thus, only the demagnetizing field and the Zeeman energy with perpendicular-to-plane external field is present in the energy, and the spin torque potential is like in eq. 2.8. Because then $\mathcal{P}$ vanishes, the expression of the equilibrium distribution is straightforward. It will be used later.

To start with, the time-dependent Fokker planck equation A.13 and the PDF are averaged with respect to the in-plane angle ϕ. Because $\mathcal{H}$ and Γ are independent of ϕ, and $\int \frac{\partial \rho}{\partial \phi} \mathrm{d}\phi = 0$, the equation for the θ-probability density $\bar{\rho}(\theta, t) = \int \rho(\theta, \phi, t) \mathrm{d}\phi$ is obtained :

$$\partial_t \bar{\rho} = \frac{D}{\sin\theta} \frac{\partial}{\partial \theta} \left(\sin\theta \left(\frac{\gamma}{D M_S V} \bar{\rho}\, \partial_\theta \Gamma + \partial_\theta \bar{\rho} \right) \right) \tag{A.17}$$

$\bar{\rho}(\theta)$ is normalized as $\int_0^\pi \bar{\rho}(\theta) \sin\theta \mathrm{d}\theta = 1$. The equilibrium distribution $\bar{\rho}_0$ is given by :

$$\bar{\rho}_0(\theta) = Z^{-1} e^{-\tilde{\Gamma}(\theta)} \qquad \text{with } \tilde{\Gamma} = \frac{\gamma \Gamma}{D M_S V} = \frac{\Gamma}{\alpha k_B T} \tag{A.18}$$

The time-dependent equation may be rewritten as :

$$\partial_t \bar{\rho} = \frac{D}{\sin\theta} \partial_\theta \left(\sin\theta e^{-\tilde{\Gamma}} \partial_\theta \left(e^{+\tilde{\Gamma}} \bar{\rho} \right) \right) = \mathcal{L}^* \bar{\rho} \tag{A.19}$$

We recall that $\mathcal{L}^*$ is the adjoint of the diffusion process generator, which is accordingly given, for any observable f, by :

$$\mathcal{L} f = \frac{D}{\sin\theta} e^{+\tilde{\Gamma}} \partial_\theta \left(\sin\theta e^{-\tilde{\Gamma}} \partial_\theta f \right) \tag{A.20}$$

A.3.1 High energy barrier, below the threshold

At equilibrium, without applied field or current, two equilibriums exist, P and AP. And, according to the equilibrium probability distribution, at long time, both equilibrium states should be equally populated, i.e. there is 50% of probability of finding the magnetization in the P and in the AP state. However, initially the magnetization is in one of these states, say P. Therefore, there is a time, called switching time, at which the reversal occurs, only due to thermal fluctuations. In the following, the equilibrium distribution is supposed to have two minimums, separated by a maximum, and the difference between the minima and the maximum value is large. It is verified when the temperature is small, and when no applied field or current is applied. It remains correct when the field (current) is small compared to the critical field (current).

In order to estimate the mean switching time, the formalism introduced by Brown without applied current[Brown 1963] is used. It has already been successfully adapted to the situation with current in the high-symmetry case[Butler 2012]. It was even estimated if the free layer is a SyF[Taniguchi 2011].

Let $S(\mathcal{D},t)$ be the observable that accounts for the probability that the magnetization is in a domain $\mathcal{D}$ around the P equilibrium state ($\theta = 0$) at time t. The initial condition is assumed to be $S(\mathcal{D},0) = 1$, i.e. the magnetization is initially in the P configuration (or close). As for the final condition, $S(\mathcal{D},\infty) = 0$, i.e. the magnetization eventually reverse, and remains in the AP configuration. S is an observable, therefore it obeys the backward Kolmogorov equation :

$$S(\mathcal{D},t) = \int_{\mathcal{D}} \bar{\rho}(\theta,t)\sin\theta \mathrm{d}\theta \qquad \text{and} \quad \partial_t S = \mathcal{L}S \tag{A.21}$$

Let $f(\mathcal{D},t)$ be the probability density that the magnetization switches at time t. Then :

$$f(\mathcal{D},t)\mathrm{dt} = S(\mathcal{D},t) - S(\mathcal{D},t+\mathrm{dt}) \qquad \Longrightarrow \quad f(\mathcal{D},t) = -\partial_t S(\mathcal{D},t)$$

Let $\tau(\mathcal{D})$ be the mean escape time (it formally depends on $\mathcal{D}$). It is, by definition, the expected value of $f(\mathcal{D},t)$:

$$\tau(\mathcal{D}) = \int_0^\infty f(\mathcal{D},t)t\mathrm{dt} = -\int_0^\infty \mathrm{t}\ \partial_\mathrm{t}\mathrm{S}(\mathcal{D},\mathrm{t})\mathrm{dt} = \int_0^\infty \mathrm{S}(\mathcal{D},\mathrm{t})\mathrm{dt}$$

Therefore, by applying the generator $\mathcal{L}$, the equation becomes :

$$\mathcal{L}\tau(\mathcal{D}) = \int_0^\infty \mathcal{L}S(\mathcal{D},t)\mathrm{dt} = \int_0^\infty \partial_\mathrm{t}\mathrm{S}(\mathcal{D},\mathrm{t})\mathrm{dt} = -1 \tag{A.22}$$

Because the problem is 1-dimensional, the inverse of $\mathcal{L}$ may be computed by integrating with respect to θ. The domain $\mathcal{D}$ is defined by $\mathcal{D} = \{\theta, \theta \leq \theta_M\}$, where θ_M is the angle for which $\tilde{\Gamma}$ is maximum. The limit condition, $\tau(\pi) = 0$ (already switched states have a vanishing switching time) is assumed :

$$\tau(\theta_M) = \frac{1}{D}\int_{\theta_M}^{\pi} \mathrm{d}\theta \frac{\mathrm{e}^{+\tilde{\Gamma}}}{\sin\theta}\int_0^\theta \mathrm{d}\vartheta \sin\vartheta\ \mathrm{e}^{-\tilde{\Gamma}} \tag{A.23}$$

In order to compute the mean escape time, the two integrals have to be estimated. For the first one (in the right), because of the exponential, only the part close to the minimum of $\tilde{\Gamma}$ is important. Using the Taylor expansion of $\tilde{\Gamma}$ around its minimum θ_m :

$$\tilde{\Gamma}(\vartheta) = \tilde{\Gamma}_m + \frac{\omega_m}{2}\Big(\vartheta - \theta_m\Big)^2 \tag{A.24}$$

The first integral gives : $\int_0^\theta \mathrm{d}\vartheta \sin\vartheta\ \mathrm{e}^{-\tilde{\Gamma}} \approx \mathrm{k_m}\ \mathrm{e}^{-\tilde{\Gamma}_\mathrm{m}}$, with $k_m = \int_0^\theta \mathrm{d}\vartheta \sin\vartheta\ \mathrm{e}^{-\frac{\omega_\mathrm{m}}{2}(\vartheta-\theta_\mathrm{m})^2} \approx 1/\omega_\mathrm{m}$.
The second integral is dominated by the neighborhood of the maximum of $\tilde{\Gamma}$. Its Taylor expansion around the maximum θ_M is :

$$\tilde{\Gamma}(\theta) = \tilde{\Gamma}_M - \frac{\omega_M}{2}\Big(\theta - \theta_M\Big)^2 \tag{A.25}$$

Let τ_0 be a characteristic time, the expression of the mean escape time writes :

$$\tau = \tau_0 \, e^{\tilde{\Gamma}_M - \tilde{\Gamma}_m} = \tau_0 \, e^{\Delta} \tag{A.26}$$

$$\text{with} \quad \tau_0 \approx \frac{1}{D\omega_m} \int_{\theta_M}^{\pi} \mathrm{d}\theta \frac{\mathrm{e}^{-\frac{\omega_\mathrm{M}}{2}(\theta-\theta_\mathrm{M})^2}}{\sin\theta} \approx \frac{1}{\mathrm{D}\omega_\mathrm{m}} \sqrt{\frac{\pi}{2\omega_\mathrm{M}}} \tag{A.27}$$

Where Δ is the stability factor, that corresponds to the difference between the maximum and the minimum of $\tilde{\Gamma}$. Without applied current, $\tilde{\Gamma} = \frac{E}{k_B T}$, so $\Delta = \frac{E_M - E_m}{k_B T}$. The general expression of the mean escape time τ and the stability factor Δ is usually extended to the case of in-plane magnetized free layer, by supposing that the problem can again be treated as a 1-dimensional problem, but this time according to the in-plane angle ϕ. However the treatment is less rigorous.
For in-plane structures, the energy barrier is taken between the local minimum of energy of the equilibrium and the saddle-point energy, which is the transverse in-plane state, along $\boldsymbol{u}_y$[Coffey 2012]. But this approach is only valid without current, when $\mathcal{P} = 0$. Otherwise, the equilibrium probability distribution is not easily defined because of $\mathcal{P}$.

In the all-perpendicular configuration, as an example, the dissipative potential is assumed to be :

$$\Gamma = \mu_0 M_S V \alpha \left(-\frac{H_d}{2} \cos^2\theta - (H_z + \tilde{\eta}_z I)\cos\theta \right) \tag{A.28}$$

Here $\tilde{\eta}_z = \frac{\hbar}{2e}\frac{\eta_z}{\alpha}$ and $\lambda_z = 0$ was assumed for simplicity. The two minima $\theta = 0$ and $\theta = \pi$ are distinguished by the superscript $\pm$, respectively. Let $\varepsilon = (H_z + \tilde{\eta}_z I)/H_c$ be the normalized field/current, with the critical "field" $H_c = \mp H_d$ arising from the roots of the second derivative of Γ. So $\Gamma = -\frac{1}{2}\mu_0 M_S V \alpha H_d(\cos^2\theta \mp 2\varepsilon\cos\theta)$.
Fig. A.1.a represents the dissipative potential Γ versus the out-of-plane component $m_z = \cos\theta$, without applied field and for different values of the current, $I/I_c = 0$, 0.5 and 1. For $I < I_c$, the potential presents two minima, but one single minimum for $I > I_c$, which is defined by the current polarity. The most probable configurations of the magnetization correspond to the minima of Γ. Hence, for $I < I_c$, the two configurations, P and AP, are meta-stable. The probability of switching is related to the barrier height between the two minima, like for a particle in a double-well. For $I > I_c$, only one configuration is stable (AP on Fig. A.1.a). The dynamics is similar to a particle with a gradient force in quantum mechanics.

For this form of the dissipative potential Γ, the minimum is defined by $\Gamma_m^{\pm} = -\frac{1}{2}\mu_0 M_S V \alpha H_d(1 - 2\varepsilon)$. The maximum is defined by the root of the first derivative of Γ by $\cos\theta_M = \pm\varepsilon$, so $\Gamma_M = \frac{1}{2}\mu_0 M_S V \alpha H_d(\varepsilon^2)$. Therefore the stability factor Δ is defined by :

$$\Delta = \frac{\mu_0 M_S H_d V}{2k_B T}(1-\varepsilon)^2 \tag{A.29}$$

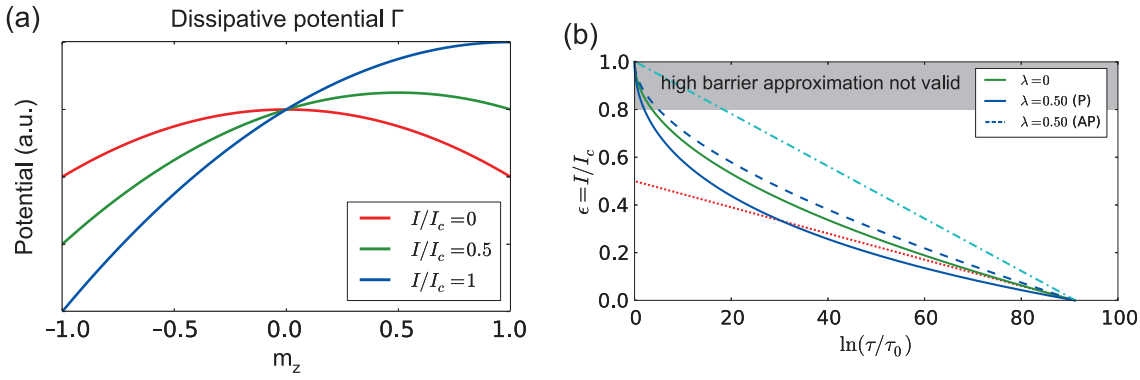

Figure A.1 – (a) Dissipative potential Γ versus out-of-plane component of the magnetization m_z, for different current $I/I_c = 0$, 0.5 and 1. The magnetization has more probability to be in the configuration where Γ is minimum. (b) Reduced current (with respect to I_c) versus average switching time in logarithmic scale with different spin polarization asymmetry λ. In green full-line, $\lambda = 0$. In blue full-line (dashed-line), $\lambda = 0.5$ with an initial P (AP, respectively) configuration. Cyan dotted-line : linear approximation giving a correct barrier height Δ_0 and critical current I_c. Red dotted-line : linear approximation for long time scales (or small applied current) which gives wrong Δ_0 and I_c.

Let Δ_0 be the stability factor for no applied field or current, hence :

$$\ln \tau = \ln \tau_0 + \Delta_0 \left(1 \pm \frac{H_z + \tilde{\eta}_z I}{H_d}\right)^2 \tag{A.30}$$

The characteristic time τ_0 is not really a constant. Nevertheless, because the exponential term is usually much bigger in applications, the dependence of τ_0 with respect to the field and current is omitted. From the expression of the dissipative potential and of τ_0, it is possible to estimate ω_m and ω_M, so :

$$\tau_0 = \frac{1}{D\omega_m}\sqrt{\frac{\pi}{2\omega_M}} = \frac{1}{\alpha\mu_0\gamma H_d}\sqrt{\frac{\pi}{4\Delta}} \tag{A.31}$$

Notice that τ_0 is very close, to a factor $\sqrt{\frac{\pi}{4\Delta}}$, from the relaxation time τ_D defined in Chapter 1. With reasonable values of the parameters, $\alpha = 0.02$, $H_d = 1.2\text{e}6$ A/m, $\tau_0 \approx 0.2\sqrt{\frac{\pi}{4\Delta}}$ ns. For memory application, an information retention time of around ten years is required . The dependence of the mean escape time on Δ is principally in the exponential factor, only the order of magnitude of τ_0 is important. As a result, for a retention of ten years, Δ should be larger than 44.
The stability factor is very critical for the retention time. For instance, if the stability factor is divided by 2, the retention time is now of 100 ms.

In [Taniguchi 2011], the stability factor is estimated for a SyF free layer with applied current, in the in-plane configuration. Even if these results are thus subject to controversy (because $\mathcal{P} \neq 0$), they are correct in the high symmetry case. Like for the single layer free layer, the

stability factor is proportional to the difference of energy between the minimum of energy and the saddle-point. Interestingly in the high-coupling regime, the minimum energy and the saddle-point energy in a SyF are independent of the RKKY coupling, as they both correspond to configurations where the two magnetizations are collinear, along $\boldsymbol{u}_x$ and $\boldsymbol{u}_y$ respectively, and thus the RKKY energy vanishes in these configurations. The stability factor in a SyF in the high coupling regime is entirely due to the anisotropy field (or the demagnetizing field in the high-symmetry configuration). Therefore, using a SyF free layer does *not* increase the thermal stability, despite the increase of the coercive field.

To come back to the single layer case, the same analysis can be accomplished when the spin polarization asymmetry λ_z does not vanish. However, it is supposed to be small. Moreover, there is no applied field. Thus :

$$\Gamma = \mu_0 M_S V \alpha \left(-\frac{H_d}{2} \cos^2\theta - \tilde{\eta}_z I \cos\theta + \frac{1}{2}\lambda_z \tilde{\eta}_z I \cos^2\theta \right) \tag{A.32}$$

The critical current (for the two equilibriums P and AP, defined with $\pm$) is defined from the root of the second derivative of Γ by $I_c = \mp \frac{H_d}{\tilde{\eta}_z} \frac{1}{1 \mp \lambda_z}$. And $\varepsilon = I/I_c$. Therefore :

$$\Delta = \Delta_0 \frac{(1-\varepsilon)^2}{1 \pm \varepsilon \dfrac{\lambda_z}{1 \mp \lambda_z}} \tag{A.33}$$

The spin polarization asymmetry changes the dependence of the stability factor with the current. If the slope of Δ for small currents is the main preoccupation, for instance to evaluate the stability factor at equilibrium Δ_0, then the parameter λ_z may be critical and lead to a wrong estimation of Δ_0.

On top of the mean escape time τ, it is possible to evaluate the probability of switching. Following the formalism of Brown[Brown 1963], the probability $S(t)$ (the domain $\mathcal{D}$ is omitted) that the magnetization is close to the P state is found to be solution of the equation :

$$\dot{S} = -\frac{S}{\tau} \qquad \Longrightarrow \quad S(t) = \exp(-t/\tau)$$

The probability of switching $P_{SW} = 1 - S$ is then given by :

$$P_{SW}(t) = 1 - \exp(-\frac{t}{\tau_0} e^{-\Delta}) \tag{A.34}$$

This expression is valid as long as the high-energy-barrier assumption is valid, which means that the field and current are small compared to their critical value of switching. Otherwise another approach is needed, or phenomenological expressions are used, typically the linear dependence of the stability factor with the current, $\Delta = \Delta_0(1 - I/I_c)$, or its 3/2-dependence with respect to the field, $\Delta = \Delta_0(1 - H/H_c)^{3/2}$, that is justified by thermodynamics considerations on domains reversal[Oh 2009, Victora 1989]. These expressions are valid close to the critical field/current.

Note that the approximation of a linear dependence of the stability factor with the current gives erroneous estimations of the barrier height Δ_0 and of the critical current I_c, as shown in Fig. A.1.b. The two dotted-lines, red and cyan, represent two different attempts of considering a linear dependence of Δ with the current I. For the cyan line, the slope and ordinate at the origin provide the correct Δ_0 and I_c. However, it does not interpolate the curve with a quadratic current dependence (green full-line). On the contrary, the red line interpolate correctly the quadratic curve for long time scales, but it gives the wrong value for Δ_0 and I_c, which are underestimated by a factor 2 according to this approximation.

A.3.2 Above the threshold

In this section, let the dissipation potential Γ be defined by eq. A.28, with the definition of the reduced field and current ε. We focus on the situation when $\varepsilon \geq 1$, i.e. above the critical field or critical current. Thus, the equilibrium distribution has only one minimum, and the magnetization will eventually reverse. In this situation, Butler et al.[Butler 2012] found an approximate expression for the probability of no-switching P_{NS} ($P_{NS} = 1 - P_{SW}$) :

$$P_{NS}(t) = 1 - \exp\left(-\frac{\pi^2(\varepsilon-1)\Delta}{\varepsilon}\, e^{-2(\varepsilon-1)t/\tau_D}\right) \tag{A.35}$$

Here $\tau_D = 1/(\alpha\mu_0\gamma H_d)$ is the relaxation time defined earlier, with an approximate value of 0.2 ns. This expression is only valid at large time, understand $(\varepsilon-1)t/\tau_D \gg 1$.
This formula was derived by linearizing the drift vector. As a result, this formula overestimates the probability of non-switching P_{NS}, especially in the vicinity of the critical current value. The larger the current, the more accurate the previous expression.

Fig. A.2.a represents the probability distribution at different time τ in arbitrary unit, for a large stability factor, $\Delta = 60$, and a reduced current $\epsilon = I/I_c = 1.5$. The initial distribution is centered around the P configuration ($\theta = 0$). According to the current polarity, the AP state is favored, therefore the final configuration, for $\tau = \infty$, is centered around $\theta = \pi$. For $\tau = 4$, the distribution is almost uniform, the magnetization can be in any position with the same probability. For larger time, the probability that the magnetization is between $\theta = 0$ and $\theta = 3\pi/4$ decreases gradually, and the probability that the magnetization has switched increases.
The probability of no-switching P_{NS} versus time (in arbitrary unit) is represented in Fig. A.2.b, for the same stability factor, $\Delta = 60$ and different reduced current. The analytical expression of eq. A.35 is compared to the results of simulations of the LLGS equation including a stochastic term. They are in good agreement, especially because the values of the reduced current are large. $\epsilon > 2$. At large time scale, the logarithm of the probability P_{NS} decreases linearly with time, as expected from the analytical expression. The slope is proportional to $(\epsilon - 1)$.

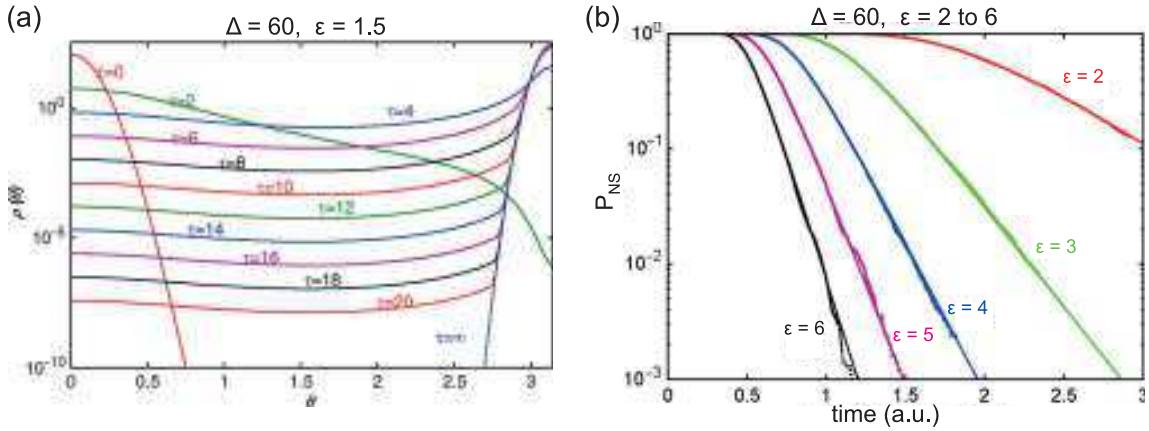

Figure A.2 – (a) Probability distribution versus out-of-plane angle θ at different times τ (in arbitrary unit), with a stability factor $\Delta = 60$ and a reduced current $\epsilon = I/I_c = 1.5$. The magnetization is initially in the P configuration ($\theta = 0$) and it is in the AP state at infinite time. (b) Probability of no-switching P_{NS} in logarithmic scale versus time (in arbitrary unit) for different reduced current. Full-line, analytical expression of eq. A.35. Dotted-line, from simulation of LLGS with gaussian white noise. The stability factor is $\Delta = 60$. Both from [Butler 2012].

A.3.3 A more general model

The reversal with thermal noise is not an easy problem. Two particular cases were shown in this appendix, however one interesting case remains difficult to treat analytically, when the current or field is close to the critical value, below or above it.
Another restriction of this analysis is that it is only valid in the one-dimensional case. To accurately treat the in-plane configuration, it is necessary to solve the Fokker-Planck equation numerically, but this is beyond the scope of this work.

Bibliography

[Baibich 1988] M. N. Baibich, J. M. Broto, A. Fert, F. Nguyen Van Dau and F. Petroff. *Giant Magnetoresistance of (001)Fe/(001)Cr Magnetic Superlattices*. Physical Review Letters, vol. 61, no. 21, pages 2472–2475, November 1988, DOI:10.1103/PhysRevLett.61.2472. (Cited on page 12.)

[Bazaliy 2007] Ya. Bazaliy. *Precession states in planar spin-transfer devices: The effective one-dimensional approximation*. Physical Review B, vol. 76, no. 14, page 140402, October 2007, DOI:10.1103/PhysRevB.76.140402. (Cited on page 102.)

[Bazaliy 2012] Ya. B. Bazaliy. *Planar approximation for spin transfer systems with application to tilted polarizer devices*. Physical Review B, vol. 85, no. 1, page 014431, January 2012, DOI:10.1103/PhysRevB.85.014431. (Cited on page 87.)

[Berger 1996] L Berger. *Emission of spin waves by a magnetic multilayer traversed by a current*. Physical Review B, vol. 54, no. 13, pages 9353–9358, October 1996, DOI:10.1103/PhysRevB.54.9353. (Cited on page 24.)

[Bertotti 2001] G. Bertotti, I.D. Mayergoyz and C Serpico. *Perturbation technique for Landau-Lifshitz-Gilbert equation under elliptically polarized fields*. Physica B: Condensed Matter, vol. 306, no. 1-4, pages 47–51, December 2001, DOI:10.1016/S0921-4526(01)00966-8. (Cited on page 94.)

[Binasch 1989] G. Binasch, P. Grünberg, F. Saurenbach and W. Zinn. *Enhanced magnetoresistance in layered magnetic structures with antiferromagnetic interlayer exchange*. Physical Review B, vol. 39, no. 7, pages 4828–4830, March 1989, DOI:10.1103/PhysRevB.39.4828. (Cited on page 12.)

[Brown 1963] William Fuller Brown. *Thermal Fluctuations of a Single-Domain Particle*. Physical Review, vol. 130, no. 5, pages 1677–1686, June 1963, DOI:10.1103/PhysRev.130.1677. (Cited on pages 159 and 163.)

[Butler 2001] W. Butler, X.-G. Zhang, T. Schulthess and J. MacLaren. *Spin-dependent tunneling conductance of Fe/MgO/Fe sandwiches*. Physical Review B, vol. 63, no. 5, page 054416, January 2001, DOI:10.1103/PhysRevB.63.054416. (Cited on page 16.)

[Butler 2008] William H Butler. *Tunneling magnetoresistance from a symmetry filtering effect.* Science and Technology of Advanced Materials, vol. 9, no. 1, page 14106, April 2008, DOI:10.1088/1468-6996/9/1/014106. (Cited on page 16.)

[Butler 2012] W H Butler, Tim Mewes, Claudia K A Mewes, P B Visscher, William H Rippard, Stephen E Russek and Ranko Heindl. *Switching Distributions for Perpendicular Spin-Torque Devices Within the Macrospin Approximation.* IEEE Transactions on Magnetics, vol. 48, no. 12, pages 4684–4700, December 2012, DOI:10.1109/TMAG.2012.2209122. (Cited on pages 159, 164 and 165.)

[Coey 2010] J. M. D. Coey. Magnetism and Magnetic Materials. 2010. (Cited on page 12.)

[Coffey 2012] William T. Coffey and Yuri P. Kalmykov. *Thermal fluctuations of magnetic nanoparticles: Fifty years after Brown.* Journal of Applied Physics, vol. 112, no. 12, page 121301, 2012, DOI:10.1063/1.4754272. (Cited on page 161.)

[Devolder 2008] T. Devolder, J. Hayakawa, K. Ito, H. Takahashi, S. Ikeda, P. Crozat, N. Zerounian, Joo-Von Kim, C. Chappert and H. Ohno. *Single-Shot Time-Resolved Measurements of Nanosecond-Scale Spin-Transfer Induced Switching: Stochastic Versus Deterministic Aspects.* Physical Review Letters, vol. 100, no. 5, pages 2–5, February 2008, DOI:10.1103/PhysRevLett.100.057206. (Cited on pages 40 and 143.)

[Devolder 2011] T. Devolder, M. Belmeguenai, H. W. Schumacher, C. Chappert and Y. Suzuki. *Precessional strategies for the ultrafast switching of soft and hard magnetic nanostructures.* MRS Proceedings, vol. 746, page Q8.4, February 2011, DOI:10.1557/PROC-746-Q8.4. (Cited on page 47.)

[Devolder 2012] T. Devolder and K. Ito. *Spin torque switching and scaling in synthetic antiferromagnet free layers with in-plane magnetization.* Journal of Applied Physics, vol. 111, no. 12, page 123914, 2012, DOI:10.1063/1.4729776. (Cited on pages 58 and 73.)

[Dieny 2010] Bernard Dieny, RC Sousa, J. Herault, C Papusoi, G Prenat, U Ebels, D Houssameddine, B Rodmacq, S Auffret, L.D. Buda Prejbeanu, M.C. Cyrille, B. Delaet, Olivier Redon, C. Ducruet, J P. Nozieres and I.L. Prejbeanu. *Spin-transfer effect and its use in spintronic components.* International Journal of Nanotechnology, vol. 7, no. 4/5/6/7/8, page 591, 2010, DOI:10.1504/IJNT.2010.031735. (Cited on page 38.)

[Ebels 2008] U Ebels, D Houssameddine, I Firastrau, D Gusakova, C Thirion, B Dieny and L Buda-Prejbeanu. *Macrospin description of the perpendicular polarizer-planar free-layer spin-torque oscillator.* Physical Review B, vol. 78, no. 2, July 2008, DOI:10.1103/PhysRevB.78.024436. (Cited on pages 29, 43, 45, 46, 87, 90, 92, 102, 103, 105 and 137.)

[Firastrau 2013] I. Firastrau, L. D. Buda-Prejbeanu, B. Dieny and U. Ebels. *Spin-torque nano-oscillator based on a synthetic antiferromagnet free layer and perpendicular to plane polarizer.* Journal of Applied Physics, vol. 113, no. 11, page 113908, 2013, DOI:10.1063/1.4795160. (Cited on page 60.)

[Guckenheimer 1983] J. Guckenheimer and P. Holmes. Nonlinear Oscillations, Dynamical Systems, and Bifurcations of Vector Fields. 1983. (Cited on page 29.)

[Houssameddine 2007] D Houssameddine, U Ebels, B Delaët, B Rodmacq, I Firastrau, F Ponthenier, M Brunet, C Thirion, J-P Michel, L Prejbeanu-Buda, M-C Cyrille, Olivier Redon and B Dieny. *Spin-torque oscillator using a perpendicular polarizer and a planar free layer.* Nature materials, vol. 6, no. 6, pages 441–7, June 2007, DOI:10.1038/nmat1905. (Cited on pages 43, 136 and 137.)

[Houssameddine 2009] Dimitri Houssameddine. *Dynamique de l'aimantation de nano-oscillateurs micro-ondes à transfert de spin.* PhD thesis, 2009. (Cited on page 13.)

[Ichimura 2009] M. Ichimura, T. Hamada, H. Imamura, S. Takahashi and S. Maekawa. *Spin transfer torque in magnetic tunnel junctions with synthetic ferrimagnetic layers.* Journal of Applied Physics, vol. 105, no. 7, page 07D120, 2009, DOI:10.1063/1.3070627. (Cited on page 78.)

[Ichimura 2011] M. Ichimura, T. Hamada, H. Imamura, S. Takahashi and S. Maekawa. *Spin transfer torque in MTJs with synthetic ferrimagnetic layers by the Keldysh approach.* Journal of Applied Physics, vol. 109, no. 7, page 07C906, 2011, DOI:10.1063/1.3549437. (Cited on page 78.)

[Ikeda 2008] S. Ikeda, J. Hayakawa, Y. Ashizawa, Y. M. Lee, K. Miura, H. Hasegawa, M. Tsunoda, F. Matsukura and H. Ohno. *Tunnel magnetoresistance of 604% at 300 K by suppression of Ta diffusion in CoFeB/MgO/CoFeB pseudo-spin-valves annealed at high temperature.* Applied Physics Letters, vol. 93, no. 8, page 082508, 2008, DOI:10.1063/1.2976435. (Cited on page 16.)

[Izhikevich 2010] Eugene M. Izhikevich. Dynamical Systems in Neuroscience: The Geometry of Excitability and Bursting. 2010. (Cited on page 42.)

[Kent 2004] A. D. Kent, B. Özyilmaz and E. del Barco. *Spin-transfer-induced precessional magnetization reversal.* Applied Physics Letters, vol. 84, no. 19, page 3897, 2004, DOI:10.1063/1.1739271. (Cited on page 48.)

[Khalili Amiri 2011] P. Khalili Amiri, Z. M. Zeng, J. Langer, H. Zhao, G. Rowlands, Y.-J. Chen, I. N. Krivorotov, J.-P. Wang, H. W. Jiang, J. A. Katine, Y. Huai, K. Galatsis and K. L. Wang. *Switching current reduction using perpendicular anisotropy in CoFeB–MgO magnetic tunnel junctions.* Applied Physics Letters, vol. 98, no. 11, page 112507, 2011, DOI:10.1063/1.3567780. (Cited on pages 38 and 146.)

[Kim 2008] Joo-Von Kim, Vasil Tiberkevich and Andrei Slavin. *Generation Linewidth of an Auto-Oscillator with a Nonlinear Frequency Shift: Spin-Torque Nano-Oscillator.* Physical Review Letters, vol. 100, no. 1, pages 1–4, January 2008, DOI:10.1103/PhysRevLett.100.017207. (Cited on pages 87 and 107.)

[Kittel 1963] Charles Kittel. Introduction to Solid State Physics. 1963. (Cited on page 33.)

[Lee 2005] K. J. Lee, Olivier Redon and Bernard Dieny. *Analytical investigation of spin-transfer dynamics using a perpendicular-to-plane polarizer*. Applied Physics Letters, vol. 86, no. 2, page 022505, 2005, DOI:10.1063/1.1852081. (Cited on pages 43, 87 and 91.)

[Liu 2010] H. Liu, D. Bedau, D. Backes, J. a. Katine, J. Langer and a. D. Kent. *Ultrafast switching in magnetic tunnel junction based orthogonal spin transfer devices*. Applied Physics Letters, vol. 97, no. 24, page 242510, 2010, DOI:10.1063/1.3527962. (Cited on page 99.)

[Manchon 2006] A. Manchon and J C Slonczewski. *Generalization of a circuit theory for current perpendicular to plane magnetoresistance and current-driven torque*. Physical Review B, vol. 73, no. 18, pages 1–6, May 2006, DOI:10.1103/PhysRevB.73.184419. (Cited on page 25.)

[Manchon 2008] A. Manchon, C. Ducruet, L. Lombard, S. Auffret, B. Rodmacq, B. Dieny, S. Pizzini, J. Vogel, V. Uhlíř, M. Hochstrasser and G. Panaccione. *Analysis of oxygen induced anisotropy crossover in Pt/Co/MOx trilayers*. Journal of Applied Physics, vol. 104, no. 4, page 043914, 2008, DOI:10.1063/1.2969711. (Cited on page 19.)

[Marins de Castro 2011] Maria Marins de Castro. *Commutation précessionelle de mémoire magnétique avec polariseur à anisotropie perpendiculaire*. (Cited on page 132.)

[Marins de Castro 2012] M. Marins de Castro, R. C. Sousa, S. Bandiera, C. Ducruet, a. Chavent, S. Auffret, C. Papusoi, I. L. Prejbeanu, C. Portemont, L. Vila, U. Ebels, B. Rodmacq and B. Dieny. *Precessional spin-transfer switching in a magnetic tunnel junction with a synthetic antiferromagnetic perpendicular polarizer*. Journal of Applied Physics, vol. 111, no. 7, page 07C912, 2012, DOI:10.1063/1.3676610. (Cited on pages 99 and 128.)

[Monso 2002] S. Monso, B. Rodmacq, S. Auffret, G. Casali, F. Fettar, B. Gilles, B. Dieny and P. Boyer. *Crossover from in-plane to perpendicular anisotropy in Pt/CoFe/AlO[sub x] sandwiches as a function of Al oxidation: A very accurate control of the oxidation of tunnel barriers*. Applied Physics Letters, vol. 80, no. 22, page 4157, 2002, DOI:10.1063/1.1483122. (Cited on page 19.)

[Murdock 1991] J. Murdock. Perturbations: Theory and Methods. 1991. (Cited on page 94.)

[Nistor 2010] Lavinia Elena Nistor, Bernard Rodmacq, Clarisse Ducruet, Céline Portemont, I. Lucian Prejbeanu and Bernard Dieny. *Correlation Between Perpendicular Anisotropy and Magnetoresistance in Magnetic Tunnel Junctions*. IEEE Transactions on Magnetics, vol. 46, no. 6, pages 1412–1415, June 2010, DOI:10.1109/TMAG.2010.2045641. (Cited on page 19.)

[Oh 2009] Se-Chung Oh, Seung-Young Park, Aurélien Manchon, Mairbek Chshiev, Jae-Ho Han, Hyun-Woo Lee, Jang-Eun Lee, Kyung-Tae Nam, Younghun Jo, Yo-Chan Kong, Bernard Dieny and Kyung-Jin Lee. *Bias-voltage dependence of perpendicular spin-transfer torque in asymmetric MgO-based magnetic tunnel junctions*. Nature Physics, vol. 5, no. 12, pages 898–902, October 2009, DOI:10.1038/nphys1427. (Cited on pages 25, 132 and 163.)

[Osborn 1945] J. Osborn. *Demagnetizing Factors of the General Ellipsoid*. Physical Review, vol. 67, no. 11-12, pages 351–357, June 1945, DOI:10.1103/PhysRev.67.351. (Cited on page 20.)

[Quinsat 2012] Mickael Quinsat. *Etude d'un auto-oscillateur non-isochrone : Application à la dynamique non-linéaire de l'aimantation induite par transfert de spin*. PhD thesis, 2012. (Cited on pages 44 and 67.)

[Redon 2001] Olivier Redon, Bernard Dieny and Bernard Rodmacq. *Magnetic spin polarization and magnetization rotation device with memory and writing process, using such a device*, 2001. US20010990321. (Cited on page 47.)

[Rodmacq 2003] B. Rodmacq, S. Auffret, B. Dieny, S. Monso and P. Boyer. *Crossovers from in-plane to perpendicular anisotropy in magnetic tunnel junctions as a function of the barrier degree of oxidation*. Journal of Applied Physics, vol. 93, no. 10, page 7513, 2003, DOI:10.1063/1.1555292. (Cited on page 19.)

[Rodmacq 2009] B. Rodmacq, A. Manchon, C. Ducruet, S. Auffret and B. Dieny. *Influence of thermal annealing on the perpendicular magnetic anisotropy of Pt/Co/AlOx trilayers*. Physical Review B, vol. 79, no. 2, page 024423, January 2009, DOI:10.1103/PhysRevB.79.024423. (Cited on page 19.)

[Sato 2011] H. Sato, M. Yamanouchi, K. Miura, S. Ikeda, H. D. Gan, K. Mizunuma, R. Koizumi, F. Matsukura and H. Ohno. *Junction size effect on switching current and thermal stability in CoFeB/MgO perpendicular magnetic tunnel junctions*. Applied Physics Letters, vol. 99, no. 4, page 042501, 2011, DOI:10.1063/1.3617429. (Cited on page 22.)

[Schneider 2007] M. L. Schneider, M. R. Pufall, W. H. Rippard, S. E. Russek and J. A. Katine. *Thermal effects on the critical current of spin torque switching in spin valve nanopillars*. Applied Physics Letters, vol. 90, no. 9, page 092504, 2007, DOI:10.1063/1.2709963. (Cited on page 39.)

[Seki 2010] Takeshi Seki, Hiroyuki Tomita, Masashi Shiraishi, Teruya Shinjo and Yoshishige Suzuki. *Coupled-Mode Excitations Induced in an Antiferromagnetically Coupled Multilayer by Spin-Transfer Torque*. Applied Physics Express, vol. 3, no. 3, page 033001, February 2010, DOI:10.1143/APEX.3.033001. (Cited on page 82.)

[Serpico 2003] C. Serpico, I. D. Mayergoyz and G. Bertotti. *Analytical solutions of Landau-Lifshitz equation for precessional switching*. Journal of Applied Physics, vol. 93, no. 10, page 6909, 2003, DOI:10.1063/1.1557278. (Cited on page 47.)

[Silva 2010] TJ J Silva and Mark W. Keller. *Theory of Thermally Induced Phase Noise in Spin Torque Oscillators for a High-Symmetry Case*. IEEE Transactions on Magnetics, vol. 46, no. 9, pages 3555–3573, September 2010, DOI:10.1109/TMAG.2010.2044583. (Cited on pages 90, 92 and 94.)

[Slavin 2008] Andrei Slavin and Vasil Tiberkevich. *Excitation of Spin Waves by Spin-Polarized Current in Magnetic Nano-Structures*. IEEE Transactions on Magnetics, vol. 44, no. 7, pages 1916–1927, July 2008, DOI:10.1109/TMAG.2008.924537. (Cited on pages 77, 87 and 107.)

[Slavin 2009] Andrei Slavin and Vasil Tiberkevich. *Nonlinear Auto-Oscillator Theory of Microwave Generation by Spin-Polarized Current*. IEEE Transactions on Magnetics, vol. 45, no. 4, pages 1875–1918, April 2009, DOI:10.1109/TMAG.2008.2009935. (Cited on pages 67, 87 and 107.)

[Slonczewski 1996] J C Slonczewski. *Current-driven excitation of magnetic multilayers*. Journal of Magnetism and Magnetic Materials, vol. 159, no. 1-2, pages L1–L7, 1996, DOI:10.1016/0304-8853(96)00062-5. (Cited on page 24.)

[Slonczewski 2002] J C Slonczewski. *Currents and torques in metallic magnetic multilayers*. Journal of Magnetism and Magnetic Materials, vol. 247, no. 3, pages 324–338, 2002, DOI:10.1016/S0304-8853(02)00291-3. (Cited on pages 13 and 25.)

[Slonczewski 2005] J C Slonczewski. *Currents, torques, and polarization factors in magnetic tunnel junctions*. Physical Review B, vol. 71, no. 2, pages 1–10, January 2005, DOI:10.1103/PhysRevB.71.024411. (Cited on pages 14, 15 and 25.)

[Smit 1955] J Smit and H G Beljers. *Ferromagnetic resonance absorption in BaFe12O19 , a high anisotropy crystal*. Philips Research Reports, vol. 10, pages 113–130, (Cited on page 30.)

[Taniguchi 2011] Tomohiro Taniguchi and Hiroshi Imamura. *Thermally assisted spin transfer torque switching in synthetic free layers*. Physical Review B, vol. 83, no. 5, page 054432, February 2011, DOI:10.1103/PhysRevB.83.054432. (Cited on pages 80, 159 and 162.)

[Theodonis 2006] Ioannis Theodonis, Nicholas Kioussis, Alan Kalitsov, Mairbek Chshiev and W. Butler. *Anomalous Bias Dependence of Spin Torque in Magnetic Tunnel Junctions*. Physical Review Letters, vol. 97, no. 23, page 237205, December 2006, DOI:10.1103/PhysRevLett.97.237205. (Cited on pages 26 and 132.)

[Timm 2011] Carsten Timm. Theory of Magnetism. 2011, Link. (Cited on page 11.)

[Tsunekawa 2005] Koji Tsunekawa, David D. Djayaprawira, Motonobu Nagai, Hiroki Maehara, Shinji Yamagata, Naoki Watanabe, Shinji Yuasa, Yoshishige Suzuki and Koji Ando. *Giant tunneling magnetoresistance effect in low-resistance CoFeB/MgO(001)/CoFeB magnetic tunnel junctions for read-head applications*. Applied Physics Letters, vol. 87, no. 7, page 072503, 2005, DOI:10.1063/1.2012525. (Cited on page 16.)

[Victora 1989] R. Victora. *Predicted time dependence of the switching field for magnetic materials*. Physical Review Letters, vol. 63, no. 4, pages 457–460, July 1989, DOI:10.1103/PhysRevLett.63.457. (Cited on page 163.)

[Widom 2010] a. Widom, C. Vittoria and S. D. Yoon. *Gilbert ferromagnetic damping theory and the fluctuation-dissipation theorem*. Journal of Applied Physics, vol. 108, no. 7, page 73924, 2010, DOI:10.1063/1.3330646. (Cited on page 22.)

[Yang 2011] H. X. Yang, M. Chshiev, B. Dieny, J. H. Lee, A. Manchon and K. H. Shin. *First-principles investigation of the very large perpendicular magnetic anisotropy at Fe/MgO and Co/MgO interfaces*. Physical Review B, vol. 84, no. 5, page 054401, August 2011, DOI:10.1103/PhysRevB.84.054401. (Cited on page 19.)

[Zhang 2004] X.-G. Zhang and W. H Butler. *Large magnetoresistance in bcc Co/MgO/Co and FeCo/MgO/FeCo tunnel junctions*. Physical Review B, vol. 70, no. 17, page 172407, November 2004, DOI:10.1103/PhysRevB.70.172407. (Cited on page 16.)

Glossary

GMR Giant magneto-resistance

IPP In-plane precession

IPS In-plane static equilibrium

MRAM Magnetic random access memory

OPP Out-of-plane precession

OPS Out-of-plane static equilibrium

SAF Synthetic antiferromagnet

STO Spin torque oscillator

STT Spin transfer torque

SyF Synthetic ferrimagnet

TMR Tunnel magneto-resistance

α Adimensional Gilbert damping constant

β_{IEC} IEC coefficient : $b_J = -\alpha\beta_{IEC}a_J$

$\boldsymbol{H}_a$, H_a Applied field, vector and norm

$\boldsymbol{H}_{eff}$ Effective field. Unit : A/m, sometimes T implicit multiplication by μ_0.

$\boldsymbol{M}$ Magnetic moment by unit volume, or magnetization

$\boldsymbol{m}$ Magnetization direction. Unit vector.

$\boldsymbol{u}_x, \boldsymbol{u}_y, \boldsymbol{u}_z$ Cartesian coordinates unit vectors

χ Magneto-resistance ratio : $\chi = \dfrac{R_{AP} - R_P}{R_P}$

$\Delta\omega$ Linear linewidth

η_{LONG} Spin polarization along the easy axis

η_{PERP} Spin polarization in the out-of-plane direction

Γ Dissipative potential : $\Gamma = \alpha E - P$

γ Gyromagnetic ratio : $\gamma = 1.76 \times 10^{11}$ rad/(s.T)

λ_{LONG} Spin polarization asymmetry along the easy axis

λ_{PERP} Spin polarization asymmetry in the out-of-plane direction

$\mathcal{H}$ Conservative potential : $\mathcal{H} = E + \alpha\beta_{IEC}P$

μ_0 Vacuum permeability : $\mu_0 = 4\pi \times 10^{-7}$ Tm/A

ω_0 Natural or FMR frequency

θ, ϕ Angles in spherical coordinates

a_J Spin transfer torque amplitude. Unit: A/m

b_J Interface exchange coupling (or field-like term) amplitude. Unit: A/m

E Magnetic free energy. Unit : J

H_c Coercive field

H_d Demagnetizing field

H_k Anisotropy field

I_c Critical current

J_{RKKY} Ruderman-Kittel-Kasuya-Yosida interaction energy per unit area. Unit : J/m^2

M_S Saturation magnetization

P Spin torque potential. Unit: J

V Volume of the free layer

Contents

Résumé en français

Introduction

La découverte de la magnéto-résistance géante (GMR), indépendamment par A. Fert et P. Grünberg en 1988, définit le point de départ de la spintronique. Depuis cette découverte, pour laquelle leurs auteurs ont reçu le Prix Nobel de Physique en 2005, de nombreux composants électroniques qui exploitent le moment magnétique de l'électron, plus connu sous le nom de spin, ont vu le jour. Une de ces applications spintroniques parmi les plus connues est sans doute la tête de lecture de disque dur (HDD) de grande capacité, qui équipe la plupart des ordinateurs. En raison de la diffusion dépendante en spin et/ou de la polarisation en spin des électrons de conduction, la résistance d'un empilement composé de deux couches magnétiques dépend de l'orientation relative de l'aimantation de ces deux couches. Les deux couches ont généralement leurs aimantations soit parallèles (P), soit antiparallèles (AP), orientations qui se traduisent par deux états de résistance différents. Dans les têtes de lectures de disques durs, les deux couches magnétiques sont séparées par un espaceur métallique non-magnétique, mais les deux niveaux de résistance sont plus différenciés si les couches magnetiques sont séparées par une couche isolante. Dans ce cas, l'effet magnétorésistif (MR) peut être utilisé pour lire l'information stockée dans des bits magnétiques à base de nanopilliers composés de deux couches magnétiques séparées par un isolant, ce qu'on appelle un jonction tunnel magnétique (MTJ). Les MTJ sont à la base des mémoires vives magnétiques (MRAM), qui ont pour avantages d'être non-volatiles, rapides, d'avoir une endurance quasi-infinie, une grande densité de stockage et une faible consommation.
Prédit par J.C. Slonczewski et L. Berger en 1996, le couple de transfert de spin (STT) permet de modifier la direction d'aimantation d'une couche dans un nanopilier en faisant circuler un courant électrique à travers la jonction. En combinant les deux effets, la MR pour la lecture et le STT pour l'écriture, une nouvelle génération de MRAM a vu le jour, les STT-MRAM, qui sont actuellement en recherche et développement. De nombreuses pistes de recherche sont

en cours d'investigation pour le STT-MRAM: des empilements avec des couches à aimantation perpendiculaire, le retournement assisté thermiquement et le polariseur orthogonal. Cette thèse se focalise principalement sur le dernier type de STT-MRAM, une MTJ planaire avec polariseur perpendiculaire, une couche supplémentaire à aimantation perpendiculaire.
Dans les STT-MRAM conventionnelles, la couche de stockage est renversée par STT, grâce au courant polarisé en spin dû à l'autre couche magnétique planaire, dite couche de référence. Or, le STT est nul lorsque les aimantations des couches de stockage et de référence sont alignées, il est maximal si leurs aimantations sont orthogonales. C'est pourquoi le retournement est stochastique si les deux aimantations sont alignées, initié par les fluctuations thermiques aléatoires, ce qui donne des temps de retournement de l'ordre de la dizaine de nanosecondes. Pour remplacer la mémoire vive actuelle, ces temps d'écriture sont convenables, mais pour une utilisation des STT-RAM en tant que mémoire cache, il faut un temps d'écriture en dessous de la nanoseconde. Pour y remédier, l'ajout d'un polariseur perpendiculaire, dont l'aimantation est orthogonale à celle de la couche de stockage, a été proposé et a fait l'objet d'un brevet par O. Redon et al. de SPINTEC en 2001. En 2009, O.J. Lee et al. ainsi que C. Papusoi et al. ont montré expérimentalement que l'on pouvait réduire le temps de retournement à moins d'une nanoseconde dans des dispositifs comparables tout-métalliques. En 2011, M. Marins a montré que le polariseur perpendiculaire induit une oscillation de l'aimantation de la couche de stockage qui est préjudiciable pour des applications mémoire. En effet, le polariseur perpendiculaire entre aussi dans la fabrication de nano-oscillateurs à STT pour l'émission radio-fréquence, ainsi le comportement d'oscillation et de retournement peuvent s'obtenir avec la même structure.
Le but de cette thèse est de comprendre la dynamique d'une MTJ planaire avec polariseur perpendiculaire, en étudiant cette structure à la fois théoriquement, par le biais de simulations macrospins et enfin expérimentalement, le tout dans le but de réduire le temps de renversement avec un retournement déterministe. Nous discuterons de l'avantage d'utiliser une couche de stockage synthétique ferromagnétique. Nous déterminerons théoriquement les conditions pour rencontrer un comportement oscillant ou bien un retournement, puis nous comparerons ces résultats aux simulations macrospins. Enfin, nous réaliserons des mesures en temps-réel de la dynamique de retournement, qui s'avèrent être en accord avec les prédictions théoriques.

La **partie I** est une introduction aux phénomènes spintroniques et aux dispositifs qui ont rapport avec cette thèse. Le chapitre 1 présente le principe de la magnétorésistance et la dynamique de l'aimantation d'une couche libre magnétique. La dynamique d'une couche libre est décrite par l'équation de Landau-Lifshitz-Gilbert-Slonczewski (LLGS) dans l'approximation macrospin. Elle est constituée d'un terme conservatif, relatif à l'énergie magnétique de la

couche, plus un terme dissipatif qui décrit la relaxation et le STT. La stabilité de la configuration magnétique à l'équilibre est déduite en linéarisant l'équation du mouvement, ce qui permet d'obtenir les courants et champs critiques de retournement. Le chapitre 2 offre une description des STT-MRAM de première et deuxième génération, ainsi que des nano-oscillateurs avec polariseur perpendiculaire. Nous présenterons enfin le dispositif qui nous intéresse dans cette thèse, à savoir une MTJ planaire avec polariseur perpendiculaire.

La **partie II** des résultats théoriques préliminaires sur la structure complète. Dans le chapitre 3, nous étudierons une couche libre constituée d'une couche ferromagnétique synthétique, en particulier la dynamique avec courant appliqué, indépendamment avec un polariseur planaire, puis perpendiculaire. Nous comparerons ces résultats à ceux d'une couche libre simple, notamment les courants critiques. Dans le chapitre 4, nous présenterons une étude théorique des oscillations hors du plan de l'aimantation de la couche libre (pour une couche simple), sous l'effet du STT du polariseur perpendiculaire, dans laquelle le champ externe, le champ d'anisotropie et le STT de la couche de référence sont introduit en tant que perturbations. Une telle approche permet de calculer le changement de fréquence ainsi que les courants critiques dus à ces perturbations.

La **partie III** présente une analyse théorique en macrospin d'une MTJ planaire avec polariseur perpendiculaire. En particulier, nous étudierons l'influence relative des deux couches polarisantes, ainsi que l'influence du champ d'anisotropie sur la dynamique d'aimantation de la couche libre et sur l'existence d'oscillations ou d'un retournement. Ces résultats seront comparés à des simulations micromagnétiques, qui confirment bien qu'un fort champ d'anisotropie favorise le retournement au détriment des oscillations. Enfin, des mesures de retournement en temps réels réalisées sur des nano-piliers à section elliptiques avec différents rapport d'aspect confirme cette tendance, les échantillons à faible rapport d'aspect montrant des oscillations, et ceux à fort rapport d'aspect un retournement en moins d'une nanoseconde. Nous étudierons aussi expérimentalement l'effet des fluctuations thermiques dans les deux régimes.

L'annexe est dédié à l'analyse théorique des fluctuations thermiques dans le modèle macrospin. Nous présenterons quelques résultats de probabilité de retournement sous courant, dans le cas particulier des couches à aimantation perpendiculaire qui est résoluble. Nous discuterons ces résultats par rapport à la structure qui nous intéresse dans cette thèse.

I - Chapitre 1 - Phénomènes spintroniques et dynamique de l'aimantation

L'effet de magnétorésistance géante est à la base des dispositifs spintroniques. Si on considère un empilement de deux couches magnétiques métalliques séparées par une couche isolante, la résistance de l'empilement dépend de la direction relative des aimantations des deux couches magnétiques. On observe un état de résistance minimale quand les deux couches ont des aimantations parallèles (P), et maximale pour des orientations antiparallfles (AP). Ce principe est à la base des mémoires magnétiques, entre autres.
La dynamique de l'aimantation est régie par l'équation de Landau-Lifshitz-Gilbert-Slonczewski (LLGS), équation 1.37. On peut diviser cette équation en deux termes, un terme conservatif et un terme dissipatif. Le terme conservatif est un terme de précession à énergie constante. Le terme dissipatif est composé de la relaxation dans la direction du gradient d'énergie, ainsi qu'un terme de couple de transfert de spin (STT), qui est proportionnel au courant appliqué à travers la couche.
Pour étudier la stabilité de la couche magnétique par un champ ou un courant appliqué, on linéarise l'équation LLGS. La stabilité de l'équilibre magnétique est alors donné par le signe de la partie réelle des valeur propres—au nombre de deux, complexes conjuguées, pour une couche simple. A partir des formules analytiques on peut extraire la valeur des champs et courants critiques pour une couche simple.

I - Chapitre 2 - Dispositifs spintroniques

Les mémoires magnétiques STTRAM sont l'objet principal de cette thèse, une mémoire magnétique à écriture par STT. Pour lire un bit de la STTRAM, il suffit de mesurer la résistance de la jonction tunnel magnétique—deux couches magnétiques séparées par une couche isolante, généralement du MgO. Si les deux aimantations sont parallèles, on mesure une faible résistance et donc un bit 0, si les aimantations sont antiparallèles, on mesure une forte résistance et un bit 1. Pour l'écriture, une des deux couches étant fixe, nommée couche de référence, on envoie un courant électrique pour modifier l'orientation de l'autre couche, dite couche libre ou de stockage, par effet STT. Cependant, l'amplitude du STT dépend de l'orientation relative des aimantations des deux couches, prenant une valeur maximale lorsque les aimantations sont perpendiculaire, et nulle si elles sont colinéaires. Pour ces STTRAM conventionnelles, le STT est donc nul à l'équilibre, le retournement n'est possible que grâce aux fluctuations thermiques

de l'aimantation. C'est pourquoi le retournement se produit généralement en une dizaine de nanosecondes. Pour accélérer le retournement il faut donc trouver une autre solution.
Les nano-oscillateurs à STT (STO) sont un autre type de dispositif spintronique intéressant pour cette thèse. Sous l'effet du STT, en courant continu, l'aimantation de la couche libre suit une trajectoire périodique, qui se traduit par une résistance variable en fonction du temps, un oscillateur. Les STO sont généralement composés de couches à aimantation planaire, dont la précession est de petite amplitude autour de l'état d'équilibre. Cependant, il est possible de réaliser de STO à large amplitude de précession en rajoutant une couche à aimantation perpendiculaire au plan. Sous l'effet de STT du polariseur perpendiculaire, l'aimantation de la couche libre est tirée hors du plan, ainsi l'aimantation rentre alors en précession autour de l'axe normal au plan qui est la direction du champ effectif le plus fort, à savoir le champ démagnétisant. De cette manière, l'aimantation oscille entre les configuration P et AP, conférant une amplitude maximale á la variation de résistance. Ce type de dispositif est très encourageant pour les applications STO car la puissance émise est grande, mais il est peu pratique pour une application MRAM. Il faudrait alors calibrer la durée de l'impulsion de courant envoyée pour que celle-ci ait exactement la durée d'une demi-précession pour renverser l'aimantation. Cela correspond à des impulsions de moins d'une nanoseconde, ce qui est impossible à réaliser dans les circuits CMOS actuels.
En revanche, le polariseur perpendiculaire peut servir à initier le renversement de la couche, car le STT qu'il induit est maximal à l'équilibre. On cherche donc à optimiser le dispositif qui fait l'objet de cette thèse, une MTJ planaire avec polariseur perpendiculaire, pour qu'il présente un fonctionnement de retournement bipolaire (en fonction du sens du courant, la position finale est P ou AP), et pas d'oscillations.

II - Chapitre 3 - OPP induites par STT et courants critiques dans un ferrimagnétique synthétique

Les échantillons réalisés sont composés d'une couche libre dite ferrimagnétique synthétique SyF, i.e. composée de deux couche magnétiques séparées par une fine couche de Ru pour les coupler par effet RKKY. C'est donc l'occasion d'étudier la dynamique de ces couches sous courant puisque cela n'a pas était fait de manière théorique. Dans un premier temps, on s'intéresse aux courants critiques quand la couche libre SyF est sujette seulement au STT du polariseur perpendiculaire. On trouve les formules des courants critiques, et leur dépendance en fonction du couplage RKKY par exemple. Le courant critique dépend aussi des épaisseurs relatives des

deux couches.
Ensuite on s'intéresse au courant critique du SyF quand le STT provient de la couche de référence planaire, qui est plus important pour réaliser des MTJ planaires avec une couche libre SyF. Après quelques calculs, dans l'approximation d'une faible constante de relaxation α et d'un couple RKKY assez fort (correspondant aux valeurs calssiques dans les applications), on obtient l'expression du courant critique. En revanche, il y a deux types de courants critiques, qui correspondent aux deux modes d'excitation du SyF, acoustique et optique. Au dessus du courant critique, un de ces modes est déstabilisé, ce qui fait que lorsque le mode acoustique est déstabilisé des oscillations auto-entretenues dans le plan (IPP) peuvent apparaitre, ce qui est intéressant pour une application STO mais pas MRAM, et si le mode optique est déstabilisé, ces IPP n'existent pas, ce qui est une configuration favorable aux applications MRAM.
De plus, on étudie différentes manières de réduire le courant critique dans un SyF, ce qui est possible si on introduit une asymétrie entre les deux couches du SyF. Cela peut être fait de différentes manières, on propose deux cas particuliers, une asymétrie en épaisseur, puis une asymétrie en champ démagnétisant, qui est introduite par l'anisotropie perpendiculaire de surface qui réduit le champ démagnétisant d'une des deux couches.

II - Chapitre 4 - Perturbation de la précession hors du plan dans une MTJ planaire avec polariseur perpendiculaire

On revient ensuite à une couche libre simple pour étudier plus précisément l'oscillation de large amplitude (OPP) due au STT du polariseur perpendiculaire. D'un point de vue théorique, ces OPP ne sont bien comprises que si l'anisotropie planaire, le champ externe et le STT de la couche de référence sont exclus du modèle. En effet, dans ce cas, seul le STT du polariseur perpendiculaire et le champ démagnétisant interviennent et la trajectoire de l'aimantation est très simple : c'est un cercle à aimantation hors du plan m_z constant. Pour introduire les trois autres termes pré-cités, il faut utiliser une approche perturbative, en l'occurrence en utilisant des séries de Lindstedt qui sont particulièrement judicieuses pour traiter des cas de trajectoires périodiques. Chaque terme est traité individuellement.
Pour prendre l'exemple du champ d'anisotropie H_K, le paramètre de perturbation est le rapport entre la fréquence de Larmor associée à ce champ et la fréquence propre des OPP. Les OPP ayant une fréquence autour de 1 GHz, l'approche en perturbation est valable pour de grandes

valeurs du champ d'anisotropie, bien au-delà de celles mesurées expérimentalement. Avec cette approche, on obtient l'expression approchée (au premier ordre pour l'instant) de la trajectoire avec H_K. Cette trajectoire approché contient la trajectoire non-perturbée circulaire, plus une petite modification sinusoïdale : lors de la précession, l'aimantation hors du plan m_z est plus grande que la valeur moyenne quand elle est en face de l'axe facile (direction de $\mathbf{H}_K$), est plus petite quand elle est proche de l'axe difficile. Si on calcule la trajectoire à l'ordre 2, on trouve que la fréquence des OPP est modifiée sous l'influence de H_K, la fréquence diminue de manière quadratique par rapport à H_K. Pour de fortes valeurs de H_K, la fréquence devient nulle, ce qui donne un critère sur H_K, mais aussi sur le courant appliqué, pour une disparition des OPP. Cela permet de déduire l'expression d'un courant critique, en fonction de H_K, en dessous duquel les OPP n'existent plus. Ce courant critique est proportionnel à la racine carrée de H_K. En augmentant H_K, on peut donc détruire les OPP dans la gamme de courant utilisée pour des applications. Malheureusement de telles valeurs de champ d'anisotropie sont un peu trop grande en pratique.
De la même manière, on applique ce traitement en perturbation pour le champ externe et le STT de la référence. En ce qui concerne le STT de la référence, pour les valeurs de polarisation en spin rencontrées dans les applications, on se rend compte que celui-ci n'affecte que très peu la trajectoire des OPP, ce qui est une bonne nouvelle pour les STO avec polariseur perpendiculaire, puisque la couche de référence indispensable à la mesure de résistance, ne perturbe pas beaucoup la dynamique attendue. En revanche, cela n'est d'aucune aide pour éliminer les oscillations pour une application MRAM.

III - Chapitre 5 - Etude théorique et expérimentale de la dynamique induite par STT dans une MTJ planaire avec polariseur perpendiculaire

On arrive enfin au dispositif complet, composé d'une couche libre à aimantation planaire (couche simple dans le modèle théorique, toutefois), d'une couche de référence planaire et d'un polariseur perpendiculaire. En première analyse, on peut comparer les courants critiques I_c^{PERP}, de mise en oscillation OPP à cause du STT du polariseur perpendiculaire, et I_c^{LONG}, de retournement à cause du STT de la référence. Pour une application MRAM, on cherche à appliquer un courant plus grand que le courant de retournement I_c^{LONG}, mais plus petit que le courant de mise en OPP I_c^{PERP}. Pour cela, il faut augmenter I_c^{PERP}, tout en diminuant I_c^{LONG}. Pour cela on a

deux paramètres, le rapport $r = \eta_{PERP}/\eta_{LONG}$ et le champ d'anisotropie H_K. Comme seul le courant critique de mise en OPP dépend de H_K, de manière linéaire, il apparait judicieux, pour favoriser le retournement bipolaire et éliminer les oscillations, d'augmenter H_K. Dans la pratique, cela revient à réaliser des échantillons cylindriques avec une section ellipsoïdale à fort rapport d'aspect d'ellipse.
Des calculs théoriques en macrospin plus précis confirment cette tendance, de même que les simulations macrospins. Les simulations micromagnétiques s'éloignent légèrement des calculs macrospins, notamment parce que les OPP ne sont pas vraiment macrospins, mais la tendance à une élimination des OPP quand le rapport d'aspect augmente est aussi avérée.
Enfin, des mesures de retournement en temps-réel ont été réalisées, en observant le signal transmis à travers la jonction pendant l'application de l'impulsion de courant avec un oscilloscope. Ces mesures ont été réalisées sur des échantillons avec différents rapports d'aspect, faible et fort. Avec un faible rapport d'aspect, les nano-piliers étant presque circulaires, on observe bien une oscillations entre les états de résistance correspondants aux équilibres P et AP pendant l'application de l'impulsion. La fréquence et la reproductibilité de ces oscillations ont été mesurées à différentes températures, entre 80 K et 400 K, en collaboration avec Thibault Devolder à l'IEF, Orsay. On observe que la décohérence des oscillations est liée aux fluctuations thermiques, qui sont à l'origine aussi de la largeur de raie observée dans les STO avec polariseur perpendiculaire.
Pour les échantillons à fort rapport d'aspect, on observe un retournement de la couche libre sans oscillation lorsque l'impulsion de courant est appliquée. Plus le courant appliqué est fort et plus le retournement est rapide, avec un retournement en moins d'une nanoseconde pour les plus forts courants appliqués.

Conclusion

Dans la partie expérimentale de ce travail, nous avons montré qu'en fonction de l'amplitude relative des STT du polariseur perpendiculaire et de la couche de référence, une MTJ planaire avec polariseur perpendiculaire présente deux comportements différents. Lorsque le STT du polariseur perpendiculaire est dominant, l'aimantation de la couche libre entre en oscillation avec un courant appliqué. Au contraire, si le STT de la couche de référence est prépondérant, la couche libre se renverse dans la configuration P, ou AP, ce en fonction du sens du courant. Nous avons également constaté que le champ d'anisotropie affecte le régime de fonctionnement, en l'occurrence qu'un fort champ d'anisotropie favorise le retournement bipolaire. C'est donc

un moyen de contrôler la dynamique de retournement dans une MTJ avec polariseur perpendiculaire, dans le but d'obtenir un retournement déterministe en moins d'une nanoseconde.
En réduisant le champ démagnétisant grâce à l'anisotropie perpendiculaire de surface à l'interface avec la couche de MgO, on obtient une MTJ planaire à courant critique fortement réduits. Les dispositifs à champs démagnétisant réduits sont donc très intéressant pour des applications mémoire faible consommation, mais la miniaturisation de telles structures est limitée à des dimensions de l'ordre de 150nm×60nm en raison de la stabilité thermique de la couche de stockage planaire.

D'un point de vue théorique, les résultats de la partie II sont encourageants.
Tout d'abord, nous avons présenté une analyse de la stabilité des couches libres SyF sous courant. Après avoir calculé le courant critique dans un SyF, nous avons montré que celui-ci était plus faible dans le cas de couches SyF asymétriques. Nous avons aussi montré que le mode de déstabilisation pouvait être acoustique ou optique, et qu'il était possible d'ajuster les paramètres du SYF pour sélectionner l'un ou l'autre de ces modes.
Cependant, la linéarisation présentée dans ce chapitre n'était pas suffisante pour prédire l'existence d'oscillations auto-entretenue de l'aimantation de la couche libre, ce qui serait d'un intérêt majeur en vue d'intégrer des couches libres SyF dans des nano-oscillateurs STT. Une perspective de cette analyse linéaire serait d'utiliser le formalisme de la théorie KTS pour extraire les paramètres non-linéaires d'un SyF.
Le deuxième résultat de cette partie était le traitement en perturbation du champ externe, du champ d'anisotropie et du STT de la couche de référence par rapport au mouvement de précession de l'aimantation d'une couche libre à aimantation planaire avec polariseur perpendiculaire. Nous avons montré que ces perturbations modifient la trajectoire de l'aimantation de la couche libre, qui est initialement circulaire quand un courant est appliqué. Nous avons calculé les trajectoires perturbées avec succès et nous avons quantifié les changements de fréquence engendrés, qu'il faudrait mesurer expérimentalement pour comparaison. Les courants critiques dus à ces perturbations ont également été extraits grâce à cette analyse.
Ces résultats sont applicables aux oscillateurs STT avec polariseur perpendiculaire, mais les STO sont généralement basés sur des couches à aimantation planaire, qui donnent lieu à des précessions dans le plan et non hors du plan. Par conséquent, il serait intéressant d'un point de vue applicatif d'adapter cette approche perturbative aux précessions dans le plan. Le formalisme le plus pratique pour atteindre cet objectif semble être, une fois de plus, la théorie KTS. En raison du grand nombre de recherches théoriques et expérimentales sur les STO planaires, ces résultats de précession hors du plan sont encourageant et présentent un fort intérêt.